UNIVERSITAT POLITÈCNICA DE CATALUNYA BARCELONATECH

Infrared optical filters based in macroporous silicon for spectroscopic gas detection

David Cardador Maza

UNIVERSITAT POLITÈCNICA DE CATALUNYA
BARCELONATECH
Departament d'Enginyeria Electrònica

"INFRARED OPTICAL FILTERS BASED IN MACROPOROUS SILICON FOR SPECTROSCOPIC GAS DETECTION"

Thesis submitted in partial fulfilment of the requirement for the PhD Degree issued by the Universitat Politècnica de Catalunya, in its Electronic Engineering Program.

Thesis by compendium of publications

David Cardador Maza

Director: *Ángel Rodríguez Martínez*

September 2019

Agradecimientos

Cuando comencé el doctorado no podía imaginar lo que me deparaban estos cinco intensísimos años. Han pasado muchísimas cosas. Ha habido idas y venidas, miles de comienzos y otros muchos finales. Ha habido momentos en que pensé que tenía que dejar la tesis, o acabarla cuanto antes. En esos momentos, la solidaridad y los consejos de mis seres más queridos me hicieron coger aire, ver las cosas con cierta distancia y que no me precipitara en decisiones que, visto en retrospectiva, no me hubieran traído buenas consecuencias. No tengo la menor duda que sin ellas ahora mismo no estaría escribiendo estas letras que concluyen más que una tesis, un periodo.

Un periodo que, siendo estrictos, empezó cuando Ramón y Moisés me acogieron para hacer el TFM y me abrieron el hambre por la investigación. Les agradezco esa oportunidad y que me pusieran en contacto con Ángel y Dídac, gracias a los cuales me introduje en el apasionante mundo de los cristales fotónicos. Ahí empezó uno de los muchos viajes en los que me embarcaría a lo largo de estos últimos años y en el que me he encontrado con verdaderos amigos. Dani, trobar-te va ser una gran sort. Que sàpigues que et valoro molt i que espero que el projecte en el que ens embarquem potenciï encara més aquesta entesa. Chenna: it was really nice to know you and to become your friend. Thank you for being always there. Yannis: trabajar contigo fue toda una gozada, ¡pero más aún compartir los partidillos de básquet! También me gustaría agradecer a Sofiane y Guillermo los momentos compartidos, a Gema y a Miguel por estar siempre dispuestas a prestar ayuda y a Kata por su amistad franco-húngara.

Si de una cosa estoy orgulloso es que mi vida no se reduce a un solo ámbito. Hay muchos de ellos y, asimismo, muchas personas que me gustaría agradecer por estar siempre allí. De todas, quiero dedicar especialmente esta tesis a tres de ellas. Kike, Isa y Vic, con vosotros han sido muchos los viajes y las luchas que hemos compartido. Hace mucho tiempo que tengo la suerte de conoceros y espero que encontremos siempre los momentos para seguir compartiendo. Gracias por hacerme sentir que soy importante en vuestras vidas. Sabéis de sobra que os quiero.

Y hablando de querer: ¡qué suerte que tengo con todas vosotras, Àgueda, Maria, Aida, Eloi, Papa y Mama! ¡Muchas gracias por vuestra comprensión y ayuda durante las tres semanas de redacción de esta tesis en Cubelles! Sois un lujo de familia. Lo digo en serio. Las mejores hermanas que se pueda tener. Os quiero un montón a las dos y sabéis que sois un referente para mí. Me encanta cómo vivís la vida, cada una a su manera y estilo, pero ambas sabéis hacer lo que a mí muchas veces me cuesta, aprovechar el momento. Espero que sepáis que siempre estoy ahí para lo que necesitéis. Como, por ejemplo, para hacer vuestro el piso donde vivo o para hacer de canguro de esa preciosidad que me ha hecho tío. Àgueda, tu encara no saps llegir, però has de saber que el tiet t'estima moltíssim i que s'ho passa molt bé amb tu perquè, saps?, ets una persona meravellosa. Se't veu de lluny, i això que no aixeques un pam de terra! Eloi, ¡menudo cuñao más saleroso me ha tocado! Em sembles una persona molt valiosa i em fa feliç que estiguis amb nosaltres. Moltes gràcies per enrecordar-te'n cada 28 d'octubre. Y por último mama y papa. Sé que no os he puesto la vida fácil. Sabéis que seguirá siendo así, ¿verdad? Siempre habéis estado presentes y me habéis apoyado en todas las decisiones que he tomado. Por locas que fueran, siempre habéis estado allí. Incluso cuando más os ha debido doler, siempre me habéis demostrado que me queréis. Muchas gracias por ese quererme sordo e incondicional. Por estar siempre dispuestas a pasar una temporada con Ergo porque necesito hacer recocidos o ataques electroquímicos. Gracias por esa labor de curas tan y tan invisibilizada, pero a la vez tan y

tan importante. Vuestra ayuda ha sido mi descanso. Gracias por quererme. Espero que ese amor los sintáis también vosotras de mí.

Pero si hay alguien que sepa por todo lo que he pasado durante la tesis, esa eres tú, Mònica. Moltes gràcies pel teu recolzament constant, per les teves bromes sobre la física i la ciència, per la teva comprensió, implicació i consells. Per ser la meva confident. Gràcies per demostrar-me que on no arriben els coneixements o la raó, arriba l'empatia. Una empatia que va més enllà de la tesis. Inclús més enllà de la parella. Perquè al llarg d'aquests anys també m'has fet arribar el teu escalf des de la solidaritat i l'amistat. I per mi això, sentir-me estimat com a amic i com a company, en definitiva, sentir-me estimat simple i rasament pel que sóc, es valuosíssim. Moltes gràcies per estar al meu costat sempre, ja sigui a la Patagònia, al desert o a la platja mentre escric la tesis. Moltes gràcies per fer tan fàcil compartir la vida amb tu i moltíssimes gràcies més per ser com ets. T'estimo molt! (no, no utilitzaré l'exemple del bosó de Higgs).

Per cert! Uri, Marc, Pau, Àlex, Salud i Mònica: os espero con vuestros atuendos y vuestras libretas en la presentación, pero más aún en la celebración. Gràcies grup per fer-me sentir un mes!

Aquesta tesis va dedicada a totes vosaltres!

Resum

La detecció de gasos és de gran importància en àrees tan diverses com la indústria, la salut o la seguretat en entorns domèstics o espais públics, entre d'altres, i és altament específica per a cada aplicació. El mètode de detecció a utilitzar depèn de factors com ara el gas a detectar, el rang de concentració, la resolució requerida, la sensibilitat, l'especificitat, el temps de resposta, l'entorn operatiu (temperatura, humitat, espècies interferents, etc. .), la mida i el cost, entre altres consideracions.

Els sensors òptics de gas són una solució atractiva per a la detecció de gas. La majoria d'ells es basen en l'absorció molecular i ofereixen respostes ràpides, deriva mínima i són intrínsecament fiables gràcies a la realització de mesures auto-referenciades. La sensibilitat i la selectivitat depenen de les característiques del dispositiu. Per exemple, els sensors de gas basats en tecnologia làser són altament selectius, no presenten resposta creuada a altres gasos i són altament sensibles. El desavantatge és que són cars. Els sensors d'infrarojos no dispersius (NDIR) són una alternativa molt estesa per a la detecció òptica de baix cost. Tenen un rendiment inferior en termes de sensibilitat i selectivitat que els sensors basats en làser, però són dos o tres ordres de magnitud més barats.

Aquesta tesi està dedicada a millorar la selectivitat i la sensibilitat dels dispositius NDIR mitjançant la tecnologia de silici macroporós. Més específicament, estudia com els cristalls fotònics fabricats mitjançant el gravat electroquímic poden ser usats com a filtres estrets d'infraroig mitjà per a la detecció de gasos. És a dir, els cristalls fotònics estan dissenyats de tal manera que només un petit rang de freqüències d'una font externa es transmet mentre que els voltants estan bloquejats. Aquests filtres són més estrets que els disponibles en el mercat i poden utilitzar-se per millorar la selectivitat i la sensibilitat dels dispositius NDIR, així com per reduir la detecció creuada amb altres gasos. A més, l'estudi mostra com els cristalls fotònics de silici macroporós poden funcionar com a emissors selectius si són escalfats. Això pot ser usat per reduir la complexitat dels dispositius NDIR alhora que es mantenen característiques òptiques similars. A més, s'ha demostrat que les molècules fotòniques poden emprar-se per realitzar una detecció dual tant en la transmissió com en l'emissió, donant un nou enfocament a les mesures auto-referenciades.

Les conclusions del treball mostren que la tecnologia de silici macroporós és una plataforma versàtil que proporciona solucions en el rang d'infraroig mitjà per al desenvolupament de sensors de gas òptics compactes, sensibles i selectius.

Paraules clau: cristall fotònic, silici macroporós, atac electroquímic, detecció NDIR, filtre estret, emissor selectiu, detecció dual.

Abstract

Gas detection is of great importance in areas as diverse as industry, health or safety in domestic environments or public spaces, among others, and it is highly specific to each application. The detection method depends on factors such as the species of gas to be detected, concentration range, required resolution, sensitivity, specificity, response time, operating environment (temperature, humidity, interfering species, etc.), size and cost, among other considerations.

Optical gas sensors are an attractive solution for gas detection. Most of them rely on molecular absorption and offer fast responses, minimal drift and are intrinsically reliable thanks to perform self-referenced measurements. Sensitivity and selectivity depend on the characteristics of the device. For example, laser-based gas sensors are highly selective with zero cross response to other gases and also with first-in-class sensitivity. The downside is that they are expensive. Non-dispersive infra-red (NDIR) sensors are a widespread alternative for cost-effective optical detection. They have inferior performances in terms of sensitivity and selectivity than laser-based sensors, but are two or three orders of magnitude less expensive.

This thesis is dedicated to improving the selectivity and sensitivity of NDIR devices through the use of macroporous silicon technology. More specifically, it studies how photonic crystals manufactured by electrochemical etching can be used as narrow mid-infrared filters for gas detection purposes. That is, the photonic crystals are designed in such a way that only a small range of frequencies from an external source are transmitted while the surroundings are blocked. These filters are narrower than those available on the market and can be used to improve the selectivity and the sensitivity of NDIR devices as well as to reduce cross detection with other gases. In addition, the study shows how macroporous silicon photonic crystals can be heated to work as selective emitters. This can be used to reduce the complexity of the NDIR device while maintaining similar optical characteristics. Furthermore, it is proven that photonic molecules can be employed to perform dual detection in both transmission and emission, giving a new approach to self-referenced measurements.

Conclusions of the work show that macroporous silicon technology is a versatile platform to provide solutions in the mid-infrared range for developing compact, sensitive and selective optical gas sensing.

Keywords: photonic crystal, macroporous silicon, electrochemical etching, NDIR detection, narrow filter, selective emitter, dual detection.

Contents

List of Figures

List of Tables

Introduction

1.1 Aim and objectives

The goal of this thesis is to contribute in the field of gas detection by providing a new technology, based on macroporous silicon, for an easy, versatile, cheap and compact sensing. To accomplish it, several intermediate objectives must be previously achieved. The following list shows the roadmap from the starting point of the thesis to the final goal of it, as well as further objectives:

Starting point: macroporous silicon photonic crystals with 4 µm and 2 µm pitch.

- **Specific objective #1:** fabrication and analysis of photonic crystals with 4 µm and 2 µm pitch.
  i. Study the impact of silicon absorption in the optical response.
  ii. Model the photonic crystals with and without defect using OptiFDTD tools.
  iii. Extrapolate these models to propose a profile for 700 nm pitch working in the mid-infrared.
- **Specific objective #2:** consolidate photonic crystal technology with defects using a pitch of 700 nm.
  i. Create macroporous silicon photonic crystals with 700 nm of pitch.
  ii. Introduce defects in the structure and study the optical response of it in different ranges of the mid-infrared.
  iii. Optimize the optical response of them.
  iv. Evaluate the thermal response of these photonic crystals.
- **Specific objective #3:** preliminary results of gas detection with the new platform.
  i. Specific design to point to CO_2 absorption band.
  ii. Create a new measuring setup.
  iii. Perform calibrated measurements in controlled environment.
  iv. Extrapolate to other gases in the MIR

Final goal: provide and characterize macroporous silicon technology for NDIR gas detection in relevant ambient.

- **Further objectives #4:** fabricate CO_2 detector prototype with the photonic crystals as narrow filters.

i. Design the electrical circuit and the encapsulation and build the prototype.
ii. Test it in relevant ambient.

- **Further objectives #5:** explore other options of gas sensing with macroporous silicon photonic crystals.

i. Using them as thermal selective emitters.
ii. Using dual detection.
iii. Applying atomic reorganization to generate 1D photonic crystals in order to improve the optical response of them.

1.2 Thematic

The present thesis involves three different fields that have to be deeply studied for the proper conception of the work. These are *Spectroscopic gas detection*, *Photonic Crystals* and *Electrochemical etching*.

The first chapter begins by describing a brief state of the art of gas sensing. Next, it focuses on the NDIR detection and the description of the different elements involved (emitter, receiver, filter and cell). The second chapter discusses about photonic. It starts by giving a general background about 1-, 2-, and 3-dimensional photonic crystals and then it focuses in exploring the possibilities that the introduction of defects gives in gas sensing. In this chapter it is discussed the software used for simulating the optical response of 3D photonic crystals as well as it is given some notions about thermal emission in photonic crystals. The third chapter introduces the electrochemical etching process and in particular it focuses on the photo-assisted electrochemical etching. The following describes the set-up used in the fabrication of 3D macroporous silicon photonic crystals and the post-processing techniques. Finally, FT-IR spectroscopy, the characterization method used to obtain the transmittances, reflectance and emittance of the fabricated structures, is explained.

1.3 Contributions of the present thesis

The articles that are contributed in this thesis follow the line specified in the section '*Aim and Objectives*'. The starting point is the 2- and 4-micron technology which rapidly evolves towards the 700 nm technology, where different designs of photonic crystals and their optical responses are studied. Then, the study focuses on gas detection –more specifically, on carbon dioxide sensing– to finally address the efforts to demonstrate the validity of this methodology in the rest of MIR range. Other studies include the design and fabrication of a sensor prototype based on the reported technology, as well as the exploration of other photonic crystal techniques/functionalities in order to improve the design and detection characteristics.

In the following lines the published works are briefly described:

- *Impact of the Absorption in Transmittance and Reflectance on Macroporous Silicon Photonic Crystals* is the starting point of the thesis. The impact that absorption losses have in the transmission and reflection spectrum of a PhC with 4 µm pitch within a planar defect inside the structure is reported. May be, the most important contribution of the paper is the first approximation, using simulation programs, to the design of photonic crystals of lower dimensions working in the MIR range. Fulfills **specific objective #1.**
- In *Study of resonant modes in a 700 nm pitch macroporous silicon photonic crystals*, it is shown the basic PhC structure used in this thesis: a modulated area of 5 periods, a planar defect and another modulated area of 5 periods. It is reported the impact that little variations in defects' length and depth have in the optical response. Fulfills **specific objective #2i and #2ii.**
- In *Enhanced geometries of macroporous silicon photonic crystals for optical gas sensing applications,* the design of the photonic crystals evolved. In particular, in this paper analyzes two different strategies for improving the quality factors of PhCs. The first is to add a straight part at the ending of the pores to produce interferences so that the main peak is somehow filtrated. The second strategy is to increase the number of periods in the modulated areas. Fulfills **specific objective #2iii.**
- The aim of the next paper, *Photonic Molecules for Improving the Optical Response of Macroporous Silicon Photonic Crystals for Gas Sensing Purposes*, is also to increase the quality factor of the PC with new designs. For that purpose, new cavities were introduced (and their respective modulation areas), obtaining better results than in the previous case. In addition, these new structures lead to a bandgap widening of about a 50 %. Fulfills **specific objective #2iii.**
- *Coupling Defects in Macroporous Silicon Photonic Crystals*, was the seed of previous article. Besides the contribution of quality factor and bandgap enhancement, in this conference paper it is firstly proposed to use two coupled cavities for dual gas detection. Fulfills **specific objective #2iii.**
- In *Transmission and Thermal Emission in the NO_2 and CO Absorption Lines using Macroporous Silicon Photonic Crystals with 700 nm Pitch* two photonic crystals working at carbon monoxide and nitrogen dioxide are presented. In this conference paper it is firstly discussed thermal emission using the reported technology, showing a poor quality response to be improved. Fulfills **specific objective #2iv.**
- In *Macroporous Silicon Filters, a Versatile Platform for NDIR Spectroscopic Gas Sensing in the MIR* it is shown the spectroscopic detection of carbon dioxide using macroporous silicon PCs. The dynamic of these structures when exposed to different gas concentrations is revealed. Some other specifications, such as working range, limit of detection and influence to external fluctuations is also provided. Furthermore, previous results are extrapolated to other MIR gases in order to obtain the optical response of the fabricated photonic crystals when exposed to them. Fulfills **specific objective #3.**
- In the same vein as the previous article, in *Macroporous silicon selective emitters for the detection of CO_2* it is reported the detection of carbon dioxide. However, in this article PhCs are not used as a narrow filter but as a selective emitter. In addition, the impact of inhomogeneities in the optical response is analyzed. This work can be understood as the continuation of *Transmission and Thermal Emission in the*

NO_2 and CO Absorption Lines using Macroporous Silicon Photonic Crystals with 700 nm Pitch. Fulfills **specific objectives #2iv, #3iii and further objective #5i.**

Spectroscopic detection

There are a number of different platforms and methods for gas sensing. The most commercialized are chemical sensors since they are portable and ultra-low cost. They rely in the fact that gases change some property of the active material. For example, in the case of metal-oxide gas sensors the conductivity of their metal layers is changed when they interact with oxidizable gases at high temperatures [1]. Other examples are found in solid electrolyte detectors [2], capacitive detectors [3] or polymer detectors [4]. A description of these and more conventional gas sensors can be found elsewhere [5], [6].

One of the most important drawbacks of chemical sensors is their inherently lack of selectivity with respect to specific gases. Other disadvantages are their long time response, limited lifetimes, drift issues and cross-response problems, e.g. humidity or temperature variations [7].

An alternative to them are optical gas sensors, which solve many of the aforementioned drawbacks. There are different techniques that can be grouped according to their operating principle. Table 2.1 shows that the most of them are based on infrared absorption. This is a conceptually very easy method based on molecular absorption.

Principle	Specific techniques
Absorption	➢ Non-dispersive infrared (NDIR) ➢ UV absorption ➢ Fourier Transform infrared (FTIR) ➢ Differential optical absorption spectroscopy (DOAS) ➢ Photoacustic Spectroscopy (PAS) ➢ Cavity ring-down spectroscopy (CRDS) ➢ Tuneable diode laser absorption spectroscopy (TDLAS) ➢ Differential absorption light detection and ranging (DIAL) ➢ Gas cloud imaging
Luminescence/ fluorescence	➢ Chemiluminescense (CL) ➢ UV fluorescence (UVF)
Ionization	➢ Photoionization detection/detector (PID)

Table 2.1. Optical gas sensing techniques and principles [8].

The aim of this chapter is to give the basic notions about spectroscopic gas detection. It begins by introducing the general theory of molecular absorption and in the following it focusses on Non-Dispersive Infrared (NDIR) detection, the method used in this thesis for gas sensing using our macroporous silicon photonic crystals.

2.1 Molecular absorption, a brief overview

It is well known that energy is quantized at the atomic scale. For instance, a molecule that is in a specific energy level can be promoted to a higher level only if it absorbs a specific amount of energy or *quantum*. In the same manner, if the molecule emits energy it will be degraded to lower energy. No middle positions can be found in microscale, as it happens in macroscale where energy is considered to be continuous [9]. In the IR region, these transitions between energy levels are related to the vibrational modes of the molecule –see Table 2.2.

Spectral region	Wavelength	Wavenumber	Type of excitation
UV	200 nm -400 nm	$5.0 \cdot 10^4$ cm^{-1}- $2.5 \cdot 10^4$ cm^{-1}	Electronic transitions
Near IR	700 nm-2.5µm	$1.4 \cdot 10^4$ cm^{-1}- $4.0 \cdot 10^3$ cm^{-1}	Molecular vibrations and rotations, overtones.
Mid IR	2.5 µm-14 µm	$4.0 \cdot 10^3$ cm^{-1}-714 cm^{-1}	Molecular vibrations and rotations, fundamental.
Far IR	14 µm-1000 µm	714 cm^{-1}-10 cm^{-1}	Lattice vibrations. Molecular rotations.

Table 2.2. Origin of absorption spectra in different regions of the electromagnetic spectrum [7].

The fundamental frequency in which a molecule *absorbs* energy is called *absorption line.* Each molecule presents a set of specific absorption lines related to each one of the vibrational or rotational modes. All of them compose the absorption spectrum of the gas, also called fingerprint. Figure 2.1 depicts the absorption spectra of several gases at the MIR region.

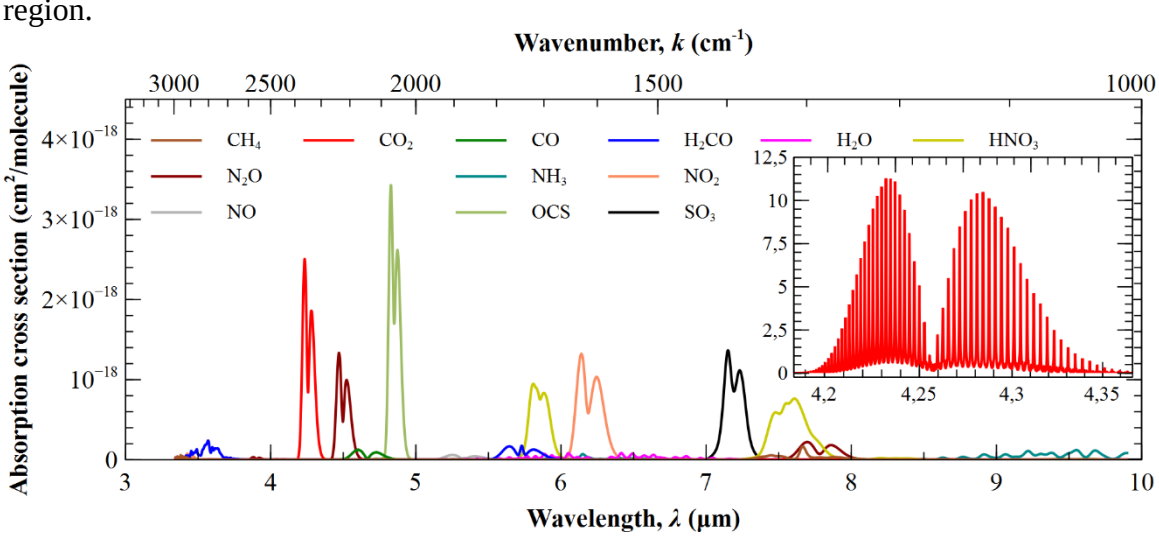

Figure 2.1. Absorption cross section of mid-infrared gases. Spectra have been obtained from [10] at normal conditions (P = 1 atm., T = 25 ºC) and a resolution of 4 cm^{-1}. Inner image depicts the absorption cross section of CO_2 at normal conditions but at high resolution.

It can be seen that every gas presents its own shape and position. In the inner image it is possible to distinguish very close absorption lines for CO_2. These absorption lines are only distinguishable using high resolution devices.

Spectroscopic detection uses the fact that a single molecule absorbs a quantized amount of radiation in a specific frequency to determine the volume of gas in the atmosphere. Indeed, the number of molecules in the ambient can be inferred by comparing the energy before the interaction with gas molecules and the energy just after. The relationship between optical absorption and the gas concentration at a specific wavelength has been known since 1852, when the so-called Beer-Lambert law was firstly introduced [11],

$$I = I_0 e^{-\sigma c l} \tag{2.1}$$

where I_0 and I are, respectively, the light intensity before and after the interaction with gas molecules [W cm^{-2}], c is the gas concentration [molecules cm^{-3}], σ is the absorption cross section of the molecule for the working frequency [cm^{-2} molecule] and l is the cell's optical path length [cm].

It has to be remarked that B-L Law is only valid for monochromatic sources and low absorbance values. Above a threshold value, absorbance starts to evidence non-monochromatic effects due to scattering, chemical reactions –such as dimer formation– or stray radiation effects, among others [12]–[15]. The reformulation of B-L law will be a key factor to understand the results reported in publications 5.7, 5.8 and Appendix II.

Most of spectroscopic gas sensors rely on Beer-Lambert's Law. The highest gas detection performance can be achieved by using a narrow tunable IR laser centered in one of the gas modes. Their best-in-class sensitivity and selectivity makes laser-based gas detection systems ideal for laboratory use and trace gas detection [16]; however, its increased complexity and cost [17] makes them not appealing for widespread application.

A popular alternative is Non-dispersive infrared (NDIR) gas detection. It is a powerful technique that follows the same principle as in laser spectroscopy, but instead of measuring in a single gas absorption line, detection is performed over its entire absorption range.

2.2 NDIR detection

NDIR gas sensors work on the mid infrared region because it is where gases exhibit their fundamental modes, two or three order of magnitude stronger than the harmonics observed in NIR –see Table 2.2. The basic structure of an NDIR device consist on a broadband light source, a gas cell and a detector. Its typical operation process is as follows; a broad-spectrum source, such a filament lamp, is used to expose the gas to a wide range of infrared frequencies. As discussed in previous section, molecules only interact with the light in the absorption range of the gas. Thus, only this small part of the spectrum arriving the receiver is modified in respect to the initial one. The difference between the input and the output power is used to determine the concentration of gas, as shown in Figure 2.2.

It should be noticed that Beer-Lambert Law is not directly applicable to NDIR devices because they use broadband sources instead of monochromatic. In the case that the sources are wider than absorption lines of the gas, B-L Law has to be rewritten as follows

$$I(\lambda_i) = I_0(\lambda_i)\ \mathrm{e}^{-c\sigma(\lambda_i)L} \tag{2.2}$$

where now $I_0(\lambda_i)$ represents the initial intensity of the source at the wavelength λ_i and $\sigma(\lambda_i)$ the cross section of the gas at the same wavelength. In other words, both absorption cross section and input intensity have to be equally discretized in order to apply B-L Law in each point –see Figure 2.7.

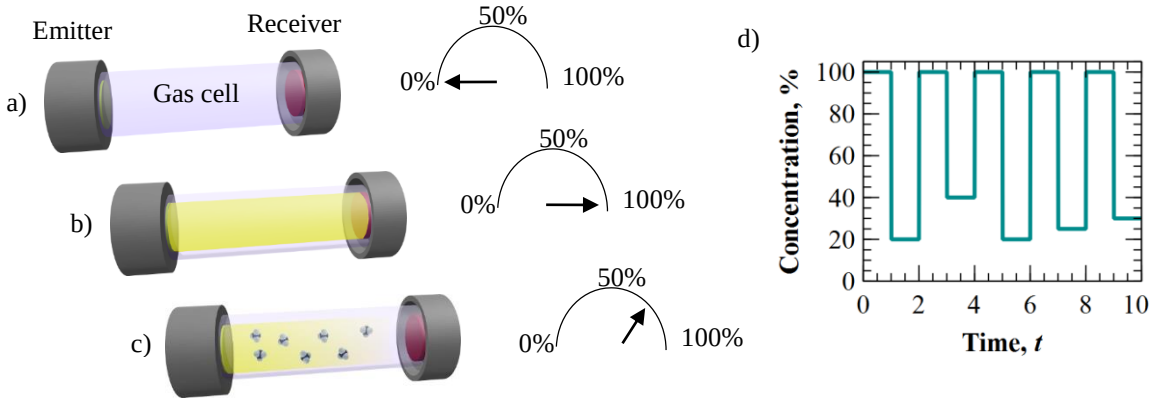

Figure 2.2. Schematic representation of NDIR detection. a) Basic NDIR device consisting on an emitter, a gas cell and a receiver. When it is OFF, receiver does not detect any signal (0%). b) When it is ON and there is no gas, the detected signal is the 100% of the emitted. c) In the case of gas presence, the signal exchanges energy with the molecules and the detected signal is less than the emitted. d) Typical calibration curve for a gas sensor: known concentrations are introduced and correlated with the output on the receiver. The gas has to be removed from the gas cell before each measurement.

NDIR is a widespread method for gas sensing (see Table 2.3) because it presents long-term stability, short time responses and the optical characteristics of the material are independent of humidity or temperature variations. In addition, it presents low energy consumption and it is a cost-effective solution. However, its main drawback is the lack of sensitivity and selectivity due to the wide emission/detection window. To overcome both limitations, many NDIR devices use a filter before the detector to specifically sense in the absorption region of the gas [18]. Other options to increase the sensitivity and the detection limit of the device, as well as to miniaturize it, is path length enhancement though the implementation of different gas cell topologies.

Emitter	**Detector**	**Central λ (μm)**	**Path Len. (cm)**	**Gas detected**	**Detect. Limit (ppm)**	**Topology cell**	**Power cons. (mW)**	**Ref.**
MEMS heater	Thermo-pile	8.26 10.6	10	C_3H_6O NH_3	50 10	FF	//	[19]
LED	Photo-diode	4.26	//	CO_2	//	Planar (dome)	35	[20]
MEMS heater	Bolometer	4.26	8	CO_2	30	Planar (open)	45	[21]
LED	Photo-diode	0.34	19.5	CH_2O	4.3	FF	//	[22]
LED	Photo-diode	0.226	50	NO	2	FF	//	[23]
DFB	//	1.65	20	CH_4	11	FF	//	[24]
MEMS heater	Pyro-electric	4.65 4.26	39.3	CO CO_2	8.8 8.7	Planar (open)	//	[25]

		3.31		CH_4	10.3			
MEMS heater	Thermo-pile	4.26	8	CO_2	50	FF	350	[26]
//	//	4.26	0.5	CO_2	~400	FF	//	[27]
HeNe laser	PbSe	3.4	0.15	CH_4	//	Cavity (~25 µm)	//	[28]
Lamp	Pyro-electric	4.66 4.26 3.33	2.6	CO CO_2 CH_4	//	Planar (dome)	//	[29]
MEMS heater	Thermo-pile	4.26	7.5	CO_2	//	FF	~80	[30]
AlInSb LED	InSb	4.2	8	CO_2	1000	Planar (open)	//	[31]
MEMS heater	Thermo-pile	4.26	7	CO_2	//	FF	~50	[32]
LED	Photo-diode	1.66	12	CH_4	100	FF	//	[33]
MEMS heater	Pyro-electric	8.4 9.6	30	C_2H_4 O_2 CH_3OH	165 184	FF	//	[34]
Laser	PbTe	3.31	0.1	CH_4	1000	WG	//	[35]
QCL	MCT	4.23	1	CO_2	5000	WG	//	[36]
DFB	InGaAs	1.65	10	CH4	100	WG		[37]

Table 2.3. Reported NDIR gas sensors and their characteristics (extracted from [38]) .

In the following a more detailed description of the components involved in NDIR detection is given.

2.2.1 Choice of emitter/receiver combination

A key point in NDIR detection is the choice of the emitter/receiver combination. The election will, basically, determine the sensing window and therefor the range in which the gases will be detected.

Table 2.3 gives a glimpse to the most commonly used options in the literature of optical gas sensors. Two types of combinations can be distinguished (ignoring laser-based gas sensors, which, as mentioned above, are too expensive). The first is a thermal emitter combined with a temperature sensor (either pyroelectric or a thermopile). The second option is a LED combined with a photodiode.

2.2.1.1 LED/photodetectors

The physics of mid-infrared light emitting diodes (LEDs) has been extensively studied since the last decades of the 20th century [39], [40]. Like visible LEDs, MIR LEDs rely on the physical principle of carrier's recombination in a *p-n* junction when a voltage is applied between the terminals of both materials –see Figure 2.3. Excess of energy not used during the recombination is emitted in the form of light.

Emission properties depend on the materials employed and can be engineered either by using an alloy composition, a quantum well structure, or superlattices –further details

for mid-infrared LEDs can be found somewhere else [41]. The optical spectra of these components are usually [1-2] µm wide. In addition, the commercial mid-infrared light emitting diodes typically range from NIR to a maximum wavelength of 5 µm (see, for example, *LED microsensor NT* or *Thorlabs*, mid-infrared models). As an example, in the right image of Figure 2.3 it is shown the response of two LEDs.

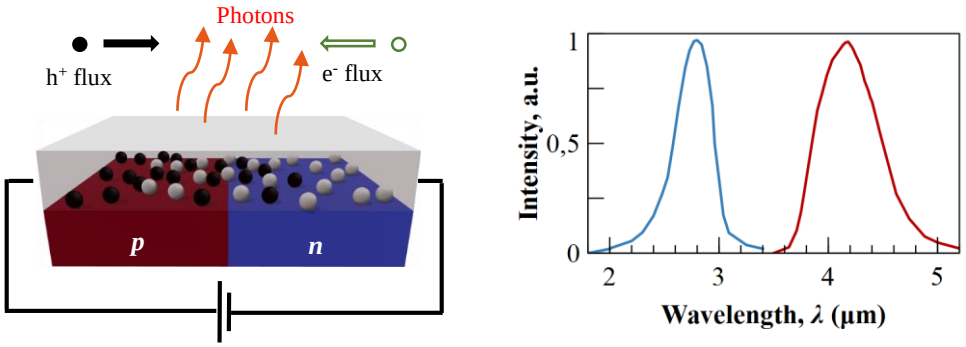

Figure 2.3. a) Schematic representation of LED emission. When a voltage is applied to the junction, carriers moves to the other side (jumping the energy barrier) and recombine near the interface with their complementary. The excess of energy that is not used during this process is emitted. b) Spectral response of mid-infrared LED43 from *Frankfurt Laser Company* (Red. It has been used for the developing of the first CO_2 sensor prototype based on the reported macroporous silicon technology, see Appendix III) and Lms28LED from *LED microsensor NT* company (blue).

In conclusion, LED emitters are devices that convert a voltage difference into a light signal, i.e. photons. Photodetectors are the responsible of converting this signal back again into an electrical value. Generally speaking, the principle they follow is the opposite of that of LEDs. That is, they convert photons into electron-hole current utilizing some form of *p-n* junction, e.g. *p-i-n*, p^+-*p*-n^+, etc. There are a number of efficient technologies for converting light into an electrical signal: bulk detectors, quantum well infrared detectors, or stained-layer superlattices, among others [42]. Bulk detectors, in essence photodiodes (photovoltaic or photoconductive), are currently the most popular photodetectors in the market due to their ease of fabrication as well as the maturity that this technology has reached since the 1950's. The most commonly used materials are Indium antimonide (InSb) and mercury cadmium telluride (HgCdTe) which, depending on the characteristics of the device, they can be designed to cover different ranges of the electromagnetic spectrum –see Figure 2.4.

The combination of the emitting and detecting windows gives the sensing range of the device. For example, if *LED43* of Figure 2.3 is combined with the InAsSb detector at 25 ºC, the resulting sensing area would be from 3.75 µm to 5 µm (note that this is the complete emission spectrum of the LED). In other cases, one of the two cut-off wavelengths of the receiver may fall inside the emission frequency range of the emitter, reducing the sensing window. This will be the case of the combination of *Lms28LED* model of Figure 2.3 and the long wavelength type InGaAs (25 ºC) photodetector, where the sensing window would be between 2 µm (given by left cut-off wavelength of the emitter) and 2.7 µm (given by left cut-off wavelength of the receiver).

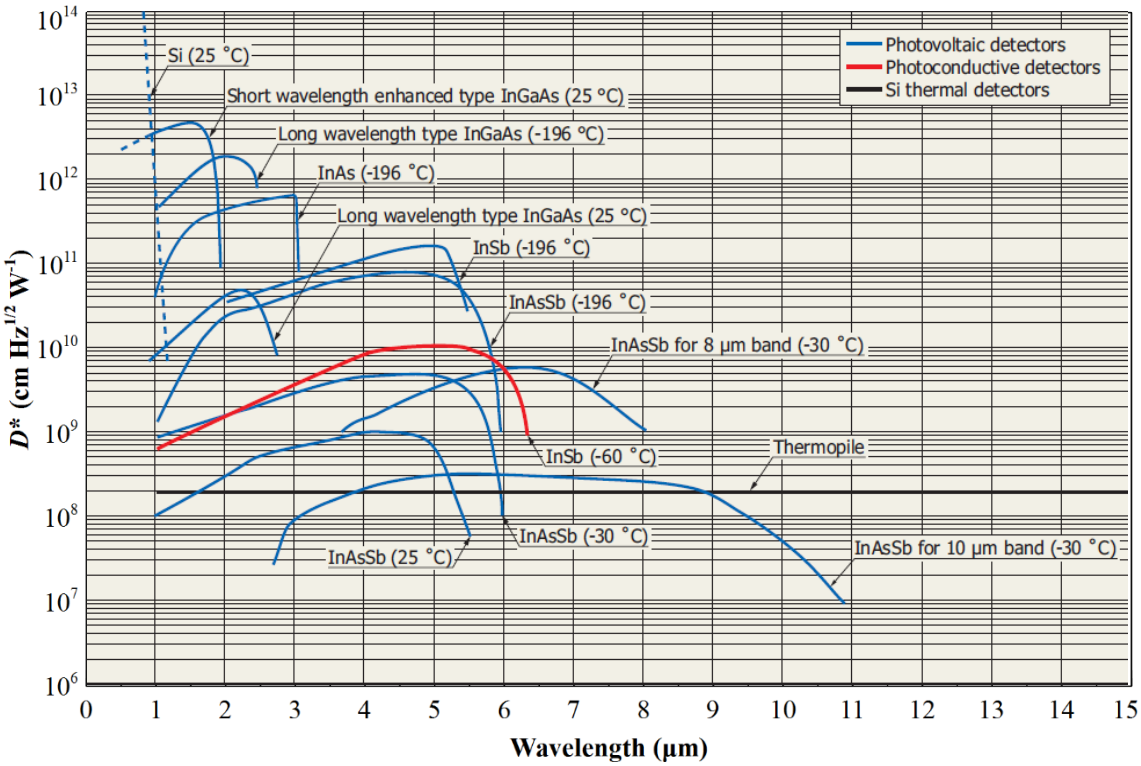

Figure 2.4. Detectivity (*D**) of bulk photodiodes infrared detectors from *Hamamatsu* company. The thermopile response is given as completeness.

2.2.1.2 Heater/thermal infrared detector

This option is based on the effect that temperature variation has in a thermal transducer. Essentially, a blackbody-like emitter (a heated body that emits power, see next chapter, Photonic Crystals, section 3.2) transfers energy to the receiver that transduces the heat into an electric signal –see Figure 2.5.

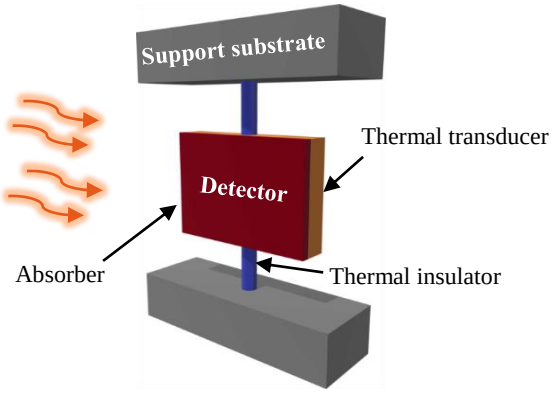

Figure 2.5. Common thermal model for thermopile and detectors. Radiation impinges the detector area, that is composed by the absorber and the transducer. The absorber layer optimizes the percentage of radiation transmitted to the transducer, which converts the heat into an electric signal. A support substrate holds the detector through thermal insulators that, ideally, should not exchange heat with the sensor.

There are two main temperature infrared detectors; pyroelectric, which is based on its homonym effect, and thermopiles, based on the Seebeck effect.

The thermopile detector consists of an array of thermocouples connected in series as differential pairs. Each one of these pairs have two different conductor materials that have different thermal response to radiation. In other words, for the same radiance they stabilize at different temperatures. This difference in the temperature ΔT leads to a small variation in the voltage,

$$V = (S_{\mathrm{A}} - S_{\mathrm{B}})\Delta T \tag{2.3}$$

where S_{A} and S_{B} are the Seebeck's coefficient for materials A and B, respectively. The output of a single thermocouple is in the range of 1 mV to 10 mV for a temperature difference of 500 ºC depending on the type of materials used [43]. For certain applications a higher output is required. Therefore, a number of thermocouples are connected in series to satisfy those requirements.

With regard to pyroelectric detectors, they rely on the fact that specific materials (pyroelectric crystals) undergo changes in electrical polarization when exposed to a temperature variation. That is, an electric field is induced inside the material, caused by movement of positive and negative charges between opposite ends of the surface. The generated pyroelectric current is given by

$$j_{\mathrm{p}} = Ap\frac{d\theta}{dt} \tag{2.4}$$

where A is the area of the pyroelectric element, p is the pyroelectric coefficient, and $\frac{d\theta}{dt}$ is the rate of change of the element temperature with time [44]. It should be noticed that these kind of detectors only work for temperature variations in time. That is, for a constant thermal emitter, a chopper is needed in order to create this difference in time and, therefore obtaining an electric response.

A common feature of thermal detectors is that they have not dependent on wavelength. Therefore, they can detect without any restriction along the entire infrared regions which, of course, comprises the MIR band. If desired, as it is the case of gas sensing, the spectra response of the detectors can be reshaped by combining them with some coatings or materials that act as bandpass filters.

Both types of detector have their own advantages and disadvantages. For example, pyroelectrics present higher responsivity and higher signal to noise ratio (SNR) than thermopiles. However, as pyroelectric crystals are inherently piezoelectric, they produce unwanted signal when stressed mechanically [45]. This is, they are sensitive to vibrations, unlike thermopiles. In addition, the latter are more cost-effective than the firsts [46]. Perhaps it is because of this economic advantage that current market is tending to the use of thermopiles as infrared detector.

2.2.1.3 Comparison between LED/photodetector and heater/thermopile combinations

From the above it can be inferred that LED-photodetector systems are much more selective than heater-thermopile option; they can ensure a reasonable mid-infrared detection window at moderate costs.

The counterpart of it is that the emitter/receiver configuration restricts considerably the detection range. Therefore, they can only be designed to sense a single gas (or gases which absorption spectrum is very close one to the other). However, the detection window is still too wide to avoid cross reference detection with gases with near absorption spectra. This broad detection range, also restricts the sensitivity of the devices, which can be

partially solved by incorporating different topologies of gas cell –see 2.2.3 *Gas cells and path lengths*.

As mentioned before, current market tendency is to use heater/thermopiles as emitter/receiver elements in NDIR devices. This is because of two main factors. The first one is because they are the most cost-effective solution. The second factor is because they can be used to sense any gas in the MIR area due to their large sensing window. To do so, it is essential for them to incorporate bandpass filters in order to specifically target the gas under study. Thus, unlike LED/photodiode combination, with a single emitter and a single receiver, multiple gas sensing can be done using different bandpass filters located at the desired frequencies. Furthermore, thanks to the consolidation over the last few years of mid-infrared filter technology, the combination of heater-thermopile with bandpass filters leads to much narrower sensing ranges than LED-photodiode. This gives more sensitive and selective devices at reduced final cost.

As a consequence of this enhancement in the figure-of-merits in heater/thermopile-based devices, LED/photodetector combination are also forced to incorporate narrowband filters in their system in order to effectively compete against them. Nevertheless, the cost is an important factor that market has seem to have taken into account.

2.2.2 Filters

From all the discussion of this chapter it is clear that an NDIR device should, at least, measure in a window very similar to that of the gas to be detected. This would reduce cross measurements with other gases and, thus, the errors associated with such measurement. In addition, higher sensitivities would be achieved. For that purpose, NDIR gas devices incorporate mid-infrared filters in between the emitter and the receiver to specifically point to the target gas. Figure 2.6 shows the most common way to proceed by adding two filters, conforming the so-called dual detectors. As depicted in the figure, one of these filters targets the gas and the other acts as the reference. Usually, this reference filter is centered at the 3.9 µm since in the surroundings there are no gas absorption spectra.

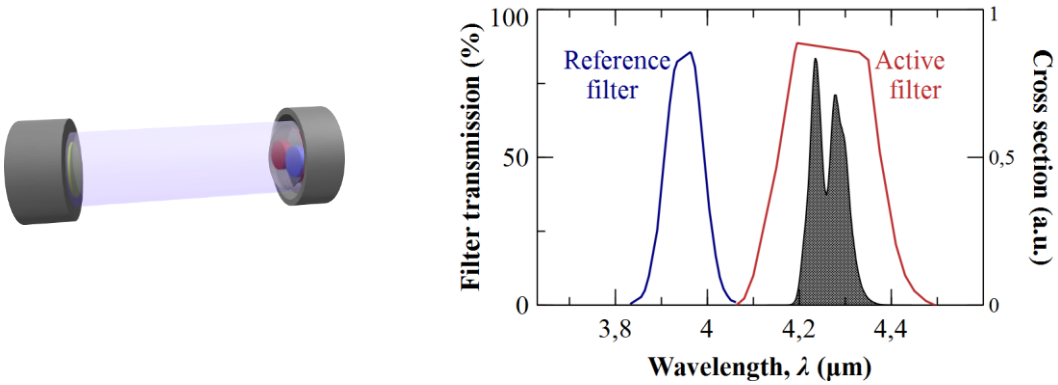

Figure 2.6. (left) Dual configuration for NDIR gas detectors and (right) their optical response superimposed on the absorption spectra of carbon dioxide (black shadowed curve). Adapted figure from [7].

To know the output intensity that it is measuring the detector, B-L has to be applied in each wavelength, and then the integration of the resulting curve has to be performed. In other words, equation (2.2) has to be applied. The only difference in respect to the non-filtered case is that $I_0(\lambda_i)$ is now the filtered emission signal,

$$I = \int_{\lambda_{\min}}^{\lambda_{\max}} I_0(\lambda)\, \mathrm{e}^{-c\sigma(\lambda)L}\, \mathrm{d}\lambda \tag{2.5}$$

This is schematized in Figure 2.7.

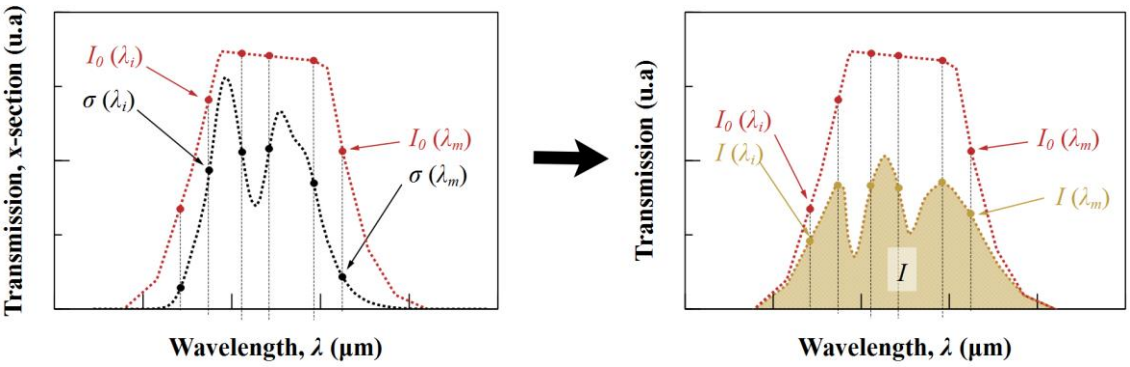

Figure 2.7. (Left) Equally discretized transmission spectrum of the active filter of Figure 2.6 (red points) and absorption cross section of carbon dioxide (black points). For a more proper visualization, 6 points per each graph have been highlighted. (Right) Discretized transmission spectra for the filter before (red) and after (gold) applying Beer Lambert's formula. The shadowed area is the total output intensity.

From Figure 2.7 it can be deduced that if the filter, despite of being broader than the absorption spectrum of gas, is thinner than the absorption range, both selectivity and sensibility would increase.

Currently there are a number of available mid-infrared filters that could be used for gas sensing purposes [47]–[49]. Prices range from 234 $ to 1,000 $ per filter, depending on the features. Generally, they present higher transmittance than 60%, they block all other wavelengths in the MIR band and they have FWHM (Full Width at Half Maximum) values in the order of hundreds. A complete description of the referenced filters is given in Table 2.4.

	Iridian		**Thorlabs**		**Electro Optical Components**	
	Min	**Max**	**Min**	**Max**	**Max**	**Max**
Center wavelength	2.7 μm	9.5 μm	1.7 μm	9.5 μm	1.4 μm	11.6 μm
FWHM	150 nm	150 nm	50 nm	500 nm	20 nm	600 nm
Q-factor	10	30	5	60	5	110
Min. Transmission	65 %	65 %	70 %	75 %	50 %	90 %
Block range	1-10 μm	1-10 μm	0.2-16 μm	1.8-9.5 μm	0.1-30 μm	0.1-30 μm
Size (outer diameter)	25.4 mm	25.4 mm	25.4 mm	25.4 mm	5 mm	100 mm

Price	265 $	265 $	234 $	487 $	300 $ *	1000 $ *

* This prices are not available online. They have been obtained under consult.

Table 2.4. Comparison between different mid-infrared narrowband pass filters currently commercialized.

Although those filters can be cut in small pieces in order to be used in gas sensing detection, they still represent an important increase of the total amount of the final device. However, the principal drawback is the low quality factor most of them have. This may make them useless for sensitive and selective detection of gases. In the case depicted in Figure 2.7, the filter, even being wider than the absorption range of the gas, is narrow enough to prevent from cross detection to the closest gas, N_2O which is in the range of [4.4-4.6] μm. However, there are many other cases where gases partially overlap –see Figure 2.1. For instance, CO and N_2O overlap in the P-branch of the first. A filter as wide as the one depicted in Figure 2.7 will not be useful for avoiding cross-detection. In this particular, a filter with quality factors above 90 is required.

Another limiting factor is the fabrication process. These commercial filters consist on a multilayer stack, formed by vacuum deposition techniques, that conform a Bragg reflector (additional layers of absorbing materials are also deposited to remove extra transmission outside the peak.). Nevertheless, although notorious advances have been done in the fabricating systems, reducing the manufacturing costs as well as enabling the fabrication of more diverse shapes, it is still a complex fabrication method that involves several steps [50].

One of the main purposes of the Thesis is to provide higher-quality narrow filters in the MIR using a cheap, versatile and all-silicon platform in order to increase the benefits of current optical gas sensors. This idea is extensively explored in the paper *Macroporous Silicon Filters, a Versatile Platform for NDIR Spectroscopic Gas Sensing in the MIR* (section 5.7).

2.2.3 Gas cells and path lengths

Dimensions of NDIR devices are limited in lot of applications because they have to fulfil the gas industry standard size (20 mm diameter × 16 mm high). However, there are few gases that can be sensed with high sensitivity and low detection limits with such dimensions. In order to overcome those limitations, different topologies have been proposed in order to enhance the effective path length and miniaturize the entire device taking into account referential measurement.

The simplest topology to sense a gas by NDIR method is using a face-to-face dual filter either in an open or a closed cell –see images a) and b) of Figure 2.8. In this case, two different filters are used. An alternative to the dual detector is to use a beam splitter before the light beam enters the gas cell. In this way, the beam is divided into two equal parts. One of them interacts with the gas and the other serves as a reference. This is a mechanism that adds more complexity to the device but allows a direct comparison.

More complex structures have been proposed for NDIR gas sensing. For instance, two elliptical structures for measuring ethanol [51]; White-cell configuration for measuring several gases (methane, ethanol, ammonia, dinitrogen dioxide and carbon dioxide) [52]; or embedded parabolic reflector to measure carbon dioxide in a chamberless device [53], are different explored options.

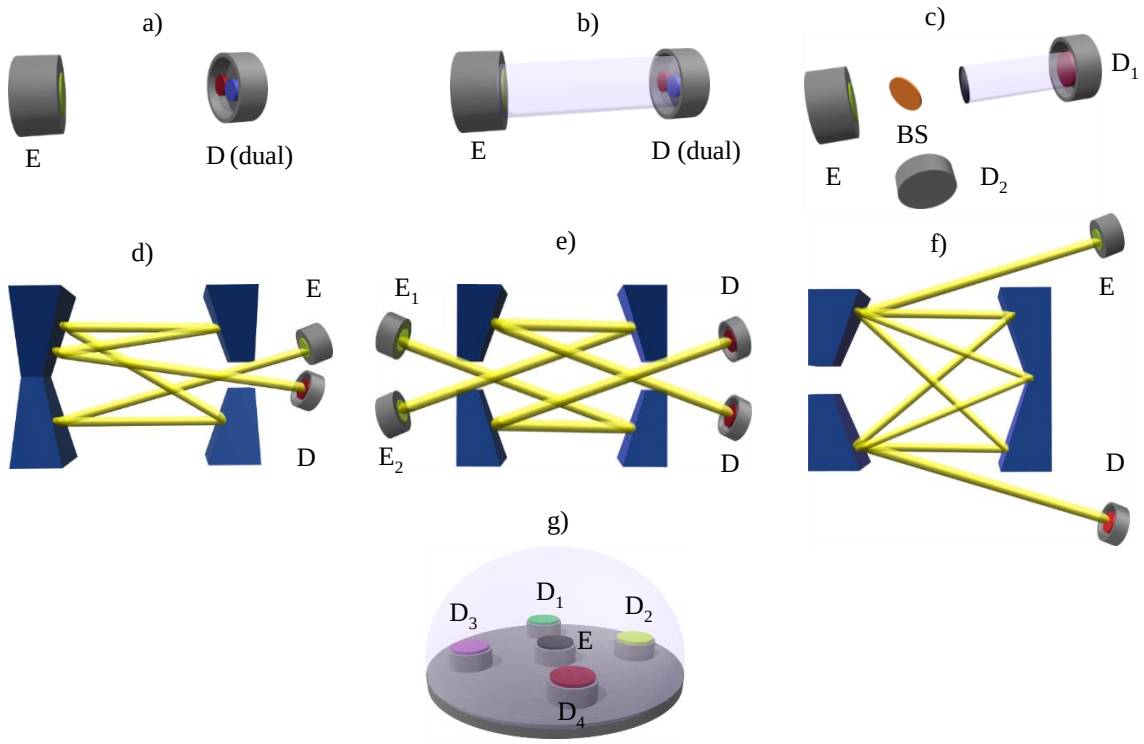

Figure 2.8. Different gas cells topologies. a), b) dual detector without and with gas cell. c) a beam splitter can be used for referential measurement instead of dual filtering. Second and third row depict four types of multipass absorption cells for path length enhancement. d) Herriot cell. e) Pfund cell. f) White cell and g) dome cell. Nomenclature: E (emitter), D (detector), BS (beam splitter).

The chosen topology in this Thesis is the face-to-face configuration. Other options based on the ones depicted in Figure 2.8 should be taken into account in further version of the prototype sensors based on macroporous silicon PhCs.

References

[1] J. C. Belmonte et al., “Micromachined twin gas sensor for CO and O2 quantification based on catalytically modified nano-SnO2,” Sensors Actuators B Chem., vol. 114, no. 2, pp. 881–892, Apr. 2006.

[2] G. Jasinski and P. Jasinski, “Solid electrolyte gas sensors based on cyclic voltammetry with one active electrode,” IOP Conf. Ser. Mater. Sci. Eng., vol. 18, no. 21, p. 212007, Oct. 2011.

[3] T. Ishihara and S. Matsubara, “Capacitive Type Gas Sensors,” J. Electroceramics, vol. 2, no. 4, pp. 215–228, 1998.

[4] A. D. S. Gomes, New polymers for special applications. InTech, 2012.

[5] T. M. Geppert, “Towards Photonic Crystal-Based Spectroscopic Gas Sensors,” Thesis, Hälle-Wittenberg, 2006.

[6] X. Liu, S. Cheng, H. Liu, S. Hu, D. Zhang, and H. Ning, “A survey on gas sensing technology.,” Sensors (Basel)., vol. 12, no. 7, pp. 9635–65, 2012.

[7] J. Hodgkinson and R. P. Tatam, “Optical gas sensing: a review,” Meas. Sci. Technol., vol. 24, no. 1, p. 012004, Jan. 2013.

[8] R. Bogue, “Detecting gases with light: a review of optical gas sensor technologies,” Sens. Rev., vol. 35, no. 2, pp. 133–140, Mar. 2015.

[9] G. M. Barrow, Introduction to molecular spectroscopy. Tokio: McGraw-Hill, 1964.

[10] R. V. Kochanov, I. E. Gordon, L. S. Rothman, P. Wcisło, C. Hill, and J. S. Wilzewski, “HITRAN Application Programming Interface (HAPI): A comprehensive approach to working with spectroscopic data,” J. Quant. Spectrosc. Radiat. Transf., vol. 177, pp. 15–30, Jul. 2016.

[11] Beer, “Bestimmung der Absorption des rothen Lichts in farbigen Flüssigkeiten,” Ann. der Phys. und Chemie, vol. 162, no. 5, pp. 78–88, Jan. 1852.

[12] K. Fuwa and B. L. Valle, “The Physical Basis of Analytical Atomic Absorption Spectrometry. The Pertinence of the Beer-Lambert Law.,” Anal. Chem., vol. 35, no. 8, pp. 942–946, Jul. 1963.

[13] H. Öjelund and J. F. Offersgaard, “Correction of Nonlinear Effects in Absorbance Measurements,” Appl. Spectrosc. Vol. 56, Issue 4, pp. 469-476, vol. 56, no. 4, pp. 469–476, Apr. 2002.

[14] L. Kocsis, P. Herman, and A. Eke, “The modified Beer–Lambert law revisited,” Phys. Med. Biol., vol. 51, no. 5, pp. N91–N98, Mar. 2006.

[15] M. Bhatt, K. R. Ayyalasomayajula, and P. K. Yalavarthy, “Generalized Beer–Lambert model for near-infrared light propagation in thick biological tissues,” J. Biomed. Opt., vol. 21, no. 7, p. 076012, Jul. 2016.

[16] S. M. Cristescu, S. T. Persijn, S. te Lintel Hekkert, and F. J. M. Harren, “Laser-based systems for trace gas detection in life sciences,” Appl. Phys. B, vol. 92, no. 3, pp. 343–349, Sep. 2008.

[17] THORLABS, “Quantum Cascade Lasers (QCLs), 4.05 - 11 μm.” [Online]. Available:

https://www.thorlabs.com/newgrouppage9.cfm?objectgroup_id=6932&gclid=CjwKCAjw98rpBRAuEiwALmo-yknu0HBBtMXOBb6BMf-nlgVgZ10qeJN7k5dZld01U93StpQongV6WRoCSbwQAvD_BwE. [Accessed: 31-Jul-2019].

[18] N. Neumann, K. Hiller, S. Kurth, and I. Gmbh, "Micromachined mid-infrared tunable fabry-perot filter," pp. 1–4.

[19] Y. Xing, B. Urasinska-Wojcik, and J. W. Gardner, "Plasmonic enhanced CMOS non-dispersive infrared gas sensor for acetone and ammonia detection," in 2018 IEEE International Instrumentation and Measurement Technology Conference (I2MTC), 2018, pp. 1–5.

[20] L. Fleming, D. Gibson, S. Song, C. Li, and S. Reid, "Reducing N2O induced cross-talk in a NDIR CO2 gas sensor for breath analysis using multilayer thin film optical interference coatings," Surf. Coatings Technol., vol. 336, pp. 9–16, Feb. 2018.

[21] V. Avramescu and M. Gologanu, "Oxygen sensor based on photo acoustic effect," in 2017 International Semiconductor Conference (CAS), 2017, pp. 97–100.

[22] J. J. Davenport, J. Hodgkinson, J. R. Saffell, and R. P. Tatam, "Non-Dispersive Ultra-Violet Spectroscopic Detection of Formaldehyde Gas for Indoor Environments," IEEE Sens. J., vol. 18, no. 6, pp. 2218–2228, Mar. 2018.

[23] F. Mehnke et al., "Gas Sensing of Nitrogen Oxide Utilizing Spectrally Pure Deep UV LEDs," IEEE J. Sel. Top. Quantum Electron., vol. 23, no. 2, pp. 29–36, Mar. 2017.

[24] C.-T. Zheng et al., "Demonstration of a portable near-infrared CH4 detection sensor based on tunable diode laser absorption spectroscopy," Infrared Phys. Technol., vol. 61, pp. 306–312, Nov. 2013.

[25] M. Dong et al., "Development and Measurements of a Mid-Infrared Multi-Gas Sensor System for CO, CO2 and CH4 Detection," Sensors, vol. 17, no. 10, p. 2221, Sep. 2017.

[26] T. A. Vincent and J. W. Gardner, "A low cost MEMS based NDIR system for the monitoring of carbon dioxide in breath analysis at ppm levels," Sensors Actuators B Chem., vol. 236, pp. 954–964, Nov. 2016.

[27] S. Moumen, I. Raible, A. Krauß, and J. Wöllenstein, "Infrared investigation of CO2 sorption by amine based materials for the development of a NDIR CO2 sensor," Sensors Actuators B Chem., vol. 236, pp. 1083–1090, Nov. 2016.

[28] N. P. Ayerden, G. de Graaf, P. Enoksson, and R. F. Wolffenbuttel, "A highly miniaturized NDIR methane sensor," 2016, vol. 9888, p. 98880D.

[29] Q. Tan et al., "Three-gas detection system with IR optical sensor based on NDIR technology," Opt. Lasers Eng., vol. 74, pp. 103–108, Nov. 2015.

[30] A. Pusch et al., "A highly efficient CMOS nanoplasmonic crystal enhanced slow-wave thermal emitter improves infrared gas-sensing devices," Sci. Rep., vol. 5, no. 1, p. 17451, Dec. 2015.

[31] E. G. Camargo et al., "NDIR gas sensing using high performance AlInSb mid-infrared LEDs as light source," in Infrared Sensors, Devices, and Applications VII, 2017, vol. 10404, p. 31.

[32] A. De Luca, S. Z. Ali, R. Hopper, S. Boual, J. W. Gardner, and F. Udrea, “Filterless non-dispersive infra-red gas detection: A proof of concept,” in 2017 IEEE 30th International Conference on Micro Electro Mechanical Systems (MEMS), 2017, pp. 1220–1223.

[33] C. Massie, G. Stewart, G. McGregor, and J. R. Gilchrist, “Design of a portable optical sensor for methane gas detection,” Sensors Actuators B Chem., vol. 113, no. 2, pp. 830–836, Feb. 2006.

[34] A. Genner, C. Gasser, H. Moser, J. Ofner, J. Schreiber, and B. Lendl, “On-line monitoring of methanol and methyl formate in the exhaust gas of an industrial formaldehyde production plant by a mid-IR gas sensor based on tunable Fabry-Pérot filter technology,” Anal. Bioanal. Chem., vol. 409, no. 3, pp. 753–761, Jan. 2017.

[35] P. Su et al., “Monolithic on-chip mid-IR methane gas sensor with waveguide-integrated detector,” Appl. Phys. Lett., vol. 114, no. 5, p. 051103, Feb. 2019.

[36] C. Ranacher et al., “Mid-infrared absorption gas sensing using a silicon strip waveguide,” Sensors Actuators A Phys., vol. 277, pp. 117–123, Jul. 2018.

[37] L. Tombez, E. J. Zhang, J. S. Orcutt, S. Kamlapurkar, and W. M. J. Green, “Methane absorption spectroscopy on a silicon photonic chip,” Optica, vol. 4, no. 11, p. 1322, Nov. 2017.

[38] D. Popa, F. Udrea, D. Popa, and F. Udrea, “Towards Integrated Mid-Infrared Gas Sensors,” Sensors, vol. 19, no. 9, pp. 2076–2090, May 2019.

[39] A. (Anthony) Krier, Mid-infrared semiconductor optoelectronics. Springer, 2006.

[40] A. Krier, “Physics and technology of mid–infrared light emitting diodes,” Philos. Trans. R. Soc. London. Ser. A Math. Phys. Eng. Sci., vol. 359, no. 1780, pp. 599–619, Mar. 2001.

[41] H. Jonathan Paul, “Development of Mid-Infrared Light Emitting Diodes to Replace Incandescent Airfield Lighting,” Lancaster University, 2016.

[42] C. Downs and T. E. Vandervelde, “Progress in infrared photodetectors since 2000.,” Sensors (Basel)., vol. 13, no. 4, pp. 5054–98, Apr. 2013.

[43] G. Yakaboylu, R. Pillai, K. Sabolsky, and E. Sabolsky, “Fabrication and Thermoelectric Characterization of Transition Metal Silicide-Based Composite Thermocouples,” Sensors, vol. 18, no. 11, p. 3759, Nov. 2018.

[44] R. W. Whatmore, “Pyroelectric Arrays: Ceramics and Thin Films,” J. Electroceramics, vol. 13, no. 1–3, pp. 139–147, Jul. 2004.

[45] N. Norbert and S. Hannjo, “How to reduce the microphonic effect in pyroelectric detectors?,” in Sensor + Test 2008 : proceedings , 2008, pp. 277–282.

[46] N. Norbert and B. Victor, “Comparison of Pyroelectric and Thermopile Detectors · AMA Science,” in IRS2 Proceedings, 2013.

[47] Iridian Spectral Technologies, “Highest Quality Mid-IR Bandpass Filters.” [Online]. Available: https://www.iridian.ca/product-category/mid-ir-bandpass/. [Accessed: 04-Apr-2019].

[48] THORLABS, “IR Bandpass Filters: 1.75 - 9.50 µm Central Wavelength.” [Online]. Available:

https://www.thorlabs.com/newgrouppage9.cfm?objectgroup_id=5871. [Accessed: 20-Aug-2019].

[49] Electro Optical Components, “Narrow Bandpass Filters,” 2017.

[50] G. D. Cole et al., “High-performance near- and mid-infrared crystalline coatings,” Optica, vol. 3, no. 6, p. 647, Jun. 2016.

[51] J. Kim, K. Lee, and S. Yi, “NDIR Ethanol Gas Sensor with Two Elliptical Optical Structures,” Procedia Eng., vol. 168, pp. 359–362, Jan. 2016.

[52] C. Hummelga˚rd et al., “Low-cost NDIR based sensor platform for sub-ppm gas detection,” Urban Clim., vol. 14, pp. 342–350, Dec. 2015.

[53] M. Vafaei, A. Amini, and A. Siadatan, “Breakthrough in CO2 Measurement with a Chamberless NDIR Optical Gas Sensor,” IEEE Trans. Instrum. Meas., pp. 1–1, 2019.

Photonic crystals

The study of one-dimensional periodical structures started at the endings of the 19th century with the so-called Bragg mirrors. However, it was not until the pioneering publications of Yablonovitch and John that the term of *Photonic Crystal* (PhC) was firstly coined [1], [2]. These two words resume perfectly their condition. On one hand, the word *Photonic* refers to the fact that they are sub-micrometer structures that interact with light. On the other hand, *Crystal* refers to the essence of their structure. This is, they are formed by periodical arrangement of *(photonic) atoms* or *(photonic) molecules*. In other words, PhCs are structured materials with a refractive index distribution that affect the motion of photons when light interacts with them. The optical properties of PhC can be inferred from Maxwell's equations.

$$\boldsymbol{\nabla} \times \boldsymbol{H} = \boldsymbol{J} + \frac{\partial \boldsymbol{D}}{\partial t} \tag{3.1}$$

$$\boldsymbol{\nabla} \times \boldsymbol{E} = -\frac{\partial \boldsymbol{B}}{\partial t} \tag{3.2}$$

$$\boldsymbol{\nabla} \cdot \boldsymbol{D} = \rho \tag{3.3}$$

$$\boldsymbol{\nabla} \cdot \boldsymbol{B} = 0 \tag{3.4}$$

where $\boldsymbol{H}$ is the magnetic field (A m^{-1}), $\boldsymbol{J}$ is the electric current density (A m^{-2}), $\boldsymbol{D}$ is the electric displacement field (C m^{-2}), $\boldsymbol{E}$ is the electric field (V m^{-1}), $\boldsymbol{B}$ is the magnetic induction field (T) and ρ is the charge density (C m^{-3}).

These equations describe the propagation of electromagnetic waves in arbitrary media. For a better understanding, and without loss of rigor, the following calculations are done under the assumption of isotropic, homogeneous, non-magnetic and non-electric media. For other kind of media, the procedure is the same, but involves more complex calculations.

In the specified case, the four equations are given by the following expressions,

$$\boldsymbol{\nabla} \times \boldsymbol{H}(\boldsymbol{r}, t) = \varepsilon_0 \varepsilon(r) \frac{\partial \boldsymbol{E}(\boldsymbol{r}, t)}{\partial t} \tag{3.5}$$

$$\boldsymbol{\nabla} \times \boldsymbol{E}(\boldsymbol{r}, t) = -\mu_0 \frac{\partial \boldsymbol{H}(\boldsymbol{r}, t)}{\partial t} \tag{3.6}$$

$$\boldsymbol{\nabla} \cdot \varepsilon(r) \boldsymbol{E}(\boldsymbol{r}, t) = \rho \tag{3.7}$$

$$\boldsymbol{\nabla} \cdot \boldsymbol{H}(\boldsymbol{r}, t) = 0 \tag{3.8}$$

where μ_0 is the vacuum permeability (H m^{-1}), ε_0 vacuum permittivity (F m^{-1}) and ε relative permittivity. In these equations, it has been evidenced that both $\boldsymbol{E}$ and $\boldsymbol{H}$ are time- and space-dependent functions. According to Fourier's theory, any expression can be approximated by a set of appropriated harmonics. Therefore, since Maxwell equations are linear, $\boldsymbol{H}$ and $\boldsymbol{E}$ can be separated into two parts, that for space and that for time, and express them in terms of harmonic modes.

$$\boldsymbol{E} = \boldsymbol{E}_0 e^{i(\boldsymbol{kr}-\omega t)} = \boldsymbol{E}(\boldsymbol{r})e^{-i\omega t} \tag{3.9}$$

$$\boldsymbol{H} = \boldsymbol{H}_0 e^{i(\boldsymbol{kr}-\omega t)} = \boldsymbol{H}(\boldsymbol{r})e^{-i\omega t} \tag{3.10}$$

where the wave vector $\boldsymbol{k}$, that points in the direction of wave propagation, must be independent of $\boldsymbol{r}$. Same reasoning must be considered for the frequency ω and t. When these relationships are introduced in equations (3.5) and (3.6) to finally obtain

$$\boldsymbol{\nabla} \times \boldsymbol{H}(\boldsymbol{r})e^{-i\omega t} = -i\omega\varepsilon_0\varepsilon(r)\boldsymbol{E}(\boldsymbol{r})e^{-i\omega t} \tag{3.11}$$

$$\boldsymbol{\nabla} \times \boldsymbol{E}(\boldsymbol{r})e^{-i\omega t} = i\mu_0\omega\, \boldsymbol{H}(\boldsymbol{r})e^{-i\omega t} \tag{3.12}$$

Note that previous equations evidence through $\varepsilon(\boldsymbol{r})$ that the refractive index of the media where light travels through –i.e. photonic crystals– depends on the position.

Equations (3.11) and (3.12) can be reorganized to obtain the **curl equations**.

$$\boldsymbol{\nabla} \times \boldsymbol{H}(\boldsymbol{r}) + i\omega\varepsilon_0\varepsilon(\boldsymbol{r})\boldsymbol{E}(\boldsymbol{r}) = 0 \tag{3.13}$$

$$\boldsymbol{\nabla} \times \boldsymbol{E}(\boldsymbol{r}) - i\omega\mu_0\boldsymbol{H}(\boldsymbol{r}) = 0 \tag{3.14}$$

Both equations can be synthesized into one. For this purpose, divide (3.12) by $\varepsilon(\boldsymbol{r})$. Then use (3.11) to release $\boldsymbol{E}(\boldsymbol{r})$ from the equation and combine ε_0, μ_0 to yield the vacuum speed of light, $c = 1/\sqrt{\varepsilon_0\mu_0}$. As a result, the **master equation**, which depends exclusively from $\boldsymbol{H}(\boldsymbol{r})$, is obtained.

$$\boldsymbol{\nabla} \times \left(\frac{1}{\varepsilon(\boldsymbol{r})}\boldsymbol{\nabla} \times \boldsymbol{H}(\boldsymbol{r})\right) = \left(\frac{\omega}{c}\right)^2 \boldsymbol{H}(\boldsymbol{r}) \tag{3.15}$$

In left side of equation, three linear transformations to $\boldsymbol{H}(\boldsymbol{r})$ are performed –in fact, three composed linear transformations can be simplified into one linear transformation. As a result, the same $\boldsymbol{H}(\boldsymbol{r})$ multiplied by a scalar factor is obtained. In essence, this is an eigenvalue problem.

$$A\boldsymbol{v} = \boldsymbol{\lambda v} \equiv \Theta\boldsymbol{H}(\boldsymbol{r}) = \left(\frac{\omega}{c}\right)^2 \boldsymbol{H}(\boldsymbol{r}) \tag{3.16}$$

where A is a square matrix, $\boldsymbol{v}$ the characteristic vector, or eigenvector, and λ is the characteristic value, or eigenvalue. In this case, A is the corresponding matrix after performing the curl operations and the division by $\varepsilon(\boldsymbol{r})$, $\boldsymbol{H}(\boldsymbol{r})$ is the eigenvector, and $\left(\frac{\omega}{c}\right)^2$ the eigenvalue.

Dispersion Relation & Photonic Crystals

The solution of Equation (2.14) gives interesting results when applied to different type of media. The first general conclusion is that there is a relationship between ω and k. This is resumed in the dispersion relation.

$$\boldsymbol{k^2} - \mu_0\varepsilon\omega^2 = 0 \Leftrightarrow \omega = \frac{c}{n}\boldsymbol{k} \tag{3.17}$$

This has important implications. From previous equation it follows that there are different solutions depending on the value of $n = \sqrt{\varepsilon(r)}$. For the case n = 1, i.e. when modes travel through the air, exists a continuous set of solutions; on the contrary, when n > 1, modes propagate in the medium and find discrete solutions when solving the master equation.

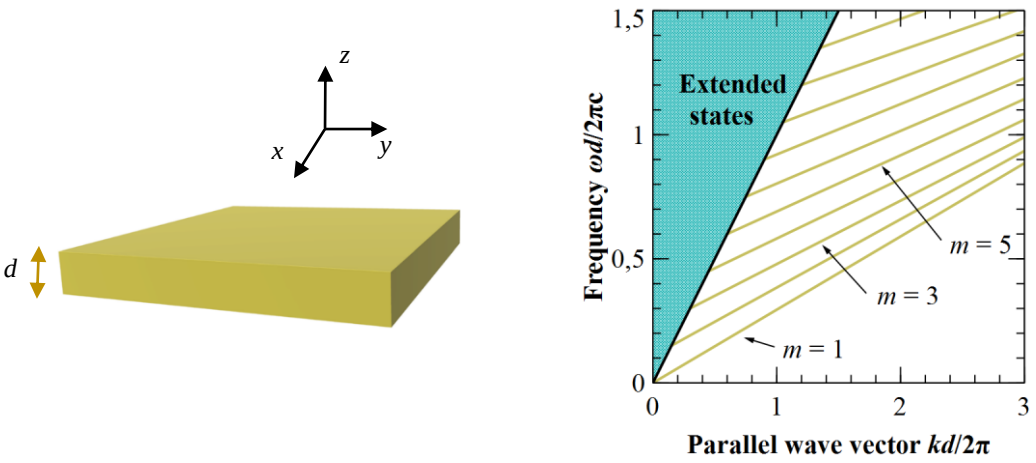

Figure 3.1. (Left) Silicon slab (n = 3.42) of thickness d which dispersion relation shows different propagating modes (right). Extended states (blue) are above the light line (black). Below, there are the discretized modes localized in the silicon media. In both regions the propagation is considered to be in the z direction.

Let's start showing the simplest case of an *XY* infinite slab of silicon with a generic thick d placed in air –see Figure 3.1. Consider the light traveling in the z direction. The solution of the master equation gives a region, over the *light line* ($\omega > ck$), with a continuum of extended states. Below the light line there are only discrete states that are solution of the equation. This is, only certain frequencies are allowed to travel through the medium.

If more layers are added, conforming an array of alternating pieces of silicon and air as in Figure 3.2, a one-dimensional photonic crystal is created (indeed, it is a Bragg grating). As commented at the beginning of the section, these structures have been studied since the endings of the 19th century. Therefore, it is well known that they present a total reflection band (or bandgap) for electromagnetic waves travelling along the **z** direction. In other words, for specific frequency ranges and directions, the light is not allowed to go through the media.

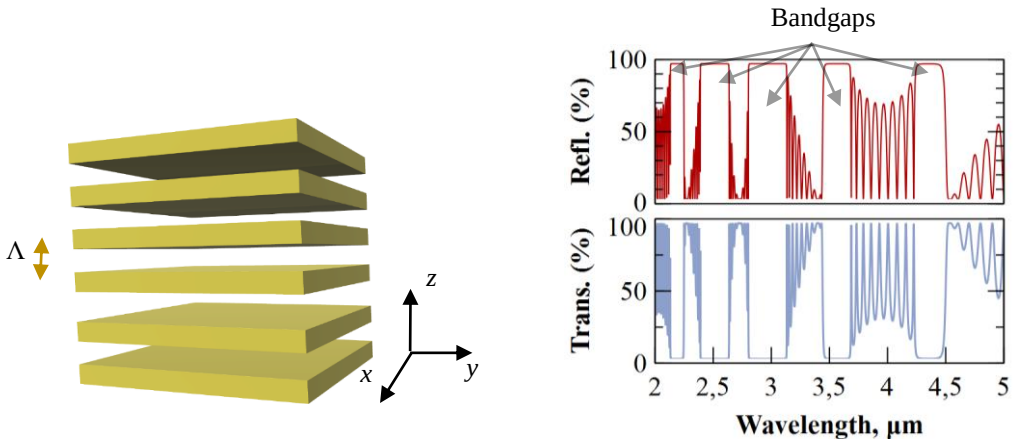

Figure 3.2. (Left) Stack of silicon slabs in air. (Right) Transmission and reflection spectra for light propagation in the z-direction.

The traditional way to analyze Bragg gratings (or 1D Photonic crystals), is using the propagation of plane waves travelling in the *z* direction through the structure. Thus, the total reflection or transmission in a specific position within the PhC can be determined. In concrete, it is possible to know the total reflectance and transmittance for the entire structure and, therefore, the transmission or reflection response of the photonic crystal [3].

However, this Thesis will follow the formalism proposed by Joannopoulos, the so-called *analysis of band structures*, to understand the nature of the optical response of PhCs. Despite it can be less obvious or less visual than the conventional methodology, this approach is more suitable for generalizing to 2D and 3D structures. Furthermore, this formalism gives a simpler way to numerically compute the response in arbitrary media and arbitrary shapes for the photonic crystals.

Let's go back to the analysis of band structures for 1D photonic crystals. This is, it has to be found the frequencies that fulfil the **master equation** for an arbitrary structure of a periodical air-material array. For the sake of simplicity, both materials are considered to have constant value in the refractive index.

$$\frac{\mathrm{d}^2\psi}{\mathrm{d}z^2} + k_0^2 n^2(z)\psi(z) = 0 \quad \text{with} \quad k_0 = \frac{\omega}{c} = \frac{2\pi}{\lambda_0} \tag{3.18}$$

This equation can be analytically solved. In concrete, the solutions are plane waves propagating in ± *z* which expression is given by,

$$\psi(z) = e^{ikz} \quad \text{with} \quad k = \pm n k_0 = \pm n\frac{\omega}{c} \tag{3.19}$$

Furthermore, Floquet-Bloch theorem states that a general solution for Maxwell equations, in the case of having a modulated refractive index, as it is the case, is

$$\psi(z) = e^{ikz}u_k(z) \tag{3.20}$$

In which $u_k(z)$ is a periodic function with the same period as $n(z)$ and *k* is no longer given by $k = \pm nk_0$. All the periodical information that was previously contained in $k(z)$, now has balanced to the function $u_k(z)$. Therefore, joining the two last equations, the solutions to the eigenvalue problem is

$$e^{ikz}u_k(z) = e^{ikz}u_k(z + \Lambda) \tag{3.21}$$

Or more generally,

$$e^{i\boldsymbol{k}z}u_{\boldsymbol{k}}(\boldsymbol{r}) = e^{i\boldsymbol{k}r}u_{\boldsymbol{k}}(\boldsymbol{r} + \Lambda) \tag{3.22}$$

These results highlight two interesting properties, symmetry and periodicity, that have important consequences in photonic crystals. They show that the set of values *k*, *-k*, *k+mK* and *–k+mK* have the same eigenvalues and similar eigenfunctions, where $K = \frac{2\pi}{\Lambda}$ being Λ the period of the grating or lattice and *m* an integer number.

It is only necessary to study the solutions in the interval *k* = [0, $\frac{K}{2}$] to completely characterize the whole system. Others values can be obtained applying symmetry operations. This *primitive* cell is called the *first Brillouin zone* or *Irreducible Brillouin zone*.

Let's try to understand the meaning of these results. Imagine a photon propagating through the air with a frequency ω and thus, an energy $E = \frac{hc}{\lambda} = \frac{hc}{2\pi}k$. Then, imagine the same photon but now traveling through the periodical 1D structure. Its energy cannot vary,

therefore, the only option is that the frequency changes. However, there is an energy limit inside the Brillouin zone, which is evidenced at the boundary $k_{max} = \frac{\pi}{\Lambda}$. It can be seen that this k_{max} (for higher k symmetry and periodic considerations must be applied) implies a maximum frequency, i.e., the one in air, $\omega_{max\_air} = \frac{c\pi}{\Lambda}$. In the case of being in the material, the maximum frequency is $\omega_{max\_structure} = \frac{c\pi}{\Lambda\sqrt{\varepsilon}}$. For $\varepsilon > 1$, it is found that $\omega_{max\_structure} < \omega_{max\_air}$. Therefore, there is a maximum energy given by $E_{max} = \frac{hc}{2\pi} k_{max} = \frac{h}{2}\frac{c}{\Lambda\sqrt{\varepsilon}}$.

The energy seems to be not conserved for values between $\omega_{max\_structure}$ and ω_{max_air}. What happened?

Two are the possible answers. The first is that there is an imaginary term in the refractive index $n = \sqrt{n_{re} + in_{im}}$ that absorbs part of the energy. This is a commonly used equation to denote absorbing materials. However, at the beginning it was stated that the 1D structure was composed by two materials with constant refractive index values. Therefore, this option has to be discarded. The other option is the existence of an imaginary part for the wavenumber. In this way, the energy would be given by $E = \frac{hc}{2\pi}|k_{re} + ik_{im}|$, therefore, solving the problem of energy conservation. These imaginary terms are also known as evanescent modes and will have a key role in the thesis, as explained in next section.

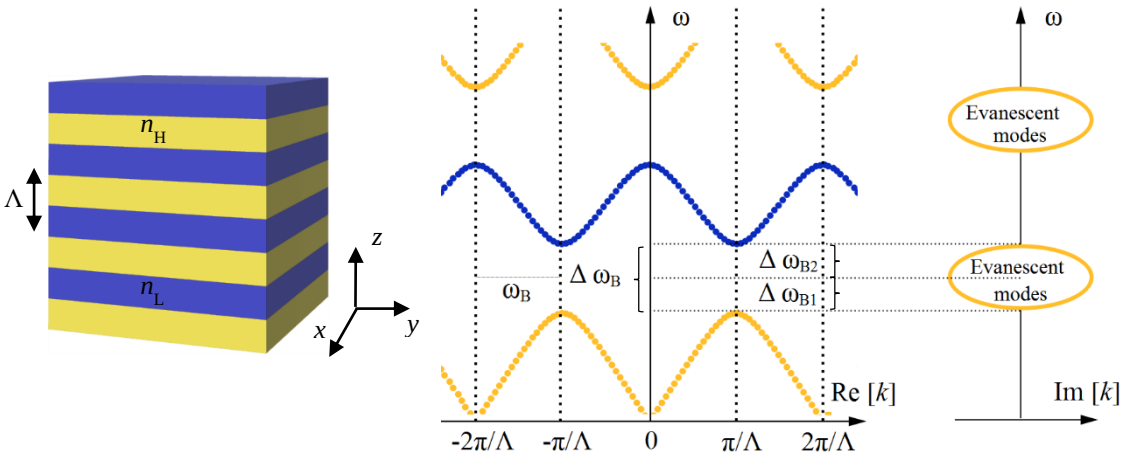

Figure 3.3. Band diagram of high- and low- refractive index structure in the Brillouin zone (n_H = 3.42 (Si), and n_L = 1.00 (air)). Imaginary modes appear at the bandgap. A total of 5 periods (ten alternated layers with the same depth, 1 micron), have been used for the calculation. Bands have been intentionally painted with similar colors than the stack in the left image in order to denote the *dielectric band* (orange) and the *air band* (blue). These terms are coined to evidence where the energy of the modes is concentrated, either in high-refractive regions or low-refractive regions [4]

It has been explained that energy has its maximum value (associated to a maximum frequency) at the boundaries of the Brillouin zone. When the high-refractive material is different than air, a gap, $\Delta\omega_{B1}$, appears between the expected frequency in air, ω_B, and the maximum frequency achieved in the material, $\omega_{max\_structure}$. It is known from Floquet-Block theorem that there is a symmetry in the solutions of the master equation. This means that for the next band of solutions m =2, a frequency gap, $\Delta\omega_{B2}$, between the minimum wavenumber achieved for $k = \frac{\pi}{\Lambda}$ and the one obtained in air also will be found. Only when the frequency increases enough, a real k value is achieved, thus giving the minimum energy value of m = 2. The sum of both gaps, gives the so-called **bandgap**,

$$\Delta\omega_{B1} + \Delta\omega_{B2} = \Delta\omega_{B} \tag{3.23}$$

The same argument can be applied for all points in the irreducible Brillouin zone and for all *m* to obtain the whole diagram value, as depicted in Figure 3.3, where it is plotted the band diagram for real and imaginary terms of frequency. In this case, the simulations have been done using silicon in the high refractive layer and air in the lower.

Figure 3.4 shows that the bandgap depends on the refractive index of the material. Left image depicts propagation of electromagnetic waves in air media. Of course, no bandgap is observed. Central image corresponds to alternate layers of silicon dioxide (n = 1.33 @ 5 μm) and air. In this case, it is noticeable the existence of a bandgap. Finally, the same band diagram as in Figure 3.3 with only the two first bands is depicted in right image. It can be seen that the bandgap has clearly increased. Thus, forbidden bands become wider for higher refractive contrast.

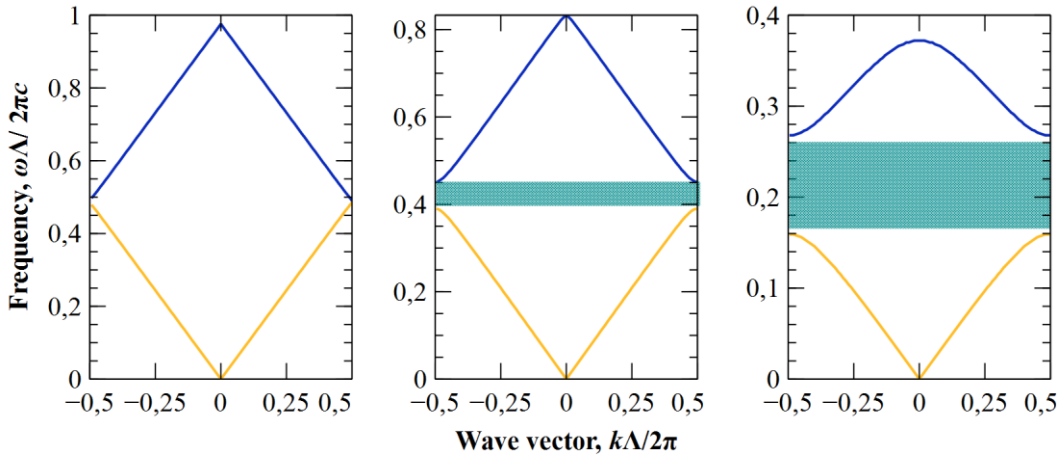

Figure 3.4. Bandgap widening by changing the refractive index contrast. In the image on the left there is no separation between first and second band because both materials have the same refractive index (there is no refractive index contrast). In the central image the bandgap is represented when the high refractive layer is silicon dioxide and in the right image when it is silicon. In all cases, the material of the low refractive index layer is air.

It can also be observed from Figure 3.4 that using higher refractive materials moves the spectrum towards lower frequencies (higher wavelengths). Therefore, bandgap position depends on the choice of materials. Furthermore, results of Figure 3.4 depends on the constant lattice, Λ. This means that, as demonstrated by Joannopoulos, photonic crystals are scalable. Both, materials' refractive index and materials' depth, are the factors that determine the position of the bandgap. This is an important property that will be used in the design of our 3D photonic crystals. In fact, silicon is an exceptional material to work in the entire mid-infrared range with the sizes that have been used during the thesis.

Same arguments can be applied for 2D and 3D photonic crystals. Figure 3.5 shows typical image of 2D and 3D photonic structures and their corresponding band diagram.

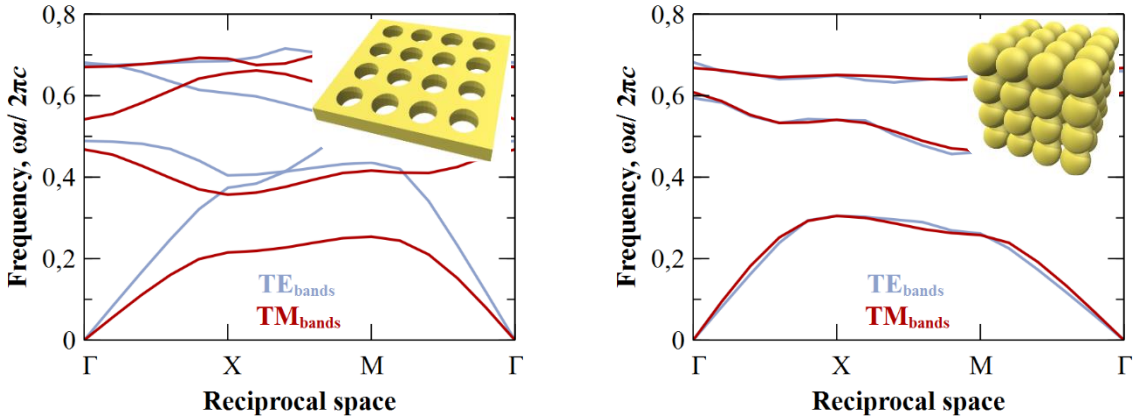

Figure 3.5. 2D and 3D photonic crystals and their respective photonic band diagrams. Materials of both structures are silicon (gold color) and air. Results have been referred to the reciprocal lattice, a common way to report the results. For a better explanation of the Brillouin zone and reciprocal lattice, see Appendix B in [4].

It has to be remarked that 3D photonic crystals have demonstrated to be the only ones, on the contrary of 1D and 2D, to exhibit complete bandgaps. In other words, that they can block a certain frequency range for all ***k*** vectors.

This thesis will focus on 3D photonic crystals as well as will mainly work on ***k*** perpendicular to the surface. But, instead of working with PhCs which consist on a periodic lattice, a defect in the structure will be introduced in order to rise a resonant mode in the middle of the bandgap. This mode will be the one that will be used for the spectroscopic detection of gases.

3.1 Photonic crystals with defects

3.1.1 A single point defect

It is well known from classical theory that localized modes appear when introducing a defect in a Bragg grating, i.e. by lengthen or shorten a period or by changing the local refractive index [5]. From the *band diagram* point of view, this means that it is possible to enable a resonant mode within the bandgap. This is, an evanescent mode, or small range of them, that were not allowed to traverse the perfectly periodic photonic crystal, take profit of the resonance in the defect in order to propagate through the structure. This is represented in Figure 3.6. It shows the typical structure of a photonic crystal with a defect that consist on doubling the thickness of a high refractive layer. Low refractive index layers on both sides of the cavity act like frequency-specific mirrors. As a consequence, light is trapped in the defect due to back and force propagation of the electromagnetic field at the chosen frequencies. Thus, the electric-filed is concentrated in the defect, allowing its further propagation through the rest of the photonic crystal.

This idea can be more clearly represented using the concept of *Density of States*. *Density of states* is the number of modes allowed to travel through the structure per unit frequency. For a better understanding of the concept, let's go back to Figure 3.3. It can be seen that for the case without refractive index contrast, i.e. for a homogenous media (left image), there is a linear relationship along the entire irreducible Brillouin zone. In other

words, the extended states are equally distributed in relative to the wave vector. Therefore, there is a constant density of states. But when the contrast in the refractive index increases, the linear relation is lost, and a greater concentration of states appears at the limits of the irreducible Brillouin due to the existence of a photonic bandgap (middle and right images).

Right image of Figure 3.6 shows the density of states for the Bragg grating of the left, where the resonant mode is depicted inside the bandgap.

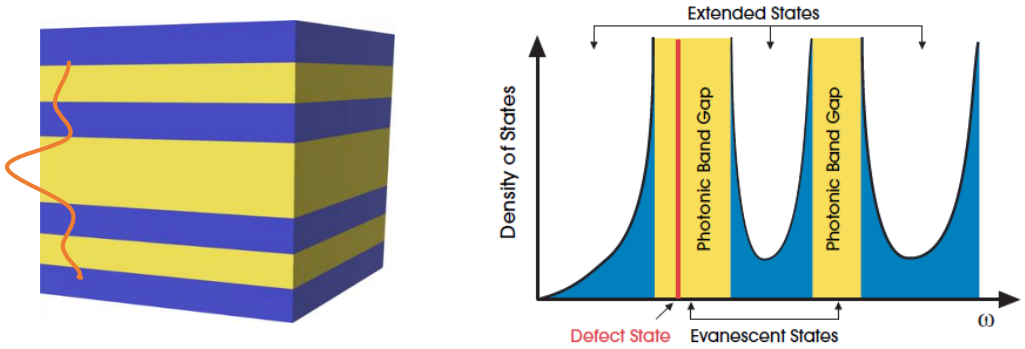

Figure 3.6. (Left) 1D photonic crystal with a defect in the middle and artistic representation of the electric-field distributed along the Bragg grating (orange line). (Right) Density of states with a resonant mode in the bandgap. Image extracted from [4].

The same reasoning applies to 2D and 3D structures with the exception that, in the three-dimensional case, the defect must be larger than a critical size to enable defect states. This has a clear analogy with the weak potential problem in quantum mechanics, where it is demonstrated that a bound-state always exists for one and two-dimensional attractive potentials for any size. But, for higher dimensions, a minimum volume or depth for the potential is required [6]. This aspect will be crucial when designing the 3D macroporous silicon photonic crystals with defects.

Figure 3.7 depicts a typical 3D macroporous silicon photonic crystal with a defect and its transmittance and reflectance [7].

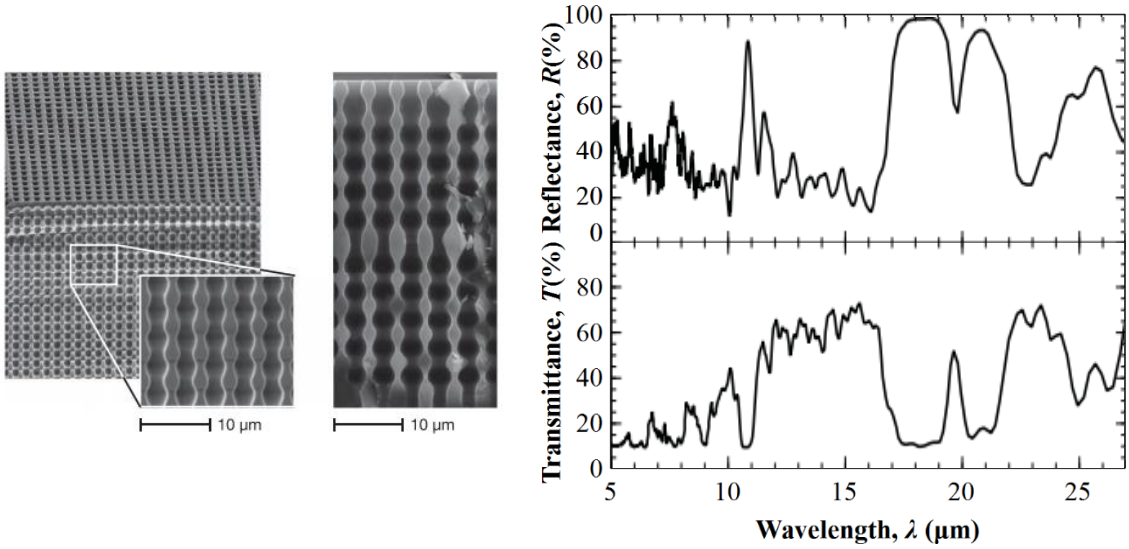

Figure 3.7. In-house fabricated macroporous silicon photonic crystal with a planar defect in the middle fabricated in our lab. Transmittance and reflectance show a peak and a tip inside the bandgap as a consequence of resonance in the defect. Images extracted from [7].

It can be seen that the resonant modes are depicted in the transmission spectrum as a peak and in the reflection as a dip. Thesis will work mainly in transmission and the transmitted peak will be placed inside the absorption spectra of the gas in order to determine the gas concentration.

3.1.2 Multiple point defects or photonic molecules

Multiple defects can be used to guide light or to couple resonant modes. The usual name of the first ones are linear defects and constitute the basis of wave guiding using photonic crystals. This topic, despite of being of high interest, is out of scope of the Thesis.

The coupling of two or more resonant modes is called *photonic molecule* (PM). To understand the coupling of the resonant modes, it is useful to go back to the master equation. From the first section it is known that the general solution can be expressed as a plane wave. In the case of having more than one mode, we will use the superposition of as many plane waves as modes, or photonic atoms, we have in the PM. For the sake of simplicity, it will be exemplified for two cavities.

A general plane wave can be expressed by the sum of two different individual plane waves [8]

$$\boldsymbol{E}(\boldsymbol{r},t) = [c_1\boldsymbol{E}_1 + c_2\boldsymbol{E}_2]e^{-i\omega t} \tag{3.24}$$

where c_1, c_2 and ω have to be determined. $\boldsymbol{E}_1$ and $\boldsymbol{E}_2$ are general eigenfunctions for each one of the modes. A system with two homogenous equations with coefficients c_1 and c_2 is obtained when equation 3.24 is introduced to the master equation. The non-trivial solution for the case of two identical cavities is

$$\omega_{\pm} = \omega_0\sqrt{\frac{1 \mp \beta}{\alpha \mp \gamma}} \tag{3.25}$$

where $\alpha = \int n_r^2\boldsymbol{E}_1^2(\boldsymbol{r})d\mathbf{r}$, $\beta = \int n_{r,1}^2\boldsymbol{E}_1(\boldsymbol{r})\boldsymbol{E}_2(\boldsymbol{r})d\mathbf{r}$ and $\gamma = \int n_r^2\boldsymbol{E}_1(\boldsymbol{r})\boldsymbol{E}_2(\boldsymbol{r})d\mathbf{r}$ are the coupling parameters of the problem. It should be noticed that here $n_r(\boldsymbol{r})$ is the refractive index along the entire photonic molecule, which it equals $n_{r,j}(\mathbf{r})$ in the *j*th cavity and unity in the air.

From equation (3.25) it can be seen that the resonant frequency, ω_0, has been split in two terms symmetrically separated from it. The distance between both frequencies depends on the confinement or defect separation [9]; for increasing periods between cavities, the coupling strength is weaker. Therefore, it is reported a reduction in the splitting. On the contrary, for less periods, there is a stronger coupling and, as a result, peaks become more separated one to the other. This phenomena is depicted in Figure 3.8, where two identical cavities of 2 μm thickness have been introduced in a Bragg grating with Λ = 1 μm.

Another consequence of the coupling is the quality factor enhancement of the peaks. Generally speaking, the peak centered in ω_0 in the case of a single defect is now divided in two. Thus, each peak has narrowed in respect to the original while transmission has been maintained.

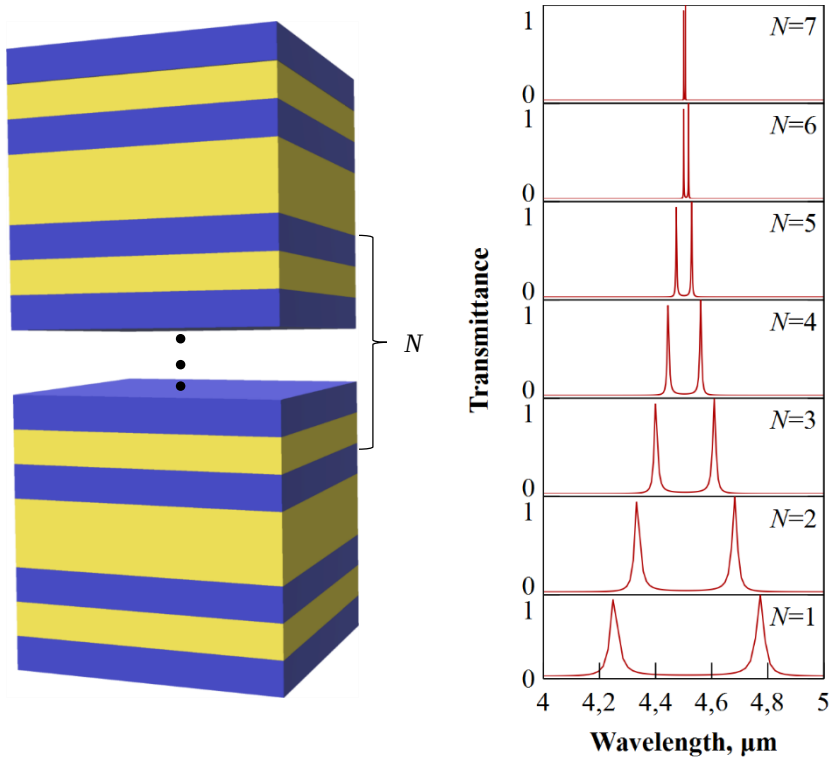

Figure 3.8. Photonic crystal with two identical cavities of thickness d = 2 μm with a periodical lattice of Λ = 1 μm (500 nm per layer) and 3 periods (6 layers) before and after the cavities. Between the defects, a number N of periods ranging from 1 to 7 have been used for calculations. For N = 7 both peaks are almost at the same frequency ω_0 as in the case of a single cavity.

Besides the abovementioned, it is reported that if the coupling is unbalanced, i.e. slightly differentiating the atomic molecules by enlarging or widen one of them, the optical response can be drastically changed [10]. In other words, the optical response of the photonic molecule can be reshaped by modifying the physical characteristics of the defects. As a consequence, instead of having two *twin* peaks, as in the case of equal defects, the optical response of the photonic molecule is reshaped in such a way that there is a predominant resonant mode –see Figure 3.9.

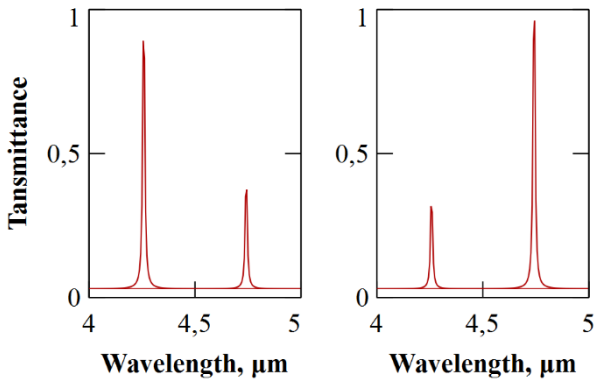

Figure 3.9. The optical response of the photonic crystal is modified in the case of asymmetric coupled cavities.

This Thesis will take advantage of photonic molecules in two different ways. On one hand non-symmetrical photonic molecules will be used to control the density of states to favor bandgap widening with a single peak remaining in the middle of it. This peak, in conjunction with the increase of the forbidden band, will facilitate spectroscopic gas

detection. On the other hand, symmetrical photonic molecules will be used to rise two similar peaks for dual gas detection either in transmission or emission. This is, use one of the peaks for measuring the target gas and the other as a reference.

3.2 Photonic crystals as selective emitters for gas sensing purposes

In previous sections light manipulation by means of photonic crystals was explained; PhCs modified the radiation of a broadband light that crossed them. This is a passive way to control the spectral radiance. This section will focus in the active control of emissivity. In concrete, it will discuss about emittance engineering in order to maximize it into a specific region of the electromagnetic spectrum and minimize it in the rest. Materials that accomplish this characteristic are called selective thermal emitters. For the ease of comprehension, black-body theory will be firstly introduced and in the following those concepts will be used in order to develop the idea of selective emitters.

3.2.1 Black-body theory

Planck's law states that all bodies above absolute zero emit radiation. Consequently, they transfer energy to the rest of the universe covering all ranges of the electromagnetic spectrum. In other words, each body in the Universe radiate energy just for being at a given temperature *T*. The most efficient absorber/emitter is the so-called blackbody which spectral radiance per unit of frequency B_ν follows next equation,

$$B_\nu(\nu, T) = \frac{2h\nu^3}{c^2} \frac{1}{e^{\frac{h\nu}{k_B T}} - 1} \tag{3.26}$$

Or expressed in terms of wavelengths,

$$B_\lambda(\lambda, T) = \frac{2hc^2}{c^5} \frac{1}{e^{\frac{hc}{\lambda k_B T}} - 1} \tag{3.27}$$

where k_B and *h* are the Boltzmann and the Planck constant, respectively, *c* is the speed of light in the medium and ν and λ are the frequency and the wavelength, respectively. Units for B_ν are W sr^{-1} m^{-2} Hz^{-1} and W sr^{-1} m^{-3} for B_λ.

The spectral radiance in respect to wavelengths is depicted in Figure 3.10. It can be seen that distribution is a continuous non-homogeneous function where the major part of it is concentrated in the range of [1-10] μm.

It can also be observed in Figure 3.10 that there is a shift of the whole spectrum towards higher wavelengths for increasing temperatures. This displacement was firstly interpreted by Wien in his homonymous law, which states that the spectral radiance of black-body has it maximum value at

$$\lambda_{max} = \frac{b}{T} \tag{3.28}$$

where b ≈ 2898 [μm K] is a constant of proportionality called Wien's displacement constant.

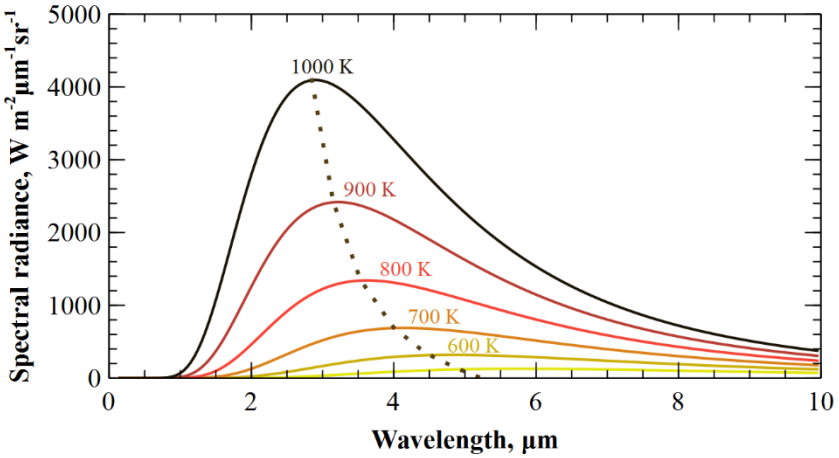

Figure 3.10. Black body spectral radiance as a function of wavelength and temperature. Dotted line represents Wien's displacement law.

To know the radiated power of a black-body, ΔP (W), with an area A (cm^2), at a given temperature T, and within a wavelength range [λ_1, λ_2] (cm) integrate equation (3.27) has to be integrated as follows,

$$P = A\int_{\lambda_1}^{\lambda_2} B_\lambda(\lambda,T) = A\frac{2hc^2}{c^5}\int_{\lambda_1}^{\lambda_2}\frac{1}{e^{\frac{hc}{\lambda k_B T}}-1} \tag{3.29}$$

3.2.2 Selective emission

In certain applications it is useful to maximize the emission in a specific region of the spectrum and minimize it in the rest. This is the case, for example, of NDIR sensing and thermophotovoltaic energy conversion where selective thermal emitters are used to, respectively, excite the vibrational modes of the fluid molecules and to concentrate radiative heat transfer at wavelengths bellow the bandgap of a paired photocell [11], [12].

There are several ways to achieve the aforementioned selective thermal radiation. The most straightforward is by using materials that naturally exhibit the desired behavior, i.e. having high emissivity in a certain range of the electromagnetic spectrum while very low in the rest. This is the case of rare-earth based ceramics and garnets, that can exhibit very sharp thermal emission peaks [13] –[15].

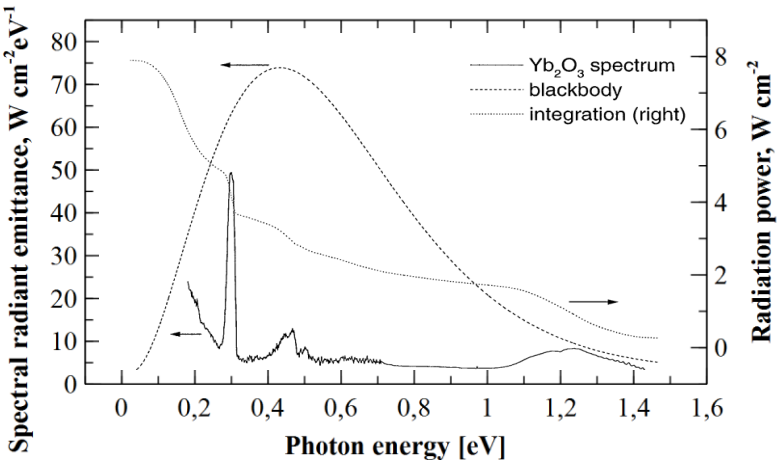

Figure 3.11. Spectral radiant emittance and radiation power (the latter is the integration of the first) versus the photon energy. The emission peak of Ytterbium(III) oxide (Yb_3O_2) ranges between 0.26 eV (4.77 µm) and 0.30 eV (4.13 µm). Data extracted from [11].

However, despite the ease of this method, the great disadvantage is that, as it is an intrinsic characteristic of the material, it is not easy to control the emission wavelength, thereby restricting its application range. Another, more appealing, option is to design 2D and 3D microstructured materials (so-called metamaterials) so as to obtain a tailored thermal emission spectrum. One of the most extensively explored solution are thermal emitters based on metallic nanostructures which, a priori, can be engineered to present narrow emission bands at the near infrared (NIR). However, losses due to free carrier absorption, ends up limiting the quality factor of the emission peak to poor values (typically $Q < 10$) [16]–[18]. All-dielectric emitters have demonstrated to be a good platform to overcome the limitations of metallic nanostructures [19], [20]. Different strategies based on plasmon resonances [21] or multi-quantum-well structures [22] –[24] have proved high-quality factors (around 150) when combined with photonic crystals. Furthermore, some of them have experimentally demonstrated the feasibility of generating narrowbands at the fingerprint of organic solvents and gases for filterless detection in the infrared region [23], [25]. This, filterless detection with narrow emission bands, is a remarkable achievement in the state of the art because it reduces complexity of NDIR devices (no filtering is required).

Figure 3.12 represents the operation mode in those devices; selective emitters are designed to point uniquely to the desired gas and the absorbance is quantified by relating the output and input signal as explained in section *2.2.2 Filters*.

Selective emission has also the advantage of enhancing energy efficiency, which is a key parameter for reducing energy consumption in thermal devices. As explained in [26] black-body-based emitters are energetically inefficient in applications where only a small part of the spectrum is used. This is the case of those NDIR devices that use a black-body emitter and a selective filter; they use only a very small portion of the electromagnetic spectrum while the rest is wasted. Structured surfaces concentrate the emission in a particular wavelength range. Therefore, the input power for heating is more optimized.

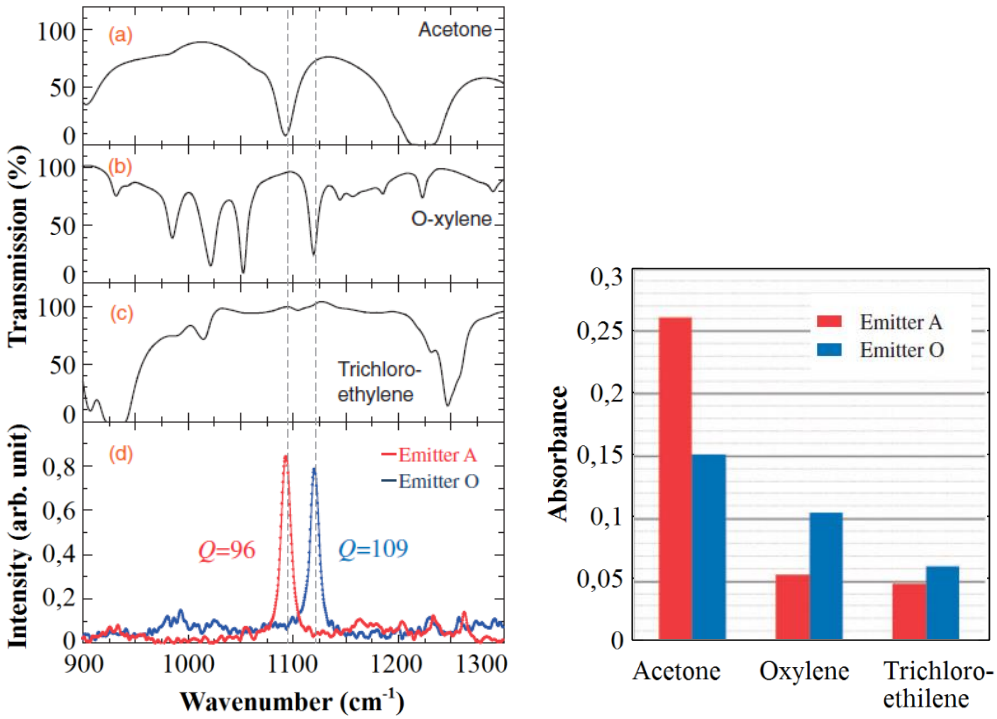

Figure 3.12. Filterless detection of Acetone and O-xylene. A third element, Tricholoro-ethylene, is introduced in order to show the cross-detection between it and the target species. Selective emitters (lower image of left picture) are designed to point uniquely to the desired range. The signal is read in the detector in order to determine the absorbance of all components (right image). This figure has been extracted from [25].

In regard to macroporous silicon, there are some previous works showing that 2D and 3D macroporous silicon photonic crystals can be used as thermal sources. In 2005 Konz et al demonstrated in their pioneering work that two-dimensional macroporous silicon PhC enhanced the emissivity of bulk silicon due to its higher roughness, leading to excellent black body behavior [25]. Other works in our team demonstrated that 3D photonic crystals could be used to tailor blackbody radiation for long infrared thermal emission [26]. Furthermore, these structures could be used in thermophotovoltaic applications when combined with metals [27]. Nevertheless, none of them reported narrow emission bands.

A goal this thesis pursues is to explore new solutions in NDIR gas sensing with macroporous silicon photonic crystals. In chapter 2, *Spectroscopic detection*, different strategies for gas detection were discussed. An option was to use a LED/photodiode combination with a filter for sensitive and selective detection. Another more low-cost option was to use a heater combined with a thermopile and a filter. The idea is to use the reported photonic crystals as narrowband emitters in the absorption region of gases in the mid-infrared region.

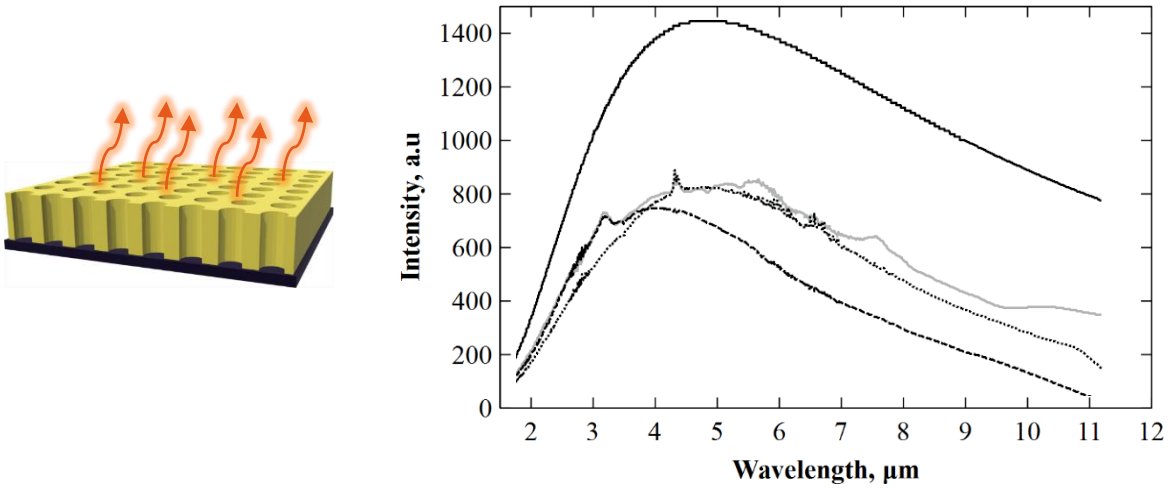

Figure 3.13. (Left) Artistic representation of 2D macroporous silicon photonic crystal used as thermal emitter. A backside platinum heater heats the porous structure that emits radiation. (Right) The silicon-micromachined IR-emitter (grey) shows higher emittance than two conventional emitters, *Ion Optics reflectIR-P1C* (dotted line) and *Laser Components SA 1037-5M3* (dashed line). Blackbody emissivity has been depicted for comparison (solid line). Data extracted from [27].

3.3 Simulation programs

3.3.1 FDTD Software

There are different computational methods to numerically obtain the optical response of structures with refractive index variation. Among the most used methods are Transfer Matrix Method (TMM) and Finite-Difference Time Domain (FDTD) method. TMM is based on the propagation of plane waves through one-dimensional layers. This is a very computing power efficient approach that can be used to predict the optical response of PhCs with higher dimensions if a series of approximations are done [30]. However, the latter gives more accurate results for any-dimensional geometry [31]. The method relies on the resolution of the Maxwell equation in discretized time and space. Figure 3.14 schematizes the way of proceeding.

The space is divided in small portions, conforming a grid, which is also called Yee lattice [31]. Curl equations are explicitly calculated in every portion of space. Thus, magnetic and electric fields are obtained in each step taking into account the spatial geometry. Next step takes the calculated $\boldsymbol{E}$ and $\boldsymbol{B}$ and, applying the external conditions, calculate again the new $\boldsymbol{E}$ and $\boldsymbol{B}$ in a step further. The whole process is complete when all the mesh is done.

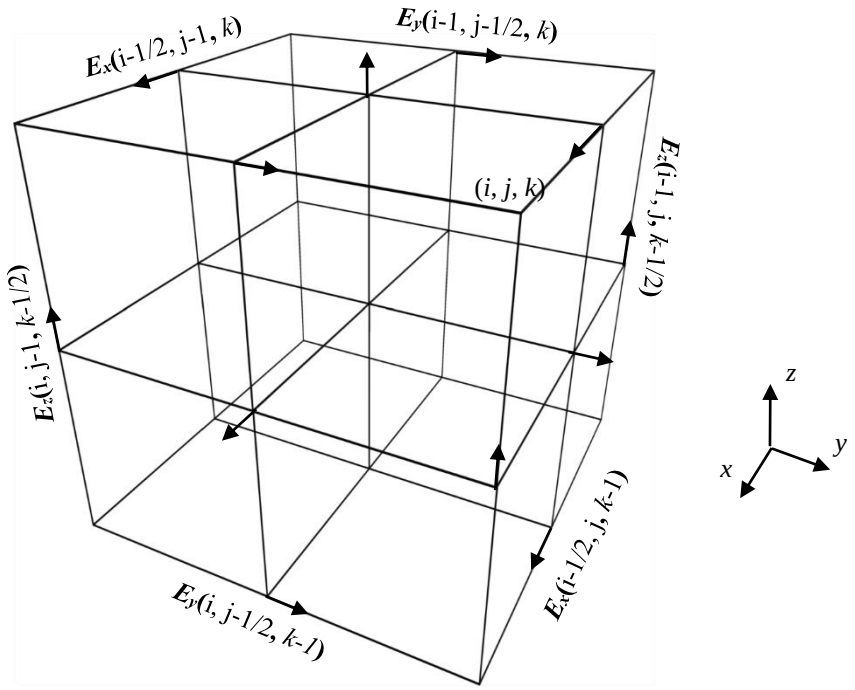

Figure 3.14. Displacement of the electric field vector components in a cubic unit cell from a Yee lattice.

The key factor of the FDTD algorithm is the step size both for time and space. Indeed, the latter depends on the first, as discussed in the following. They are key factors because accuracy, numerical dispersion and stability of FDTD depends on them. Therefore, some considerations have to be done in order to obtain representative and trustful results. The rule of thumb in this case is that the mesh size has to have, at least, 10 cells per wavelength. This is, each dimension of the cell has to fulfil with the condition of being 1/10th or less of the shortest wavelength to simulate. This can be numerically expressed as follows [32],

$$\max(\Delta x, \Delta y, \Delta z) \leq \frac{\lambda_{\min}}{10 n_{\max}} \tag{3.30}$$

where $n_{\max}$ is the maximum refractive index value in the computational domain.

Once the special steps are set, the time interval is immediately determined through the Courant-Friedrichs-Levy condition in a three-dimensional problem [33],

$$\Delta t \leq \frac{1}{v\sqrt{\left(\frac{1}{\Delta x}\right)^2 + \left(\frac{1}{\Delta y}\right)^2 + \left(\frac{1}{\Delta z}\right)^2}} \tag{3.31}$$

where *v* is the speed of the light in the medium [34].

There are a number of different FDTD software programs. The preferred one in this Thesis is the OptiFDTD solution.

3.3.1.1 Profiles and materials

The graphical interface of OptiFDTD was used to generate two different pore shapes in order to analyze our photonic structures. The simplest one is represented in Figure 3.15a.

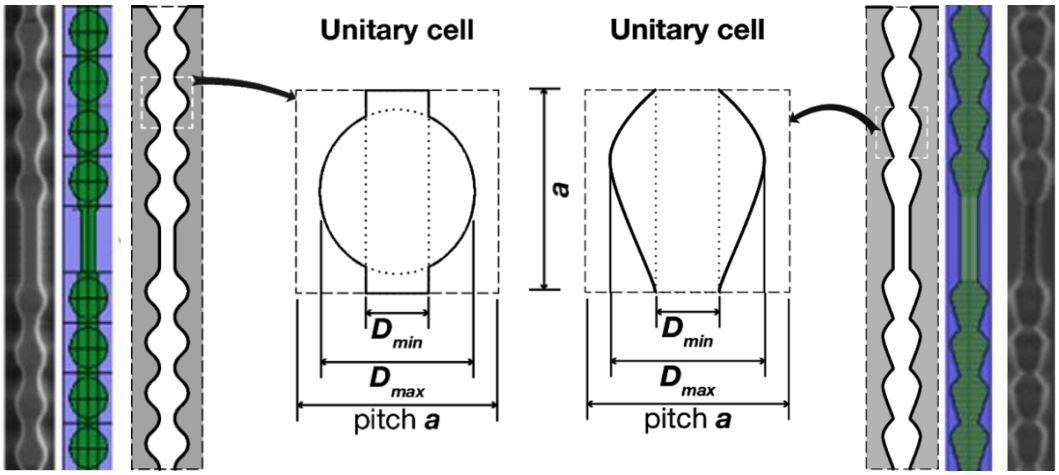

Figure 3.15. The two main profiles used in this Thesis. In the left image of each profile it is depicted a schematic of the pore and its unitary cell. Blue and green image corresponds to the profile designed using the Optiwave graphical support. Finally, it is compared to a real fabricated pore. Data are extracted from [35], [36].

Each period consists on a composition of an ellipsoid and a cylinder inserted in a unitary cell of silicon. In both cases, the material is air. This configuration fairly match with the geometry of the pores fabricated at the beginning of the Thesis. Further work showed that pear-shaped pores optimized the optical response of the photonic crystals. Therefore, a change in the simulated profile was needed. In this case, the profile consisted on a number of flat cylinders attached one to another in order to reproduce the shape. Again, a good match between the simulated and the physical pore allowed to predict the transmission and the reflection through the photonic crystal.

Up to now, the shape of a unitary cell of the pores has been explained. To create the complete pore, as many periods as desired have to be added one after each other and they have to be connected through a cylindrical cavity. Next, periodic boundary conditions must be applied at the side of the pores in order to reproduce a limitless pore structure in the transversal plane. In addition, perfect absorbing layers have to be introduced at the bottom and the top of the profile.

Finally, it has been commented that both cylinders and ellipsoids are filled by air material. However, this Thesis will deal with gases. In this case, the pores are filled with a conveniently chosen dispersive material which is characterized by two Lorentzian oscillators. The imaginary part of the dielectric function of those materials, ε_i (which is the responsible of the dispersive behavior) is given by the free-electro or Lorentz-Drude model equation [37]

$$\varepsilon_i(\omega) = \frac{S\Omega^2}{\omega_0^2 - \omega^2 + i\omega\Gamma} \tag{3.32}$$

where *S* is a dimensionless parameter that represents the strength of the corresponding resonance, Ω is the plasma frequency (rad/s), ω_0 is the resonant frequency (rad/s) and Γ the damping factor (rad/s).

In the firsts publications of this thesis these two Lorentzian curves were assumed to be the contour of the absorption lines [38] –black dashed line in Figure 3.16. This assumption did not have into account the resolution factor. In effect, at atmospheric pressure and low resolutions, as the ones used during the thesis, the absorption lines of gases are not observed. Instead of them, a very similar curve as the contour appears. However, it has to be noticed that the amplitude of this curve is almost six times weaker than the one used in

the contour approximation –solid black line in Figure 3.16. Taking this into account, the values of the Lorentzian curves were corrected for next studies.

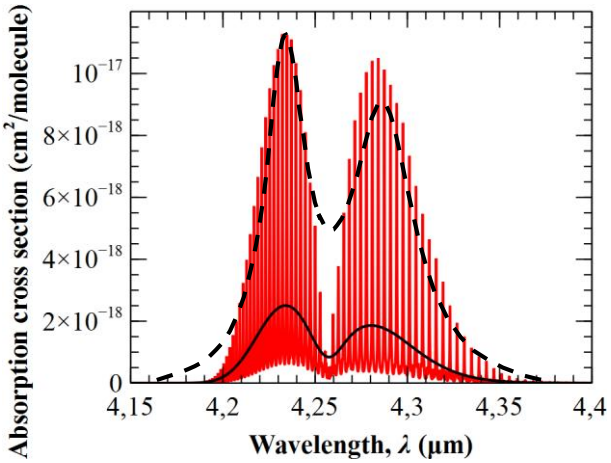

Figure 3.16. CO_2 absorption lines (red) and the successive approximations used in the Thesis.

FDTD simulations will work only with CO_2. The values for the different variables comprehended in the Lorentz oscillators are given in next table.

Approximation		***S***	***P***	***R***	***D***
Contour	Lorentzian 1	$4.0 \cdot 10^{-1}$	$7.00 \cdot 10^{12}$	$3.395 \cdot 10^{14}$	$3.10 \cdot 10^{12}$
	Lorentzian 2	$4.2 \cdot 10^{-1}$	$6.00 \cdot 10^{12}$	$3.438 \cdot 10^{14}$	$2.00 \cdot 10^{12}$
Low resolution	Lorentzian 1	$9.1 \cdot 10^{-2}$	$7.00 \cdot 10^{12}$	$3.395 \cdot 10^{14}$	$3.10 \cdot 10^{12}$
	Lorentzian 2	$9.5 \cdot 10^{-2}$	$6.00 \cdot 10^{12}$	$3.438 \cdot 10^{14}$	$2.00 \cdot 10^{12}$

Table 3.1. Parameters for the Lorentzian approximation used in simulations.

3.3.2 In-house program for modeling spectroscopic detection

In previous section it was commented that the gas filled the pores. However, the length of the pores is two short, in the order of few tens of microns, for NDIR gas sensing. There is a need of a gas cell of, at least, several millimeters, in order to perform correct gas detection. Doing it with OptiFDTD program will lead to unaffordable time consumption. Thus, an in-house software was created in order to predict the optical response of the photonic crystals when exposed to any gas for any length of the gas cell. This program relies on the formula given in equations (2.2) and (2.5).

As explained in *NDIR detection* section, the transmission peak resulting from the resonance in the cavity is discretized. The same discretization is done in the case of the gas. Next, the Beer-Lambert formula is applied for each discretized frequency (or wavelength). The envelop of all the calculated output intensities is the final response that the user will see in a spectrometer –see Figure 2.7.

The cross section of all mid-infrared gases inside the HITRAN database were obtained at atmospheric pressure and the same resolution used in the FT-IR, 4 cm^{-1}.

References

[1] E. Yablonovitch, “Inhibited Spontaneous Emission in Solid-State Physics and Electronics,” *Phys. Rev. Lett.*, vol. 58, no. 20, pp. 2059–2062, May 1987.

[2] S. John, “Strong localization of photons in certain disordered dielectric superlattices,” *Phys. Rev. Lett.*, vol. 58, no. 23, pp. 2486–2489, Jun. 1987.

[3] Sophocles J. Orfanidis, *Electromagnetic Waves and Antennas*. Rutgers University, 2002.

[4] J. D. Joannopoulos, S. G. Johnson, J. N. Winn, and R. D. Meade, *Photonic Crystals: Molding the Flow of Light (Second Edition)*. 2011.

[5] E. Hecht and A. Zajac, *Optics*. Boston: Addison-Wesley, 1974.

[6] C. A. Kocher, “Criteria for bound-state solutions in quantum mechanics,” *Am. J. Phys.*, vol. 45, no. 1, pp. 71–74, Jan. 1977.

[7] D. Vega, D. Cardador, M. Garín, T. Trifonov, and Á. Rodríguez, “The Effect of Absorption Losses on the Optical Behaviour of Macroporous Silicon Photonic Crystal Selective Filters,” *J. Light. Technol. Vol. 34, Issue 4, pp. 1281-1287*, vol. 34, no. 4, pp. 1281–1287, Feb. 2016.

[8] A. V. Tsukanov, “Quantum dots in photonic molecules and quantum informatics. Part I,” *Russ. Microelectron.*, vol. 42, no. 6, pp. 325–346, Nov. 2013.

[9] D. M. Beggs, “Computational studies of one and two-dimensional photonic microstructures,” University of Durham, 2006.

[10] S. V. Boriskina, “Photonic Molecules and Spectral Engineering,” Springer, Boston, MA, 2010, pp. 393–421.

[11] J. Hodgkinson and R. P. Tatam, “Optical gas sensing: a review,” *Meas. Sci. Technol.*, vol. 24, no. 1, p. 012004, Jan. 2013.

[12] R. Sakakibara *et al.*, “Practical emitters for thermophotovoltaics: a review,” *J. Photonics Energy*, vol. 9, no. 03, p. 1, Feb. 2019.

[13] B. Bitnar, W. Durisch, J.-C. Mayor, H. Sigg, and H. R. Tschudi, “Characterisation of rare earth selective emitters for thermophotovoltaic applications,” *Sol. Energy Mater. Sol. Cells*, vol. 73, no. 3, pp. 221–234, Jul. 2002.

[14] G. Liu and B. Jacquier, *Spectroscopic properties of rare earths in optical materials*. Springer, 2005.

[15] P. C. de Sousa Filho, J. F. Lima, O. A. Serra, P. C. de Sousa Filho, J. F. Lima, and O. A. Serra, “From Lighting to Photoprotection: Fundamentals and Applications of Rare Earth Materials,” *J. Braz. Chem. Soc.*, vol. 26, no. 12, pp. 2471–2495, 2015.

[16] K. L. Tsakmakidis, R. W. Boyd, E. Yablonovitch, and X. Zhang, “Large spontaneous-emission enhancements in metallic nanostructures: towards LEDs faster than lasers [Invited],” *Opt. Express*, vol. 24, no. 16, p. 17916, Aug. 2016.

[17] B. Liu, W. Gong, B. Yu, P. Li, and S. Shen, “Perfect Thermal Emission by Nanoscale Transmission Line Resonators,” *Nano Lett.*, vol. 17, no. 2, pp. 666–672, Feb. 2017.

[18] A. Lochbaum, Y. Fedoryshyn, A. Dorodnyy, U. Koch, C. Hafner, and J. Leuthold, “On-Chip Narrowband Thermal Emitter for Mid-IR Optical Gas Sensing,” *ACS*

Photonics, vol. 4, no. 6, pp. 1371–1380, Jun. 2017.

[19] T. Inoue, M. De Zoysa, T. Asano, and S. Noda, "Realization of narrowband thermal emission with optical nanostructures," *Optica*, vol. 2, no. 1, p. 27, Jan. 2015.

[20] M. O. Ali, N. Tait, and S. Gupta, "High-Q all-dielectric thermal emitters for mid-infrared gas-sensing applications," *J. Opt. Soc. Am. A*, vol. 35, no. 1, p. 119, Jan. 2018.

[21] Z. Wang, J. K. Clark, Y.-L. Ho, B. Vilquin, H. Daiguji, and J.-J. Delaunay, "Narrowband Thermal Emission Realized through the Coupling of Cavity and Tamm Plasmon Resonances," *ACS Photonics*, vol. 5, no. 6, pp. 2446–2452, Jun. 2018.

[22] M. De Zoysa, T. Asano, K. Mochizuki, A. Oskooi, T. Inoue, and S. Noda, "Conversion of broadband to narrowband thermal emission through energy recycling," *Nat. Photonics*, vol. 6, no. 8, pp. 535–539, Jul. 2012.

[23] T. Inoue, M. De Zoysa, T. Asano, and S. Noda, "Single-peak narrow-bandwidth mid-infrared thermal emitters based on quantum wells and photonic crystals," *Appl. Phys. Lett.*, vol. 102, no. 19, p. 191110, May 2013.

[24] T. Inoue, M. De Zoysa, T. Asano, and S. Noda, "Realization of dynamic thermal emission control," *Nat. Mater.*, vol. 13, no. 10, pp. 928–931, Oct. 2014.

[25] T. Inoue, M. De Zoysa, T. Asano, and S. Noda, "Filter-free nondispersive infrared sensing using narrow-bandwidth mid-infrared thermal emitters," *Appl. Phys. Express*, vol. 7, no. 1, p. 012103, Jan. 2014.

[26] H. T. Miyazaki, T. Kasaya, M. Iwanaga, B. Choi, Y. Sugimoto, and K. Sakoda, "Dual-band infrared metasurface thermal emitter for CO_2 sensing," *Appl. Phys. Lett.*, vol. 105, no. 12, p. 121107, Sep. 2014.

[27] W. Konz *et al.*, "Micromachined IR-source with excellent blackbody like behaviour," in *Smart Sensors, Actuators, and MEMS II. Vol. 5836. International Society for Optics and Photonics*, 2005, vol. 5836, pp. 540–548.

[28] M. Garín, T. Trifonov, A. Rodríguez, and R. Alcubilla, "Infrared thermal emission in macroporous silicon three-dimensional photonic crystals," *Appl. Phys. Lett.*, vol. 91, no. 18, p. 181901, Oct. 2007.

[29] M. Garín, D. Hernández, T. Trifonov, and R. Alcubilla, "Three-dimensional metallo-dielectric selective thermal emitters with high-temperature stability for thermophotovoltaic applications," *Sol. Energy Mater. Sol. Cells*, vol. 134, pp. 22–28, Mar. 2015.

[30] D. Hernández García, "Selective thermal emitters based on photonic crystals." Universitat Politècnica de Catalunya.

[31] K. Yee, "Numerical solution of initial boundary value problems involving Maxwell's equations in isotropic media," *IEEE Trans. Antennas Propag*, 1966.

[32] Optiwave, *OptiFDTD Technical Background and Tutorials Finite Difference Time Domain Photonics Simulation Software*. 2011.

[33] R. Courant, K. Friedrichs, and H. Lewy, "On the Partial Difference Equations of Mathematical Physics," *IBM J. Res. Dev.*, vol. 11, no. 2, pp. 215–234, Mar. 1967.

[34] A. Taflove and S. C. Hagness, *Computational Electrodynamics-The Finite-Difference Time-Domain Method*, Second Edi. Norwood: Artech House, 1995.

[35] D. Cardador, D. Vega, D. Segura, and A. Rodríguez, "Study of resonant modes in a 700 nm pitch macroporous silicon photonic crystal," *Infrared Phys. Technol.*, vol. 80, 2017.

[36] D. Vega, D. Cardador Maza, T. Trifonov, M. Garin Escriva, and A. Rodriquez Martinez, "The Effect of Absorption Losses on the Optical Behaviour of Macroporous Silicon Photonic Crystal Selective Filters," *J. Light. Technol.*, vol. PP, no. 99, pp. 1–1, 2015.

[37] K. H. Lee, I. Ahmed, R. S. M. Goh, E. H. Khoo, E. P. Li, and T. G. G. Hung, "IMPLEMENTATION OF THE FDTD METHOD BASED ON LORENTZ-DRUDE DISPERSIVE MODEL ON GPU FOR PLASMONICS APPLICATIONS," *Prog. Electromagn. Res.*, vol. 116, pp. 441–456, 2011.

[38] D. Cardador, D. Vega, D. Segura, T. Trifonov, and A. Rodríguez, "Enhanced geometries of macroporous silicon photonic crystals for optical gas sensing applications," *Photonics Nanostructures - Fundam. Appl.*, vol. 25, pp. 46–51, Jul. 2017.

Fabrication and optical characterization

This chapter describes both fabrication and optical characterization of the macroporous silicon photonic crystals. First part is devoted to the mechanism responsible of pore formation through Lehmann's model of the photoelectrochemical etching. Then, the fabrication set-up is presented and some insights of the fabrication process, such as sample preparation and post-etching techniques, will be given. Finally, it is described the optical characterization of the fabricated samples.

4.1 Macroporous silicon formation

4.1.1 Electrochemical etching: a brief description

Porous silicon was firstly discovered in 1956 by Arthur Uhlir Jr. and Ingeborg Uhlir at Bell's Labs [1]. They were carrying electropolishing experiments on silicon wafers when they accidentally found that, under specific conditions, the silicon did not dissolve uniformly but instead little pores were formed along the <100> direction of the wafer. The electropolishing is a process which uses a cathode and an anode to induce a current in an electrolyte, typically a solution of hydrofluoric acid (HF) –see Figure 4.1–, to remove material from a dielectric or metallic sample. With this discovery, the Uhlir proved that depending on the percentage of HF and the current applied the electrolyte different results may be found.

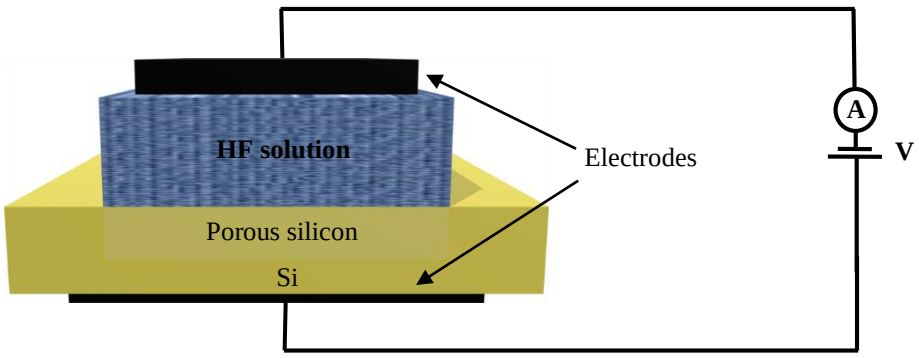

Figure 4.1. Schematic of the porous silicon formation. The surface of a silicon wafer is in contact with a solution of HF. The voltage applied between the wafer backside contact and the electrolyte leads to a pore growth.

This opened a new area of investigation based on the electrochemical etching and the properties of the porous silicon [2]. The basic mechanism follows, as a first approximation, the same behavior than a Schottky diode; semiconductor-electrolyte can be interpreted as two parallel-faced layers with opposite charge that forms a rectifying potential barrier. In this case, however, it has to take into account that chemical reaction will take place at the semiconductor-electrolyte. The dynamics of the ions in the electrolyte and the carriers in

the semiconductor in function to the external conditions, i.e. polarizations and applied current, determines the different regimes of porous silicon formation. Thus, as it happened for the Schottky diode, the *I*-*V* curves are essential to understand those dynamics. Figure 4.2 shows the curve response of the semiconductor-electrolyte system for both, *n*-type and *p*-type silicon wafers.

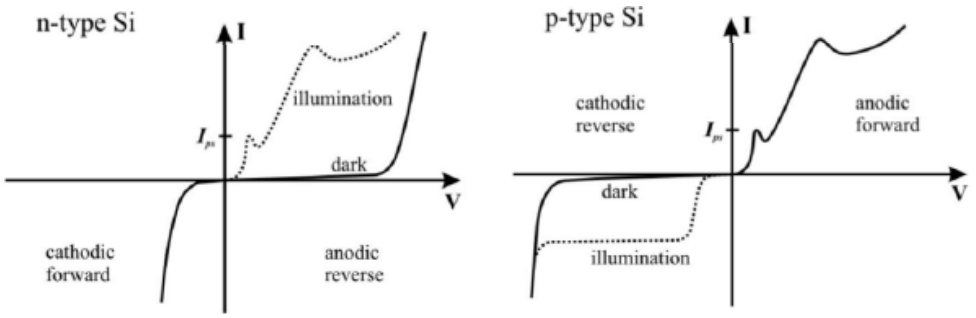

Figure 4.2. *I*-*V* curve of semiconductor-electrolyte system for *n*- and *p*-type silicon. Image extracted from [3]. Dotted and solid curves show the response of the system under illumination and dark conditions.

It can be observed that there are some clear parallelisms with the Schottky diode's curve, including photogenerated currents at revers bias. However, there are some differences that should be noticed. The first of them is that despite of having different majority carriers in *n*-type and *p*-type wafers, the same chemical reactions are given at the interface. Another important difference is that the reverse-bias dark current is much larger, typically three order of magnitudes, than in Schottky diodes.

Another important characteristic of the semiconductor-electrolyte system is that silicon dissolution only occurs under anodic polarization. Furthermore, there is a critical I-V point that divides the different regimes of dissolution. This point is the I_{ps}-V_{ps}. Electropolishing occurs for higher values while pore formation is only given at low overpotentials. In the latter case, *the surface morphology is dominated by a dense array of channels penetrating deeply into the bulk silicon* [4].

Porous silicon is divided into three categories based on the width of its pores; microporous (less than 2 nm), mesoporous (between 2 nm and 50 nm) and macroporous (more than 50 nm). In all cases, pores can be obtained under a variety of conditions. Key parameters are the HF concentration, the electrolyte type (aqueous, organic, oxidizing), the doping type of Si and its corresponding level (n, n^+, p, p^+) and, in some cases, the illumination, which can be either back-sided or front-sided [5]. Different mechanisms are involved in the formation of pores depending on their size. For instance, quantum confinement effects are the responsible of microporous silicon formation while mesoporous silicon is mainly formed by tunneling processes. In the case of macroporous silicon the mechanisms involved depend on the type of doping of the chosen silicon. In particular, pores are formed as a result of thermoionic emission in *p*-type silicon and as the collection of minority charge carriers in n-type doping. In both cases the growth direction is dependent on crystal orientation (in microporous silicon it is independent) and shows a preference for the <100> direction [6].

This Thesis will focus on macropores formation obtained through the so-called photoelectrochemical etching in n-type <100> oriented samples.

4.1.2 Photoelectrochemical etching

Photoelectrochemical etching was firstly discovered by Lehmann and Föll in 1990 [7]. This method is based on the back side illumination of low-doped n-type silicon to promote a current of photogenerated holes (always under the electropolishing current, J_{ps}) towards the electrolyte-semiconductor interface. For an ordered growth of the pores, the surface has to be pre-patterned in such a way that the defects act as seeding points for macropores. This can be done performing a lithography process and a TMAH attack, as shown in next section.

There are several models that try to explain pore formation [5]. In this Thesis it will be used to so-called Space Charge Region (SCR) model proposed by Lehman [8]–[10]. In this approach, the SCR is the responsible of accumulating the holes at the pores' tips, as shown in Figure 4.3. For proper values of the applied voltage, the SCR presents a sinusoidal shape that can reach up to several tenths of microns in width,

$$W_{SCR} = \sqrt{\frac{2\varepsilon\varepsilon_0 V_{\mathrm{app}}}{eN_{\mathrm{D}}}} \tag{4.1}$$

where ε is the dielectric constant of silicon (11.9), ε_0 the permittivity of the free space, e the elementary charge, N_{D} the density of dopants and $V = V_{\mathrm{bi}} - V_{\mathrm{app}} - \frac{kT}{e}$. In this case, V_{bi} is the built-in potential of the silicon-HF contact (about 0.5 V) and V_{app} the applied voltage to the system.

This SCR prevents holes (h^+) to go to the pores' walls so that they all concentrate at the tips. The anodic semi-reaction given in the interface is described by

$$\mathrm{Si} + 4\mathrm{HF}_2^- + h^+ \rightarrow \mathrm{SiF}_6^{2-} + 2\mathrm{HF} + \mathrm{H}_2 + e^- \tag{4.2}$$

If the generated current density J is higher than J_{ps}, then the reaction is limited by the reagents in the electrolyte. And, although the SCR directs the holes towards the tips, the excess of holes causes them to be distributed along the surface. Thus, silicon dissolves faster and along the entire inner surface, resulting in the electropolishing.

If the photocurrent density is less than J_{ps}, the opposite case will occur. This is, every hole reaching the surface will immediately react with HF ions at the pore's tips thereby propitiating the pore growth.

For the proper design of the pores, two parameters have to be taken into account, the radial dimension and the vertical dimension. Lehman's model gives a theoretical approach to calculate them.

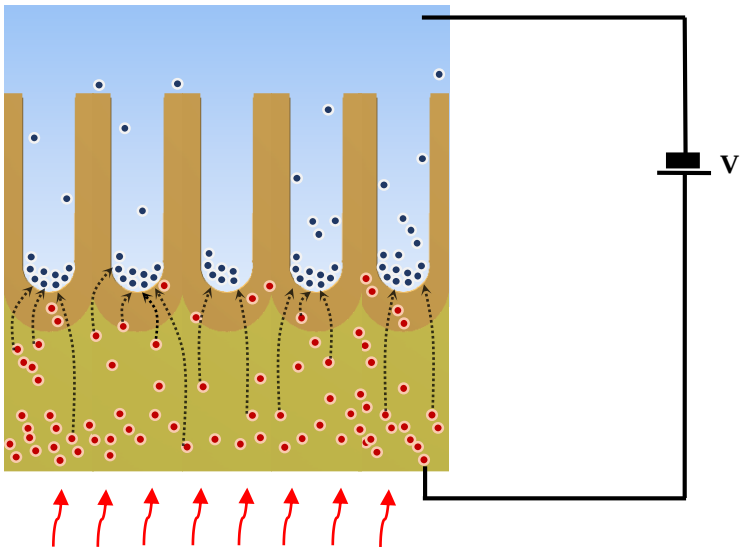

Figure 4.3. Schematic representation of pore formation. The SCR extends to the brown line in silicon. Photogenerated holes concentrate at the pore's tips due to electric field depletion. Silicon is removed at those point where holes and HF ions coincide [6].

4.1.2.1 Pore diameter (radial dimension)

From the above, it is clear that at $J = J_{ps}$ the number of holes reaching the tips equals the number of HF ions supplied by the electrolyte. Therefore, ionic transfer and charge supply are in steady-state [8]. Based on that, Lehmann made a very basic assumption that simplified the understanding of the physics beyond electrochemical etching. He assumed that for a stable pore growth, which occurs when $J < J_{ps}$, the current density reaching the tips J_{tip} is the same as J_{ps}. In other words, the current density ratio arriving to the tips from both sides of the interface is 1:1. This assumption was experimentally validated in [8] and allowed to relate the diameter of the pores with the applied current density of the system, J, following next calculations,

$$p = \frac{A_{\text{cell}}}{A_{\text{po}}} = \frac{J}{J_{\text{ps}}} \tag{4.3}$$

where p is the porosity, A_{po} is the cross-sectional area of the pores and A_{cell} represents the area of a unit cell of the pore lattice area between the silicon and the electrolyte. In the case of square pore arrangement with a pitch a (the one used in this Thesis), the porosity is given by

$$p = \frac{\pi r^2}{a^2} \tag{4.4}$$

Therefore, the diameter of the pores can be easily chosen depending on the current density, i.e. the rear illumination –see Figure 4.4.

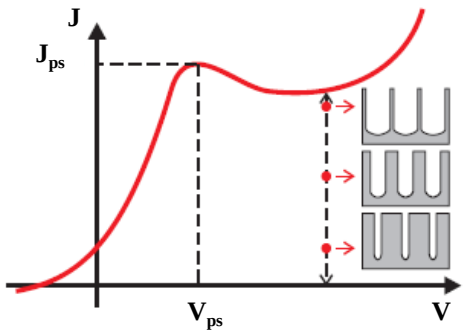

Figure 4.4. Pore's diameter depends on the working current [6].

4.1.2.2 Etching speed (vertical dimension)

Another important parameter to understand pore formation is the etching speed which characterizes the longitudinal dimension. The etching depends on the current arriving the tips. This is J_{ps}, which expression was experimentally obtained,

$$J_{\mathrm{ps}} = C_{\mathrm{ps}} c_{\mathrm{HF}}^{3/2} \mathrm{e}^{\frac{-E_{\mathrm{a}}}{kT}} \tag{4.5}$$

and showed its dependency with HF concentration and temperature. In the equation, C_{ps} is an experimental constant that amounts 3300 A cm^{-2}, c_{HF} is the HF percentage and $E_{\mathrm{a}} = 0.343$ eV is the activation energy. An etching speed of about 1 µm/min is obtained for a 5% HF concentration at 10 ºC.

To sum up, the SCR model gives us the way to estimate the pore diameter and the length of the pore in respect to the backside illumination. This allows the design of not only straight pores but also modulated pores, such as the ones we of this Thesis.

4.1.3 Sample preparation and operation procedure of EEL

4.1.3.1 Sample preparation

The sample has to be pre-processed before the electrochemical attack. Sample preparation begins by the implantation of a N^{+} layer at the back side of an *n*-type ⟨1 0 0⟩ crystalline silicon wafer with an initial resistivity between 0.1-0.3 Ω cm. A Nanoimprint Lithography (NIL) consisting on an array of squared windows is then performed with a pitch of 700 nm. It is worth mentioning that choosing the correct pitch value is crucial to obtain the desired optical response. This is because the horizontal distance between pores, the pitch, limits the vertical periodicity that can be achieved in modulated pores [6]. In other words, the lower the pitch, the shorter the modulation periods that can be achieved. It is demonstrated that a 700 nm lithography allows to naturally work in the mid-infrared spectral region. Next a Reactive-Ion Etching (RIE) and a tetramethylammonium hydroxide (TMAH) etching is performed. RIE opens the silicon windows within the silicon oxide, and the TMAH bath creates the inverted pyramids that will act as the nucleation points for pore growth. Finally, the silicon oxide is removed from the wafer. The entire process is schematized in Figure 4.5.

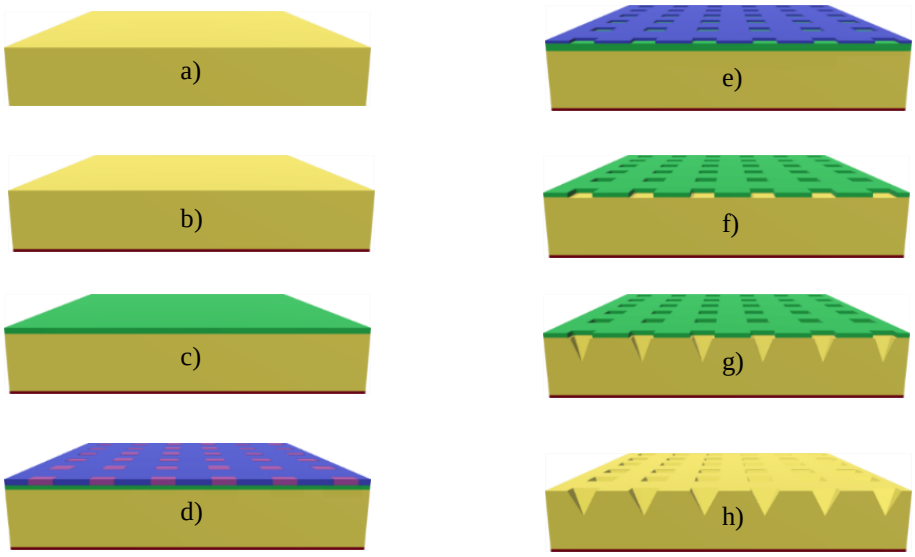

Figure 4.5. Sample preparation for the electrochemical etching. a) *n*-type Silicon wafer. b) Back-side implantation of ohmic contact. c) Oxidation. d) and e) Nanoimprint lithography: imprint with a mold and pattern transfer to the resin. f) Reactive-ion etching (pattern transfer to silicon oxide). g) TMAH attack to create inverted pyramids. h) Remove the silicon oxide. Wafer is ready for electrochemical etching.

4.1.3.2 Set-up operation and explanation of in-lab procedure

After this initial step, the sample is prepared for the electrochemical etching. For this purpose, it is introduced in the set-up that our group developed for the fabrication of macroporous silicon, especially during Dr. Trifon Trifonov thesis [11]. In concrete, the sample is inserted in a Polyvinyl Chloride (PVC) cell designed to process 2.5 cm $\times$ 2.5 cm samples. As Figure 4.6 shows, the rear part of the wafer faces the LED array while the patterned surface is in touch with the electrolyte.

The contacts provide the voltage polarization as well as the current that is flowing through the system. Both of them have been generated with an in-house program running in Matlab, which was programed following the design rules of Lehmann model explained in previous section. A Labview program is the responsible of real-time regulation of the system. This is a crucial part of the electrochemical attack since the current applied to the sample may differ from the initial profile for a number of reasons (HF concentration, temperature variation, etc.). Thus, thanks to a feedback circuit, the Labview program can specify the difference between them and rectify the real-time current in order to achieve the desired profile (right image of Figure 4.6).

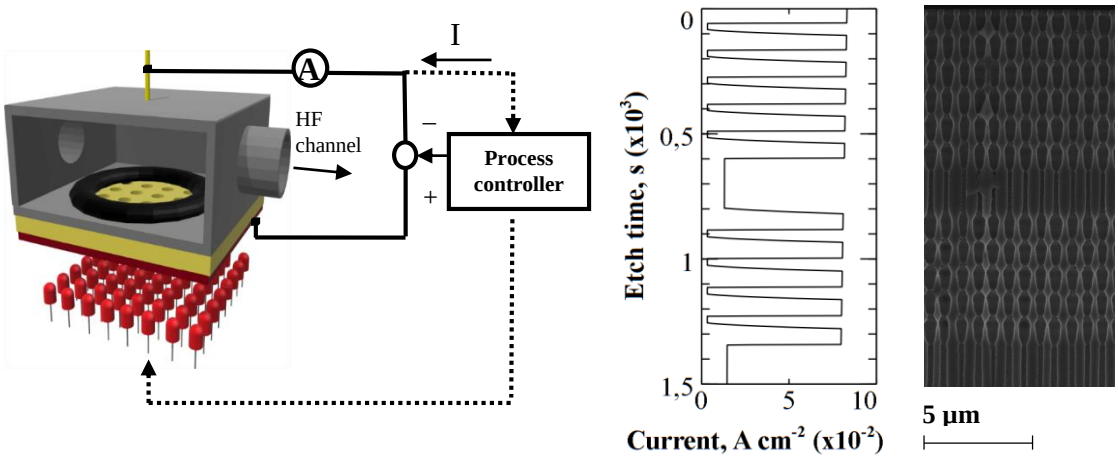

Figure 4.6. (Left) Schematic representation of the photoelectrochemical etching. PVC cell (grey) designed to attack 1 cm^2 from the 2.5 cm × 2.5 cm sample. HF goes through the channel and interacts to the exposed area. Current (central image) and polarization are provided through the contacts. They are real-time regulated by a process controller. Adapted figure from [12]. (Right) SEM picture of the fabricated photonic crystal.

4.1.3.3 Electrolyte specifications

A key point to obtain spatial homogeneity in macropores is the need of incorporating surfactants in the electrolyte in order to reduce the surface tension and, therefore, avoiding the sticking probability of hydrogen bubbles [13], [14]. Indeed, in the anodic semi-reaction equation (4.2), can be seen that there is a production of H_2 ions. These ions tend to stay at the electrolyte-silicon interface due to the high hydrophobia that hydrogenated silicon shows. Therefore, they prevent from fresh electrolyte arriving to the pores. The inclusion of a surfactant allows these H_2 ions to be released to the electrolyte and to prevent them from sticking again to the pore's walls.

During the Thesis an electrolyte with a 4.5 wt.% of HF and a 16.5 wt.% of ethanol was used.

4.1.4 Post processing techniques

Generally, it is not enough to perform an electrochemical attack. Depending on the application of the structure that has just been manufactured, it may require certain post-processing techniques to achieve the functionality sought. In the following, the three techniques that have been used during the thesis are shown.

4.1.4.1 Thermal oxidation/HF bath

Thermal oxidation combined with an HF bath has been the most used post-etching technique during the Thesis period. When silicon is exposed to high temperatures in an oxygen ambient, a 45% of the grown oxide is in-depth while the 55% is extended above the original surface (see Figure 4.7). If the oxidized piece of silicon is immersed in an HF bath, all the oxide will be removed, flattening the substrate. The total growth of the silicon oxide depends on the temperature and is extensively reported in literature [15].

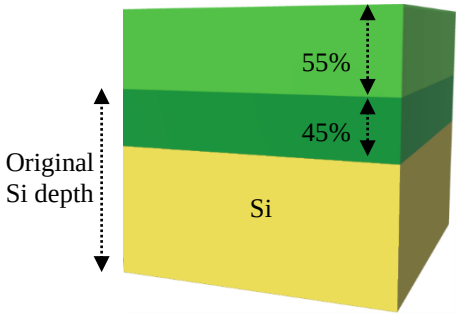

Figure 4.7. Sketch of silicon oxide growth on a piece of silicon.

This concept can be applied to our structures in order to obtain a pore widening –see Figure 4.8– thereby obtaining some interesting optical benefits.

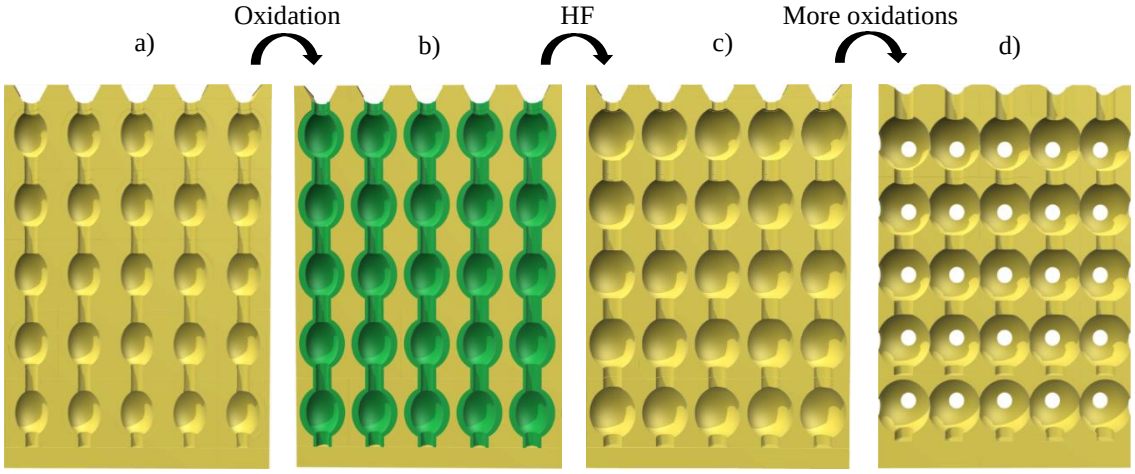

Figure 4.8. Pore widening through dry oxidation. a) Initial modulated pores. b) Oxidation of the pores at furnance. c) Silicon oxide is removed. d) Lateral connection (or lateral membranes) can be achieved after several repetitions or after a longer oxidation.

As a consequence of it, the effective refractive index of a unit cell –i.e. the imaginary cell that comprehends a whole period of the structure– is reduced since there is more air than before the thermal oxidation and HF bath. In this way, the optical response of the photonic crystals moves towards lower wavelengths. This can be done to precisely tune the optical response of those photonic crystals whose spectrum is slightly placed above the expected. Furthermore, the smoothing of the pore's walls, due to the removing of microporous structure [10], [16], reports also optical benefits. In essence, more defined bandgaps and better quality factors for the peak are obtained. However, oxidizing in excess may lead to structural collapse.

In addition, this post-processing technique can be understood as a way of providing in-depth interconnected channels that could be used, for instance, in micropumps [17] or lateral porous membranes applications [18], among others.

Thermal oxidations were done at 1050 ºC, during an average time of 5 minutes under dry oxygen conditions. They led to an optical excursion of the spectrum of about 150 nm and the entire process could be done several times.

4.1.4.2 Membrane fabrication

Sometimes it is useful to remove the bulk silicon in order to have both sides of the samples connected. It can be used for catalytic membranes [19] or simply for boosting the

transmission signal of the photonic crystal –rear implantation as well as some bulk silicon absorption mechanisms reduce the optical transmittance.

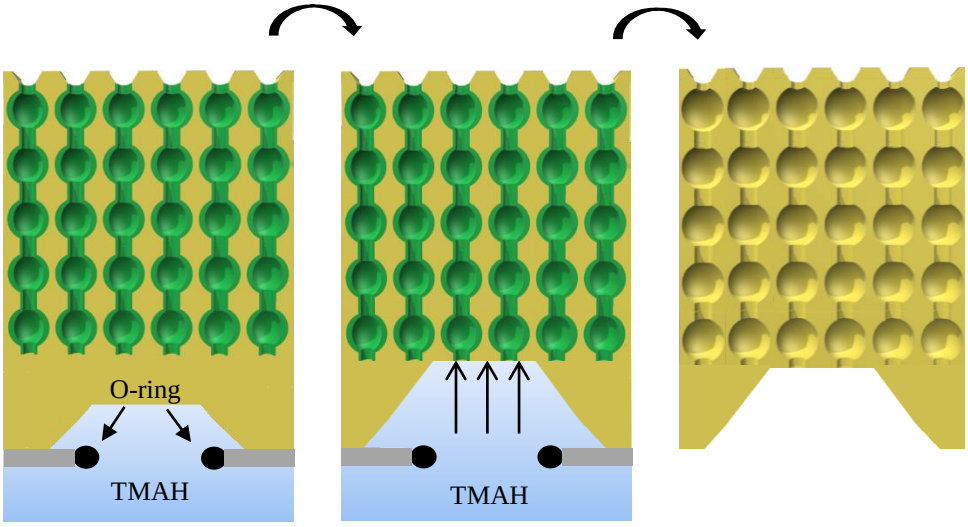

Figure 4.9. Schematization of the macroporous silicon vertical membranes through a TMAH rear attack.

This process is done through a wet etching of either KOH (potassium hydroxide) or TMAH. In order to prevent from pore cracking, the entire wafer has to be previously passivated through a thermal oxidation. This is because the silicon oxide etch ratio is much lower than the etch speed of silicon for both chemical agents. Thus, the oxidized layer protects the porous structure to be dissolved when the membrane is created. The thermal oxidation time at 1050 ºC is 1 or 7 minutes depending on whether TMAH or KOH is used in the wet etching, respectively. This is because KOH etches both silicon and silicon oxide several times faster than TMAH [20]. Despite the higher speed of KOH, the preferred method has been the TMAH wet etch since it has been demonstrated to be more controllable and a more reliable way to achieve the membranes.

The etching process is as follows: after the thermal oxidation, the silicon oxide of the rear side of the sample is removed. Then, it is placed in a specific fabricated cell that has an aperture that enables the TMAH attack at this specific region –see Figure 4.9–. The solution, 25 wt% TMAH, is heated at a constant temperature of 85 ºC. It takes about 6 hours to remove the 250 µm of bulk silicon necessary to create the membrane.

4.1.4.3 Atomic reorganization (annealing)

Atomic reorganization of porous structures has demonstrated to be an effective mechanism to create ultra-thin monocrystalline layers for both electronic and photovoltaic applications [21]. In this Thesis a new twist to the silicon multilayers created through the *Millefeuille process* is given. The idea consists on creating 1D photonic crystals from 3D macroporous structures. The goal is to achieve better optical figures as well as other mechanical performances, such as deep buried channels.

The *Millefeuille process* is based on Plateau-Rayleigh instability, which states that a straight pore will break and reorganize into a series of air droplets periodically distributed along the vertical axis [22], [23]. As Garin et al. propose in their work, the spacing between droplets can be controlled using modulated pores instead of straight pores. Moreover, if the unitary cell of the pores has enough volume/air ratio, the droplets or bubbles collapse laterally, giving raise to periodically distributed layers.

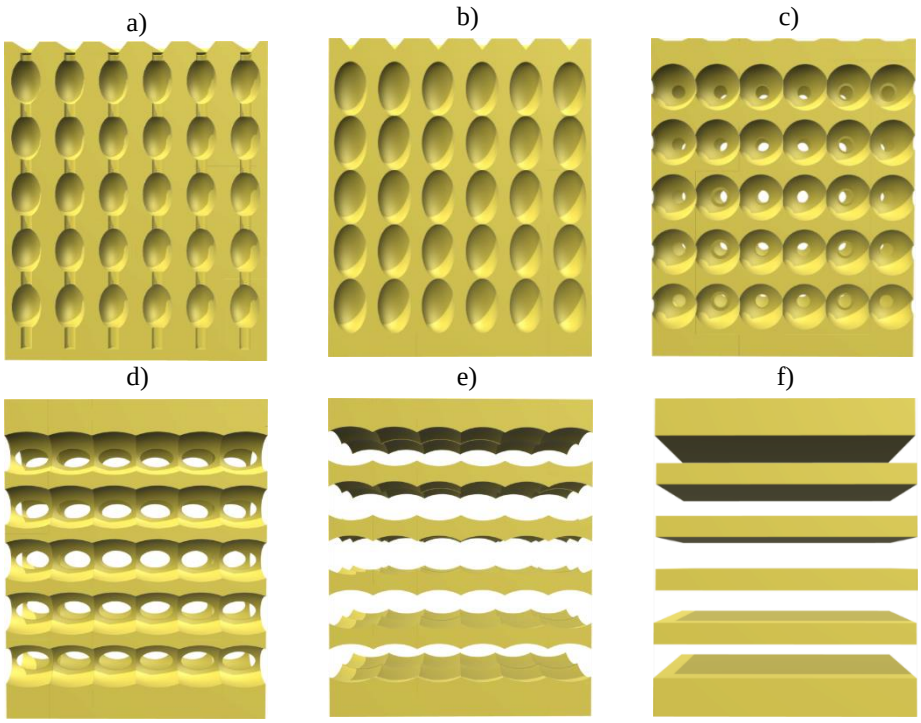

Figure 4.10. *Silicon Millefeuille* process. a) Initial modulated pores. When pores are exposed to high temperatures and at argon atmosphere, silicon atoms reorganize, tending to minimize the curvature of the profiles. b) Low diameter regions are 'absorbed' by those with higher diameter (within a range of aspect ratios). c) Each period of the modulation tends to an air sphere. If the pores are closer enough, they collapse laterally, forming air channel connections. d) Surface evolve to diminish the surface curvature. e) There is no more vertical connection. f) Flat layers of silicon are finally formed.

The creation of 1D all-silicon structures, or Distributed Bragg Reflectors (DBR), exhibit some very interesting characteristics which rely in the fact that these structures have a maximum refractive index contrast. On one hand, the bandgaps are the highest that can be achieved using silicon technology. On the other hand, for a transversal wave propagation, the quality factor of the peaks is improved in respect to the ones obtained in 3D photonic crystals with the same number of periods.

This is a promising post-processing technique that in the near future could give very interesting results that could be applied for filtering, narrow thermal emission, terahertz or biosensing applications, among others.

The annealing was done in an argon ambient at 1150 ºC during 90 minutes. Figure 4.10 depicts the images before and after the pore reorganization as well as their optical responses for different pore profiles (Appendix I).

4.2 FT-IR characterization

Reflectance, transmittance and emittance of the fabricated photonic crystals have been obtained by Fourier Transform Infrared (FT-IR) spectroscopy. This section describes the optical set-up and the calibration techniques used in such measurements.

The goal of FT-IR spectroscopy is obtaining the infrared absorption, transmission or reflection spectrum of a solid, a liquid or a gas. In other words, the goal is to see how much

a sample absorbs at each wavelength of the infrared region. The most straightforward option is to illuminate the sample into a set of different monochromatic lights that cover the spectral region and to measure the absorption at each one of them. However, this methodology, which is called dispersive spectroscopy, has some drawbacks that FT-IR spectroscopy overcomes. For instance, FT-IR spectrometers have better signal to noise ratio, better resolution and they process data over a wider range than dispersive spectrometers [24].

The basic components of an FT-IR spectrometer are a source, a Michelson interferometer, a sample compartment, a detector, an amplifier, an analog/digital convertor, and a computer. Its operation is as follows; the source radiates a broadband light that is processed in the interferometer, it is conducted to the sample and reaches the detector. Then, the received signal is amplified, converted to digital signal and finally transferred to a computer in which Fourier Transform is performed. The key point of the process relies in the Michelson interferometer [25].

4.2.1 Michelson Interferometer

The Michelson interferometer consists of a collimator, a beam splitter and two mirrors, one at a fixed position and the other that covers a range of distances. Figure 4.11 schematizes the operation mode of a typical interferometer; the broadband light emitted from E_1 and E_2 is divided in two beams. The first one travels in the fixed optical path, *p*, while the other travels through the moving path, *q*. When they reflect in the respective mirrors and come back to the beam splitter, they recombine and interfere at two different points, giving two different outputs, R_1 and R_2. According to the position of the tunable mirror, i.e. the path difference, these interferences are constructive, destructive or in a point in between, depending on the frequency. This process is repeated for many distances of the moving mirror in a short span. In this way, all the different wavelengths within the target range are modulated at different rates, i.e. the recombined beam comes out with a different interferogram at each different path length.

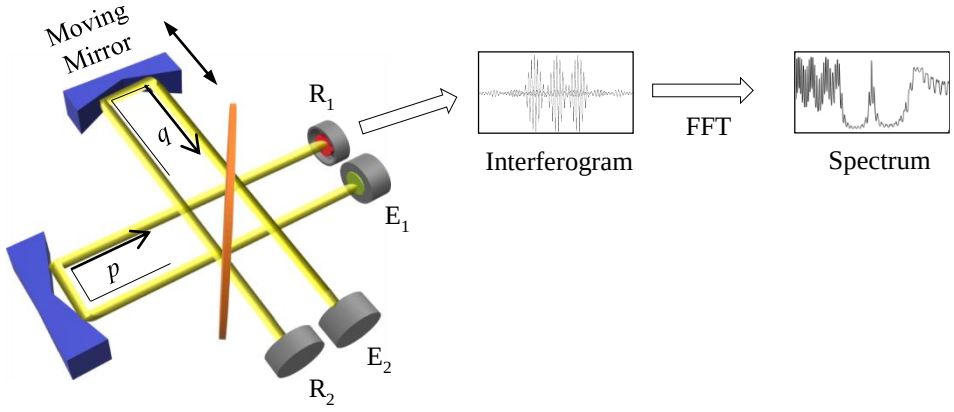

Figure 4.11. The scheme of Michelson interferometer and the operation mechanism for FT-IR measurement.

All the different interferograms that the receiver collects are stored and analyzed in a computer, which applies the Fourier transform. This operation converts one domain, the path length difference in cm, into its inverse domain, in wavenumbers, cm^{-1}. In other words, the Fourier transform converts the set of interferograms into an absorption spectrum.

In the current thesis a Bruker Vertex 70 FT-IR spectrometer was used in all optical measurements. However, there are some differences with the emittance measurements in respect to the reflectance and transmittance measurements.

4.2.1.1 Reflectance and Transmittance measurement

For reflectance and transmittance measurements, the sample to study was placed between the beam splitter and the detector, which is in one of the two outputs. We used a KBr splitter and a DLaTGS (Deuterated Lanthanum Alanine doped TriGlycine Sulphate) detector for measuring in the range of 2 µm to 27 µm. In both cases measurements were done at room temperature.

Transmittance was directly obtained by comparing the received light with and without the sample. In the case of reflectance, a specular setup was used. It consists on angular resolver tool that can measure samples from the quasi-parallel reflection, 13º, to the quasi-normal reflection, 83º. The background signal was obtained using a rectangular piece of gold at the same position of the sample. Gold reflectivity at those wavelengths is supposed to be almost 1. Therefore, the reflectance was obtained normalizing the reflection of the samples in respect to the signal obtained for gold.

4.2.1.2 Thermal emission

Figure 4.12 shows the typical set-up configuration for thermal emission using the A540 emission adapter (heater), which can be warmed up to a maximum of 400 ºC. A water-cooled metallic structure allows the user to be safe from burns.

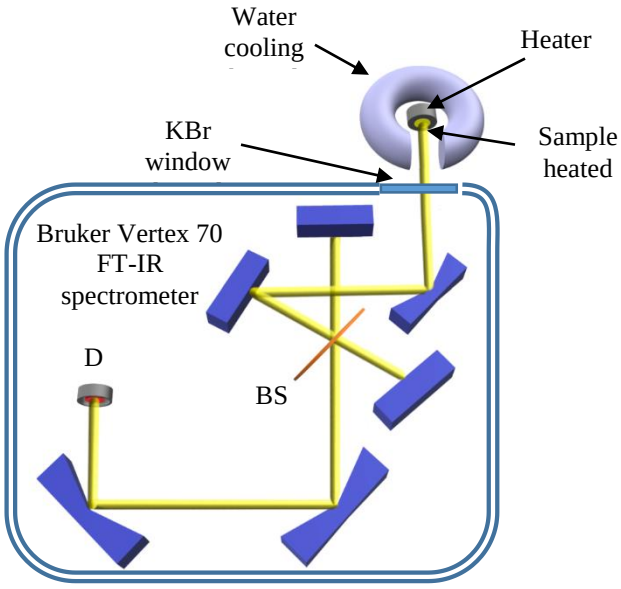

Figure 4.12. FT-IR thermal emission configuration.

As it can be observed, the sample acts now as an emitter. For this purpose, it is mechanically fixed to the heater using a piece of aluminum that has four screws in the corners. In addition, the piece has an aperture of 1 cm^2 in the center that determines the active emitting area of the sample. Radiation is directed through a system of mirrors to the beam splitter after passing through a KBr window, which is transparent at the MIR. Then, the same operation mode as explained in the *Michelson Interferometer* section is applied to obtain the emission spectrum of the sample. It may happen that this directly obtained

spectrum is not suitable for gas sensing measurements because of atmospheric absorption, mainly CO_2 and water vapor. Furthermore, the obtained spectrum accuses the non-linear effects that both detector and beam splitter exhibit in respect to the frequency of the incoming light. In order to compensate these non-desirable effects, a normalization (or calibration) of the measurement is required. This calibration is done by measuring the emission response of a black body placed at the same point and the same temperature as the sample. The black body consist of a burned piece of bulk silicon with the same area and thickness than the sample.

For the final normalization, which is the emittance, both spectra are divided frequency per frequency.

References

[1] A. Uhlir, “Electrolytic Shaping of Germanium and Silicon,” *Bell Syst. Tech. J.*, vol. 35, no. 2, pp. 333–347, Mar. 1956.

[2] D. R. Turner, “Electropolishing Silicon in Hydrofluoric Acid Solutions,” *J. Electrochem. Soc.*, vol. 105, no. 7, p. 402, Jul. 1958.

[3] V. Lehmann, *The electrochemistry of silicon : instrumentation, science, materials and applications*. Wiley-VCH, 2002.

[4] E. Xifré Pérez, *Design, fabrication and characterization of porous silicon multilayer optical devices*. Universitat Rovira i Virgili, 2007.

[5] H. Föll, M. Christophersen, J. Carstensen, and G. Hasse, “Formation and application of porous silicon,” *Mater. Sci. Eng. R Reports*, vol. 39, no. 4, pp. 93–141, Nov. 2002.

[6] A. Langner, “Fabrication and characterization of macroporous silicon,” *Doktorarbeit, Martin-Luther-Universität*, 2008.

[7] V. Lehmann, “Formation Mechanism and Properties of Electrochemically Etched Trenches in n-Type Silicon,” *J. Electrochem. Soc.*, vol. 137, no. 2, p. 653, Feb. 1990.

[8] V. Lehmann, “The Physics of Macropore Formation in Low Doped n-Type Silicon,” *J. Electrochem. Soc.*, vol. 140, no. 10, p. 2836, Oct. 1993.

[9] V. Lehmann and U. Grüning, “The limits of macropore array fabrication,” *Thin Solid Films*, vol. 297, no. 1–2, pp. 13–17, Apr. 1997.

[10] V. Lehmann and S. Ronnebeck, “The Physics of Macropore Formation in Low-Doped p-Type Silicon,” *J. Electrochem. Soc.*, vol. 146, no. 8, p. 2968, Aug. 1999.

[11] T. Todorov Trifonov, “Photonic Bandgap Analysis and Fabrication of Macroporous Silicon by Electrochemical Etching.” Universitat Rovira i Virgili, 13-May-2010.

[12] G. Barillaro, a. Nannini, and M. Piotto, “Electrochemical etching in HF solution for silicon micromachining,” *Sensors Actuators, A Phys.*, vol. 102, no. 1–2, pp. 195–201, Dec. 2002.

[13] G. Sotgiu, L. Schirone, and F. Rallo, “On the use of surfactants in the electrochemical preparation of porous silicon,” *Thin Solid Films*, vol. 297, no. 1–2, pp. 18–21, Apr. 1997.

[14] K. J. Chao, S. C. Kao, C. M. Yang, M. S. Hseu, and T. G. Tsai, “Formation of High Aspect Ratio Macropore Array on p-Type Silicon,” *Electrochem. Solid-State Lett.*, vol. 3, no. 10, p. 489, Oct. 1999.

[15] H. Z. Massoud, “Thermal Oxidation of Silicon in Dry Oxygen Growth-Rate Enhancement in the Thin Regime,” *J. Electrochem. Soc.*, vol. 132, no. 11, p. 2685, 1985.

[16] T. Trifonov, “Photonic bandgap analysis and fabrication of macroporous silicon by electrochemical etching,” Universitat Rovira i Virgili, 2010.

[17] S. Yao, A. M. Myers, J. D. Posner, K. A. Rose, and J. G. Santiago, “Electroosmotic Pumps Fabricated From Porous Silicon Membranes,” *J.*

Microelectromechanical Syst., vol. 15, no. 3, pp. 717–728, Jun. 2006.

[18] T. Leïchlé and D. Bourrier, “Integration of lateral porous silicon membranes into planar microfluidics.,” *Lab Chip*, vol. 15, no. 3, pp. 833–8, Feb. 2015.

[19] D. Vega Bru *et al.*, “Catalytic membrane reactors based on macroporous silicon for hydrogen production,” in *VI Encuentro Franco-Español de Química y Física del Estado Sólido*, 2010, pp. 104–105.

[20] K. Biswas and S. Kal, “Etch characteristics of KOH, TMAH and dual doped TMAH for bulk micromachining of silicon,” *Microelectronics J.*, vol. 37, no. 6, pp. 519–525, Jun. 2006.

[21] M. Garín, C. Jin, D. Cardador, T. Trifonov, and R. Alcubilla, “Controlling Plateau-Rayleigh instabilities during the reorganization of silicon macropores in the Silicon Millefeuille process,” *Sci. Rep.*, vol. 7, no. 1, p. 7233, Dec. 2017.

[22] J. Plateau, *EXPERIMENTAL AND THEORETICAL STATICS OF LIQUIDS SUBJECT TO MOLECULAR FORCES ONLY*. Gauthier-Villars, 1873.

[23] Lord Rayleigh, “On the instability of cylindrical fluid surfaces,” *London, Edinburgh, Dublin Philos. Mag. J. Sci.*, vol. 34, no. 207, pp. 177–180, Aug. 1892.

[24] P. R. Griffiths and J. A. De Haseth, *Fourier transform infrared spectrometry*. Wiley-Interscience, 2007.

[25] A. A. Michelson and E. W. Morley, “On the relative motion of the Earth and the luminiferous ether,” *Am. J. Sci.*, vol. s3-34, no. 203, pp. 333–345, Nov. 1887.

Publications

5.1

2015 Spanish Conference on Electron Devices (CDE), pp. 1-3, (2015)

https://doi.org/10.1109/CDE.2015.7087479

Date of conference: 11-13 February 2015

Impact of the Absorption in Transmittance and Reflectance on Macroporous Silicon Photonic Crystals

D. Cardador*, D. Vega, and A. Rodríguez

Micro i Nanotecnologies, Departament d'Enginyeria Electrònica, Universitat Politècnica de Catalunya, C/Jordi Girona, 31, 08031, Barcelona, Spain

Abstract: The characteristics of reflection and transmission peaks in the spectra of photonic crystals have been studied theoretically and the results compared to measurements performed in fabricated samples. The aim of this work is to investigate the relation between material losses and the effective Q factors that can be obtained in photonic crystals made with it. Photonic crystals have been designed with defects of periodicity to introduce states in the band gap that give place to reflectance and transmittance peaks at adjustable specific wavelengths. The fabricated structures are described together with their reflection and transmission spectra. The influence of losses in the material in these spectra is evaluated.

5.1.1 Introduction

Photonic crystals (PhC) are attracting a growing interest for a wide variety of applications, especially for communications, signal processing and sensing [1], [2]. For many of these applications it is often necessary the existence of one or several resonance peaks of high Q factor, or very abrupt transition band filters.

Photonic crystals show great potential for these applications thanks to the ability to create forbidden bands for light propagation through the crystal. Furthermore, geometry can be adapted and tuned to place these gaps in precise frequency margins. The design includes the possibility of introducing defects such as to create resonating states embedded in the bandgaps, which can be similarly tuned to the desired wavelengths. The overall quality of these devices depends on an accurate geometrical definition of the crystal, and an adequate choice of materials.

Macroporous silicon is a material produced from silicon crystal wafers that allow the parallel fabrication of many identically shaped objects with nanometric precision. The technique used to create the pores in the bulk material is the electrochemical etching method, which is done with hydrofluoric acid. This method allows the production of macroporous silicon scalable to large areas. This characteristic makes the electrochemical etching an economically attractive method. The resulting macroporous silicon presents high integrability, high mechanical and optical stability and it is compatible with VLSI fabrication technology.

The porous structures obtained are of interest for photonic applications in different fields, i.e optoelectronics, microphotonics, sensorics, etc. A particular case of macroporous structure are PhC for their use in sensors or light signal processors [3], [4]. Absorption has a key role in the achievable performance of these devices. The influence of losses in the material of photonic crystals is an issue that is attracting the attention of the research groups involved in this subject [5]. Nevertheless, this subject requires more investigation in order to improve the functionality of the devices based on macroporous silicon PhC.

In this paper we analyze the effect that absorption losses in the material have in the resonant peaks and dips in the transmitted and reflected signal and their respective Q factors. The goal is to deduce guidelines for determining the maximum value of losses that can be allowed for a macroporous silicon structure in a specific device.

There are several mechanisms that affect the optical losses of photonic crystal devices. In one hand intrinsic losses are due to the material absorption. This material absorption generally is a complex function with strong frequency dependence. Nevertheless, there are spectral regions where it can be approximated by a constant imaginary value for the refraction index of the material. Such approximation is obviously only valid in a restricted frequency range, but allows to make some assessments of the material influence in the photonic response.

For macroporous silicon the main material absorption factor is due to free carriers in the doped silicon wafer. Nevertheless, as the doping levels used for macroporous silicon are relatively low, it can be predicted that its influence should be relatively small. Furthermore, intrinsic silicon is mostly transparent for Infrared light— broadly, in the 1 micron to 20 microns range—, but some absorption peaks are present.

On the other hand, an important factor for optical losses is light scattering. There exist several causes for scattering losses, particularly related with structural imperfections. Nevertheless, it is possible to model the total loss as a simple single absorption value.

5.1.2 Fabrication of macroporous silicon

Macroporous silicon photonic crystal samples have been fabricated by electrochemical etching techniques [6]. The fabrication details have been published elsewhere [7], [8]. This method allows us to create ordered arrays of pores with very high aspect ratios and with a precise control over the pores' diameter in depth -see Figure 5.1.1-.

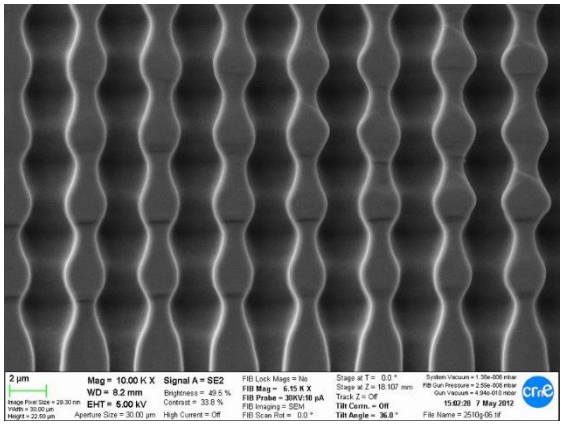

Figure 5.1.1. Profiles made by MNT group for gas sensors applications.

The process starts with the lithographic definition of the placement of the pores. It consists in opening in a silicon oxide etch windows through which shallow dips in the silicon wafer surface are etched. These dips constitute the seeding points from which pores will grow. In this work have been used square configurations of inverted pyramids with pitches of 4 µm, 2 µm and 0.7 µm. The electrochemical dissolution of silicon in HF requires holes which are minority carriers in n- type silicon. Controlling the hole current, it is possible to modulate the pore growth, i.e. pore diameter. This current is photogenerated by backside illumination of the sample with an IR source. Hole current concentrates preferentially on the pore tips (and pyramid tips) giving place to the growth in depth of the pores. In this way, the diameter of pores and their depth are related to the instantaneous current flowing through the wafer and the current is in turn controlled by the intensity of the back-side illumination. Using this mechanism, we could fabricate samples with pores whose diameter alternate in-depth between narrow and wide diameter regions.

Taking advantage of the capability to modulate the pores, periodic 3-d structures can be made by applying a sinusoidal pore depth profile, depicted in Figure 2. Furthermore, it is possible to introduce defects in this regular profile, like for instance, maintaining a constant diameter for a period, as can be seen in Figure 5.1.2b.

5.1.3 Numerical study

Reflection and transmission spectra of the considered Photonic Crystals have been simulated by the FDTD technique using Optiwave's OptiFDTD software package. Thanks to its graphical interface, a close approximation of the profile of one pore, of the samples fabricated in laboratory. has been simulated -see Figure 5.1.2a-. Adequate boundary conditions were introduced to approximate the periodicity of the fabricated macroporous silicon PhC structure.

For simulations, input signals consisting in Gaussian pulses of light are used as excitation. Two detectors to sense the reflected and propagated part of the pulse are also

defined. The propagation of the light pulses in the crystals was simulated in stationary regime and reflection and transmission spectra were obtained.

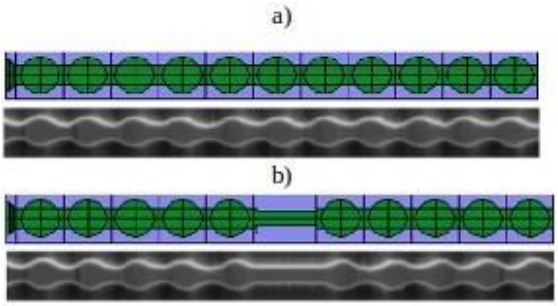

Figure 5.1.2. Comparison between the simulation (up) and the experimental (down) profiles without and with defects -**a)** and **b)** respectively-.

Using the plane wave expansion (PWE) Band Solver tool provided by OptiFDTD, its bandgap is calculated. Next, a defect in our PhC, consistent on disabling one of the periodicities of the porous, is introduced -Figure 5.1.2b-. This defect creates a reflection peak - and transmission dip- which is the object of our study.

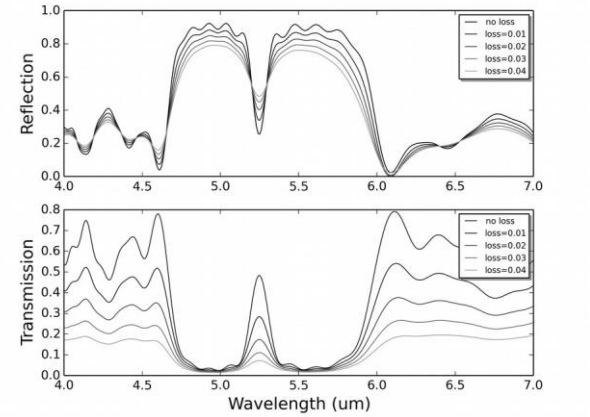

Figure 5.1.3. Reflection dip in the transmission band (up) and transmitted peak in reflection band (down) for k= 0, 0.1, 0.2, 0.3 and 0.4.

Results obtained in the initial simulation -without absorption in the process- match with the experimental results in [8], [9] where we fabricated an optical filter based on 4 μm pitch macroporous silicon PhC for gas detection.

Systematic analysis consisting in simulations varying absorption coefficients was carried out and the values of the peak and the dip were recorded and plotted to show the way they diminished their amplitude as the extinction factor was increased-see Figure 5.1.3-.

The effect of absorption in the peak and the dip amplitude and in the Q-factor is shown in Figure 5.1.4.

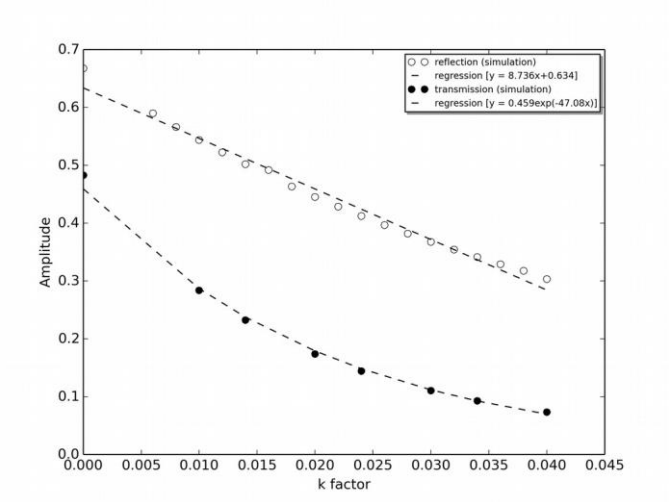

Figure 5.1.4. Relation between amplitude and the extinction factor in transmitted and reflected signals.

5.1.4 Results

From the numerical study it can be seen that a decrease of the whole spectrum is produced in both, reflection and transmission as the absorption increases. It can be also appreciated that transmission suffers a higher reduction with respect to the case without losses –see for instance the difference between 'no loss' values and 'loss=0.04' values in Figure 3-. This fact can be explained because the light travels a longer path before it arrives to the transmission receptor than to the reflection one. This long path is also the reason why the amplitude of the transmission peak decreases following an exponential function of the extinction coefficient. Otherwise, in the reflection receptor we observe that the relationship between the k-factor and the amplitude of the dip is practically linear -see Figure 5.1.4-.

Concerning the Q-factor, in both, reflection and transmission, it exists a fairly linear relationship between Q value and the extinction coefficient. In the simulations performed in this work, reflected signals present higher Q- factors. It is also noticeable that, peaks and dips have almost the same width in spite of the decreasing height.

5.1.5 Conclusions

The effect of material loses in the equivalent Q factor of reflection and transmission peaks, or dips, of the spectral response of photonic crystals has been investigated. Macroporous silicon photonic crystals have been fabricated and characterized. Measured spectral responses have been used to extract the effective losses in the photonic crystals. The position of the spectral peaks as well as the extension of the forbidden band is well predicted by simulations. The height and Q factors obtained in simulations can be fairly predicted assuming a given value of material absorption. These results are useful to design photonic crystals in order to maximize the selectivity in wavelength of the devices fabricated with them.

5.1.6 References

[1] H. Föll, M. Christophersen, J. Carstensen, and G. Hasse, “Formation and application of porous silicon,” *Mater. Sci. Eng. R Reports*, vol. 39, no. 4, pp. 93–141, Nov. 2002.

[1] H. Föll, M. Christophersen, J. Carstensen, and G. Hasse, “Formation and application of porous silicon,” *Mater. Sci. Eng. R Reports*, vol. 39, no. 4, pp. 93–141, Nov. 2002.

[2] R. B. Wehrspohn *et al.*, “Macroporous silicon and its application in sensing,” *Comptes Rendus Chim.*, vol. 16, no. 1, pp. 51–58, Jan. 2013.

[3] C. Pacholski and Claudia, “Photonic Crystal Sensors Based on Porous Silicon,” *Sensors*, vol. 13, no. 4, pp. 4694–4713, Apr. 2013.

[4] J. Van Campenhout, P. Bienstman, and R. Baets, “Membrane-type photonic-crystal microlasers for the integration of electronic and photonic ICs,” in *Procreedings Symposium IEEE/LEOS*, 2004, pp. 279–282.

[5] G. V. Li *et al.*, “Tunable Microcavity Based on Macroporous Silicon:Feasibility of Fabrication,” *J. Light. Technol.*, vol. 31, no. 16, pp. 2694–2700, Aug. 2013.

[6] V. Lehmann, *The electrochemistry of silicon : instrumentation, science, materials and applications*. Wiley-VCH, 2002.

[7] T. Trifonov, M. Garín, A. Rodríguez, L. F. Marsal, and R. Alcubilla, “Tuning the shape of macroporous silicon,” *Phys. status solidi*, vol. 204, no. 10, pp. 3237–3242, Oct. 2007.

[8] T. Trifonov, L. F. Marsal, A. Rodríguez, J. Pallarès, and R. Alcubilla, “Fabrication of two- and three-dimensional photonic crystals by electrochemical etching of silicon,” *Phys. status solidi*, vol. 2, no. 8, pp. 3104–3107, May 2005.

[9] D. Hernández García, “Selective thermal emitters based on photonic crystals.” Universitat Politècnica de Catalunya.

5.2

Infrared Physics & Technology 80, 6–10 (2017)

http://dx.doi.org/10.1016/j.infrared.2016.11.004

Received: 13 September 2016; **Revised:** 10 November 2016; **Accepted:** 12 November 2016; **Available online:** 14 November 2016

Study of resonant modes in a 700 nm pitch macroporous silicon photonic crystal

D. Cardador*, D. Vega, D.Segura and A. Rodríguez

Micro i Nanotecnologies, Departament d'Enginyeria Electrònica, Universitat Politècnica de Catalunya, C/Jordi Girona, 31, 08031, Barcelona, Spain

Abstract: In this study the modes produced by a defect inserted in a macroporous silicon (MPS) photonic crystal (PC) have been studied theoretical and experimentally. In particular, the transmitted and reflected spectra have been analyzed for variations in the defect's length and width. The performed simulations show that the resonant frequency is more easily adjusted for the fabricated samples by length tuning rather than width. The optimum resonance peak results when centered in the PC bandgap. The changes in the defect geometry result in small variations of the optical response of the PC. The resonance frequency is most sensitive to length variations, while the mode linewidth shows greater change with the defect width variation. Several MPS photonic crystals were fabricated by the electrochemical etching (EE) process with optical response in the range of 5.8 μm to 6.5 μm. Results of the characterization are in good agreement with simulations. Further samples were fabricated consisting of ordered modulated pores with a pitch of 700 nm. This allowed to reduce the vertical periodicity and therefore to have the optical response in the range of 4.4 μm to 4.8 μm. To our knowledge, modes working in this range of wavelengths have not been previously reported in 3-d MPS structures. Experimental results match with simulations, showing a linear relationship between the defect's length and working frequency inside the bandgap. We demonstrate the possibility of tailoring the resonance peak in both ranges of wavelengths, where the principal absorption lines of different gases in the mid infrared are placed. This makes these structures very promising for their application to compact gas sensors.

5.2.1 Introduction

Optical properties of photonic crystals (PCs) are very interesting for a wide range of application areas, such as optical communications or sensing [1]. The particular optical spectrum of a PC is obtained by the periodical ordering of different refractive index materials. The main characteristic of PCs is the occurrence of photonic bandgaps (PBG) at which wavelengths light cannot propagate through the PC. The introduction of defects, that break the periodicity in the structure, confers new optical features to the PC [2]. One example is the embedding of line defects that work as waveguides [3]. Likewise, planar or point defect cavities can be included in a PC. These kind of cavities create resonant states—modes—within the photonic bandgap at specific frequencies [4], [5], that are used for the development of optical resonators [6], thermal emitters[7] or tunable filters [8].

As reported in the literature, the crystal's structure, and, in particular, the shape of the defect, influence the optical response of the PC [4]. An important number of papers have dealt with this issue in 1-d and 2-d PCs [9]–[12]. However, the influence of the defect's morphology on the optical response of 3-d photonic crystals has not been so thoroughly analyzed. This may be due to the high dependence of the optical spectrum on the method used to fabricate the PC [13], [14]. A number of different techniques have been proposed to incorporate defect structures within the PCs in woodpile structures [15], synthetic opals [16], [17] or macroporous silicon [18], among others.

In this paper we focus on macroporous silicon (MPS), which is a versatile material that can be successfully fabricated by the *electrochemical etching* (EE) of silicon. With this technique it is possible to etch pores with different radius profiles and incorporate planar defects inside the crystal structure, see Figure 5.2.1. Previous studies reported MPS structures with a cavity in the middle of the PC that had a resonant mode around $\lambda = 7\,\mu$m [18]. The reported PC had a pitch of $2\,\mu$m and a vertical periodicity of about $2.5\,\mu$m. In general, the EE of silicon limits the depth minimum modulation period to be about the lattice pitch for a stable pore growth [19]. The work herein considers PCs with an embedded cavity in the middle. Samples have been fabricated of MPS with a pitch of 700 nm. Vertical periodicities of the samples were close to the lattice parameter, giving a PBG centered at $\lambda \approx 4.5\,\mu$m and with a band-width approximately of 22 %. The included defect was designed for an initial resonance in the range $\lambda = 4.4\,\mu$m to $4.8\,\mu$m.

We firstly report the influence that small variations in the defect's length and width have on the resonating modes inside the bandgap. It is shown that there exists an optimal defect shape that ensures the best quality factor as well as that lengthening the defect is a better choice than widening it, to control the frequency of the resonant modes. Experimental data exhibit a linear relationship between the defect's length and the peak's position inside the bandgap. These results are in good agreement with the results of the theoretical study.

5.2.2 Experimental and simulations

Preparation of macroporous silicon PC with defect

Samples of 3-d MPS PC were fabricated using the EE technique, as first described by Lehmann and Föll [20]. An n-type ⟨1 0 0⟩ silicon wafer with suitable resistivity was used to etch pores in a square arrangement with a 700 nm separation. Nano Imprint Lithography (NIL) was used to define the nucleation centers. The 3-d structures were obtained by modulating the currents during EE, thus changing the diameter along the pore depth. This

allows to design the profile beforehand and to create smooth, complex 3D structures. An example of the fabricated samples is shown in Figure 5.2.1. The depth periodicity was set to be near 1.1 μm, resulting in a PBG in the range $\lambda = 5\,\mu$m to 7 μm. As seen in Figure 5.2.1, a planar defect was introduced halfway the PC by suppressing one of the modulations and leaving a constant diameter section. The length of the cavity was varied from $l_{\mathrm{def}} = 2.1\,\mu$m to 2.6 μm while the width was set to $w_{\mathrm{def}} = 0.23\,\mu$m for all the samples. To work at shorter wavelengths, the vertical modulation period of the pore was reduced. In particular, it was set to the lattice constant value (~ 700 nm). This results in a PBG in the range of $\lambda = 4\,\mu$m to 5 μm. The defect's length was adjusted to the range $l_{\mathrm{def}} = 1.5\,\mu$m to 1.8 μm. The total depth of the PC was about 15 μm. A complete description of the process can be found elsewhere [21].

The optical response of the fabricated samples was measured in the MIR range using a Bruker Optic's Vertex 70 FT-IR spectrometer. Measurements were taken with light incidence aligned to the $\Gamma - \mathrm{M}$ direction (along one lattice axis in the surface), an aperture of 1 mm, and a resolution of 4 cm^{-1} was used. Normalized measurements were done for both reflectance and transmittance. Additionally, all measurements are specular.

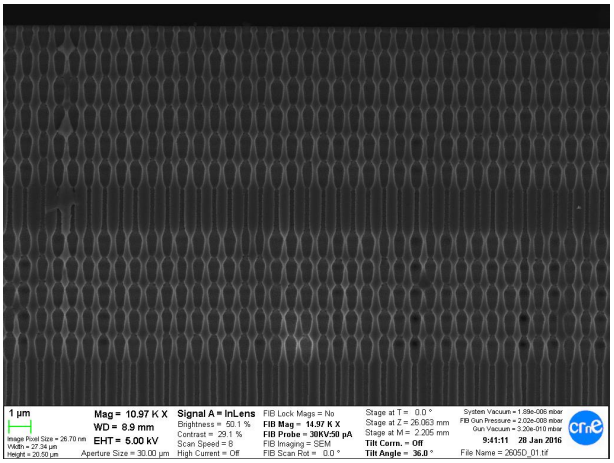

Figure 5.2.1. Cross section view of a 3-d PC fabricated by EE of silicon with a 0.7 µm pitch. A plane defect in the PC lattice is included in the middle of the structure.

Simulations

To study the effects that morphological changes in the defect produce in a finite PC structure, the Optiwave's OptiFDTD software suite was used. This software uses the finite-difference time-domain method (FDTD) to simulate EM wave propagation through a PC, schematized in Fig. 2(a). A single pore was designed using its graphical interface. Each period was inserted in a normalized cell size of 1 µm ×1 µm ×1 µm box –see Figure 5.2.2a. The pore axis was aligned to the Z axis. Periodic boundary conditions were set on the side walls—*XZ* and *YZ*—while perfect absorbing layers were used for the top and bottom of the simulation cell.

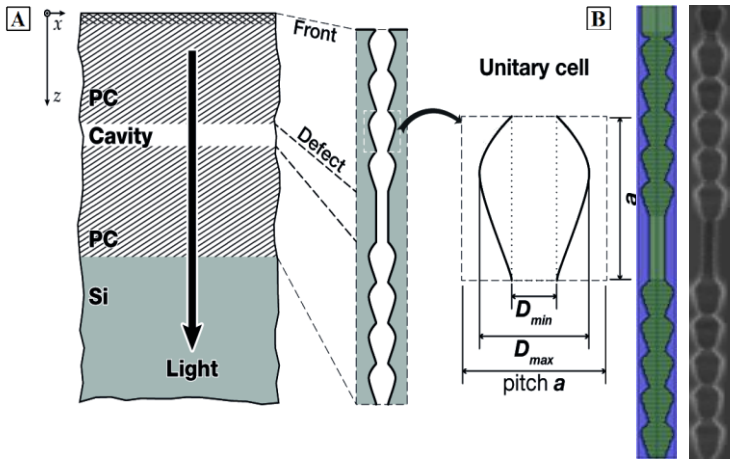

Figure 5.2.2. (A) Schematic representation of the structure and its mode of operation. The unitary cell is one period of the PC in the three space directions. The unitary cell detail gives the principal design parameters. (B) comparison of simulated profile (left), which is a staircase approximation of the experimental profile (right).

The illumination was done with a plane wave arriving from the top and impinging on the front face of the PC. The light wave was a Gaussian pulse with a linewidth of $\Delta = 4\,\mu$m and a central wavelength $\lambda_{\mathrm{src}} = 5.5\,\mu$m. The reflection and transmission spectra were obtained by placing a plane detector $1\,\mu$m and $5\,\mu$m before and after the pore, respectively. Both spectra were calculated by integrating the power flux through the detector plane and normalized to the incident wave.

The refractive index of the bulk material was set to $n \approx 3.43$, which corresponds to the average value of silicon in the mid- infrared range at room temperature [22]. Previous works reported that the absorption in low doped silicon has almost no effect on the propagation of light along the PC [23]. Consequently, in this study no losses were considered in the bulk material. The cavities inside the bulk material were filled with air. The considered PC structure used in the simulations is an approximate geometrical description of the profile depicted in Figure 5.2.1. In concrete, the staircase approximation (see Figure 5.2.2b) has been used in order to reduce the morphological differences between both profiles and diminish, as a consequence, the divergence in the optical response between experimental and simulated structures. Several simulations were performed changing the dimensions of the defect site, both length and diameter, to determine the evolution of the cavity mode and the correlation with the measured samples.

5.2.3 Results and discussions

The main results of the theoretical study are summarized in Figure 5.2.3; Figure 5.2.3a shows the spectra variation of the PC when the length of the defect takes values from 1.6 µm up to 2.4 µm. In Figure 5.2.3a, the different spectra correspond to a width variation in the range of $0.07\,\mu$m to $0.35\,\mu$m for the mentioned defect. The optimum solution—highest Q-factor—is emphasized with a thicker line, and lies in the middle of the bandgap, in agreement with previous studies made in 1-d and 2-d [24]. Comparing Figure 5.2.3a to 3 Figure 5.2.3b, two differences stand out. The first one is that the central frequency of the resonant mode f_{res} is much more sensitive to changes in the length of the defect than to the width of the defect. A length variation of ± 30 % allows the peak to move anywhere in the PBG. However, in the case of modifying the width, a ± 67 % variation results in a much smaller shift of the peak.

The second difference is higher sensitivity of the resonance Q-factor to changes of the defect's width—widening and thus reducing the Q-factor, — while remaining practically constant with the variation of the length of the cavity. However, the EE fabrication limits for the pore geometry impose restrictions on the realizable PC structures. In particular, too small diameter may lead to pores dying, and too large diameter can result in uncontrolled growth or electropolishing [25]. Considering this, the range of the simulated parameters has been adjusted accordingly. On the other hand, the length of the defect has looser constraints, and can be extended many periods. As observed in Figure 5.2.3b, it is enough, with the simulated interval, to place the peak at any position inside the bandgap. Nonetheless, further studies should explore the convenience of lengthening the defect. Several reports have demonstrated in 1-d and 2-d that longer defects may allow to excite two or more frequencies that, in turn, will enable the appearance of two or more peaks [26,27].

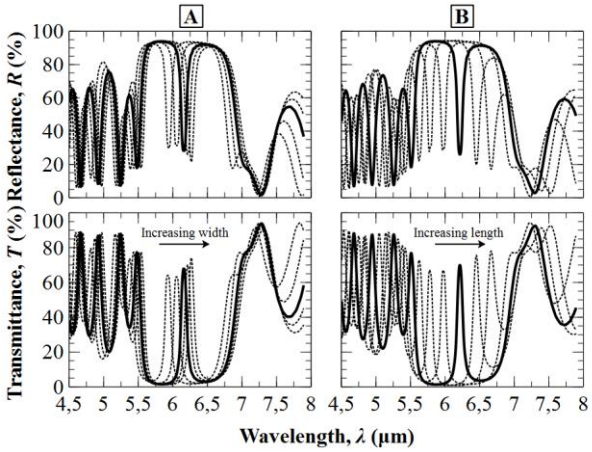

Figure 5.2.3. Reflectance (upper images) and transmittance (lower images) spectra obtained by varying the width (A) and the length (B) of the defect. The length took values from 1.6 μm to 2.4 μm and the with from 0.07 μm to 0.35 μm. In the image it is shown the evolution of the peaks when increasing the size and the length of the cavity. The solid line represents the central —and optimal— frequency, that corresponds to the mean value of the length and the width: 2 μm long and 0.21 μm high.

Taking into account all these considerations, we can conclude that the best way of controlling the position of the peak is to modify the length of the defect, instead of its width. According to this, some MPS PCs were fabricated with different defect lengths to place the resonant mode in the range of $\lambda = 5.8\,\mu$m to $6.5\,\mu$m. In Figure 5.2.4a is shown the reflectance and transmittance spectra for 3 different samples. It can be observed that the peak's amplitude in the reflectance spectrum matches fairly well with that predicted by simulations. In particular, the simulation data for reflection show that amplitude at the resonance frequency is $R_0^{\text{sim}} \approx 70\%$, while the measured data has $R_0^{\text{meas}} \approx 40\%$. This difference in R_0 and, as a consequence, in the Q-factor, can be attributed to the irregularities in the experimental profile with respect to the simulated one [28–30].

On the other hand, the measured transmitted spectra of the MPS samples are significantly weaker than expected from the simulated results. This is because the PCs fabricated have a total thickness—$250\,\mu$m approximately—of the wafer used as a substrate for the EE: i.e. the PC sits on top of the silicon bulk. Furthermore, the backside of the samples is not polished, so light scattering further reduces the light intensity. A solution that is explored elsewhere [31] is to use MPS membranes, such that the total thickness is substantially reduced.

To achieve shorter wavelengths, several PCs with shorter modulation period were fabricated. As depicted in Figure 5.2.4b, the resonance position could also be tuned,

although the features of the cavity modes were a little worse than that obtained in the larger design. The cause is attributed to the increased irregularity of the etched pores. This stems from the added difficulty to control the pore growth when the period approaches the pitch of 700 nm. Even so, these results show the feasibility of working at the range of $\lambda = 4.4\,\mu$m to $4.8\,\mu$m with such MPS PCs.

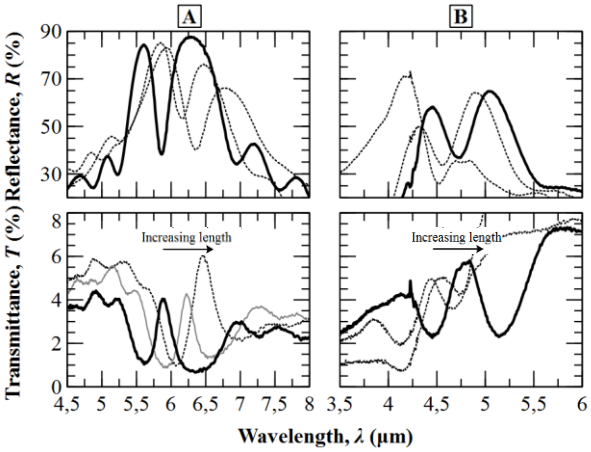

Figure 5.2.4. Experimental spectra of reflection (upper) and transmission (lower) for three different defect length for both cases: (A) 2.06 μm (solid line), 2.34 μm and 2.62 μm (dotted lines). (B) 1.54 μm, 1.60 μm (dotted lines) and 1.76 μm (solid line).

In Figure 5.2.5 the relationship between the defect length and the position of the resonant frequencies is plotted for the long and short period PCs. The center wavelength of the cavity λ_0 is compared for the fabricated and numerically studied PCs. It can be seen that there is some offset for the fabricated samples with respect to the simulated case. It is suggested that this offset arises because of the difference between the simulation model and the etched pores –see Figure 5.2.2b. As reported in previous studies, subtle variations in the porosity—volume fraction of silicon over the total unitary cell volume, *p = VSi/Vtot*—will affect the local effective refractive index, what will generate some modifications in the optical response of the photonic crystal [23]. In concrete, if those differences are given in the defect—i.e. a little eccentricity or roughness in the cavity respect to the perfect cylinder used in simulations—, there will be a shift in the peak position in reference to the ideal case. As seen in Figure 5.2.2b, the shape of the simulated and experimental pores fit fairly well. However, there are some visible differences between them in both, cavity and modulated zones, such as little variations in the radius and the unitary cell period. These differences may lead to a displacement of the whole bandgap and also a shift in the peak position what, in tum, would produce the offset between the expected and the experimental results. Looking at the slopes in Figure 5.2.5, it can be seen that for the larger period samples, there seems to be a good match between theoretical and actual values. However, for the shorter period PCs, the slope for the samples appears to be different from the theoretical one. This may be also attributed to the greater difference of shape in these samples with respect to the desired profile. Further studies are necessary to search how to accurately predict this offset at λ_0. Nevertheless, as λ_0 can be precisely shifted experimentally, this can be used to tune the PC to work at a desired frequency; for instance, at the absorption line of a target gas. Therefore, such MPS devices may be proposed for use as spectroscopic gas sensors.

Tuning the resonances in the mid-infrared range for the long vertical period PCs, allows targeting the absorption spectrum substances such as ammonia, formaldehyde (CH_2O) or the contaminant agent nitrogen dioxide (NO_2). On the other hand, for the short

period PCs, it is possible to detect gases involved in industrial processes—such as carbon monoxide, carbon dioxide or nitrous oxide.

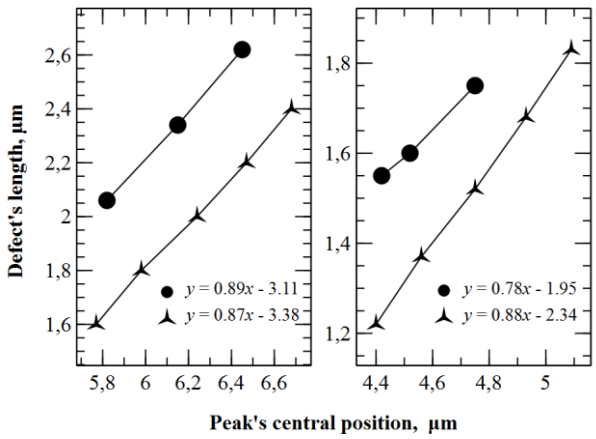

Figure 5.2.5. Experimental (dots) and simulated (stars) relationship between the defect length and the central position of the peak for the two intervals studied: [5.8-6.5] µm (left) and [4.4-4.8] µm (right). They follow a linear regression, written at the bottom of the figure for both cases.

5.2.4 Conclusions

Macroporous silicon photonic crystals with a defect embedded in the middle of the structure have been studied. The PCs have a PBG in the MIR region with a resonance state due to the cavity formed by the defect. The simulations show a shift in the resonating states when we change either the width or the length of the defect and leave the rest of the PC unchanged. Our results show that the defect length is the best option for tuning the resonance position. This helps the design of sharp MIR filters with little variation of the Q-factor for all the tuning range. The relationship between the geometrical variation and the working frequency of the resonating states follows a linear regression.

From the theoretical study, samples with different defect lengths were fabricated with optical response in two wavelength intervals: 7 μm and 4.5 μm. The experimental data show good agreement with the theoretical results in both cases, although some improvements have to be done in further studies to improve the transmission amplitude and the Q-factor of the resonance, especially for the short period samples in the range of 4.5 μm. Finally, we show that MPS PCs are a viable solution for the design of gas detection devices in the mid-infrared, which includes formaldehyde, carbon monoxide, nitrogen dioxide or nitrous oxide, among others.

5.2.5 Acknowledgement

This work has been founded by TEC-2013-48-147-C6-2-R. The authors wish to acknowledge the help from P. Eglitis for his useful comments during the writing of this paper.

5.2.6 References

[1] C. Soukoulis, “Photonic crystals and light localization in the 21st century,” 2012.

[2] K. Sakoda, *Optical Properties of Photonic Crystals*. Springer Science & Business Media, 2004.

[3] S. A. Rinne, F. García-Santamaría, and P. V. Braun, “Embedded cavities and waveguides in three-dimensional silicon photonic crystals,” *Nat. Photonics*, vol. 2, no. 1, pp. 52–56, Dec. 2007.

[4] J. D. Joannopoulos, S. G. Johnson, J. N. Winn, and R. D. Meade, *Photonic Crystals: Molding the Flow of Light (Second Edition)*. 2011.

[5] P. V. Braun, S. A. Rinne, and F. García-Santamaría, “Introducing Defects in 3D Photonic Crystals: State of the Art,” *Adv. Mater.*, vol. 18, no. 20, pp. 2665–2678, Oct. 2006.

[6] M. Youcef Mahmoud, G. Bassou, A. Taalbi, and Z. M. Chekroun, “Optical channel drop filters based on photonic crystal ring resonators,” *Opt. Commun.*, vol. 285, no. 3, pp. 368–372, Feb. 2012.

[7] B. Gesemann, S. L. Schweizer, and R. B. Wehrspohn, “Thermal emission properties of 2D and 3D silicon photonic crystals,” *Photonics Nanostructures - Fundam. Appl.*, vol. 8, no. 2, pp. 107–111, May 2010.

[8] N. Neumann, M. Ebermann, S. Kurth, and K. Hiller, “Tunable infrared detector with integrated micromachined Fabry-Perot filter,” *J. Micro/Nanolithography, MEMS MOEMS*, vol. 7, no. 2, p. 021004, 2008.

[9] I. Alvarado-Rodriguez, “Fabrication of two-dimensional photonic crystal single-defect cavities and their characterization by elastic scattering,” *A Diss. Dr. Philos. Electr. …*, 2003.

[10] X. Xiao *et al.*, “Investigation of defect modes with Al2O3 and TiO2 in one-dimensional photonic crystals,” *Opt. - Int. J. Light Electron Opt.*, vol. 127, no. 1, pp. 135–138, Jan. 2016.

[11] M. Mohebbi, “Refractive index sensing of gases based on a one-dimensional photonic crystal nanocavity,” *J. Sensors Sens. Syst.*, 2015.

[12] W. Zhou *et al.*, “Progress in 2D photonic crystal Fano resonance photonics,” *Prog. Quantum Electron.*, vol. 38, no. 1, pp. 1–74, 2014.

[13] E. Nelson, “Three-dimensional photonic crystal optoelectronics,” 2011.

[14] P. V. Braun, S. A. Rinne, and F. García-Santamaría, “Introducing Defects in 3D Photonic Crystals: State of the Art,” *Adv. Mater.*, vol. 18, no. 20, pp. 2665–2678, Oct. 2006.

[15] M. Taverne, Y. Ho, and J. Rarity, “Investigation of defect cavities formed in three-dimensional woodpile photonic crystals,” *JOSA B*, 2015.

[16] P. Massé, S. Reculusa, K. Clays, and S. Ravaine, “Tailoring planar defect in three-dimensional colloidal crystals,” *Chem. Phys. Lett.*, vol. 422, no. 1–3, pp. 251–255, Apr. 2006.

[17] E. Palacios-Lidón, J. F. Galisteo-López, B. H. Juárez, and C. López, “Engineered Planar Defects Embedded in Opals,” *Adv. Mater.*, vol. 16, no. 4, pp. 341–345, Feb. 2004.

[18] G. Mertens, R. B. Wehrspohn, H.-S. Kitzerow, S. Matthias, C. Jamois, and U. Gösele, “Tunable defect mode in a three-dimensional photonic crystal,” *Appl. Phys. Lett.*, vol. 87, no. 24, p. 241108, Dec. 2005.

[19] A. Langner, “Fabrication and characterization of macroporous silicon,” *Doktorarbeit, Martin-Luther-Universität*, 2008.

[20] V. Lehmann, “Formation Mechanism and Properties of Electrochemically Etched

Trenches in n-Type Silicon," *J. Electrochem. Soc.*, vol. 137, no. 2, p. 653, Feb. 1990.
[21] V. Lehmann, "The Physics of Macropore Formation in Low Doped n-Type Silicon," *J. Electrochem. Soc.*, vol. 140, no. 10, p. 2836, Oct. 1993.
[22] B. J. Frey, D. B. Leviton, and T. J. Madison, "Temperature-dependent refractive index of silicon and germanium," in *SPIE Astronomical Telescopes + Instrumentation*, 2006, pp. 62732J-62732J–10.
[23] D. Vega, D. Cardador Maza, T. Trifonov, M. Garin Escriva, and A. Rodriquez Martinez, "The Effect of Absorption Losses on the Optical Behaviour of Macroporous Silicon Photonic Crystal Selective Filters," *J. Light. Technol.*, vol. PP, no. 99, pp. 1–1, 2015.
[24] M. Mohebbi, "Refractive index sensing of gases based on a one-dimensional photonic crystal nanocavity," *J. Sensors Sens. Syst.*, 2015.
[25] H. Föll, M. Christophersen, J. Carstensen, and G. Hasse, "Formation and application of porous silicon," *Mater. Sci. Eng. R Reports*, vol. 39, no. 4, pp. 93–141, Nov. 2002.
[26] A. Reynolds and U. Peschel, "Coupled defects in photonic crystals," *Microw. Theory …*, 2001.
[27] S. Lan, S. Nishikawa, Y. Sugimoto, and N. Ikeda, "Analysis of defect coupling in one-and two-dimensional photonic crystals," *Phys. Rev. B*, 2002.
[28] M. Minkov, U. P. Dharanipathy, R. Houdré, and V. Savona, "Statistics of the disorder-induced losses of high-Q photonic crystal cavities," *Opt. Express*, vol. 21, no. 23, 2013.
[29] Y. Taguchi, Y. Takahashi, and Y. Sato, "Statistical studies of photonic heterostructure nanocavities with an average Q factor of three million," *Opt. Express*, 2011.
[30] D. Gerace and L. Andreani, "Effects of disorder on propagation losses and cavity Q-factors in photonic crystal slabs," *Photonics Nanostructures-fundamentals …*, 2005.
[31] D. Cardador, D. Vega, D. Segura, T. Trifonov, and A. Rodríguez, "Enhanced geometries of macroporous silicon photonic crystals for optical gas sensing applications," *Photonics Nanostructures - Fundam. Appl.*, vol. 25, pp. 46–51, Jul. 2017.

5.3

Photonics and Nanostructures – Fundamental and applications, 25, 46-51 (2017)

http://dx.doi.org/10.1016/j.photonics.2017.04.005

Received: 14 November 2016; **Revised:** 21 March 2017;
Accepted: 18 April 2017; **Available online:** 10 May 2017

Enhanced geometries of macroporous silicon photonic crystals for optical gas sensing applications

D. Cardador[a,*], D. Vega[a], D. Segura[a], T. Trifonov[b] and A. Rodríguez[a]

a Micro i Nanotecnologies, Departament d'Enginyeria Electrònica, Universitat Politècnica de Catalunya, C/Jordi Girona, 31, 08031, Barcelona, Spain
b Center for Research in NanoEngineering, CrNE—Universitat Politècnica de Catalunya, UPC, Barcelona 08028, Spain

Abstract: a macroporous silicon photonic crystal is designed and optimized theoretically for its use in gas sensing applications and IR optical filters. Light impinges perpendicularly onto the sample surface (vertical propagation) so a three-dimensional (3-d) structure is used. For gas sensing, a sharp resonance is desired in order to isolate an absorption line of the gas of interest. The high Q-factors needed mandate the use of a plane defect inside the PhC to give rise to a resonant mode inside the bandgap tuned to the gas absorption line. Furthermore, to allow gas passage through the device, an open membrane is required. This can affect the mechanical resilience. To improve the strength of the photonic crystal the pores are extended after the "active" 3-d part. The number of modulations, and the extension length have been optimized to obtain the largest Q-factor with reasonable transmitted power. These proposed structures have been experimentally performed, probing an enhancement of almost an order of magnitude in the Q-factor in respect with the basic case. Simulations considering CO_2 have been performed showing that the proposed structures are promising as precise optical gas sensors.

5.3.1 Introduction

Photonic crystals (PhCs) exhibit photonic bandgaps (PBGs) in their optical spectra [1,2], because of the periodical modulation of their refractive index. This feature allows creating resonating cavities, and thus PhCs can be used to create IR filters and devices for the optical detection of gases [3,4]. These cavities are created by placing defects in the periodical structure of the PhC [5]. The detection can be then performed by directly monitoring the absorption of light, or by measuring a frequency shift of the peak. The direct measure method is based on the Beer-Lambert law, which states that the intensity absorption is an exponential function of substance concentration and optical length [6]. Gases, in particular, have strong optical absorption bands at specific wavelengths unique for each gas; its *fingerprint* [6]. Therefore, to sense a certain gas, it is necessary to measure the absorption at some of its specific wavelengths. That imposes isolating the absorption line, which can be accomplished with a high Q-factor PhC filter. The main drawback of such method is that to have good sensitivities, long interaction lengths must be attained.
An alternative to the previous methods was reported in other studies [7]–[9]. In them, it is proposed the use of the slow group velocities that the band structure of carefully crafted macroporous silicon (MPS) PhCs have at the band edges of the PBG. Theoretically this method was shown to work well, but light coupling was shown to be a major problem. Furthermore, losses due to scattering and absorption were also very high as the signal had to traverse a very long silicon structure.

In this paper we study a 3d MPS structure as proposed elsewhere [4], [10] for gas sensing, using out-of-plane (vertical) propagation. Although these PhCs are more complex, they can be fabricated using cheap methods, such as electrochemical etching (EE), and are very versatile structures. Furthermore, light coupling into and out of the sample is simpler than for in-plane devices. Additionally, MPS can be made to be inert to ambient conditions and aggressive gases, and are mechanically very stable.

The MPS PhC device analyzed in this paper has a spherical modulated profile, and would be fabricated by EE. The proposed structure has a cavity to induce a resonance state which has been engineered to correspond with the absorption band of CO_2 at $\lambda = 4.25\ \mu$m. This device works according to the Beer-Lambert principle, thus to improve the sensitivity, the peak is placed inside the PBG to confine light and improve the Q-factor of the cavity. In order to optimize the optical response, the number of periods used in the modulated part of the PhC is changed from a few periods to a large number of them. Besides, as the PhC structure is a membrane to allow the passage of gas through its pores, the mechanical resilience has to be considered. As these membranes are very thin, porosification is continued after the 3d part of PhC is finished, consisting of straight pores. This section forms the *tail* of the pores. This is done in the same fabrication step and results in a thicker and robust device. This tail may result in unwanted optical features, and therefore the effect of its length is studied. The tail length is changed from non-existent to about the double of the PhC depth, to determine its impact or possible benefits to the optical transmittance of the proposed device. These proposed photonic crystals have been experimentally fabricated, showing a good accordance with the theoretical study. Although the experimental Q-factors are lower than the theoretical ones (due to non-idealities in the fabricated design), we report an enhancement of almost an order of magnitude in the quality factor of the peak. This achievement show that the new structures are a promising option to be used in spectroscopic gas sensing. Finally, an improvement of the sensitivity due to the increase in the peak's quality factor is theoretically predicted.

5.3.2 Numerical study

The simulations of the 3D photonic crystals were done in Optiwave's OptiFDTD software, which uses the finite-difference time-domain method (FDTD). For the simulations, a single pore was designed with its axis aligned to the Z axis, and with light propagating along the Z axis. Periodic boundary conditions were applied on the *XZ* and *YZ* walls while perfect absorbing layers were used for the top and bottom of the simulation space in order to model an ideal PhC. The base shape of this pore consisted in two main parts: the modulated areas and the defect. Modulations were done by an number of periods composed, each one of them, by an ellipsoid and a cylinder—whose radius were optimized in our previous works [10].—Simulations dimensions were normalized to the lattice XY periodicity and each modulation period was defined in a normalized cell box of size 1×1×1 units. The defect, embedded halfway the pore depth, was introduced by removing a period, keeping a constant radius and extending as needed its length. For a real device, the lattice period would be $p_{\text{lattice}} = 0.7\ \mu$m in order to make the bandgap and defect state correspond with the carbon dioxide absorption line at $\lambda = 4.25\ \mu$m. In order to be rigorous, it should be taken into account that the profile obtained experimentally shows a certain deviation when compared to the simulated one. As it can be inferred from Figure 5.3.1, these variations are very small and have almost no impact on the bandgap, as reported somewhere else [11]. However, small variations in the length of the defect can lead to a mismatch with respect to the working frequency for which it was designed. But, as demonstrated in previous studies, the position of the peak within the bandgap can be easily adjusted in few iterations in fabrication [11].

The quality factor of the cavity is calculated using the usual definition as $Q = f_{\text{peak}}/\text{FWHM}$ from the spectral data, where f_{peak} is the central frequency of the resonant state, and FWHM is the width of the peak at half of its maximum value. In order to achieve the strongest resonance and the highest Q-factor in transmission, and enhance the optical features of the photonic crystal, two modifications of the initial structure were performed. The first one was to introduce a region of porous silicon with a straight profile—i.e. with a constant radius—as a continuation of the modulated pores, that is a *tail* of the pores. The second was to increase the number of periods. All the simulated structures are permeable membranes, both pore ends open allowing the passage of gas. The studied morphologies are schematically depicted in Figure 5.3.1.

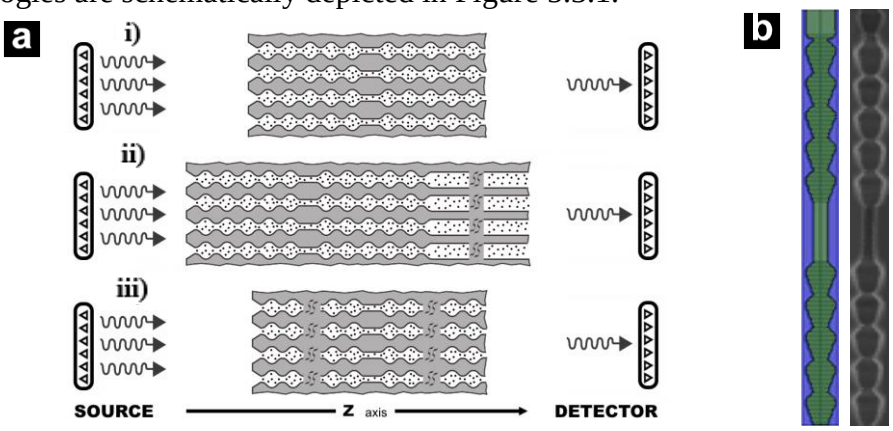

Figure 5.3.1. (a) Schematic representation of the different structure variations. A broadband light impinges the sample and travels through the photonic crystal (i) the basic structure consists of two modulated areas separated by a cavity in the middle. (ii) The modulated pores have been extended with a length of constant diameter pores. (iii) The number of periods before and after the defect is changed. As shown, light propagates along the Z axis, i.e. aligned to the pores' axis. (b) Comparison of simulated and etched basic profiles.

The illumination was done with a plane wave coming from the top of the pore and impinging on the front face of the PhC. The light wave was a Gaussian pulse with a linewidth of Δ= 4 units and a central wavelength about 5 units, so to make it correspond to the CO_2 absorption line. The transmission spectrum was obtained by placing a plane detector 5 units after the pore end. The spectrum was calculated by integrating the power flux through the detector plane and normalizing to the incident wave.

To perform the simulations, the refractive index of the bulk material was set to $n \approx 3.43$, which corresponds with the value of silicon in the range of $4\,\mu$m to $4.4\,\mu$m at room temperature [12]. As reported in previous works [13], the absorption in low doped silicon has almost no effect in the propagation of light through the PhC. So, in consequence, no losses were introduced in the bulk material (imaginary part of its refractive index, $\kappa = 0$). The pores were filled initially with air. The structure optimization was performed under these conditions. After optimization, the air was changed with carbon dioxide, which has strong absorption in the MIR. In particular the wavelength $\lambda = 4.25\,\mu$m was selected because is the strongest absorption band of CO_2 and MPS sensing devices have already been reported [4]. The data of the absorption coefficient were obtained from HITRAN database at standard conditions [14]. The absorption coefficient and the imaginary permittivity of the gas are related by $\varepsilon_{im} = n(\omega) \cdot \alpha(\omega)/\omega$, [15] where ε_{im} is the imaginary part of the permittivity, n is the refractive index, α is the absorption coefficient and ω is the angular frequency.

In low pressure conditions and using a high-resolution set-up, it is possible to discriminate the bundle of individual absorption lines of the gas as given by HITRAN. However, for this paper, where none of both previous conditions are given, the absorption coefficient has been modeled by the fitting of two Lorentz-Drude oscillators [15] to the envelope of absorption lines. At atmospheric pressures, the absorption lines will experience some broadening (HITRAN data is recorded in very low pressure conditions and high resolution) which can be seen in FTIR measurements. Furthermore, the resonance peak is designed to select the 4.18 µm-4.25 µm wavelength range, which as shown in Figure 5.3.2 corresponds accurately to the DL model used.

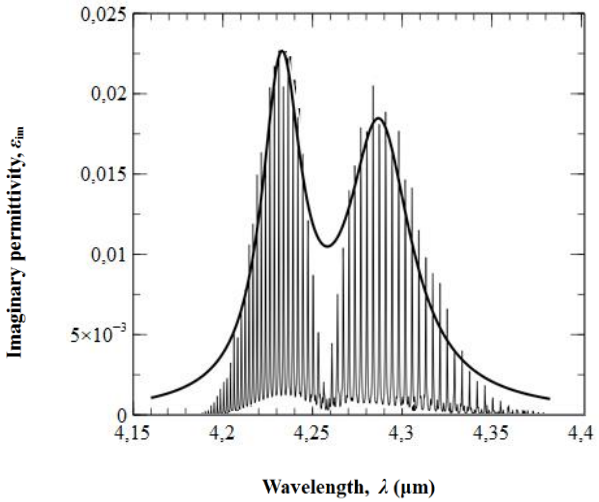

Figure 5.3.2. Absorption lines for CO_2 and the Lorentz-Drude approximation used in this paper which consists on modeling the gas absorption as the envelope (dark) of his absorption lines (grey).

5.3.3 Experimental

Preparation of macroporous silicon PC with defect

The 3D structures were obtained by electrochemical etching of *n*-type ⟨1 0 0⟩ crystalline silicon samples in hydrofluoric (HF) acid solution. The starting material had a resistivity between 0.1-0.3 Ω·cm. An N^+ layer was implanted on the backside of the wafer to provide a low-resistance transparent ohmic contact. Next, the wafer was oxidized and a lithography of 700 nm pitch was performed. A Reactive-ion Etching (RIE) and a tetramethylammonium hydroxide (TMAH) etching were done to create inverted pyramid-shaped pits that will act as nucleation centers for the ordered pore growth. Finally, an electrochemical etching was done to control the modulation of pore diameter which, in its turn, is regulated by the applied current. This method allows to design the profile beforehand and to create smooth 3D structures of great complexity. In particular, the periodical profiles attached in Fig.7 a) have been generated. As depicted in the figure, a planar defect is introduced halfway the total pore depth by suppressing one of the modulations and leaving a constant diameter section. The length of the cavity is 1.7 µm with a width value of 0.23 µm in all the samples. Finally, the longest value achieved for the tail's length is 6.5 µm. The total depth of all samples was about 12 µm in the case of $N = 5$ and about 17 µm when $N = 8$. A complete description of the process can be found elsewhere [16].

The optical response of the fabricated samples was measured in the MIR range using a Bruker Optic's Vertex FT-IR spectrometer. The lattice was aligned to the Γ – M direction (along one lattice axis in the surface) and an aperture of 1 mm and a resolution of 4 cm^{-1} was used. The measurements have been referred to the source spectrum to normalize the results in both, reflectance and transmittance.

5.3.4 Results and discussions

Creating a PhC membrane as short as the initially proposed, is a challenge in fabrication difficult to overcome. Lengthening the pores with a straight part at the end—see Figure 5.3.1(b)—is a good solution that allows to have longer pores as well as the optical properties of the photonic crystals are preserved. Furthermore, this added tail can be used to enhance the transmitted peak features. In classical optical filters, $\lambda/4$ cavities are used to optimize the coupling between dissimilar refractive index media at the working frequency, which is adjusted by setting the cavity's length. Therefore, it seems beneficial to place a $\lambda/4$ tail at the end of the pore to enhance coupling and hence the Q-factor of the main peak. Nevertheless, as reported in Geppert's thesis [7], the coupling behavior in photonic crystals cannot be explained classically; resonant conditions and Bloch's modes have to be considered for designing the tail's length in order to optimize the peak's features.

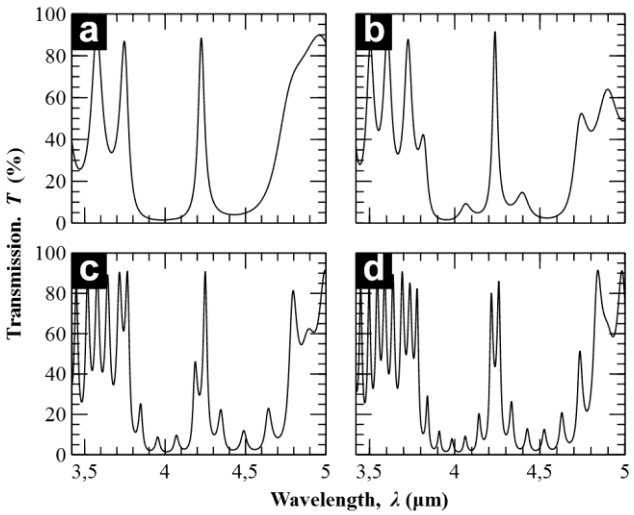

Figure 5.3.3. Keeping the number of periods constant, the straight end section length is varied. As the length increases, new, smaller, peaks appear in the optical spectrum. Here are shown the optical response of the PhC with defect when the tail is (a) 0, (b) 10, (c) 26, and (d) 40 μm long.

According to Geppert's study, simulations show that additional resonant modes appear in the bandgap as the length of the tail is increased. This further modifies the shape of the main peak, and thus its Q-factor. In Figure 5.3.3 it is depicted the influence in the peak's shape when the length of tail of the pores was varied from $0\ \mu$m to $40\ \mu$m while the rest of the parameters—porosity, periodicity, and modulation profile—remained unchanged, since they were optimized in previous works [13]. Adjusting the tail's length and diameter, the number and position of the resonances in the tail section change accordingly. As expected, the longer the tail, more modes will exist. These can be cleverly placed, by carefully adjusting the tail's length, such that these resonant peaks narrow the defect state. As seen from Figure 5.3.3, the optical transmittance for different tail sections shows almost no change in amplitude. Therefore, in the optimum case, the Q-factor of the defect's transmittance resonance is clearly improved. The trade-off is the rise of ground level in the PBG. The adjustment of the geometry can also be sensitive to process variations; as small variations can result in the loss of performance.

In the data shown in Figure 5.3.3 (d) it can be observed how the main resonance peak separates in two peaks. This can be explained as, for lengths greater than $24\ \mu$m, the resonant peaks given by the tail's length appear so close one to each other that at least two of them fall in the main peak, splitting it in two. As the length of the tail increases, this suggests that more peaks may fall over the defect resonance. However, fabrication imperfections ultimately break coherence [17] and the tail won't have any significant contribution to the optical response of the PhC. As reported in Koenderink's work [17], the total length of the PhC should not exceed some tens of times the lattice parameter to preserve the optical properties. Taking into account both constraints—length of the PhC and the emergence of two peaks,—it seems reasonable to restrict the tail's length to the range of $0\ \mu$m to $20\ \mu$m.

Another important fact observed in these simulations is that as we increase the tail's length l_{tail}, the Q-factor is also increased. In particular, the Q-factor achieved with no tail is $Q = 127$, but increases to $Q = 215$ when $l_{\text{tail}} = 20\ \mu$m. This amount allows to measure the gas concentration by the dispersive method, based in Beer-Lambert's formula [6]. The greatest sensitivity is given when the strongest absorption line of CO_2 and the cavity resonance of the PhC are aligned. In Figure 5.3.4, it can be observed that the variation

between the curves of 0% and 100% of concentration is almost the 20% of the amplitude for the initial structure.

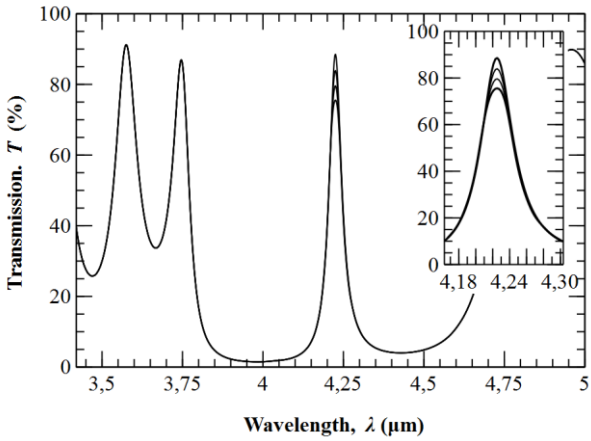

Figure 5.3.4. Evolution of peak's amplitude for the base PhC with a when exposed to 0%, 33%, 66% and 100% of gas concentration.

Previous studies have reported the impact that the number of layers *N* have in the transmission spectra in PhCs [18]–[21]. They prove that the bandgap becomes more defined as the number of periods increase. Furthermore, in the case of having a transmission peak in the gap, it can be shown that both, Q-factor and amplitude, are related with the quantity of periods [22]. According to this, we increased the number of periods before and after the defect respect to the base case, see Figure 5.3.1c. As depicted in Figure 5.3.5, increasing the number of periods *N*, rises significantly the Q-factor of the peak. However, as a counterpart, the amplitude decreases. As shown in Figure 5.3.6b, a convenient compromise between the quality factor and the transmission is reached when the number of periods is around nine, showing a Q-factor close to 500 and a transmission of 66%. These values improve the results obtained just by adding a tail to the pores.

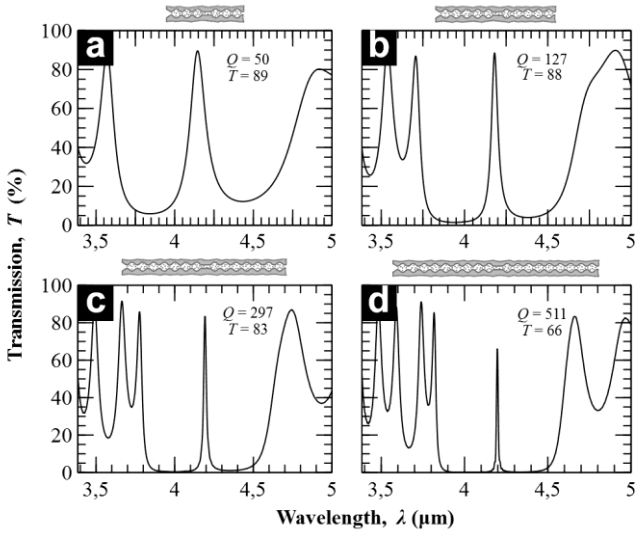

Figure 5.3.5. Evolution of the amplitude and the Q-factor with respect to the number of periods: (a) 3 periods, (b) 5 periods, (c) 7 periods, and (d) 9 periods. The actual structures are depicted above the graphs for each case.

The effect of the presence of CO_2 in these optimum conditions can be seen in Figure 5.3.6(a) for different gas concentrations. The amplitude of the peak has a greater change when exposed from 0% to 100% of gas concentrations than for the initial device of Figure 5.3.4.

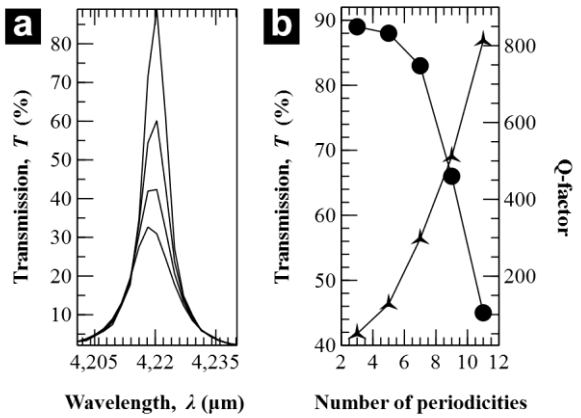

Figure 5.3.6. Detail of the peak amplitude change with gas concentration. The MPS device has 9 modulation periods and a tail section of length $l = 20\ \mu$m. In (a) the peak amplitude clearly decreases for CO_2 concentration of 0%, 33%, 66%, and 100%. In (b) the peak's amplitude (●) and Q-factor (□) dependence to the number of periods is plotted.

If both strategies for enhancing the peak features –e.g. lengthening the pore and increasing the number of periods- are applied together, the previous results are improved to the highest Q-factor of $Q = 902$ when $N = 9$ and $l = 20$ μm.

These theoretical results obtained through simulation have been experimentally tested. In Figure 5.3.7a it is depicted the transmission spectra for the studied cases. The profiles with five and eight periods are shown in Figure 5.3.7b. Due to experimental limitations, the tail length has only been able to reach 6.5 μm in both periodicities, being far from the optimal value discussed above (20 μm). In the same sense, the number of periodicities have been limited to $N = 8$ because adding more periods significantly reduced the transmittance. Even so, by introducing a tail to the profile of five modulations, the Q-factor shows a remarkable improvement, going from $Q = 12$ (case without tail) to $Q = 61$. A larger increase is obtained when more periods are introduced, reaching the value of $Q = 101$. But it is when both strategies are applied at the same time when the best quality factor is obtained, $Q = 117$, almost an order of magnitude higher than the initial value.

Although experimental values are not as good as the theoretical ones (due to non-idealities in fabrication, e.g. small variations in pore length or thickness, roughness, etc.), they do support the developed theory. Moreover, thanks to the improvement of Q-factor, experimental peaks have been obtained good enough to perform gas spectroscopic measurements with them (see Figure 5.3.4 where a peak of Q ≈ 120 has been used in the simulation). However, as Figure 5.3.8 shows, an improvement in the Q-factor would revert to a greater sensitivity of the device.

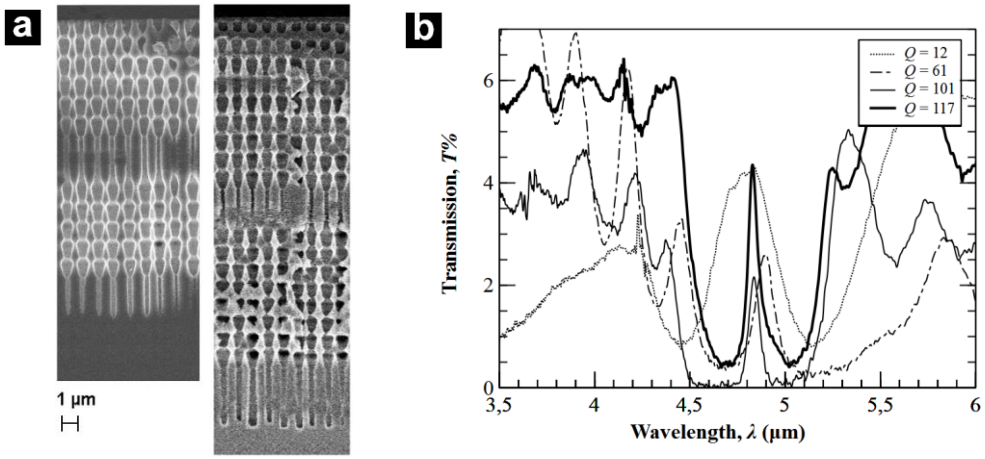

Figure 5.3.7. (a) Scanning electron microscope (SEM) image of two photonic crystals with N = 5 and 8, respectively. The tail has been lengthened until 6.5 μm in both cases. (b) Transmission spectra of the structures with and without tail: N = 5 and L = 0 μm (dotted line), N = 5 and L = 6.5 μm (dot-dashed line), N = 8 and L = 0 μm (light-black line), N = 8 and L = 6.5 μm (dark-black line).

In Figure 5.3.8a it is depicted the amplitude of the transmission peak relative to the concentration of carbon dioxide inside the pores in three cases, N = 5, 7 and 9 for $l = 20\ \mu$m in all of them. It is clear that the transmission in the PhC decreases for higher values of N in an exponential way, following the Beer-Lambert prediction. This decrement is because of the growth of the path length, which is given by two reasons. The first, and obvious one, is due to the added distance when more periods are considered. This term should apply a constant contribution to the transmission. But, as we can see in 8(b), the sensitivity S,—defined as $S = \partial T/\partial c$, where T is the amplitude of the transmitted peak, and c is the gas concentration—has a different tendency in all three cases. This leads to the second reason: due to the increment of periods, there are more resonances in the photonic crystal what, at the end, implies a higher effective path length for the transmitted modes.

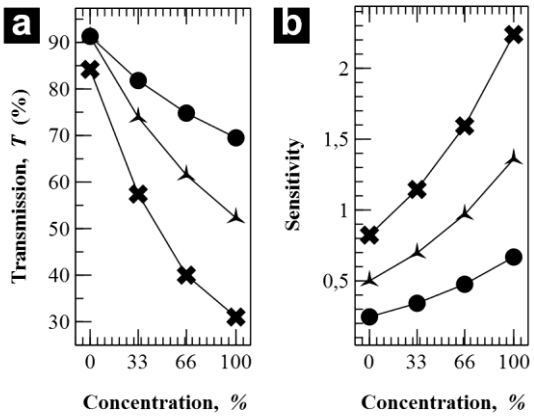

Figure 5.3.8. Fig. 1. (a) Evolution of the peak's amplitude when exposed to 0%, 33%, 66% and 100% of gas concentration in for the number of periodicities N (●) 5, (×) 7, and (□) 9. In all cases l = 20 μm. (b) Sensitivity in the three cases.

5.3.5 Conclusions

In this paper 3-d PhC based on MpS have been studied by simulation. The crystal's shape has been explored to find an optimum Q-factor of a photonic filter based on 3d MpS where light propagates along the pore's axis. The considered PhC structure in this analysis is a square array of modulated pores with an embedded plane defect that gives rise to a photonic bandgap and a transmission peak in the middle of the PBG. The shape optimization involved adjusting the pores' tail length and modifying the number of periods in the modulated section.

It has been found that the presence of a tail section of straight pores after the modulated PhC can have a noticeable effect for a certain length of this tail. In particular, the simulations show that, at wavelengths around $\lambda = 4\ \mu$m, for tails lengths up to about $20\ \mu$m several small resonance peaks appear due to resonance in the tail, which can have a positive effect in the main resonance peak due to the plane defect. This allows increasing the Q-factor without affecting appreciably the transmitted maximum. However, for tails longer than $20\ \mu$m, these secondary resonances start interfering with the main peak which can result in a loss of performance. The presence of this tail is necessary when fabricating porous membranes to provide mechanical resilience to the device. Typically, this tail has a length about $70\ \mu$m or longer. It has been found that for such long tails [17], and due to fabrication roughness on the obtained surface, these secondary resonances are virtually non-existent and can be neglected.

On the other hand, the number of periods of the modulated crystal has a greater impact on the Q-factor. Generally, increasing the number of periods will give a higher Q-factor for the resonant cavity. Nonetheless, there exists a tradeoff with the transmitted peak amplitude. As the period number increases, the peak amplitude decreases. The optimum number will therefore depend on the source intensity, the detector sensitivity and the noise floor, but from the performed study we find that using nine modulation periods both before and after the defect gives a very good compromise.

These new structures have been studied, supporting the developed theory. In concrete, the initial value of the Q-factor for the basic case (N = 5, without tail), have been increased up to Q = 117, in the case of having a photonic crystal with 8 periods in each modulation area and a tail of 6.5 microns. This new optical features are good enough to be used in spectroscopic gas sensing.

Finally, the device response to CO_2 has been studied. It has been found that for the optimized PhC structure, a large variation of 70% in transmitted peak amplitude can be obtained with a sensitivity about $0.8\ \%/c_{\%}$. Therefore, we conclude that such PhCs are suitable for the detection of strong absorbing gases by non-dispersive infrared spectroscopy.

5.3.6 Acknowledgement

This work has been founded by the Spanish Ministerio de Economía y Competitividad (MINECO) through grant TEC-2013-48-147-C6-2

The authors would like to thank P. Eglitis for his helpful comments during the preparation of this paper.

5.3.7 References

[1] J. N. Winn, Y. Fink, S. Fan, and J. D. Joannopoulos, "Omnidirectional reflection from a one-dimensional photonic crystal.," *Opt. Lett.*, vol. 23, no. 20, pp. 1573–1575, 1998.

[2] H. Xu, P. Wu, C. Zhu, A. Elbaz, and Z. Z. Gu, "Photonic crystal for gas sensing," *J. Mater. Chem. C*, vol. 1, no. 38, pp. 6087–6098, Sep. 2013.

[3] A. Zakrzewski, M. Wielichowski, and S. Patela, "Optimization of 2D slab photonic crystal geometry for gas sensing," in *2011 International Students and Young Scientists Workshop "Photonics and Microsystems,"* 2011, pp. 147–149.

[4] D. Vega, F. Marti, A. Rodriguez, and T. Trifonov, "Macroporous silicon for spectroscopic CO_2 detection," in *IEEE SENSORS 2014 Proceedings*, 2014, pp. 1061–1064.

[5] H. Ren *et al.*, "Ring resonator of surface modes based on photonic crystals," *Opt. Commun.*, vol. 284, no. 16–17, pp. 4073–4077, Aug. 2011.

[6] J. Hodgkinson and R. P. Tatam, "Optical gas sensing: a review," *Meas. Sci. Technol.*, vol. 24, no. 1, p. 012004, Jan. 2013.

[7] T. M. Geppert, "Towards Photonic Crystal-Based Spectroscopic Gas Sensors," Thesis, Hälle-Wittenberg, 2006.

[8] R. B. Wehrspohn *et al.*, "Macroporous silicon and its application in sensing," *Comptes Rendus Chim.*, vol. 16, no. 1, pp. 51–58, Jan. 2013.

[9] A. Lambrecht, S. Hartwig, S. L. Schweizer, and R. B. Wehrspohn, "Miniature infrared gas sensors using photonic crystals," 2007, p. 64800D.

[10] D. Vega, D. Cardador, M. Garín, T. Trifonov, and Á. Rodríguez, "The Effect of Absorption Losses on the Optical Behaviour of Macroporous Silicon Photonic Crystal Selective Filters," *J. Light. Technol. Vol. 34, Issue 4, pp. 1281-1287*, vol. 34, no. 4, pp. 1281–1287, Feb. 2016.

[11] D. Cardador, D. Vega, D. Segura, and A. Rodríguez, "Study of resonant modes in a 700nm pitch macroporous silicon photonic crystal," *Infrared Phys. Technol.*, vol. 80, pp. 6–10, Jan. 2017.

[12] B. J. Frey, D. B. Leviton, and T. J. Madison, "Temperature-dependent refractive index of silicon and germanium," in *SPIE Astronomical Telescopes + Instrumentation*, 2006, pp. 62732J-62732J–10.

[13] D. Vega, D. Cardador Maza, T. Trifonov, M. Garin Escriva, and A. Rodriquez Martinez, "The Effect of Absorption Losses on the Optical Behaviour of Macroporous Silicon Photonic Crystal Selective Filters," *J. Light. Technol.*, vol. PP, no. 99, pp. 1–1, 2015.

[14] L. S. Rothman *et al.*, "The HITRAN 2008 molecular spectroscopic database," *J. Quant. Spectrosc. Radiat. Transf.*, vol. 110, no. 9–10, pp. 533–572, Jun. 2009.

[15] F. Wooten, *Optical Properties of Solids*. Academic Press, 2013.

[16] V. Lehmann, "The Physics of Macropore Formation in Low Doped n-Type Silicon," *J. Electrochem. Soc.*, vol. 140, no. 10, p. 2836, Oct. 1993.

[17] A. F. Koenderink, A. Lagendijk, and W. L. Vos, "Optical extinction due to intrinsic structural variations of photonic crystals," *Phys. Rev. B*, vol. 72, no. 15, p. 153102, Oct. 2005.

[18] J. F. Bertone, P. Jiang, K. S. Hwang, D. M. Mittleman, and V. L. Colvin, "Thickness Dependence of the Optical Properties of Ordered Silica-Air and Air-Polymer Photonic Crystals," *Phys. Rev. Lett.*, vol. 83, no. 2, pp. 300–303, Jul. 1999.

[19] H. S. Lee *et al.*, "Thermal radiation transmission and reflection properties of

ceramic 3D photonic crystals," *J. Opt. Soc. Am. B*, vol. 29, no. 3, p. 450, Feb. 2012.
[20] E. Moreno, F. J. García-Vidal, and L. Martín-Moreno, "Enhanced transmission and beaming of light via photonic crystal surface modes," *Phys. Rev. B*, vol. 69, no. 12, p. 121402, Mar. 2004.
[21] C.-J. Wu and Z.-H. Wang, "PROPERTIES OF DEFECT MODES IN ONE-DIMENSIONAL PHOTONIC CRYSTALS," *Prog. Electromagn. Res.*, vol. 103, pp. 169–184, 2010.
[22] X. Xiao *et al.*, "Investigation of defect modes with Al2O3 and TiO2 in one-dimensional photonic crystals," *Opt. - Int. J. Light Electron Opt.*, vol. 127, no. 1, pp. 135–138, Jan. 2016.

5.4

Optics Express, 26 (4), 4621-4630 (2018)
https://doi.org/10.1364/OE.26.004621
Received: 1 December 2017; **Revised**: 3 February 2018; **Accepted**: 7 February 2018; **Available online**: 13 February 2018

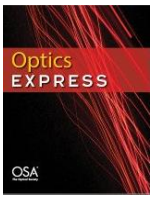

Photonic molecules for improving the optical response of macroporous silicon photonic crystals for gas sensing purposes

D. Cardador*, D. Vega, D.Segura and A. Rodríguez

Micro i Nanotecnologies, Departament d'Enginyeria Electrònica, Universitat Politècnica de Catalunya, C/Jordi Girona, 31, 08031, Barcelona, Spain

.

Abstract: In this paper we report the benefits of working with photonic molecules in macroporous silicon photonic crystals. In particular, we theoretically and experimentally demonstrate that the optical properties of a resonant peak produced by a single photonic atom of 2.6 μm wide can be sequentially improved if a second and a third cavity of the same length are introduced in the structure. As a consequence of that, the base of the peak is reduced from 500 nm to 100 nm while its amplitude is remained constant, increasing its Q-factor from its initial value of 25 up to 175. In addition, the bandgap is enlarged almost twice and the noise within it is mostly eliminated. In this study we also provide a way of reducing the amplitude of one or two peaks, depending whether we are in the two- or three-cavity case, by modifying the length of the involved photonic molecules so that the remainder can be used to measure gas by spectroscopic methods.

5.4.1 Introduction

Photonic Molecules (PMs), understood as two or more coupled micro or nanocavities, also called photonic atoms, have been extensively studied during the recent years thanks to their unique optical characteristic [1], [2]. As largely reported, a single cavity inserted in a photonic structure has the property of strong photon confinement [3], what can be used in several applications, such as biosensing [4–6], lasing [7–9] and a large etcetera. If a new cavity or a set of them is added to the structure, the optical response can not only be enhanced but also new functionalities of the system can be obtained. Photon hopping, which consists in the energy transference between adjacent cavities, is one of the most relevant properties of PMs that find its application in coupled-resonator optical waveguides [10–12], optical switching [13], [14] or quantum information processing [15], [16], among others. Furthermore, it has been shown that this energy transfer can be tuned depending on the inter-cavities conformation and on the morphology of the cavities themselves[17], [18], leading to enhanced bandwidths and boosted Q-factors [19], [20]. In this work we take advantage of the benefits of using photonic molecules for improving the optical response of macroporous silicon Photonic Crystals (PCs). In concrete, we show how by coupling several photonic atoms and by reshaping them, it is possible to obtain greater Q-factors, larger bandgaps and better filtering along the bandgap, three figures of merit for spectroscopic gas sensing.

Spectroscopic gas detection can be made using photonic crystals by adding a defect in the structure. If it is correctly designed, a transmission peak will arise inside the forbidden band, acting as a narrow band pass filter [21], [22]. If this peak is centered in the absorption band of the analyzed gas, its concentration can be determined by means of Non Dispersive Infra-Red methods (NDIR) that basically consist in calculating the area under the intensity line of the peak [23]. For a proper detection, the receiver must work within the bandgap, enveloping the peak. In that sense, the greater the bandgap, the less selective the detector has to be and, thus, the cheaper the final device would be. Besides, it is also necessary to eliminate all the noise in the bandgap since it reduces the performance of the sensor. Therefore, another requirement of the photonic crystals is that the transmission along the bandgap, except for the peak area, has to be as low as possible. Finally, and linked to the previous requirement, the peak transmission should be the maximum possible in order to obtain the greatest sensitivity when determining the amount of gas concentration.

As pointed above, we incorporate new cavities in our macroporous silicon photonic crystals in order to enhance the optical response of the single-cavity case and make these structures suitable for spectroscopic gas sensing. In particular, the study starts showing the poor optical response when only one defect is used. Next, we analyze the transmitted response of our structure when a new cavity is inserted in it. As predicted in literature for one- and two-dimensional PCs, and reported in preliminary studies in 3D, a new peak raises in the bandgap, preserving its transmission and increasing the Q-factor of both peaks[24], [25]. Not only this, the bandgap is enlarged and the transmission baseline –also called offset along this study- is reduced because more periods have been added in order to place the new cavity. Then, we corroborate this experimentally, showing narrower peaks and better figures for the bandgap. In order to filter one of the two peaks, we shorten the deeper cavity for varying the phase between the two resonant frequencies and we use a chirp modulation, consisting of a linear decreasing of the length of the periods involved in the PC, to optimize the filtering of the resonant states given in the second cavity. This procedure can be extrapolated to the case of three defects, showing a substantial improving of the optical figures respect to the previous cases.

5.4.2 Experimental and simulations

Simulations

Simulations have been done using the Optiwave's OptiFDTD software. This tool uses the Finite-Difference Time-Domain method (FDTD) to simulate the propagation of electromagnetic waves along complex structures. Taking advantage of the symmetries of the structures, periodic boundary conditions can be defined to reduce the simulation complexity and time. In our case, the studied photonic crystal can be reduced to a single pore aligned to the Z axis –see Figure 5.4.1, upper image– with periodic boundary conditions on the side walls –*XZ* and *YZ*– and multiple perfect absorbing layers before and after the emitter and the receiver, respectively. The front illumination has been done with a Gaussian modulated continuous wave with a linewidth of $\Delta\lambda = 4\,\mu$m and a central wavelength $\lambda_{\text{src}} = 5.2$ μm. The transmission spectrum has been obtained by placing a plane detector 5 μm after the ending of the pore and it has been calculated by integrating the power flux through the detector plane, normalized to the incident wave.

The refractive index of air and silicon, have been respectively set to $n = 1.00$ and $n = 3.43$ –that corresponds to the average value of silicon in the MIR range at room temperature [26]–. Regarding to previous studies, where it was reported that the absorption in low doped silicon has almost no effect on the propagation of light along the PC [27], we did not considered losses in the bulk material. However, as it can be observed in figures 5.4.2 and 5.4.3, simulated results present higher transmissions than the experimental ones. This has its explanation in the fact that the simulations do not consider bulk silicon while in the samples there is a thickness of about 240 μm continuing the photonic crystal and, hence, they absorb a large part of the transmitted signal. Unfortunately, simulating this rear silicon would lead to unaffordable times of simulations, making unfeasible the direct comparison between experimental and simulated results. However, this drawback can be experimentally solved by removing much of the bulk silicon of the samples –about 150 μm–, as done in the last step of our report.

For the last simulation, air has been replaced by Nitric Oxide (NO), a gas that comprises the wavelength range of the transmitted peak. Following the same procedure as in previous studies [22], the contour of its absorption cross section, obtained through HITRAN database [28], has been approximated by two Lorentzian curves and introduced in OptiFDTD. The amplitude of these curves has been arbitrarily varied to see the evolution of the peak when exposed to different gas concentrations. To relate both, the amplitude of the peak –that takes the 100%, 85%, 72% and 60% of the initial value– and the concentration, we have assumed that the peak is narrow enough to infer the evolution just by studying its central frequency by using Beer-Lambert formula. Therefore, the relationship is given through the absorbance –understood as the logarithm of the ratio between the peak intensity when exposed to some gas concentration and the intensity of the peak when there is no gas in the ambient [29]–. A simple calculation revealed that by arbitrary fixing the gas interaction path length to 10 cm –an admissible size for a commercial gas cell–, the four studied amplitudes imply concentrations of 0 ppm, 1000 ppm, 2000 ppm and 3000 ppm.

Some considerations about the pore structure

The simulated pores are the result of concatenating multiple thin disks with the appropriated radius in order to emulate the photonic crystals fabricated in our lab that, basically, they consist on a series of modulated areas separated by cavities. As reported in previous studies related to 3D macroporous silicon structures, the number of periods, *N*, introduced in the modulation areas will affect both the quality factor and the amplitude of

the transmission peak [22]. However, despite the fact that for a single cavity case it is reported that eight is the number of periods that maximizes the balance between the transmission and the quality factor of the PC, in this study, where we couple several cavities, we opted to use $N = 5$ for two main reasons. The first and the most important one is because the coupling between cavities inversely depends on the separation between them, among other features [30–33]. In concrete, if the number of periods between cavities increase, the coupling decreases and therefore, the transmission peaks are closer. In the counterpart, if N decreases, the PC goes towards strong-coupling regime –defined as Törma and Barnes proposed [34], [35]– and the peaks become more separated [36], [37]. As it will be explained, this separation helps to increase the bandgap and also allows to eliminate undesired transmission peak. The second reason of operating with 5 periods per modulation area is because the number of total periods increase as we add new cavities in the photonic crystal. As a consequence of this, the peak's transmission gets lower because of suffering more interferences in the material's interfaces.

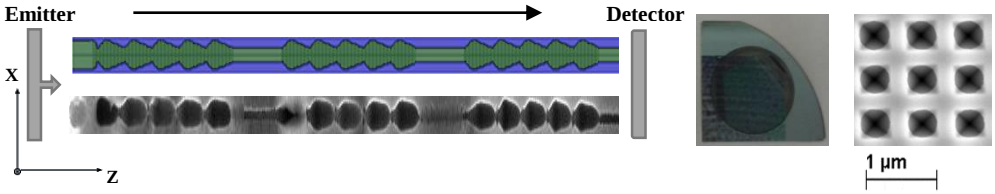

Figure 5.4.1. Left: Schematic representation of the structure and its mode of operation. The source emits light that travels through the photonic crystal. Modulation areas create the bandgap and cavities allow some transmission within it. (Up) and (down), simulated and fabricated profile in the periodical case, respectively. Middle: picture of one of the manufactured samples. All of them have an attached round area of about 1 cm in diameter. Right: top-view of the sample where the array of inverted pyramids of 700 nm pitch is depicted.

Although the basic structure is common to all simulations, we have to distinguish between the two different types of profiles analyzed in this study, the regular and the chirped. In the first one, and regardless of whether we are in the case of two or three cavities, all the periods involved in the different modulated areas have the same length of about 1.2 µm. In the same way, the cavities are designed equally long with a value of 2.6 µm. The second one, the chirped type profile, has a linear decrement in the periodicity and the length of the cavities involved. Several simulations with different values for the involved parameters were done in order to optimize the optical response of the photonic crystal, obtaining that for the two-cavity case, the periods have to decrease from the initial value of 1.4 µm to 1.0 µm. The length of the top cavity has to be maintained in 2.6 µm but the second has to be readjusted to 2.3 µm to achieve a better filtering. In the three-cavity case, the periods vary from 1.5 µm to 0.9 µm and the cavities has been designed with a length of 3.0 µm, 2.6 µm and 2.2 µm, respectively.

Fabrication of macroporous silicon photonic crystals

The fabrication of photonic crystals follows the procedure reported in previous papers [22], [38]; a n-type wafer is treated in such a way that, after a lithography and a tetramethylammonium hydroxide (TMAH) attack, its entire surface is marked by square lattice of inverted pyramids equidistantly distributed. These pyramids will act as nucleation centers where the pores will grow in the electrochemical attack. As reported in the mentioned papers, the resulting PCs operate at the mid-infrared range. According to the simulations, several samples were fabricated in order to accurately reproduce the shape of the optimized pores. In the case of the regular modulation, the vertical period is set to 1.2 µm and the length of both defects to 2.6 µm. In the case of the chirped shape with two

cavities, the period starts with 1.4 μm and linearly decreases until 1.0 μm. The length of the top cavity has been maintained in 2.6 μm but the deeper one has been lightly shortened to 2.3 μm. In the case of three cavities, the initial period takes the value of 1.5 μm and the last one, 0.9 μm, while the defect's length, from the top to the bottom, is set to 3.0 μm, 2.6 μm and 2.2 μm, respectively.

The total depth of the fabricated PCs ranges approximately between 25 μm and 35 μm, depending on whether we are in the two- or three-cavities case, resulting in an average of 210 μm of bulk silicon after the pores, since the samples have a thickness of 240 μm. In order to boost the transmission, part of the rear silicon –about 150 μm– has been etched with a TMAH attack in the final step of this study, leading an improvement from 5 % to 27 %.

Middle image of Figure 5.4.1 shows the picture of one of the manufactured samples. Scanning Electron Microscope (SEM) images reveal a great uniformity of the pores in the whole area attacked, accordingly to previous studies [39].

Optical characterization

A Bruker Optic's Vertex 70 FT-IR spectrometer has been used to obtain the transmission response of the fabricated photonic crystals. In concrete, the setting parameters for the aperture and the resolution have been 1 mm and 4 cm^{-1}, respectively. In addition, the light incidence has been aligned perpendicularly to the sample surface ($\Gamma - M$ direction) and several spots in the attacked area were measured to see the optical dispersion due to internal pore inhomogeneity. As a consequence of the pore uniformity reported above, maximum variations of less than 0.1% in both displacement and amplitude were observed in the area, showing a high reproducibility of the PC's optical response. Finally, the detected signal in the receiver has been normalized to the emittance.

5.4.3 Results and discussion

The optical response of the photonic crystal with a single-cavity is depicted in Figure 5.4.2. It is clear that the transmitted peak has not good filtering features; it has a very low quality factor ($Q \sim 25$) and the base, 0.5 μm wide, occupies large part of the 0.8 μm that covers the bandgap area –respectively defined as suggested in previous publications [22], [40]–. This principal characteristic makes the photonic crystal not suitable for conventional spectroscopic gas sensing since the fingerprint of the main gases are comprised in few hundreds of nanometers –i.e. the CO_2 has its spectrum lines within 4.20 μm and 4.35 μm–. However, they could be used in a broadband filter detection, following a similar procedure as the described in the paper of Hodgkinson et al. [41].

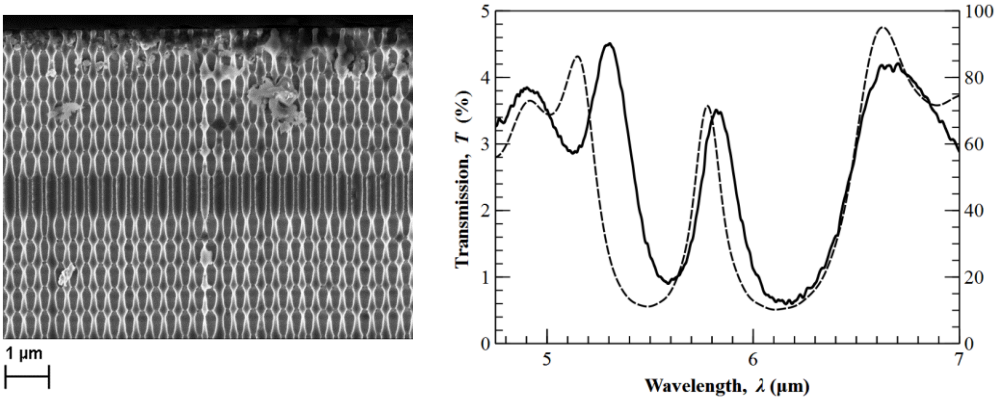

Figure 5.4.2. Left: SEM image of a PC with a single cavity. Right: optical response of the PC for both, experimental (solid line) and simulation (dashed line).

We can also appreciate in Figure 5.4.2 that there is a noticeable transmission percentage along the bandgap area in both, simulation and experimental. We point two main reasons to explain this occurrence. The first one is that the photonic crystal is very short, so the light does not experience enough refractive index changes to fully filter the frequencies inside the bandwidth. The second reason, which concerns only the experimental measures, is that the pores have some degree of inhomogeneity between them, which causes that the filtering in the bandgap loses some of its efficiency, with respect to the ideal case, among other optical effects [40].

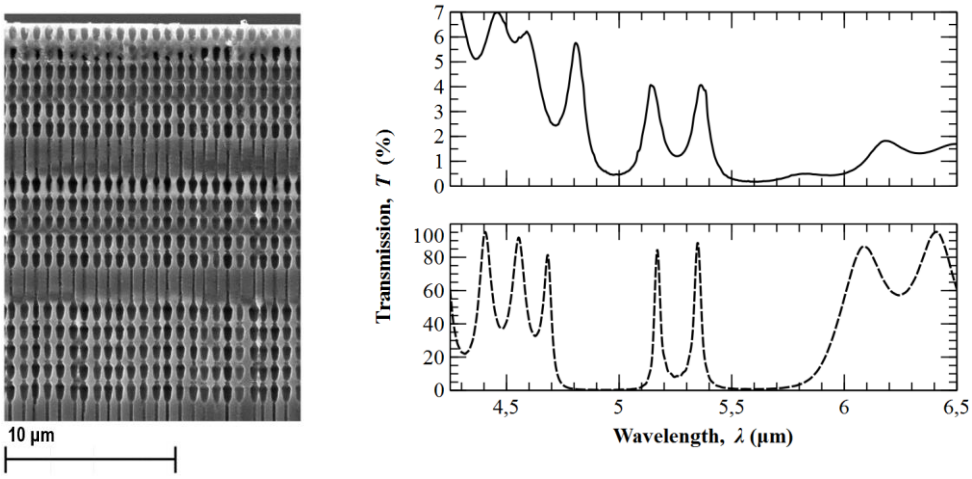

Figure 5.4.3. Left: SEM image of a PC with two cavities with the same value for all periods. Right: in the upper part is depicted the experimental optical response of the PC. The lowest image correspond to the simulations.

According to the literature, if new cavities are introduced, the main peak –that of the case of a single photonic atom– will unfold in as many cavities as have been inserted in the structure. These peaks will have practically the same transmission, but will increase their effective Q-factor due to the narrowing of their base, product of having several coupled resonators [42].

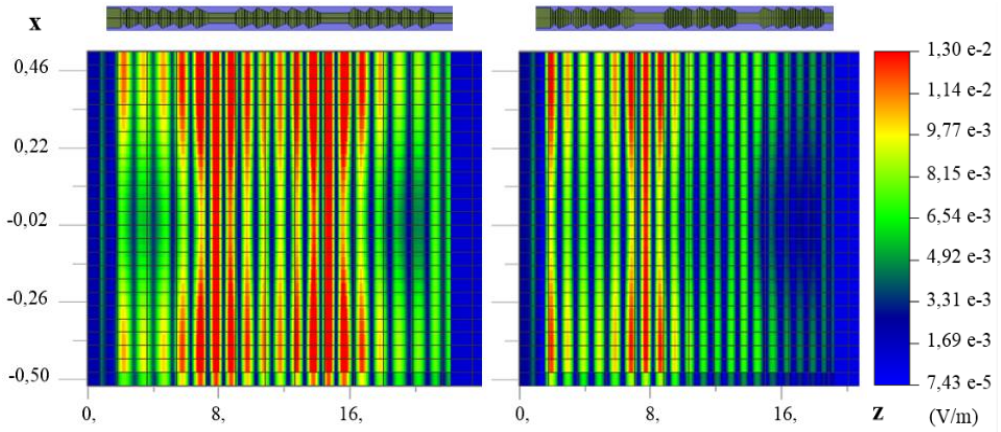

Figure 5.4.4. Section of the pore showing the electrical field (E_y) traveling along the PC. In the left image we can observe that there is the same presence of the field in both cavities (that have higer values than the rest of the PC due to the reonances). In the right image we see that, due to the chirped configuration, the presence of electrical field in the second cavity has been subtantially removed. On the top of both images it is depicted the simulated profile.

Taking this into account, we first simulated the structure by adding a new cavity, reporting a significant increment of the Q-factor, a reduction of the offset and a bandgap enlargement. Fabricated samples showed similar results, as can be observed in the Figure 5.4.3. Specifically, we observe that the Q-factor increased by a factor x3 –going from Q = 25 in the case of a single cavity to Q = 75– and the offset was reduced to more than half due to the increase in the number of periods. In addition, thanks to the introduction of a new peak, the bandgap was widened a 75 % more in comparison to the initial case, another of the properties that we wanted to improve.

However, despite the enhancement of the optical features, the transmission characteristics of the PC should be improved to be used as a narrow filter in spectroscopic gas sensing –i.e. the base of the peak is still too wide and the Q-factor and transmission still need to be enhanced–. Moreover, the introduction of this new peak is against one of the first premises that we made at the beginning: the elimination of the maximum signal within the operating area of the receiver –except that of the peak that points to the gas–. So it would seem that we shot our own foot. Nevertheless, as mentioned in literature, the optical properties of photonic molecules "can be optimally tuned by adjusting the sizes and shapes of individual cavities as well as their positions" [43]. In concrete, the phase between resonant frequencies –and therefore, the transmission of the peaks- can be modified by shortening one of the cavities, showing bonding and antibonding states. In this way, decreasing the second cavity length to 2.3 μm, we reduced the transmission of the peak centered in 5.15 μm from 90 % to almost 25 %. Furthermore, since the chirped modulation has been proved to be an efficient way of filtering light in PC structures [44], we used it to practically filter the whole peak.

As it can be observed in Figure 5.4.4, this new configuration leads to a reduction of the electric field density in the deeper cavity while it is maintained in the top one. As a consequence, the peak with shorter wavelength is substantially reduced while the other does not suffer meaningful modifications –see Figure 5.4.5–.

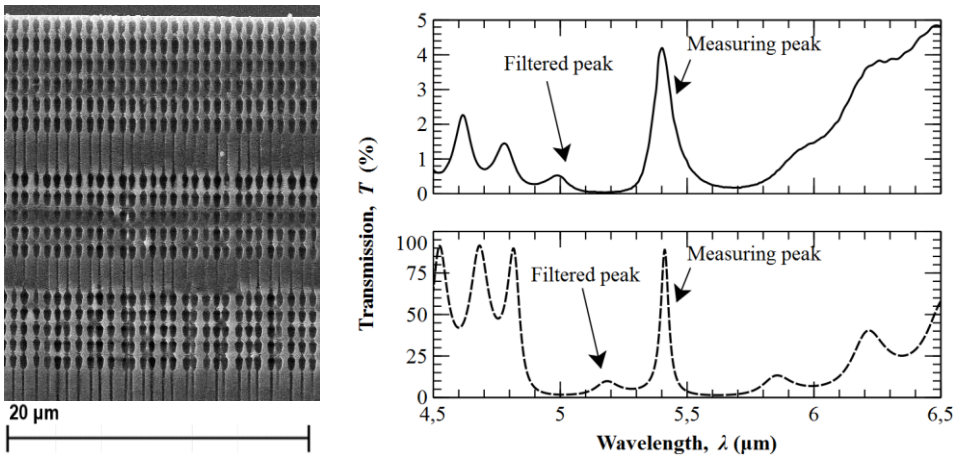

Figure 5.4.5. Left: SEM image of a PC with two cavities in the chirped configuration. Right: optical response of the PC shown in left image for both, experimental (up) and simulation (down).

Using the same arguments, we incorporated a third cavity into the photonic crystal. However, in this case we had greater difficulties when reducing the amplitude of two of the peaks while remaining the other as unaltered as possible. As can be seen in Figure 5.4.6, in the case of same length for the three cavities, the peaks are closer than in the two-cavity case. They can be separated by properly vary the length of the cavities. This leads to a modification in the coupling of the resonant frequencies due to the phase difference what has an impact in the amplitude of the peaks. After several simulations, the optimum

spectrum –see image c) of Figure 5.4.6- was reached when the cavities took the values of 3.0 μm, 2.6 μm and 2.2 μm, going from the top to the bottom. In this figure it can also be seen the appearance of new peaks in the bandgap. These peaks are harmonics of the resonant frequencies that manifest themselves in the forbidden band due to its widening after the incorporation of new cavities. Finally, a chirped modulation –values between 1.5 μm and 0.9 μm– was implemented to further reduce the amplitude of the *unwanted* peaks. A membrane was made, eliminating a large part of the bulk silicon of the wafer, thereby achieving an increase in the transmission of all the photonic crystal.

The experimental response depicted in the center image of Figure 5.4.7 shows a clear improvement in respect to previous results: the remaining peak increased its experimental Q-factor to approximately Q = 175 –2.3 times the one obtained in Figure 5.4.3 and seven times with regard to the single cavity case value–, the bandgap width enlarged to 1.5 μm and the transmission highly improved from 5% to almost 30%. The transmission base-line, however, did not improve noticeably respect to the two-cavity case because the light is not absorbed in the rear silicon –it was etched– and the photonic crystal does not reflect perfectly the wavelengths inside the bandgap. Nonetheless, the difference between the secondary and the principal peaks is more remarkable and the bandgap width is almost two times the initial case.

The advantages of adding more cavities have a limit: as the system increases in complexity, the peaks are less spaced and new harmonics appear in the bandgap, which ends up having a greater difficulty filtering all the peaks except one. Efforts have been made in this direction and, although it is true that the quality factor of the peaks increases, its filtering has been unsuccessful.

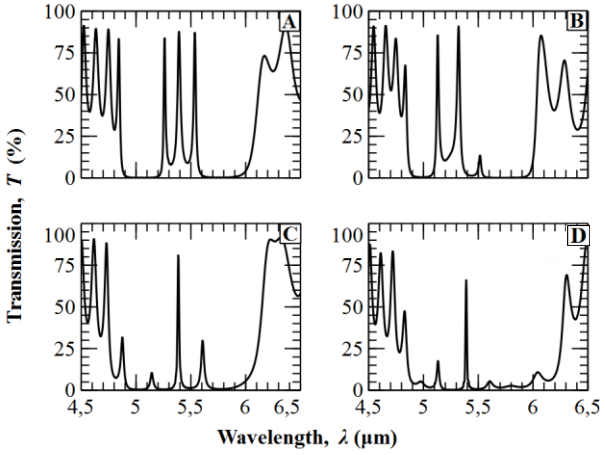

Figure 5.4.6. Optical response of a 3-defect PC (A) when the three cavities have the same length of 2.6 μm. The variation of the cavities' length has an impact in the amplitude of the involved peaks. In figure (B) we present the coupling of two cavities of 2.2 μm and one of 2.6 μm. In (C) figure, we can observe how the configuration of 3.0 μm, 2.6 μm and 2.2 μm arises the central peak and reduce the amplitude of the others. Finally, it is possible to reduce the peaks by applying a chirped modulation (D).

Finally, as a proof of concept, we show in the right image of Figure 5.4.7 the theoretical response of the peak when exposed to different concentrations of nitric oxide at the fixed path length of 10 cm. As it can be seen, its initial amplitude decreases homogenously for all wavelengths due to the fact that we have almost the same absorption cross section value for all of them. This is in accordance to the assumption made in 'Simulation' section, where we used the approximation of narrow peak to calculate the associated concentrations. In the case of wider peaks, the relationship between the concentration and the amplitude would not be homogenous and integral calculations would be required to accurately determine it [23].

This result can be extrapolated to other gases using the well-known property of scalability in photonic crystals that says that applying a proportionality factor to the geometry, the optical response of the PC is rescaled following the same ratio. Hence, after a proper readjustment of the PC dimensions, the results obtained in this study can be used to sense a number of gases in the MIR region –e.g. CO, CO_2, NO_2, NH_3 or CH_4, among others– that suit the reported absorbance values with lower optical path lengths, as their absorption cross sections are one or two order of magnitudes bigger than NO's. Therefore, the obtained structures are a promising platform for developing compact and reliable spectroscopic gas sensing.

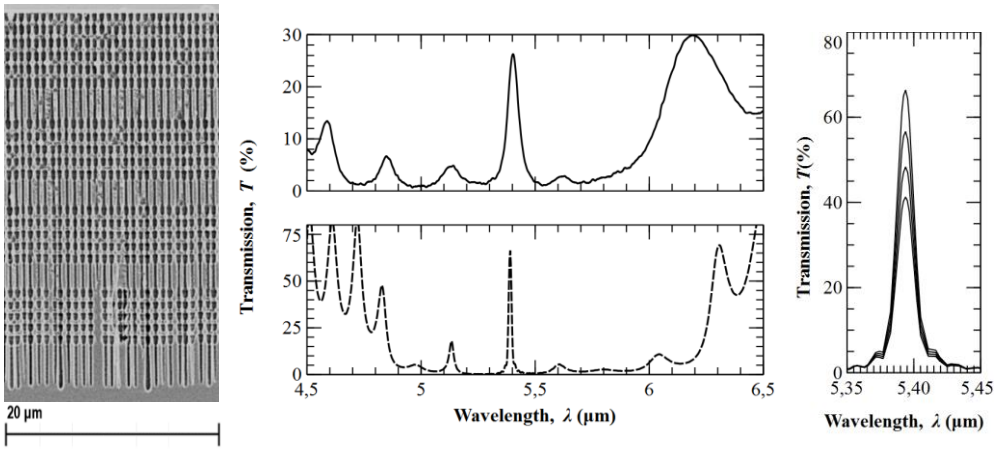

Figure 5.4.7. Left: SEM image of a PC with three cavities in the chirped configuration. Center: comparison between experimental (up) and the simulated results (bottom). Right: peak's transmission decreases as we increase the concentration in steps of 1000 ppm, from 0 ppm to 3000 ppm.

5.4.4 Conclusions

To conclude, we have reported a novel way of enhancing the features of macroporous silicon optical filters by means of photonic molecules. In particular, it is shown both, experimentally and theoretically, that the introduction of new cavities leads to an enlargement of the bandgap, to a considerable reduction of the noise inside it and to an increasing in the quality factor of the peaks associated to the resonant cavities.

We have also demonstrated that one or two of these peaks can be reduced –and, thus, the bandgap enlarged almost twice with respect to the initial case– by redesigning the photonic crystal structure using a chirped modulation and reducing the cavities' length. Furthermore, we have shown that by performing a membrane, the transmission of the remaining peak reaches almost a 30 %, driving it to a quality factor of Q = 175. Being both of them the highest values reported for macroporous silicon structures, as far as we know. Finally, a theoretical approach to gas detection has shown that the fabricated PCs are suitable for spectroscopic gas sensing.

5.4.5 Funding

Spanish Ministerio de Economía y Competitividad (MINECO) (TEC-2013-48-147-C6-2).

5.4.6 References

[1] M. Bayer *et al.*, "Optical Modes in Photonic Molecules," *Phys. Rev. Lett.*, vol. 81, no. 12, pp. 2582–2585, Sep. 1998.

[2] Y. P. Rakovich and J. F. Donegan, "Photonic atoms and molecules," *Laser Photon. Rev.*, vol. 4, no. 2, pp. 179–191, Jun. 2009.

[3] K. J. Vahala, "Optical microcavities," *Nature*, vol. 424, no. 6950, pp. 839–846, Aug. 2003.

[4] F. Vollmer and L. Yang, "Label-free detection with high-Q microcavities: a review of biosensing mechanisms for integrated devices.," *Nanophotonics*, vol. 1, no. 3–4, pp. 267–291, Dec. 2012.

[5] V. M. N. Passaro, B. Troia, M. La Notte, and F. De Leonardis, "Photonic resonant microcavities for chemical and biochemical sensing," *RSC Adv.*, vol. 3, no. 1, pp. 25–44, Nov. 2013.

[6] S. Chakravarty *et al.*, "Review of design principles of 2D photonic crystal microcavity biosensors in silicon and their applications," *Front. Optoelectron.*, vol. 9, no. 2, pp. 206–224, Jun. 2016.

[7] H. Rong *et al.*, "Low-threshold continuous-wave Raman silicon laser," *Nat. Photonics*, vol. 1, no. 4, pp. 232–237, Apr. 2007.

[8] Y. Takahashi, Y. Inui, M. Chihara, T. Asano, R. Terawaki, and S. Noda, "A micrometre-scale Raman silicon laser with a microwatt threshold," *Nature*, vol. 498, no. 7455, pp. 470–474, Jun. 2013.

[9] X.-F. Jiang, C.-L. Zou, L. Wang, Q. Gong, and Y.-F. Xiao, "Whispering-gallery microcavities with unidirectional laser emission," *Laser Photon. Rev.*, vol. 10, no. 1, pp. 40–61, Jan. 2016.

[10] A. Melloni, F. Morichetti, and M. Martinelli, "Linear and nonlinear pulse propagation in coupled resonator slow-wave optical structures," *Opt. Quantum Electron.*, vol. 35, no. 4/5, pp. 365–379, Mar. 2003.

[11] F. Xia, L. Sekaric, and Y. Vlasov, "Ultracompact optical buffers on a silicon chip," *Nat. Photonics*, vol. 1, no. 1, pp. 65–71, Jan. 2007.

[12] N. Caselli *et al.*, "Tailoring the Photon Hopping by Nearest-Neighbor and Next-Nearest-Neighbor Interaction in Photonic Arrays," *ACS Photonics*, vol. 2, no. 5, pp. 565–571, May 2015.

[13] Y. Zhao, C. Qian, K. Qiu, Y. Gao, and X. Xu, "Ultrafast optical switching using photonic molecules in photonic crystal waveguides," *Opt. Express*, vol. 23, no. 7, p. 9211, Apr. 2015.

[14] X. Zhang, S. Chakravarty, C.-J. Chung, Z. Pan, H. Yan, and R. T. Chen, "Ultra-compact and wide-spectrum-range thermo-optic switch based on silicon coupled photonic crystal microcavities," *Appl. Phys. Lett.*, vol. 107, no. 22, p. 221104, Nov. 2015.

[15] S. Bose, D. G. Angelakis, and D. Burgarth, "Transfer of a Polaritonic Qubit through a Coupled Cavity Array," Apr. 2007.

[16] J. Cho, D. G. Angelakis, and S. Bose, "Heralded generation of entanglement with coupled cavities," *Phys. Rev. A*, vol. 78, no. 2, p. 022323, Aug. 2008.

[17] H. Du, X. Zhang, G. Chen, J. Deng, F. S. Chau, and G. Zhou, "Precise control of coupling strength in photonic molecules over a wide range using nanoelectromechanical systems," *Sci. Rep.*, vol. 6, no. 1, p. 24766, Jul. 2016.

[18] T. Siegle *et al.*, "Photonic molecules with a tunable inter-cavity gap," *Light Sci. Appl.*, vol. 6, no. 3, p. e16224, Sep. 2016.

[19] S. V. Boriskina, "Theoretical prediction of a dramatic Q-factor enhancement and

degeneracy removal of whispering gallery modes in symmetrical photonic molecules," *Opt. Lett.*, vol. 31, no. 3, p. 338, Feb. 2006.
[20] M. Benyoucef, J.-B. Shim, J. Wiersig, and O. G. Schmidt, "Quality-factor enhancement of supermodes in coupled microdisks," *Opt. Lett.*, vol. 36, no. 8, p. 1317, Apr. 2011.
[21] H. Xu, P. Wu, C. Zhu, A. Elbaz, and Z. Z. Gu, "Photonic crystal for gas sensing," *J. Mater. Chem. C*, vol. 1, no. 38, pp. 6087–6098, Sep. 2013.
[22] D. Cardador, D. Vega, D. Segura, T. Trifonov, and A. Rodríguez, "Enhanced geometries of macroporous silicon photonic crystals for optical gas sensing applications," *Photonics Nanostructures - Fundam. Appl.*, vol. 25, pp. 46–51, Jul. 2017.
[23] J. Hodgkinson and R. P. Tatam, "Optical gas sensing: a review," *Meas. Sci. Technol.*, vol. 24, no. 1, p. 012004, Jan. 2013.
[24] S. Lan, S. Nishikawa, Y. Sugimoto, N. Ikeda, K. Asakawa, and H. Ishikawa, "Analysis of defect coupling in one- and two-dimensional photonic crystals," *Phys. Rev. B*, vol. 65, no. 16, p. 165208, Apr. 2002.
[25] D. Cardador, D. Segura, D. Vega, and A. Rodriguez, "Coupling defects in macroporous silicon photonic crystals," in *2017 Spanish Conference on Electron Devices (CDE)*, 2017, pp. 1–3.
[26] B. J. Frey, D. B. Leviton, and T. J. Madison, "Temperature-dependent refractive index of silicon and germanium," in *SPIE Astronomical Telescopes + Instrumentation*, 2006, pp. 62732J-62732J–10.
[27] D. Vega, D. Cardador, M. Garín, T. Trifonov, and Á. Rodríguez, "The Effect of Absorption Losses on the Optical Behaviour of Macroporous Silicon Photonic Crystal Selective Filters," *J. Light. Technol. Vol. 34, Issue 4, pp. 1281-1287*, vol. 34, no. 4, pp. 1281–1287, Feb. 2016.
[28] A. GOLDMAN *et al.*, "NITRIC OXIDE LINE PARAMETERS: REVIEW OF 1996 HITRAN UPDATE AND NEW RESULTS," *J. Quant. Spectrosc. Radiat. Transf.*, vol. 60, no. 5, pp. 825–838, Nov. 1998.
[29] J. M. Parnis and K. B. Oldham, "Beyond the Beer–Lambert law: The dependence of absorbance on time in photochemistry," *J. Photochem. Photobiol. A Chem.*, vol. 267, pp. 6–10, Sep. 2013.
[30] M. Bayindir, B. Temelkuran, and E. Ozbay, "Tight-Binding Description of the Coupled Defect Modes in Three-Dimensional Photonic Crystals," *Phys. Rev. Lett.*, vol. 84, no. 10, pp. 2140–2143, Mar. 2000.
[31] M. Bayindir, C. Kural, and E. Ozbay, "Coupled optical microcavities in one-dimensional photonic bandgap structures," *J. Opt. A Pure Appl. Opt.*, vol. 3, no. 6, pp. S184–S189, Nov. 2001.
[32] T. D. Happ *et al.*, "Coupling of point-defect microcavities in two-dimensional photonic-crystal slabs," *J. Opt. Soc. Am. B*, vol. 20, no. 2, p. 373, Feb. 2003.
[33] L. Xu-Sheng, C. Xiong-Wen, and L. Sheng, "Investigation and Modification of Coupling of Photonic Crystal Defects," *Chinese Phys. Lett.*, vol. 22, no. 7, pp. 1698–1701, Jul. 2005.
[34] P. Törmä and W. L. Barnes, "Strong coupling between surface plasmon polaritons and emitters: a review," *Reports Prog. Phys.*, vol. 78, no. 1, p. 013901, Jan. 2015.
[35] S. R.-K. Rodriguez, "Classical and quantum distinctions between weak and strong coupling," *Eur. J. Phys.*, vol. 37, no. 2, p. 025802, Mar. 2016.
[36] M. Maksimovic, M. Hammer, and E. van Groesen, "Coupled optical defect microcavities in 1D photonic crystals and quasi-normal modes," in *Proceedings of SPIE*, 2008, p. 689603.

[37] A. Majumdar, A. Rundquist, M. Bajcsy, and J. Vučković, “Cavity quantum electrodynamics with a single quantum dot coupled to a photonic molecule,” *Phys. Rev. B*, vol. 86, no. 4, p. 045315, Jul. 2012.
[38] D. Cardador, D. Vega, D. Segura, and A. Rodríguez, “Study of resonant modes in a 700nm pitch macroporous silicon photonic crystal,” *Infrared Phys. Technol.*, vol. 80, pp. 6–10, Jan. 2017.
[39] S. Matthias, R. Hillebrand, F. Müller, and U. Gösele, “Macroporous silicon: Homogeneity investigations and fabrication tolerances of a simple cubic three-dimensional photonic crystal,” *J. Appl. Phys.*, vol. 99, no. 11, p. 113102, Jun. 2006.
[40] D. Segura, D. Vega, D. Cardador, and A. Rodriguez, “Effect of fabrication tolerances in macroporous silicon photonic crystals,” *Sensors Actuators, A Phys.*, vol. 264, 2017.
[41] J. Hodgkinson, R. Smith, W. O. Ho, J. R. Saffell, and R. P. Tatam, “Non-dispersive infra-red (NDIR) measurement of carbon dioxide at 4.2μm in a compact and optically efficient sensor,” *Sensors Actuators B Chem.*, vol. 186, pp. 580–588, Sep. 2013.
[42] D. M. Beggs, “Computational studies of one and two-dimensional photonic microstructures,” University of Durham, 2006.
[43] S. V. Boriskina, “Photonic Molecules and Spectral Engineering,” Springer, Boston, MA, 2010, pp. 393–421.
[44] K. Staliunas and V. J. Sánchez-Morcillo, “Spatial filtering of light by chirped photonic crystals,” *Phys. Rev. A*, vol. 79, no. 5, p. 053807, May 2009.

5.5

2017 Spanish Conference on Electron Devices (CDE), pp. 1-3, (2017)

https://doi.org/10.1109/CDE.2017.7905236

Date of conference: 8-10 February 2017

Coupling Defects in Macroporous Silicon Photonic Crystals

D. Cardador*, D. Vega, D. Segura and A. Rodríguez

Micro i Nanotecnologies, Departament d'Enginyeria Electrònica, Universitat Politècnica de Catalunya, C/Jordi Girona, 31, 08031, Barcelona, Spain

Abstract: in this study we compare the optical response of macroporous silicon photonic crystals with several cavities inside their structure respect to the obtained in the single cavity case. We show that there are as much raising peaks in the transmission spectrum as number of cavities are inserted in the middle of the structure. Even more, this study reports the enhancement in the peaks' features –e.g. base closer to the zero transmission line and better quality factor- as the number of defects increases. This enhanced characteristic can be used to realize spectroscopic gas sensing, since the resulting peaks are narrow enough to be placed inside the absorption spectra of a target gas.

We also show that a chirped modulation has to be implemented in order to filter all peaks except the one that is going to be used to sense the gas. Furthermore, in the case of two-cavity we propose to use both peaks for differential instant measurements; one of the peaks has to be placed in the absorption spectra of the studied gas and the other, outside from the absorption band, may act as instant reference.

These improved structures should also be probed as thermal emitters.

5.5.1 Introduction

Photonic Crystals (PhCs) are used in several applications such as optical communication or gas sensing, working as optical resonators, thermal emitters, tunable filters or waveguides, among others [1].

Silicon is one of the most used materials for developing PhCs. In this study we focus on macroporous silicon (mp-Si), a versatile and inexpensive material that can be successfully fabricated through the so-called *electrochemical etching* (EE). Pores of different shapes can be produced by this technique, such as the ones depicted in Figure 5.5.1 and Figure 5.5.2. As reported in previous studies, the creation of a cavity between modulated zones propitiate resonant states that propagate along the photonic bandgap [2]. These resonant frequencies are depicted by a peak in the transmission spectrum and can be used to know the presence of gases. In effect, if the peak is properly disposed in the absorption band of the target gas, the reduction of its area will be related to the presence of the gas. However, this has an important handicap: depending on the external conditions, the features of the peak can be modified significantly. Classical photonic crystals theory indicates that if several peaks are introduced in the PhC, the same number of peaks will arise inside the photonic bandgap. Using this principle, we report in a macroporous silicon structure the coupling of two different peaks, one in the desired gas wavelength and the other outside of it (see Figure 5.5.3). The purpose of it is to use the one outside as a reference. Studying the variation of this reference peak at the external conditions respect to its response under standard conditions, we can infer the variation that the peak inside the absorption band should have. Once corrected the uncertainty due to the external conditions, we should be able to accurately determine the concentration of the gas.

Previous studies reported in macroporous silicon that chirped modulations entail bandgap enlargement [3]. In this paper we use this fact to reduce substantially the amplitude of the reference peak and for broadening the whole bandgap. Even more, if additional defects are introduced, the transmission percentage is preserved while the quality factor of the peak is increased thanks to be exposed to more periods. Otherwise, if no defects are introduced and only more periods are added to the structure, the amplitude of the peak is reduced as well as its Q-factor. The enlargement of the bandgap achieved by using the chirped modulation is almost twice the obtained in the one cavity case. Even more, with this chirped modulation, the base of the peak is closer to the zero transmission line (see Figure 5.5.4). These improved features suggest us that the fabricated samples can be used for thermal emission purposes.

5.5.2 Fabrication

The 3D macroporous silicon structures were made by EE technique, as first described by Lehmann and Föll [4]. Before the attack, an ion implantation was done in the backside of an n-type ⟨1 0 0⟩ silicon wafer with a 0.1-0.3 Ω·cm resistivity ($\sim 3 \cdot 10^{16}$/ cm^3 phosporous-doped) to provide a low-resistance transparent ohmic contact. Next, the wafer was oxidized and a lithography of 700 nm pitch was performed. A Reactive-ion Etching (RIE) and a tetramethylammonium hydroxide (TMAH) etching were done to create inverted pyramid-shaped pits that will act as nucleation centers for the ordered pore growth. Next, the EE etching was done to control the modulation of pore diameter which, in its turn, is regulated by the applied etching current. This method allows to design the profile beforehand and to create smooth 3D structures of great complexity. In particular, the periodical profile attached in Figure 5.5.1 has been generated. The depth periodicity

was set to be about 1.1-1.2. As depicted in the SEM figures, planar defects were introduced between the modulations areas by suppressing one of the modulations and leaving a constant diameter section. The length of the cavity varied from 2.1 μm to 2.6 μm with a width value of 0.23 μm in all the samples.

The optical response of the fabricated samples was measured in the MIR range using a Bruker Optic's Vertex FT-IR spectrometer. The lattice was aligned to the Γ – *M* direction (along one lattice axis in the surface) and an aperture of 1 mm and a resolution of 4 cm^{-1} was used. The measurements have been referred to the source spectrum to normalize the results in both, reflectance and transmittance.

5.5.3 Results and discussion

The regular structure for the mp-Si photonic crystals fabricated in the laboratory is depicted in Figure 5.5.1. As it can be observed, a single cavity is inserted in the middle of the PhC, what rises a peak in the transmission response (see Figure 5.5.3, dashed line).

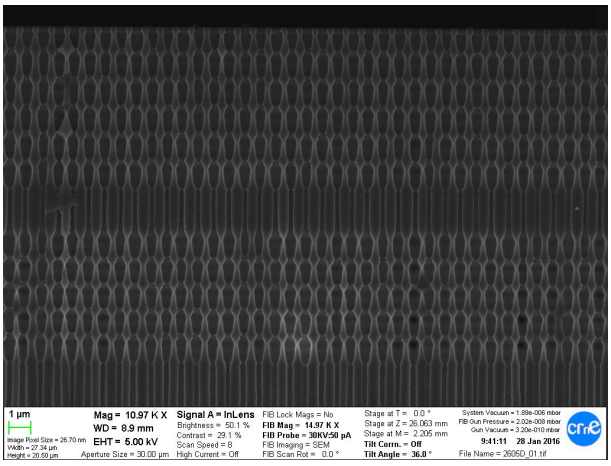

Figure 5.5.1. Cross sectional view of a 3-D PC fabricated by EE over a lithography of 0.7 μm pitch. The inclusion of a cavity in the PC lattice enables a transmitted mode close

The quality factor of the peak, defined as the ratio of the peak amplitude to its full half maximum (FWHM): f_c/ FWHM, is about Q = 30, a value too low to be used in spectroscopic gas sensing. In order to increase it, a second defect and a new modulation zone is introduced, as shown in Figure 5.5.2. Both cavities have similar length, what leads to a coupling of light between them.

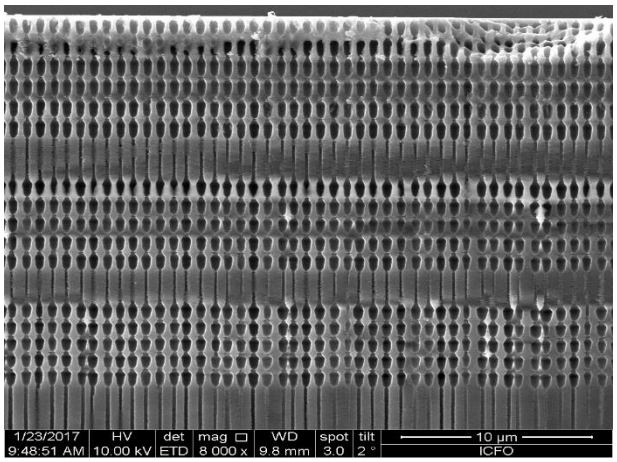

Figure 5.5.2. Cross sectional view of a 3-D PC with two cavities inserted in the structure. The chirped modulation can be observed: higher periods are longer than lower periods.

As reported in literature, the peak obtained for a single cavity is now split in two new peaks with similar transmission and better Q-factor [5], [6]. In particular, the Q-factor of the best peak is about Q = 80, what represents an increment of about a factor 3 respect to the case with a single cavity. One application of the optical response of this new structure is placing one of those peaks in the absorption spectra of the target gas and the other, outside from it, as a reference peak. This point still has to be studied, but our suggestion is that it can be used to make differential measurements in real time.

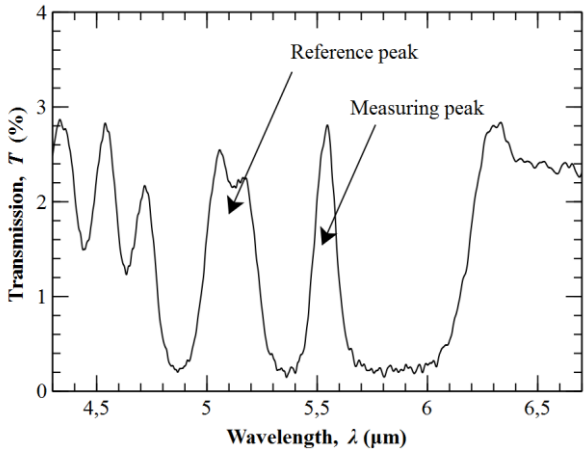

Figure 5.5.3. Transmision spectra for a MpS PC with two cavities. The Measuring peak should be at the absorption region of the target gas and the reference peak should be outside from it.

However, if only a peak is desired, a chirped modulation –e.g. a linear reduction of the periods involved in the structure- can be used in order to filter one of the peaks. Even more, combining a third cavity and an appropriated chirped modulation it is possible to obtain a single peak with high Q-factor –around Q=180- along the bandgap (see Figure 5.5.3). Another consequence is that, thanks to the higher number of periods, the base of the peak is closer to the zero transmission line than in the single cavity case (see Figure 5.5.4), improving the features as selective filter.

The optical response of these reported structures suggest us that the fabricated samples can be used for spectroscopic gas sensing purposes, using them either as selective filters or thermal emitters.

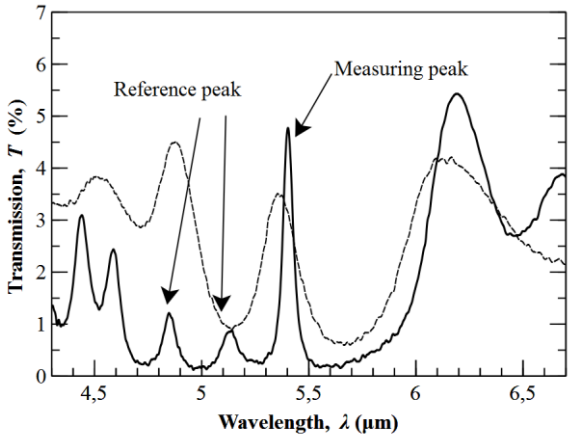

Figure 5.5.4. Transmision spectra for a MpS PC with three cavities (solid line) and one cavity (dotted line). The reference peak of Figure 5.5.3 is filtered by the chirp modulation.

5.5.4 Conclusions

In this study we report the optical response of macroporous silicon photonic crystals with one, two and three cavities. We observe that adding cavities increase the initial value of the Q-factor for a single defect, 20<Q<30, up to 150<Q<200 if three cavities are inserted inside the structure. The features observed for two and three defects are good enough to sense gases using the spectroscopic method. In concrete, in the case of two peaks in the transmission spectrum, we suggest to use one of them for sensing the target gas and the other, outside of the absorption band, as a reference. This would allow to do accurate differentail measurements. However, if only one peak is desired inside the bandgap to sense the gas, we report that a chirped modulation has to be performed in order to filter the rest of the unwanted peaks both in the case of two or three cavities. As a consecuence of implementing this new modulation, the bangap of the photonic crystal is almost twice the obtained in the single cavity case. In addition, the base line of the coupled peaks, also called offset, is very close to the non-transmission line. Both improved featrues increase the benefits as selective filter.

This improved features suggest us that fabricated samples can be also used for thermal emission purposes, since the base of the best peak is half the wavelength range of several gases, such as CO or NO.

5.5.5 Funding

This work has been founded by TEC-2013-48-147-C6-2).

5.5.6 References

[1] C. Soukoulis, “Photonic crystals and light localization in the 21st century,” 2012.
[2] S. A. Rinne, F. García-Santamaría, and P. V. Braun, “Embedded cavities and waveguides in three-dimensional silicon photonic crystals,” *Nat. Photonics*, vol. 2, no. 1, pp. 52–56, Dec. 2007.
[3] M. Garín, T. Trifonov, D. Hernández, Á. Rodriguez, and R. Alcubilla, “Thermal emission of macroporous silicon chirped photonic crystals,” *Opt. Lett.*, vol. 35, no. 20, p. 3348, Oct. 2010.
[4] V. Lehmann, “Formation Mechanism and Properties of Electrochemically Etched Trenches in n-Type Silicon,” *J. Electrochem. Soc.*, vol. 137, no. 2, p. 653, Feb. 1990.
[5] A. Reynolds and U. Peschel, “Coupled defects in photonic crystals,” *Microw. Theory …*, 2001.
[6] S. Lan, S. Nishikawa, Y. Sugimoto, and N. Ikeda, “Analysis of defect coupling in one-and two-dimensional photonic crystals,” *Phys. Rev. B*, 2002.

5.6

5th Internacional Conference on Photonics, Optics and Laser Technology

https://doi.org/10.5220/0006120101910195

Date of conference: 27 February-01 March 2017

Transmission and thermal emission in the NO_2 and CO absorption lines using macroporous silicon photonic crystals with 700 nm pitch

D. Cardador Maza, D. Segura, D. Vega and A. Rodríguez

Micro i Nanotecnologies, Departament d'Enginyeria Electrònica, Universitat Politècnica de Catalunya, C/Jordi Girona, 31, 08031, Barcelona, Spain

Abstract: Macroporous silicon photonic crystals with a cavity in the middle of their structure have been studied in both, transmission and emission. The initial transmittance of the photonic crystals was increased form 4%-6% up to the value of 25%-30% by performing a rear attach of the samples of approximately 160 µm. The use of wafers with 700 nm of pitch allowed us to fabricate the optical response of the photonic crystals in the ranges of 6.4 µm and 4.6 µm, where different gases have their absorption frequency –such as NO_2 or CO. The fabricated samples have been also heated in order to evaluate their viability to be used as selective emitters for gas sensing purposes. Results show a good agreement in the position of the respective peak compared to the transmission spectrum. However, further studies have to be done to place the base of the peak as close as possible to the 0% of emission in order to have a better selective emitter. This work is a starting point for gas detection devices using macroporous technology in the mid-infrared, which includes ammonia, formaldehyde, carbon monoxide or nitrous oxide, among others.

5.6.1 Introduction

Photonic Crystals (PC) are becoming increasingly attractive for both research and market applications. Their optical properties, obtained by creating periodical structures of different refractive index materials, are very interesting for a wide range of application areas, such as optical communications or sensing. The introduction of defects in the structure that break the periodicity confers the PC some interesting functionalities. They allow the creation of resonant states within the photonic bandgap at specific frequencies or modes [1], [2] - what can be used as waveguides [3], light couplers, optical resonators [4], thermal emitters [5] or tunable filters [6], etc.

As reported in the literature, there are several factors that affect the photonic bandgap features: the contrast between the high and the low reflective index in the PC, the morphology, the light path, etcetera [2]. In the case of introducing a defect inside the photonic crystal, it is also important to have into account its shape to predict the optical response of the structure. Several articles have dealt with this issue in 1D and 2D PCs –i.e. [7]–[9]. However, the influence of the defects morphology in the optical response of 3D photonic crystals have not been so deeply analyzed, perhaps, because of the high dependence of the method used to fabricate the PC [10], [1]. A number of different techniques have been proposed to incorporate defect structures within the PCs in woodpiles [11], synthetic opals [12], [13] or macroporous silicon [14], among others.

In this paper we focus on macroporous silicon (mp-Si), which is a versatile material that can be successfully fabricated through the so-called electrochemical etching (EE). With this technique it is possible to fabricate pores with different depth profiles -such as sinusoidal or straight- with a planar defect inside the crystal structure –see Figure 5.6.1. Previous studies reported mp-Si structures with a cavity in the middle of the PC that had a resonant wavelength around the 7 μm [14]. Nevertheless, they worked with a lattice parameter –also called pitch- of 2 μm and a vertical periodicity about 2.5 μm. This vertical periodicity is limited to the lattice parameter: when approaching to the pitch value, the vertical periodicity is more difficult to achieve and the profile is much more difficult to control by EE. Although some other studies reported modulated structures in 700 nm [15], they did not insert a cavity in their structures, probably because the profiles were not as good as the ones obtained in 2 μm of pitch. In the present study, the samples used to fabricate the macroporous silicon PCs had a pitch of 700 nm and a vertical periodicity around the lattice parameter, what enabled us to place a peak and tailor it at wavelength as short as 4.6 microns, were different gas absorption peaks can be found.

By removing around 160 μm of bulk silicon of the samples, we have been able to increase the transmission percentage from values around 4%-6% up to values between 25% and 30%. This improves the features of the peak –i.e. transmittance and quality factor- and, as a consequence, the sensitivity of the final gas sensor device is enhanced. Further improvement of the transmission could be achieved by removing some more bulk silicon, but the risk of damaging the photonic crystal –mechanical support or etching of the PC structure- becomes high and some silicon bulk has to be left to avoid these problems. In the case of thermal emission this layer has not an important impact in the relative transmission amplitude of the peak –from the base to the top of the resonant peak-, but it has a considerable effect in the position of the base point. Specifically, the more bulk silicon the more radiation of the no texturized region, which is finally reflected in a higher offset from the zero emission point to the base point, where the emission peak rises.

The conclusions drawn in this paper lead us to confirm that the studied macroporous silicon structures can be employed in gas sensing applications. However, further work has

to be done in order to improve the amplitude and the Q-factor of the peak, as well as to reduce the offset, either working in transmission or emission.

5.6.2 Experimental

The 3D structures were obtained by electrochemical etching of *n*-type ⟨1 0 0⟩ crystalline silicon samples in hydrofluoric (HF) acid solution. The starting material had a resistivity between 0.1-0.3 Ω·cm (~$3 \cdot 10^{16}$/cm^3 phosporous-doped). An N^+ layer was implanted on the backside of the wafer to provide a low-resistance transparent ohmic contact. Next, the wafer was oxidized and a nanoimprint lithography of 700 nm pitch was performed. A Reactive-ion Etching (RIE) and a tetramethylammonium hydroxide (TMAH) etching were done to create inverted pyramid-shaped pits that act as nucleation centers for the ordered pore growth. Finally, the EE etching was carried out to control the modulation of pore diameter which, is regulated by the applied etching current. This method allows to design the profile beforehand and to create smooth 3D structures of great complexity just by applying different etching currents.

In particular, the periodical profiles attached in Figure 5.6.1 have been generated. In the first sample (left) the depth periodicity was set to be about 1.1-1.2 μm what arouse a bandgap around [5-7] μm. As depicted in the figure, a planar defect was introduced halfway the total pore depth by suppressing one of the modulations and leaving a constant diameter section. The length of the cavity varied from 2.1 μm to 2.6 μm with a diameter of 0.23 μm in all the samples. In order to reduce the bandgap central wavelength, and thus the position of the peak, the vertical modulation of the pore was shortened. In concrete, it was set to the lattice constant value (~ 700 nm). Thanks to that, the bandgap moved to the range of [4-5] μm, while the defect's length took values in the range of [1.5-1.8] μm. The total depth of all samples was about 12-15 micrometers. A complete description of the process can be found elsewhere [16]. The second fabricated structure can be observed in the right image.

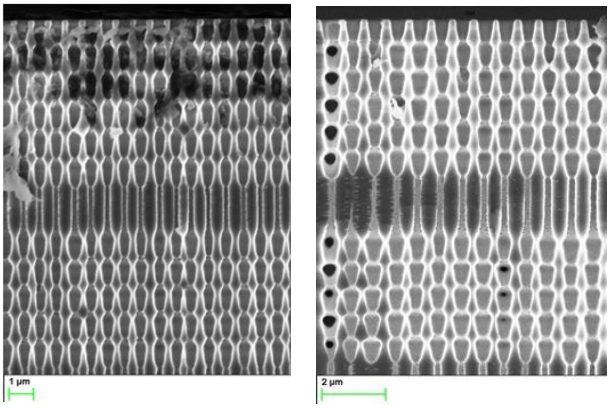

Figure 5.6.1. Cross sectional view of two 3-D PCs fabricated by EE over a lithography of 0.7 μm pitch. The inclusion of a defect in the PC lattice enables a transmitted mode in 6.4 μm (left) and 4.6 μm (right).

The transmitted response of the fabricated samples was measured in the MIR range using a Bruker Optic's Vertex FT-IR spectrometer. The lattice was aligned to the $\Gamma - M$ direction (along one lattice axis in the surface), an aperture of 1 mm and a resolution of 4 cm^{-1} was used for the calculation of the spectrum. The measurements have been referred to the source spectrum to normalize the results.

The emissivity was experimentally measured using the A540 emission adapter of the FT-IR spectrometer. This commercial setup allows normal thermal emission measurement,

with a beam opening angle of ±7,5°, from room temperature up to 400 °C. In this setup, the sample is clamped vertically to a metallic surface that is at a constant temperature. After thermalization, the sample is at a constant and homogeneous temperature very close to the temperature of the heater, since c-Si is an excellent thermal conductor. In our case, the samples were heated at the highest possible temperature in order to obtain the maximum power of the emitter. Finally, the emissivity values are obtained after conducting a standard calibration with a piece of polished Si as reference.

5.6.3 Results and discussions

The two fabricated samples of the Figure 5.6.1 are characterized in the FT-IR. In the Figure 5.6.2 the sample's transmission spectrum is shown. As depicted in it, there is a high enhancement in the transmission due to the reduction of, approximately, 160 µm of bulk silicon from the back side of the wafer. In particular, the transmission percentage rises from the value of 6% up to 29%. Previous studies reported maximal transmission peaks of almost 50% using mp-Si structures. Nonetheless, their peaks were placed out of the mid-infrared range –following the same convention as in [17]- in concrete at 20 µm, far from the interesting gas sensing mid infrared frequencies.

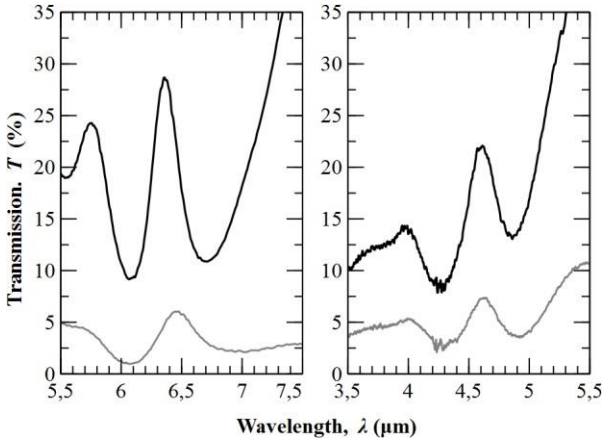

Figure 5.6.2. Transmittance of the samples before (grey) and after (black) the TMAH attack for removing part of the bulk silicon of the wafer. The different wavelength range are achieved by controlling the vertically periodicity. Left image corresponds to the image plotted in Figure 5.6.1(a) and the right image to the Figure 5.6.1(b).

The values presented in this work are the best ones reported in the mid-infrared, as far as our research reached, in 3D mp-Si structures. Moreover, the use of samples with 700 nm of pitch made possible to reduce the vertical modulation and adjust its periodicity close to the lattice constant. This entailed a proportional translation of the entire spectrum towards lower frequencies. An appropriated dimensioning of the defect's length and width lead us to correctly place a resonant mode inside the bandgap. Consequently, we were able to reproduce the transmittance figure around 4.6 µm, where the CO has its absorption lines – see Figure 5.6.2.

As explained in the introduction, below the PC there is some remaining bulk silicon. This silicon reduces the amount of ideally transmitted light, which in simulations –without any bulk silicon- can be around 60%. However, the reduction of more silicon presents some problems. The first of them is the risk of damaging the PC structure after some hours of TMAH attack. The second one is that if the attacked surface is big, some mechanical stress can appear, completely breaking the surface as a consequence.

One interesting fact is that by removing some bulk silicon the quality factor of the peak is also enhanced, improving the performance of a future gas sensor. Nevertheless, the transmission inside the band gap is also increased what, in turn, will result in less sensitivity in a gas sensor. Some research should be carried out to reduce the transmission inside the band gap for obtaining good gas sensors.

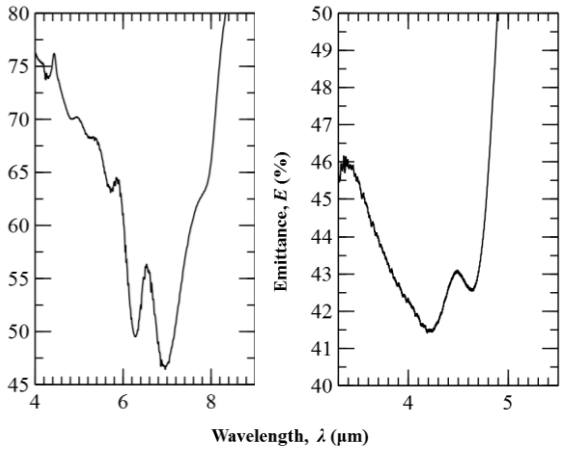

Figure 5.6.3. Experimental emission spectra for the samples depicted in Figure 5.6.1 (they are conveniently depicted. E.g.: left image in Figure 5.6.1 corresponds to the left image in Figure 5.6.3). Both samples were heated at 400 ºC.

In the right image of the Figure 5.6.2, it can be seen the trademark of the CO_2 absorption lines at a 4.25 μm wavelength. These marks correspond to variations of gas concentrations referred to the background case. If the peak is positioned on the absorption lines of a target gas, the concentration of it can be determined by comparing the area of the peak before and after the gas exposure. Even more, despite using the PC for filtering the light coming from the emitter, the sample can be heated in order to have an emission peak at the desired wavelengths. This would allow replacing the optical emitter for a selective thermal emitter, emitting in a smaller range of wavelengths, and thus, simplifying the configuration for sensing gases, probably without the need of an optical filter.

The lowered samples were used to evaluate their thermal emission in the two studied wavelengths –see Figure 5.6.3- when the samples are heated at 400ºC. The peaks are placed around 6.5 μm and 4.5 μm, in good accordance with the position of the peak in transmission. If observed insightfully a peak broadening of about 100 nm can be seen in both cases. A reduction of their respective amplitudes, compared to their transmission spectrum, is also noticeable, particularly at 4.5 μm. During the study we have verified that there are some variations in the pore's morphology due to the expansion of the silicon with the heating of the sample, which affects the optical response of the peak; these experimental variations, although they are of a few tens of nanometers, modify the local refractive index what, finally, impacts in the position and the amplitude of the peak.

Another remarkable point is that the peaks do not start at zero position; they have their beginning at the emissivity of 40%-45%. Probably part of this offset is due to the remaining bulk silicon in the bottom of the photonic crystal, which also radiates in the frequencies of the peak, reducing the performance of the samples as selective thermal emitters.

Further studies should deal with this issue in order to obtain good selective emitters that propagate a range of frequencies along its bandgap.

5.6.4 Conclusions

Macroporous silicon photonic crystals with a defect inserted in the middle of the structure have been studied. The initial transmittance of these structures is between the 4% and the 6%. Performing a rear attach of the sample –approximately 160 μm-, the transmission percentage increases to the value of 25%-30%.

The use of samples with 700 nm of pitch allows to work with sub micrometre vertical periods. Thanks to this, peaks at lower resonant frequencies can be placed, in concrete, we have fabricated two of them: at 6.4 μm and 4.6 μm, what can be used to sense different gases that have their absorption frequency in ranges close to that values –such as NO2 or CO.

Both peaks been heated at room temperature of 400 ºC in order to obtain a selective emitter. Results show a good agreement in the position of the peak compared to the position in the transmission spectrum. The little differences are attributable to the variations in the shape of the pores given by the expansion of the silicon due to higher temperatures. Further studies have to be done to place the base of the peak as close as possible to the 0% of emission in order to have a real selective emitter.

This work is a starting point for gas detection devices using macroporous technology in the mid-infrared, which includes ammonia, formaldehyde, carbon monoxide or nitrous oxide, among others.

5.6.5 Acknowledgements

This work has been founded by TEC-2013-48-147-C6-2-R.

5.6.6 References

[1] P. V. Braun, S. A. Rinne, and F. García-Santamaría, “Introducing Defects in 3D Photonic Crystals: State of the Art,” *Adv. Mater.*, vol. 18, no. 20, pp. 2665–2678, Oct. 2006.

[2] J. D. Joannopoulos, S. G. Johnson, J. N. Winn, and R. D. Meade, *Photonic Crystals: Molding the Flow of Light (Second Edition)*. 2011.

[3] S. A. Rinne, F. García-Santamaría, and P. V. Braun, “Embedded cavities and waveguides in three-dimensional silicon photonic crystals,” *Nat. Photonics*, vol. 2, no. 1, pp. 52–56, Dec. 2007.

[4] M. Youcef Mahmoud, G. Bassou, A. Taalbi, and Z. M. Chekroun, “Optical channel drop filters based on photonic crystal ring resonators,” *Opt. Commun.*, vol. 285, no. 3, pp. 368–372, Feb. 2012.

[5] B. Gesemann, S. L. Schweizer, and R. B. Wehrspohn, “Thermal emission properties of 2D and 3D silicon photonic crystals,” *Photonics Nanostructures - Fundam. Appl.*, vol. 8, no. 2, pp. 107–111, May 2010.

[6] N. Neumann, M. Ebermann, S. Kurth, and K. Hiller, “Tunable infrared detector with integrated micromachined Fabry-Perot filter,” *J. Micro/Nanolithography, MEMS MOEMS*, vol. 7, no. 2, p. 021004, 2008.

[7] I. Alvarado-Rodriguez, “Fabrication of two-dimensional photonic crystal single-defect cavities and their characterization by elastic scattering,” *A Diss. Dr. Philos. Electr. …*, 2003.

[8] X. Xiao *et al.*, “Investigation of defect modes with Al2O3 and TiO2 in one-dimensional photonic crystals,” *Opt. - Int. J. Light Electron Opt.*, vol. 127, no. 1, pp. 135–138, Jan. 2016.
[9] M. Mohebbi, “Refractive index sensing of gases based on a one-dimensional photonic crystal nanocavity,” *J. Sensors Sens. Syst.*, 2015.
[10] E. Nelson, “Three-dimensional photonic crystal optoelectronics,” 2011.
[11] M. Taverne, Y. Ho, and J. Rarity, “Investigation of defect cavities formed in three- dimensional woodpile photonic crystals,” *JOSA B*, 2015.
[12] P. Massé, S. Reculusa, K. Clays, and S. Ravaine, “Tailoring planar defect in three- dimensional colloidal crystals,” *Chem. Phys. Lett.*, vol. 422, no. 1–3, pp. 251–255, Apr. 2006.
[13] E. Palacios-Lidón, J. F. Galisteo-López, B. H. Juárez, and C. López, “Engineered Planar Defects Embedded in Opals,” *Adv. Mater.*, vol. 16, no. 4, pp. 341–345, Feb. 2004.
[14] G. Mertens, R. B. Wehrspohn, H.-S. Kitzerow, S. Matthias, C. Jamois, and U. Gösele, “Tunable defect mode in a three-dimensional photonic crystal,” *Appl. Phys. Lett.*, vol. 87, no. 24, p. 241108, Dec. 2005.
[15] A. Langner, “Fabrication and characterization of macroporous silicon,” *Doktorarbeit, Martin-Luther-Universität*, 2008.
[16] V. Lehmann, “The Physics of Macropore Formation in Low Doped n-Type Silicon,” *J. Electrochem. Soc.*, vol. 140, no. 10, p. 2836, Oct. 1993.
[17] J. Byrnes, “Unexploded ordnance detection and mitigation,” 2008.

5.7

Journal of The Electrochemical Society, ***166*** *(12) B1010-B1015 (2019)*
https://doi.org/10.1149/2.1051912jes
Received: 26 April 2019; **Revised**: 18 June 2019; **Accepted**: 16 July 2019; **Available online**: 23 July 2019

Macroporous Silicon Filters, a Versatile Platform for NDIR Spectroscopic Gas Sensing in the MIR

David Cardador Maza, [1,*] Daniel Segura Garcia,[1] Ioannis Deriziotis,[1] Angel Rodriguez,[1] and Jordi Llorca[2]

[1]*Micro i Nanotecnologies, Departament d'Enginyeria Electrònica, Universitat Politècnica de Catalunya, 08031 Barcelona, Spain*

[2]*Barcelona Research Center in Multiscale Science and Engineering, Universitat Politècnica de Catalunya, 08019, Barcelona, Spain*

Abstract: This paper describes the spectroscopic detection of gases using macroporous silicon photonic crystals as narrow filters. The study begins by demonstrating the feasibility of photoelectrochemical etching to fabricate narrow filters along the mid infrared band. Next, we focus on the filter centered on the carbon dioxide fingerprint. The filter response is described for three different cell lengths and concentrations below 1%. Results show a concordance with the reformulated Beer-Lambert law. This can be used to predict the response of the filter for longer path lengths and higher concentrations, showing broad working ranges and compact sizes for CO_2. In addition, optical robustness to external variations and long-term stability are also reported. Results are extrapolated to other macroporous silicon filters centered on the absorption spectra of N_2O, OCS, NO_2 and SO_2. Finally, high sensitivity and selectivity is demonstrated by comparing them with some commercial filters.

5.7.1 Introduction

Over the past few years, a number of detection systems based on different physical principles have proved their efficiency in gas sensing. Those that are less expensive and, therefore, have a greater projection in the market, are chemical sensors, in which some property of its active area varies accordingly to the amount of gas in the environment. However, despite the economic advantage, the improvement of cross sensitivity, selectivity, stability and response time still remains a challenge for them [1], [2]. An alternative are optical gas sensors, which solve many of those limitations. Within this group, laser-based gas detectors have the best performance since they work with monochromatic sources. This allows them to point to a specific gas absorption line and determine its concentration by comparing the received signal, that has traveled through a gas chamber, with the one emitted, as established by Beer-Lambert Law [3]. Thus, these kind of sensors are extremely selective and sensitive. The counterpart is that small variations in temperature or pressure can cause a slight shift in the emission frequency, leading to very significant errors in detection. That is why they require complex thermal control systems and computer supports to accurately target the chosen absorption line [4]. Consequently, laser-based gas sensors are non-portable high-cost devices whose applications are mainly restricted to industrial and academic environments.

Among the most commercial optical sensors are those based on Non Dispersive Infrared detection (NDIR). They are low cost, have low energy consumption, and, especially for CO2, provide high sensitivity –in the range of tens to hundreds parts per million (ppm) for a few cm of path length–. Their operation principle is similar to that in laser-based spectroscopy. But, instead of emitting a monochromatic light, NDIR sensors use broadband sources that are wider than the absorption spectrum of the target gas. This entails two main drawbacks: possible interferences between gases and considerably lower sensitivities with respect to laser-based spectroscopy [5]. The problem with interferences in NDIR devices is that they cannot distinguish between two or more gases whose spectra fall within the emission window. This disadvantage can be partially solved by placing optical filters that reduce the detection window to the range of the gas to be studied [6]. In this case, the received intensity in the detector follows the equation,

$$I = I_0 \int E_S(\lambda) T_A(\lambda) e^{\alpha(\lambda) l} \mathrm{d}\lambda \quad (1)$$

where ES is the emission envelope of the source, TA is the transmission of the filter, α the absorption coefficient in cm-1 and l is the path length in cm [169].

The second drawback, concerning the sensitivity, is also related to the fact that NDIR devices emit with sources whose spectra are wider than the absorption range of the gas. Consequently, there is always part of the signal that reaches the detector without interacting with the gas molecules. Again, the solution is to use filters to block all frequencies, except those centered on the gas. Therefore, improving the sensitivity and the limit of detection of the device.

Recently, one-dimensional narrow filters based on photonic crystal cavities [8]–[10] or crystalline coatings [11], were proposed for gas detection in the MIR and THz bands. However, although the reported devices show good performances, the experimental realization of these theoretical approaches still remains a challenge. Other 1D narrow filters based on photonic crystals were successfully commercialized for gas sensing purposes, among others [12]–[14]. They consist on a multilayer structure deposited by sputtering that exhibit bandpass regions located in the absorption range of the target gas. However, although they present high transmission values and very broad forbidden bands, they have

low quality factors. Which, at the end, has a negative impact in the reduction of sensitivity and selectivity of the devices.

In 2011, Pergande et al. reported a pioneer work with macroporous silicon PhCs developing a new technique for gas measurement [15]. They used the fact that, at the edges of the bandgap, the group velocity is substantially reduced due to a higher number of internal reflections. As a result, the light-matter interaction increased 60 times. However, despite being an interesting result which opened the door to gas sensing with macroporous silicon, the proposed method required a complex and costly fabrication setup as well as a monochromatic detection system. Few years later, our team reported a new approach using 3D macroporous silicon PhCs for gas detection [16]. In that case, a bandgap of about one micron was used as broadband filter. Consequently, only concentrations higher than 5% could be efficiently measured. In addition, the problem of selectivity was not solved and the measurement system, configured in reflection, was more complex than the one used here, which works in transmission.

Recent studies reported proofs of concept showing that macroporous silicon PhCs with a cavity in the middle can be used as narrow filters for the selective and sensitive detection of gases [17], [18]. The aim of this paper is to experimentally verify this point and to validate the technology in the entire mid-infrared band. The study begins by describing the optical response of several filters along the MIR –see Figure 5.7.1–. They were fabricated through photo-assisted electrochemical etching (PEC) using similar current profiles than the one shown in Figure 5.7.2a. The periodicity and the length of the cavity were adjusted in each case in order to place the filter at the desired frequency. Showing, in that way, the versatility of this single-etch process. Next, it is reported for the first time the use of macroporous silicon narrow filters for gas detection. Specifically for CO2, very important in many biological and industrial processes [19]–[21]. We prove a sensitivity improvement over conventional NDIR devices, i.e. without filter, as a result of detection in the R-branch of the carbon dioxide. In addition, we experimentally demonstrate its optical robustness under temperature and pressure variations. To corroborate the suitability of this technology in the MIR band, the obtained results have been extrapolated to other four gases of interest using an in-house software. Finally, the study focus on the selectivity of these MIR filters. We demonstrate that, due to the high quality factors of our filters –$Q > 120$–, it is possible to discriminate between two partially overlapping gases by pointing to the area where they do not overlap.

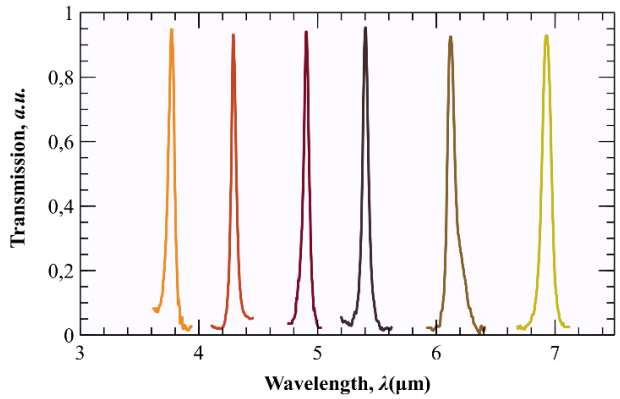

Figure 5.7.1. Fabricated macroporous silicon filters covering the mid-infrared band.

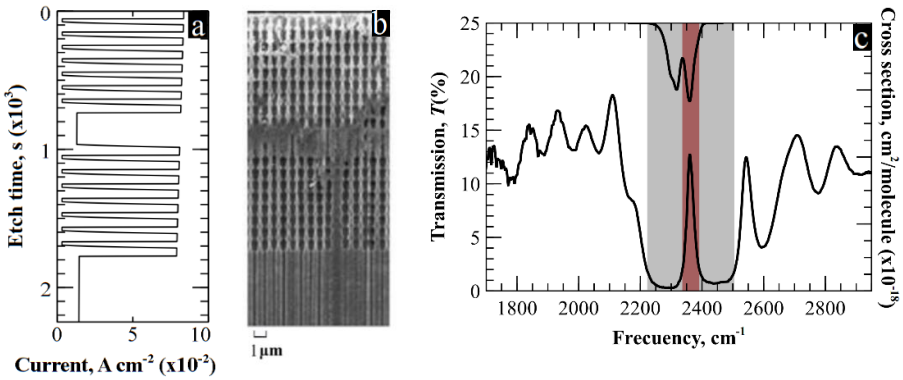

Figure 5.7.2. a) Current profile for the fabricated sample. b) SEM picture of the photonic crystal used in the measurements. c) Spectrum of the PhC –left axis– and CO_2 absorption cross section –right axis-. The framed peak, that is used for detection in the R-Branch of carbon dioxide (red), is about six times narrower than the sensing area (grey).

Conclusions of the work highlight that macroporous silicon narrow filters are a robust and long-term stable technology that can be used to reduce the problem of spectral interferences in the MIR as well as to increase the sensitivity of current optoelectronic devices. Furthermore, the authors believe that this study opens the door to the future development of low-cost, versatile and compact gas sensors using macroporous silicon technology.

5.7.2 Experimental

Fabrication of macroporous silicon narrow filters

Before photoelectrochemical etching, several pre-processes –i.e. implantation, oxidation, lithography, etc.– had to be carried out in order to prepare the samples –details can be consulted elsewhere [17], [22]–. As a result of this initial step, the front surface of the samples was pre-structured with a square array of inverted pyramids separated by a pitch of 700 nm. This was the starting point for the PEC attack. It was performed in six different samples with six different current profiles at 10ºC and with a constant polarization of 1.5 V. After the process, all samples presented the same pore morphology. That is, two modulation areas with 8 periods each, a planar defect in the middle of both, and, at the end, a region of constant radius –see Figure 5.7.2a and Figure 5.7.2b–. The only differences between samples were period length and cavity size, which ranged from 0.60 µm to 1.2 µm and from 1.2 µm to 3.0 µm, respectively. In all cases, the modulated areas were made using an asymmetrical trapezoidal current profile, in which the steepness of both ascending and descending slopes was optimized to increase the refractive index contrast of the PhCs. This improved the optical response of the filters. Particularly in the case of CO2, the quality factor of the peak was enhanced up to 120. In addition, a bandgap enlargement in respect to previous studies [23] was also reported –see Figure 5.7.2c–. This led to a greater separation between the transmitted peak and the edges of the bandgap, thereby clearly discriminating the narrow filter within the forbidden band.

Another optical improvement of the manufactured filters was the decrease of the peak base line to almost zero transmission. Despite the improvement, there was still some remaining signal, especially in the right part of the peak, which reaches approximately the 7% of the maximum transmission. Although this does not have a high impact on the

sensitivity, future works should focus on the total elimination of this transmission line to further increase the sensitivity of the proposed system.

Spectroscopic measurement of CO_2

The optical response of the macroporous silicon PhC exposed to carbon dioxide was obtained using a Bruker Optic's Vertex FT-IR spectrometer with an aperture of 1 mm and a resolution of 4 cm^{-1}. As shown schematically, in Figure 5.7.3, a gas cell with KBr windows transparent to the mid-infrared range was placed between the emitter and the receiver. In concrete, inside the sample compartment of the FT-IR. The detection process starts introducing a known concentration of carbon dioxide in the gas cell by regulating CO_2 and N_2 flowmeters. Then, a light emitted by the FT-IR source is filtered by the PhC, and afterwards, travels through the gas cell, where it interacts with the gas mixture. Finally, the FT-IR detector reads the signal and normalizes it with respect to the *background* case –i.e. the cell without carbon dioxide, only with N_2–.

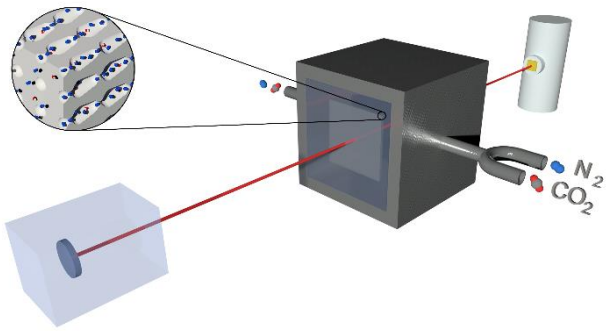

Figure 5.7.3. Schematic representation of the setup used for gas measurements; a gas chamber is in the middle of the emitter (left) and the receiver (right). Before light goes through the chamber, it is filtered by the macroporous silicon PhC. The output signal is detected and referenced to the non-CO_2 case.

We measured with three different gas cell lengths, 2.2 mm, 1.4 cm and 2.4 cm., and under the same external conditions of pressure and temperature –1.07 atm. and 23 ºC–. Measurements started at 400 ppm and increased in steps of 200 ppm to approximately 10,000 ppm. Lower steps could not be performed due to the maximum uncertainty given by the mass rotameters. Therefore, the limit of detection (LOD) was imposed by them. However, in a final device, where the concentration is the parameter to be determined, the LOD is mainly given by the resolution of the detector. As a consequence, lower LOD is expected in a final sensor.

5.7.3 Simulations

A Python code was developed to apply Equation 1 in order to compare the experimental results with the theory. The cross sections of the different gases used in this paper –CO_2, NO_2, CO, OCS, N_2O and SO_2– were obtained from HITRAN database considering the same external conditions than in measurements –1.07 atm. and 23ºC– and with the same resolution as in the FT-IR –4 cm^{-1} [24]–. As a result, cross sections, $\sigma(\lambda)$, and transmission peaks, $T(\lambda)$, were equally discretized, allowing Equation 1 to be applied at each discretized frequency for a given concentration c and a given length, l. Finally, and assuming a linear regression between points –200 frequencies were discretized between

2233 cm^{-1} and 2260 cm^{-1} –, the area of the resulting peak was calculated through the composite trapezoidal rule.

5.7.4 Results and discussion

This section is organized as follows; in subsection 4.1, experimental data are analyzed in order to model the optical response of the filter targeting the CO_2. Specifically, its response is studied when exposed to concentrations below1% –10,000 ppm– and for three cell lengths, 2.2 mm, 1.4 cm and 2.4 cm. Next, in subsections 4.2 and 4.3, the model is used to obtain the response of the filter for both higher concentrations and longer path lengths, respectively. Then, in subsection 4.4, the optical robustness of the filter is tested by changing the working temperature and pressure. In 4.5, the model obtained for CO_2 is extended to other filters pointing to four different gases in the MIR. Finally, subsection 4.6. demonstrates the selectivity of our filters compared to others.

Data analysis

Figure 5.7.4 depicts the evolution of the peak when exposed to CO_2 concentrations below 1% for three different path lengths. As expected from theory, peak reduction is more important for longer paths. As a consequence, higher sensitivities are reported for 2.4 cm than for 1.4 cm and 2.2 mm –see Figure 5.7.5–. It can be observed that in all three cases, experimental and theoretical curves follow an exponential fitting. Nevertheless, Figure 5.7.5a shows a quasi-linear relationship between the peak area and the gas concentration for the 2.2 mm case. This is in accordance with the theory since for low values of $\alpha(\lambda)l$ in Eq. (1) we are in the linear regime. Therefore, the decrease of the peak area is linearly proportional to the concentration. However, it can be observed that above 6,000 ppm, the slope of the experimental curve (green line) is lower than that obtained following Beer-Lambert's law (red line). As stated in previous reports, above a threshold concentration the absorbance starts to evidence non-monochromatic effects due to scattering, chemical reactions or stray radiation effects, among others [25]–[28]. Two models have been applied to verify this point in the optical response of macroporous silicon filters [26], [29], [30], showing a great concordance with the exponential adjustment of the experimental data.

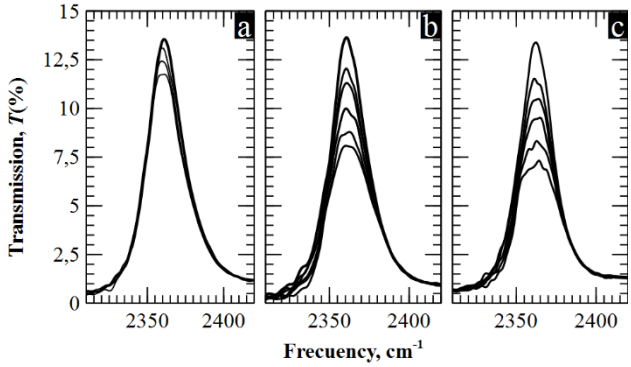

Figure 5.7.4. a) Experimental curves for 2,550, 6,400 and 10,200 ppm for a cell depth of 2.2 mm. b) and c) Measured area of the peak at different concentrations (0-2,900-4,750-6,800-8,100-10,500 ppm) for a path length of 1.4 cm and 2.4 cm, respectively.

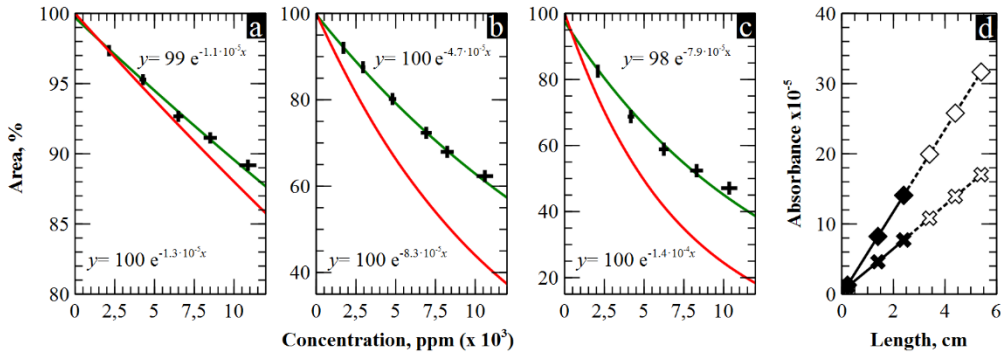

Figure 5.7.5. Experimental and simulated area for 0.22 mm a), 1.4 cm b) and 2.4 cm c). Both simulation (red) and experimental (green) follow an exponential fit. d) Absorbance vs length curve for experimental (cross) and simulation (squares) data. White marks are extrapolated values used for absorbance correction in the simulation program.

Figure 5.7.5b and Figure 5.7.5c show a stronger exponential decay than in 2.2 mm, since we are no longer in the linear regime. The relationship between the exponent of the curves, or absorbance, and the cell length is represented in Figure 5.7.5d. Non-monochromatic effects are evidenced in the less steep slope of the experimental curve. Experimental and expected absorbance can be related in order to apply corrections in the simulation program. This allows going beyond the setup limits and predict the real response of the filter for concentrations higher than 10^4 ppm and cell lengths longer than 2.4 cm.

Higher concentrations

One of the most important features of a sensor is its operating range. In the present case, the upper limit of this range is given by the maximum concentration necessary to completely eliminate the peak. It is clear from Figure 5.7.4 that this point is not reached in any of the three reported datasets. Therefore, we have used the simulation program with the corrections done in previous section in order to obtain those limits, which are around 30% for 2.2 mm, 8% for 1.4 cm, and 5% for 2.4 cm –see left image of Figure 5.7.6a–.

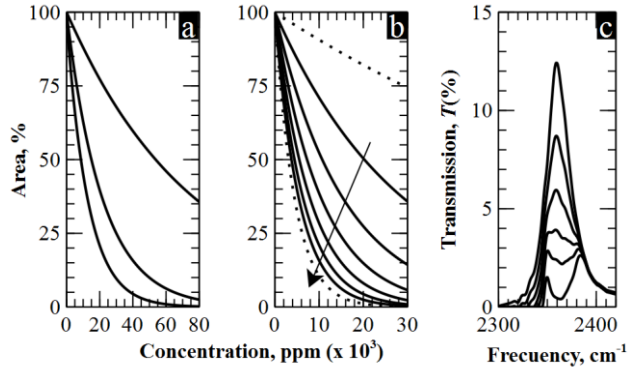

Figure 5.7.6. a) Extrapolation of the results to higher concentrations for the three lengths of 2.2 mm, 1.2 cm and 2.4 cm. b) Prediction of optical response for longer path lengths. c) Filter response for the optimal cell length of 4.5.

The shortest operating range of [0%-5%] represents an increase in the sensitivity and the resolution of more than an order of magnitude compared to the case of an unfiltered NDIR device working in the entire CO_2 absorption range. In other words, simulations show that, an NDIR almost 5 times longer than ours would be required to obtain the same sensitivity. These results show that adding a macroporous silicon narrow filter to reported

sensors [7], [31] will allow either reaching much higher sensitivity for the same length or having more compact devices for the same sensitivity.

4.3 Longer lengths

Figure 5.7.6b shows the evolution of the filter area for eight cell lengths and concentrations below 3%. It can be seen that the difference between two consecutive curves decreases as the length increases, having almost the same response for 6 cm as for 10 cm. Taking this into account, we conclude that a cell length of 4.5 cm offers a good compromise between size and optical response; it presents a very long operating range –from 0% to 2.5%– and twice the sensitivity than the 2.4 cm case. In addition, there is a substantial improvement in the LOD, as evidenced when comparing Figure 5.7.6c and Figure 5.7.4c, where a greater distance between two successive concentration curves is observed. Therefore, in a realistic gas sensor, lower concentration variations could be detected for the same resolution of the device.

On thermal and pressure stability

To know the impact that external variations have in our filters, we measured their transmission response sweeping temperature and pressure. Initially, the filter was placed inside the gas cell in nitrogen atmosphere and the pressure was increased from 1.07 bar to 1.21 bar in intervals of 0.03 bar. In all cases, equal transmission peaks were measured, proving no intrinsic changes in the filter due to pressure variations. Then, the filter was exposed to the same CO_2 concentrations as in previous sections but, in this case, at 1.21 bars. Again, no difference was observed between these measurements and those taken at atmospheric pressure. Only in the case of high pressures, the reported method experiences slight variations in the optical response. In Figure 5.7.7a and Figure 5.7.7b, it is shown the simulated response of the filter at 1 atm. and 2 atm. It can be seen that at 2 atm. the absorption spectrum of carbon dioxide gets broader in the R-branch, what slightly increases the sensitivity.

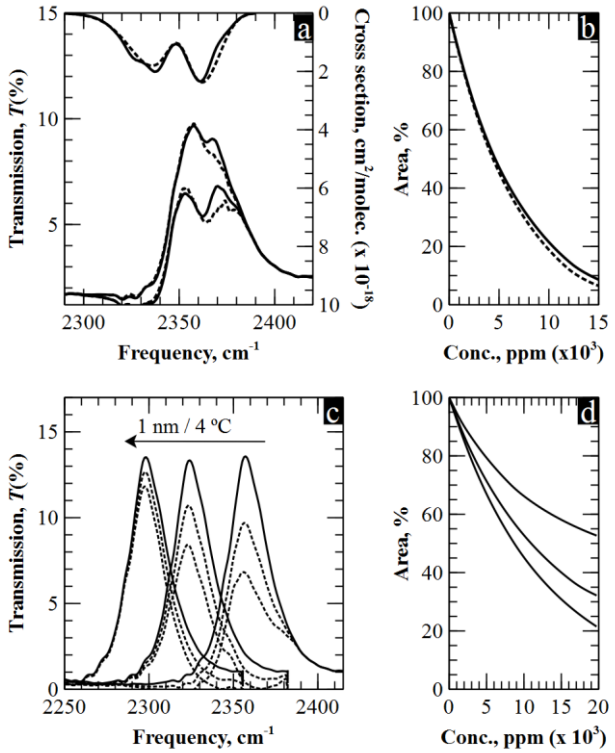

Figure 5.7.7. a) Comparison of the simulated response when the CO_2 absorption spectrum is 1 atm. and 2 atm. b) Sensitivity curves at 1 atm. (solid line) and 2 atm. (dotted line). c) Measurements at 25 ºC, 175 ºC and 350ºC and they respective optical responses d).

For testing the impact of temperature, the filters were heated up to 400 ºC with an external resistor. Figure 5.7.7c shows three experimental measurements at 25 ºC, 175 ºC and 350 ºC. It can be observed a total shift of nearly 100 nm towards lower frequencies due to thermal expansion of silicon, in good accordance to previous studies [32]. This displacement leads to a decrease in sensitivity, as a consequence of misalignment between the filter and the carbon dioxide –see Figure 5.7.7d. Nevertheless, results show that for temperature variations lower than 50 ºC the peak does not experience a noticeable difference in its optical response.

Both results in pressure and temperature show a highly robust technology. In addition, the reported filters present long-term stability since the same optical response was measured in a time span of almost two years.

Extending to other MIR gases

In this section we extend the results obtained for CO_2 to other filters distributed along the entire mid-infrared region. In concrete, we exemplify –but there are more cases– for those filters pointing dinitrogen monoxide (N_2O), carbonyl sulfide (OCS,), nitrogen dioxide (NO_2) and sulfur dioxide (SO_2). Optical robustness to external variations and long-term stability are intrinsic characteristics of the technology as well as LOD depends on the detector resolution in a final device. Therefore, working range and path length are studied. As seen in previous sections, they are directly related through the absorbance. To compare the results with the CO_2 the optimal case, the working range was set to [0-2.5%] and the path length was adjusted in the software program for each case. Figure 5.7.8 8 shows that the length is reduced to 3 cm in the case of OCS because its absorption cross section is higher than carbon dioxide's. In the other three cases, longer lengths are obtained for the same working range, 8 cm (NO_2), 8.2 cm (N_2O) and 12.6 cm (SO_2). It should be noted that in all of them, the path length is sufficiently small to consider macroporous silicon narrow filters as a platform for reliable and compact spectroscopic gas sensing.

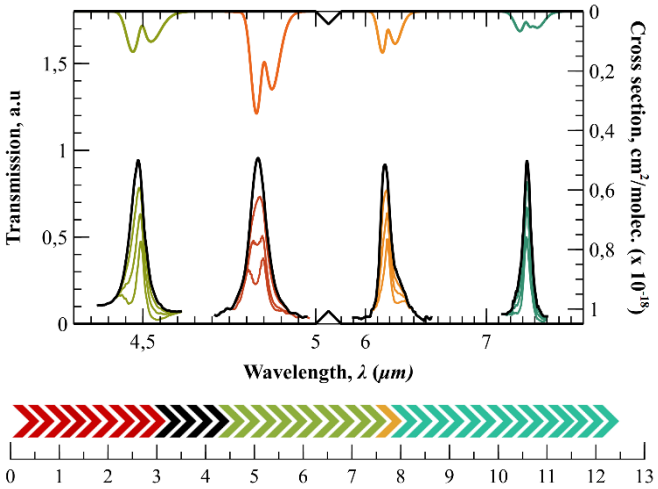

Figure 5.7.8. Cross section –right axis– of N_2O (green), OCS (red), NO_2 (orange) and SO_2 (blue). Peak transmissions –left axis– when exposed to the same concentrations [0%-2.5%]. Below, a comparison in real scale of the calculated path lengths with the reference

case of CO_2 (black). The size of the cell is depicted as the difference between the last arrow of a particular color and the x-axis origin.

On filter's selectivity and sensitivity

It may occur that the absorption spectra of two gases overlap partially in the mid-infrared region. This is the case of nitrous oxide, N_2O, and carbon monoxide, CO, whose spectra coincide in the band around 2200 cm^{-1}. In Figure 5.7.9a is shown that our filter is narrow enough to entirely fit in the green band, pointing only to the non-overlapped part of N_2O. On the contrary, the other filter [33] covers part of the grey band where both gases coincide, entailing cross reference-detection. In Figure 5.7.9b it is depicted the response of both filters when exposed to different ambient conditions. Upper dashed line is the response of the commercial filter when there is no CO in the atmosphere. Therefore, it reports only the detection of N_2O. The lower dashed line is the response of the commercial filter when the two gases complete the 100% of the atmosphere. This is, a 100% of CO when there is no N_2O –left limit– and 97% of CO at the right limit, where there is a 3% of N_2O. The grey area in between dashed lines represents inherent uncertainty of measuring N_2O using the commercial filter due to presence of carbon monoxide in the atmosphere. The solid line in Figure 5.7.9b shows the response of our filter under the same conditions as on the bottom line. In this case, no measurement uncertainties are observed because our filter completely fits in the non-overlapping part of the N_2O. In addition, in Figure 5.7.9b it can be also observed that the sensitivity of our filter is higher than the one for the commercial filter.

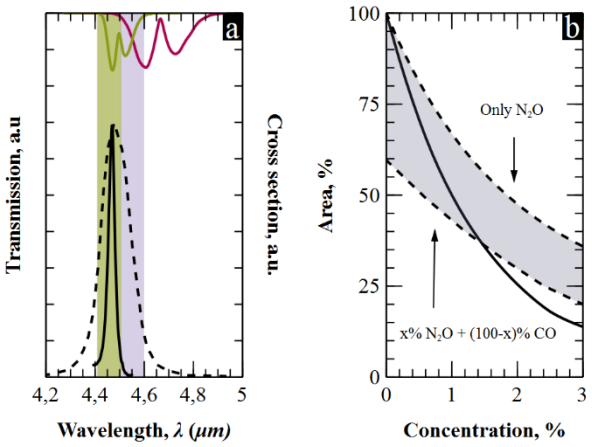

Figure 5.7.9. a) Left axis, transmission of macroporous silicon narrow filter (solid line) and a commercial filter (dashed line) [33]. Right axis, absorption cross section for N_2O and CO. b) Cross-measurements for the two filters of Figure 5.7.9a.

There is more evidence that our filters report better selectivity and sensitivity than other devices. Specifically, there are commercial CO_2 detectors that use active filters three times wider than ours [34], [35], ranging from 2470 cm^{-1} to 2220 cm^{-1}. This involves cross detection with N_2O. The use of the filter studied in sections 4.1-4.4 would avoid such cross detection. Moreover, calculations show that it would increase the LOD by almost an order of magnitude or reduce five times the path length.

5.7.5 Conclusions

The spectroscopic detection of several gases using macroporous silicon PhCs was studied both theoretically and experimentally. Carbon dioxide was the first analyzed case;

a narrow filter was placed within the R-branch of CO_2 and the evolution of its area when exposed to concentrations below 1% was measured for three different cell lengths. The response in all three cases was adjusted by exponential curves, showing a linear relationship between the exponent of the fittings, or absorbance, and the length of the gas cell. Experimental absorbance showed a mismatch when compared to the theory due to non-chromatic effect. Hence, corrections in the theoretical absorbance were introduced in the simulation program in order to obtain realistic prediction of the filter's response for higher concentrations and longer cell lengths. For the case of carbon dioxide, optimal path lengths of 4.5 cm and concentrations ranges between 0% and 2.5% were reported. In addition, LOD lower than the ±100 ppm achieved experimentally were expected. The filter was exposed to pressure and temperature variations, showing a very robust optical response in wide ranges of [1-2] atm. and [20-400] ºC, respectively. Furthermore, the filter demonstrated long-term stability. Results were extended to four other gases in the MIR, OCS, NO_2, N_2O and SO_2. Finally, higher selectivity and sensitivity was reported comparing the fabricated filter with the commercial ones.

Therefore, macroporous silicon narrow filers could be used in actual opto-electronic devices for improving their features in gas detection.

5.7.6 References

[1] J. F. Fennell *et al.*, "Nanowire Chemical/Biological Sensors: Status and a Roadmap for the Future," *Angew. Chemie Int. Ed.*, vol. 55, no. 4, pp. 1266–1281, Jan. 2016.

[2] I. Stassen, N. Burtch, A. Talin, P. Falcaro, M. Allendorf, and R. Ameloot, "An updated roadmap for the integration of metal–organic frameworks with electronic devices and chemical sensors," *Chem. Soc. Rev.*, vol. 46, no. 11, pp. 3185–3241, Jun. 2017.

[3] J. D. J. Ingle and S. R. Crouch, *Spectrochemical analysis*. London: Prentice Hall, 1988.

[4] X. Liu, S. Cheng, H. Liu, S. Hu, D. Zhang, and H. Ning, "A survey on gas sensing technology.," *Sensors (Basel).*, vol. 12, no. 7, pp. 9635–65, 2012.

[5] T.-V. Dinh, I.-Y. Choi, Y.-S. Son, and J.-C. Kim, "A review on non-dispersive infrared gas sensors: Improvement of sensor detection limit and interference correction," *Sensors Actuators B Chem.*, vol. 231, pp. 529–538, Aug. 2016.

[6] J. Hodgkinson and R. P. Tatam, "Optical gas sensing: a review," *Meas. Sci. Technol.*, vol. 24, no. 1, p. 012004, Jan. 2013.

[7] J. Hodgkinson, R. Smith, W. O. Ho, J. R. Saffell, and R. P. Tatam, "Non-dispersive infra-red (NDIR) measurement of carbon dioxide at 4.2μm in a compact and optically efficient sensor," *Sensors Actuators B Chem.*, vol. 186, pp. 580–588, Sep. 2013.

[8] T. Chen, Z. Han, J. Liu, and Z. Hong, "Terahertz gas sensing based on high Q one-dimensional photonic crystal cavity," 2014, vol. 9275, p. 92750C.

[9] P. Ma *et al.*, "High Q factor chalcogenide ring resonators for cavity-enhanced MIR spectroscopic sensing," *Opt. Express*, vol. 23, no. 15, p. 19969, Jul. 2015.

[10] X. Shi, Z. Zhao, and Z. Han, "Highly sensitive and selective gas sensing using the

defect mode of a compact terahertz photonic crystal cavity," *Sensors Actuators B Chem.*, vol. 274, pp. 188–193, Nov. 2018.

[11] G. D. Cole *et al.*, "High-performance near- and mid-infrared crystalline coatings," *Optica*, vol. 3, no. 6, p. 647, Jun. 2016.

[12] Jing Lu, "High Performance Infrared Narrow Band Pass Filters for Infrared Sensors and Systems," in *SENSOR+TEST Conference 2009 - IRS^2 2009 Proceedings*, 2009, pp. 275–280.

[13] T. J. L. R. J. G. Go Fujisawa, Sheng Chao, "US20170242149A1 - Mid-infrared carbon dioxide sensor," 2017.

[14] Iridian Spectral Technologies, "Highest Quality Mid-IR Bandpass Filters." [Online]. Available: https://www.iridian.ca/product-category/mid-ir-bandpass/. [Accessed: 04-Apr-2019].

[15] D. Pergande *et al.*, "Miniature infrared gas sensors using photonic crystals," *J. Appl. Phys.*, vol. 109, no. 8, p. 083117, Apr. 2011.

[16] D. Vega, F. Marti, A. Rodriguez, and T. Trifonov, "Macroporous silicon for spectroscopic CO_2 detection," in *IEEE SENSORS 2014 Proceedings*, 2014, pp. 1061–1064.

[17] D. Cardador, D. Vega, D. Segura, T. Trifonov, and A. Rodríguez, "Enhanced geometries of macroporous silicon photonic crystals for optical gas sensing applications," *Photonics Nanostructures - Fundam. Appl.*, vol. 25, pp. 46–51, Jul. 2017.

[18] D. Cardador, D. Segura, and A. Rodríguez, "Photonic molecules for improving the optical response of macroporous silicon photonic crystals for gas sensing purposes," *Opt. Express*, vol. 26, no. 4, pp. 4621–4630, Feb. 2018.

[19] S. Neethirajan, D. S. Jayas, and S. Sadistap, "Carbon Dioxide (CO2) Sensors for the Agri-food Industry—A Review," *Food Bioprocess Technol.*, vol. 2, no. 2, pp. 115–121, Jun. 2009.

[20] D. Y. C. Leung, G. Caramanna, and M. M. Maroto-Valer, "An overview of current status of carbon dioxide capture and storage technologies," *Renew. Sustain. Energy Rev.*, vol. 39, pp. 426–443, Nov. 2014.

[21] D. Zhao, D. Miller, X. Xian, F. Tsow, and E. S. Forzani, "A Novel Real-time Carbon Dioxide Analyzer for Health and Environmental Applications.," *Sens. Actuators. B. Chem.*, vol. 195, pp. 171–176, May 2014.

[22] D. Cardador, D. Vega, D. Segura, and A. Rodríguez, "Study of resonant modes in a 700 nm pitch macroporous silicon photonic crystal," *Infrared Phys. Technol.*, vol. 80, 2017.

[23] D. Cardador, D. Segura, D. Vega, and A. Rodríguez, "Transmission and thermal emission in the NO2 and CO absorption lines using macroporous silicon photonic crystals with 700 nm Pitch," in *PHOTOPTICS 2017 - Proceedings of the 5th International Conference on Photonics, Optics and Laser Technology*, 2017, pp. 191–194.

[24] R. V. Kochanov, I. E. Gordon, L. S. Rothman, P. Wcisło, C. Hill, and J. S. Wilzewski, "HITRAN Application Programming Interface (HAPI): A comprehensive approach to working with spectroscopic data," *J. Quant. Spectrosc.*

Radiat. Transf., vol. 177, pp. 15–30, Jul. 2016.

[25] K. Fuwa and B. L. Valle, “The Physical Basis of Analytical Atomic Absorption Spectrometry. The Pertinence of the Beer-Lambert Law.,” *Anal. Chem.*, vol. 35, no. 8, pp. 942–946, Jul. 1963.

[26] H. Öjelund and J. F. Offersgaard, “Correction of Nonlinear Effects in Absorbance Measurements,” *Appl. Spectrosc. Vol. 56, Issue 4, pp. 469-476*, vol. 56, no. 4, pp. 469–476, Apr. 2002.

[27] L. Kocsis, P. Herman, and A. Eke, “The modified Beer–Lambert law revisited,” *Phys. Med. Biol.*, vol. 51, no. 5, pp. N91–N98, Mar. 2006.

[28] J. M. Parnis and K. B. Oldham, “Beyond the Beer–Lambert law: The dependence of absorbance on time in photochemistry,” *J. Photochem. Photobiol. A Chem.*, vol. 267, pp. 6–10, Sep. 2013.

[29] A. Y. Tolbin, V. E. Pushkarev, L. G. Tomilova, and N. S. Zefirov, “Threshold concentration in the nonlinear absorbance law,” *Phys. Chem. Chem. Phys.*, vol. 19, no. 20, pp. 12953–12958, May 2017.

[30] A. Y. Tolbin, V. E. Pushkarev, and L. G. Tomilova, “A mathematical analysis of deviations from linearity of Beer’s law,” *Chem. Phys. Lett.*, vol. 706, pp. 520–524, Aug. 2018.

[31] R. Lee and W. Kester, “Complete Gas Sensor Circuit Using Nondispersive Infrared (NDIR),” 2016.

[32] M. Garín, T. Trifonov, D. Hernández, Á. Rodriguez, and R. Alcubilla, “Thermal emission of macroporous silicon chirped photonic crystals,” *Opt. Lett.*, vol. 35, no. 20, p. 3348, Oct. 2010.

[33] Electro Optical Components, “Narrow Bandpass Filters- INBP4490,” 2017.

[34] Boston Electronics, “Thermopiles for temperature measurement and gas detection,” 2012.

[35] Hamamatsu, “Thermopile detector (dual element type) T11722-01 | Hamamatsu Photonics,” 2017.

5.8

Optics Letters, 44 (28), 4621-4630 (2018)
https://doi.org/10.1364/OL.44.004535
Received: 19 July 2019; **Revised**: 19 August 2019; **Accepted**: 19 August 2019; **Available online**: 9 September 2019

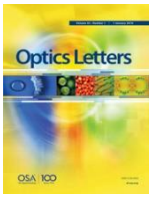

Empirical demonstration of CO_2 detection using macroporous silicon photonic crystals as selective thermal emitters

David Cardador Maza, [1,*] Daniel Segura Garcia,[1] Ioannis Deriziotis,[1] Moisés Garin, [2] Jordi Llorca,[3] and Angel Rodriguez,[1]

[1]*Micro i Nanotecnologies, Departament d'Enginyeria Electrònica, Universitat Politècnica de Catalunya, 08031 Barcelona, Spain*

[2]*GR-MECAMAT, Universitat de Vic – Universitat Central de Catalunya, Campus Torre dels Frares, c/ de la Laura 13, 08500 Vic, Spain.*

[3]*Barcelona Research Center in Multiscale Science and Engineering, Universitat Politècnica de Catalunya, 08019, Barcelona, Spain*

Abstract: This study describes the detection of CO_2 using macroporous silicon photonic crystals as thermal emitters. It demonstrates that the reduction of structural non-homogeneities leads to an improvement of the photonic crystals' emission. Narrow emission bands (Q ~ 120) located within the R-branch of carbon dioxide were achieved. Measurements were made using a DTGS photodetector and the photonic crystals, heated to 400ºC, as selective emitters. A gas cell with a CO_2 concentration between 0 ppm and 10,000 ppm was installed in the center. Results show high sensibility and selectivity that could be used in current NDIR devices for improving their features. These results open the door to narrowband emission in mid-infrared for spectroscopic gas detection.

Carbon dioxide (CO_2) is one of the gases that raises the most interest in the field of gas detection due to its importance in many biological and industrial processes. Depending on its concentration it may indicate an excess of contamination [1], reveal the existence of cardiovascular and pulmonary diseases [2] or detect an incipient food spoilage [3], among others. The most common technique to detect CO_2, and many other gasses, is by non-dispersive infrared (NDIR) spectroscopy, that aims to detect infrared (IR) absorption in the specific wavelength regions where gas molecules or chemical compounds exhibit their vibrational modes [4]. The measured absorption is then related to gas concentration through the Beer-Lambert law.

Widespread NDIR gas sensing devices employ a broadband blackbody thermal emitter combined with a mid-infrared (MIR) detector and a narrow bandpass filter tuned at a particular absorption band of the target gas [4]. This solution is simple, cost effective, and offers a good sensitivity for many gas concentration tracking applications. However, they could still improve in terms of selectivity, which would partially avoid cross detection and further improve sensitivity. One particularly interesting development in this regard is the use of optical fibers for gas sensing combining a long optical path with a good overlapping between the gas and the fiber mode fields [5], [6].

In the last years, the use of narrow thermal emission sources in NDIR systems has attracted increasing research interest as a way to simplify NDIR detector structure as well as to increase both resolution and sensitivity without resorting to the high-cost of ultra-narrow laser-based systems [7]. The basic idea is to use a selective thermal emitter that naturally radiates at the wavelength band of interest. The narrower this band, the more selective and sensitive the detection will be, allowing also for a less demanding accompanying filter. One of the most extensively explored solutions for narrowband thermal emission are photonic crystals (PhCs) owing to their inherent ability to control and engineer the optical density of states [8]–[10]. Different strategies based on plasmon resonances [11] or multi-quantum-well structures [12]–[14] have proved high-quality emissivity when combined to PhCs. Furthermore, some of them have experimentally demonstrated the feasibility of generating narrow emission bands in the long-infrared fingerprint region of organic solvents and gases [13].

Despite technological advances, the fabrication of 2D and, especially, 3D photonic crystals, is still very challenging. Furthermore, such structures need to be stable at high operation temperatures (usually >350ºC).

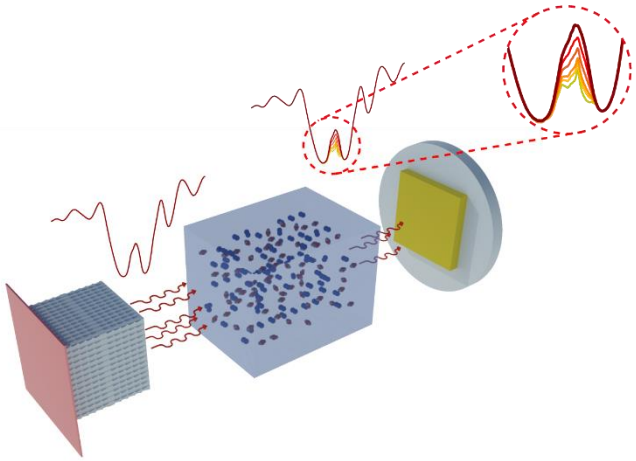

Figure 5.8.1. Schematic of the CO2 detection process using macroporous silicon photonic crystals as selective emitters; the PhC is heated up to 400 ºC radiating in the MIR with the resonance peak centered in CO2 absorption range. The electromagnetic field crosses the gas chamber and its concentration is determined by quantifying the difference between the initial and the final emission intensity arriving the detector.

A particularly appealing technique to produce large-area 2D and 3D photonic structures operating in the IR is the so-called macroporous silicon [15]. Macroporous silicon is obtained through electrochemical dissolution of *n*-type silicon in hydrofluoric acid (HF) electrolyte under back-side illumination. This technique offers a great control of the structure in-depth, making easy the introduction of plane defects within the structure [16]. Furthermore, thanks to the monocrystallinity of the material, macroporous silicon structures are stable at very high temperatures, close to the melting point of silicon [17]. Previous studies have reported that 2D-structured macroporous silicon can be used to achieve close to black-body emittance in the IR thanks to the strong surface roughness [18]. Others showed the potential application of 3D macroporous silicon PhCs as selective emitters in the absorption regions of carbon monoxide (CO) and nitrogen dioxide (NO_2) [19].

The aim of this letter is to demonstrate the viability of using 3D macroporous silicon photonic crystals as a selective thermal emitter in NDIR CO_2 gas detection. In here the use of a selective emitter does not seek energy efficiency (such as in [7]), but an increased selectivity and sensitivity as compared to the blackbody thermal source counterpart. The document is structured as follows. We first show the negative impact that non-homogeneities have in the emission quality of our samples. Next, we introduce modifications in the manufacturing process and in the design of the photonic crystals to obtain narrow band emitters located in the carbon dioxide fingerprint. Then, we describe the dispersive detection of CO_2, giving the relationship between the expected power reaching the detector and the concentration of the gas. The study ends by showing a proof of concept of the benefits that our emitters would give in terms of sensitivity and selectivity to conventional NDIR devices.

Let us start by introducing the optical response of previously reported samples that showed very low-quality thermal emission [19]. These samples were made through a 5% HF electrochemical etching at 10 ºC, with a constant polarization of 2 V and an asymmetric trapezoidal current profile. As a result of the fabrication process, 700 nm pitch PhCs consisting on two modulation areas, with five periods each, and a cavity in the middle were obtained. The total length of the PhCs was around 25 µm and the substrate depth around 250 µm (further details can be found elsewhere [20]).

It is well known that these structures raise resonant modes, or transmitted peaks, within the bandgap due to the cavity inserted in the middle of the modulated regions. Figure 2a depicts the dispersion of the peak along the attacked area. It can be seen that the central frequency, the transmittance, and the quality factor of the peak depends on the selected spot, as suggested in previous studies [21], [22]. In other words, there are a high number of cooperative resonators along the emitting area, which is around 1 cm^2. Figure 2b shows the average transmittance, *T*, and reflectance, *R*, along the area. We used them to calculate the emissivity, *E*, of the sample through Kirchhoff's Law,

$$E = 1 - R - T \tag{1}$$

Figure 2c shows a good agreement between calculated and experimental emissivity, which has been extracted from previous studies [19]. In addition, the shape of both curves have a great similarity with the average transmission of Fig. 2b. This confirms that there is a direct relationship between the dispersion, due to structural non-homogeneities of the photonic crystal, and the quality factor (Q-factor) of the emission peak. Thus, we improved the fabrication set-up in order to reduce non-homogeneities and thereby increase the quality of emissions. In particular, the uniformity of lighting during the electrochemical process was identified as a key factor; it was observed that samples presented lower quality factors and lower transmissions at the edges than in the center. Therefore, an optical diffuser was

included to disperse light and thus improve uniformity. Subsequent measurements revealed a more homogenous response across the emission area. This allowed to enhance the Q-factor of the structures by increasing the number of periods of the photonic crystals up to eight and ten periods, following the same idea as previous studies [20]. As a result of the improvements, the dispersion in 8 and 10 periods was substantially reduced –see Figs. 2d and 2g–. Consequently, narrower average transmission peaks were obtained –Figs. 2e and 3h.

We measured photonic crystals' emissivity using a Vertex 70 Fourier-Transform Infrared (FT-IR) spectrometer equipped with the A540 emission adapter. Samples were heated to 400 ºC and their spectrum was referenced to blackbody radiation, which was obtained by heating a carbonized piece of silicon at 400 ºC. Figures 2f and 2i show that emission improves as the number of periods increases. On one hand, the base of the peak is reduced from the initial value of 40% in the case of 5 periods, to 20% and 7% for 8 and 10 periods, respectively. This is due to the fact that light is more filtered as more periods are in the structure. Thus, the amplitude of the peak increases from 20% to 40% and 55%. For the same reason, the base of the peak is tightened when more periods are added. Figure 2c shows that the base is 150 cm^{-1} wide while in Fig. 2i it is reduced to 100 cm^{-1}. As a result of both improvements, amplitude enhancement and base narrowing, the quality factor of the peaks doubled and quadrupled the initial value of 30 for 8 and 10 periods, respectively. In addition, it can be seen that the experimental emissivity is very similar to the calculated using Kirchhoff's Law.

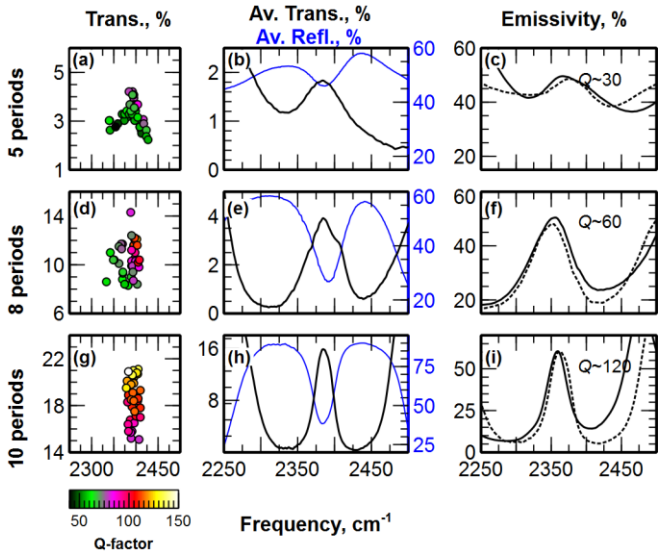

Figure 5.8.2. Dispersion, average transmittance and reflectance, and emissivity for 5, 8 and 10 periods. (Left-column) Colored circles represent the multiple peaks measured along the sample. Their *x*-value is the central frequency and the *y*-value, the transmittance. The color represents the Q-factor. (Middle-column) Average transmittance (black) and reflectance (blue) for all peaks from left column. (Right-column) Emission spectrum of each sample.

There is another interesting information in the emissivity figures; it is possible to estimate the spectral radiance (B_υ)of our peaks, i.e. the in-band emitted power, throughout the Planck's Law,

$$\Delta P = A\int_{\upsilon_1}^{\upsilon_2} B_\upsilon = A\frac{2h\upsilon^3}{c^2}\int_{\upsilon_1}^{\upsilon_2}\frac{d\upsilon}{e^{h\upsilon/k_BT}-1} \qquad (2)$$

which describes the radiated power of a black-body, ΔP (W), at a temperature T (K), within a frequency range [υ_1, υ_2] (cm^{-1}), and with an active area A (cm^2), where h and k_B

are Planck's and Boltzmann constants, and c the speed of light. To calculate it, we numerically computed the integral of the spectral radiance as described by Widger and Woodall [23]. Thus, after setting the appropriate values, T = 400 ºC, A = 1 cm^2, v_1 = 2300 and v_2 = 2400 (for 10 period's peak), we got a radiated power of ΔP ~ 5 mW. Note that this value is for a black body. In our case, our maximum emissivity is 62% and the total area of the peak represents the 40% of the blackbody emission within the frequency range, v_2-v_1. Therefore, the estimated value of the peak without CO_2 and at 400 ºC is about 2 mW.

Emission peaks for 8 and 10 periods completely fitted into the carbon dioxide fingerprint. This allowed us to perform spectroscopic measurements with the photonic crystals as thermal emitters. For this purpose, we used a deuterated triglycine sulfate (DTGS) detector from Bruker v-70 FT-IR working in the mid-infrared. We placed a gas cell of 1.4 cm depth in the middle of the optical path and we introduced CO_2 concentrations ranging from 0 ppm to 10,000 ppm. Next, we measured the variation of the peak area, in essence, the estimated power reaching the receiver, versus the concentration. Figures 3a and 3b depict the optical response of the selective emitters for 8 and 10 periods when exposed to CO_2. It can be seen that, for the same concentrations –i.e. curves with the same color–, the response of the narrower emitter is more pronounced than for the wider.

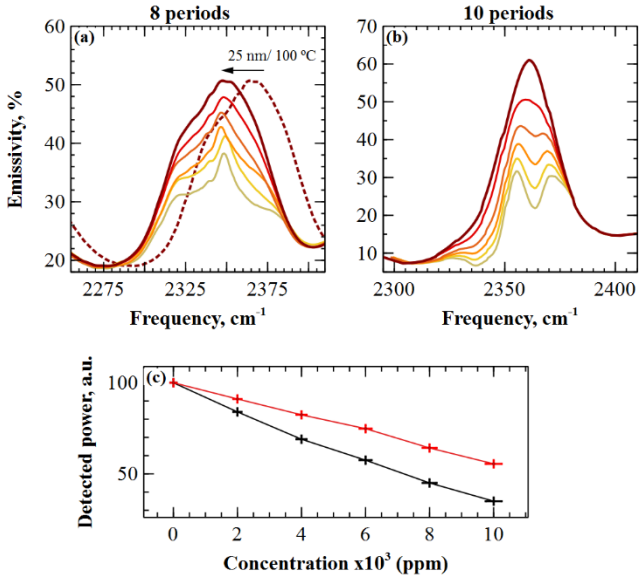

Figure 5.8.3. Emission spectra for 8, a), and 10, b), periods when exposed to 0; 2,000; 4,000; 6,000; 8,000 and 10,000 ppm of CO_2 at 400 ºC. In a), the dotted line indicates the emission spectra at 300 ºC without gas. c) Relationship between the area of the peaks and the concentration (8 periods red line, 10 periods black line).

This is because the peak for 10 periods is comprised within the R branch instead of encompassing the entire absorption range of CO_2, as happens for the 8 period's case. In addition, the central frequency of the emission can be precisely tuned by controlling the temperature –see Fig. 3a. In that manner, the position of the peak can be regulated to achieve the optimal response.

For a visual interpretation of the results, we plotted the sensitivity curves for 8 and 10 periods in Fig. 3c, which follow the reformulated Beer-Lambert rule, such as reported in recent studies [24]. In essence, each red point corresponds to the normalized area of each one of the peaks in Fig. 3a, and the same applies to black points and Fig. 3b. It is observed a steeper slope for the case of 10 periods, which means a higher selectivity than for 8 periods. In both measurements the uncertainty in the concentration is given by the error associated with the mass flowmeter and varies from ±100 ppm (lowest concentration) to ±250 ppm (highest concentration).

Up to this point it has been demonstrated that macroporous silicon photonic crystals can be used as selective emitters for CO_2 detection. Let us finish by showing a proof of concept of the benefits that our emitters would bring to current NDIR devices.

NDIR gas sensors [25], [26] work with a broadband emitter and a thermopile that detect in a wide range –typically from 2 µm to 20 µm–. Hence, they need a bandpass filter to sense only in the specific area of the gas. Figure 4a shows that our emission peaks are three times narrower than the filters used in previous gas sensors –red dashed line–. It can also be observed that the bandwidth of the reported emitters, combined with the filter, ensures that only the signal below the curve of the emission peak is detected. In other words, the rest of the spectrum is blocked by the filter and only the emission peak, pointing to the R-branch of CO_2, will survive. Consequently, higher sensitivity is reported in Fig. 4b.

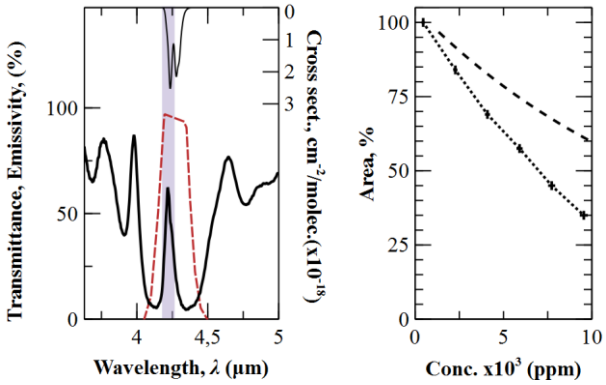

Figure 5.8.4. a) (Left axis) Transmittance of conventional bandpass filters, (dashed red line, data extracted from [25]), emissivity of macroporous silicon PhCs (black). CO_2 absorption spectrum (grey, right axis). b) PhC (dotted line) and filter (dashed line) selectivity.

We computed the Beer-Lambert Law for broadband spectroscopy to calculate the response of the NDIR device for the same path length than ours [27]. This is, we equally discretized both carbon dioxide spectrum, obtained from HITRAN database [28], and filter transmission, and we applied Eq. 3.

$$\frac{I(\nu_i)}{I_0(\nu_i)} = exp\left(-C\sigma_{CO_2}(\nu_i)L\right) \tag{3}$$

where $I_0(\nu_i)$ and $I(\nu_i)$ are the incident and received radiation intensities at frequency ν_i, respectively; $\sigma_{CO2}(\nu_i)$ (cm^2 molecule^{-1}) is the absorption cross section at frequency ν_i; C (molecules m^{-3}) is the concentration of the gas under test; and L is the absorption optical path length (cm).

To complete the description, we estimated the radiated power through Eq. 1 using the same parameters as before except for the emitter area which, in most of commercial devices is about 0.1 cm^2. Therefore, the power in the case without CO_2 would be approximately 200 µW. This is comparable to the power emitted by the broadband sources used in the device. Further studies should focus on lateral band suppression for filterless detection, e.g. depositing adequate materials in the rear side of the wafer.

Finally, the authors would like to remark that these results could be used to improve the emissivity reported in previous articles in order to detect CO and NO_2 [19]. Furthermore, thanks to the versatility of the photoelectrochemical etching process, the reported macroporous silicon structures can be designed to specifically work in the entire MIR band [24]. Consequently, these results suppose, not only the evidence of the detection of a specific gas, but the demonstration that this technology can be used to detect other gases in the MIR by optical spectroscopy.

To conclude, in this Letter we have performed corrective actions to improve the emissivity of macroporous silicon photonic crystals; we have reduced the dispersion in the samples and added more periods to the structure. In this manner, narrowband thermal emitters placed in the carbon dioxide fingerprint were achieved. The best case presented an emissivity amplitude of approximately 55% and a Q-factor of 120. This allowed spectroscopic detection at the R-branch of CO_2 and its comparison to current NDIR devices. Results show that the use of our emitters would lead to higher sensitivity and selectivity than using broadband sources. In addition, it has been estimated that the emitted power would be very similar to the one radiated using conventional emitters. Finally, we remark that these results can be extended to other gases thus, opening the door to selective emission along the mid-infrared.

Funding. Spanish Ministry of Economy and Competitiveness (MINECO) co-funded by the European Regional Development Fund (TEC-2013-48-147-C6-2, ENE2015-74009-JIN); Spanish Ministry of Science and Innovation/European Regional Development Funds (MICINN/FEDER) (RTI2018-093996-B-C31).

Acknowledgement. JL is a Serra Húnter Fellow and is grateful to ICREA Academia program and GC 2017 SGR 128.

REFERENCES

[1] D. Y. C. Leung, G. Caramanna, and M. M. Maroto-Valer, "An overview of current status of carbon dioxide capture and storage technologies," *Renew. Sustain. Energy Rev.*, vol. 39, pp. 426–443, Nov. 2014.

[2] D. Zhao, D. Miller, X. Xian, F. Tsow, and E. S. Forzani, "A Novel Real-time Carbon Dioxide Analyzer for Health and Environmental Applications.," *Sens. Actuators. B. Chem.*, vol. 195, pp. 171–176, May 2014.

[3] S. Neethirajan, D. S. Jayas, and S. Sadistap, "Carbon Dioxide (CO2) Sensors for the Agri-food Industry—A Review," *Food Bioprocess Technol.*, vol. 2, no. 2, pp. 115–121, Jun. 2009.

[4] J. Hodgkinson and R. P. Tatam, "Optical gas sensing: a review," *Meas. Sci. Technol.*, vol. 24, no. 1, p. 012004, Jan. 2013.

[5] G. Stewart, W. Jin, and B. Culshaw, "Prospects for fibre-optic evanescent-field gas sensors using absorption in the near-infrared," *Sensors Actuators B Chem.*, vol. 38, no. 1–3, pp. 42–47, Jan. 1997.

[6] T. Ritari *et al.*, "Gas sensing using air-guiding photonic bandgap fibers," *Opt. Express*, vol. 12, no. 17, p. 4080, Aug. 2004.

[7] S. M. Cristescu, S. T. Persijn, S. te Lintel Hekkert, and F. J. M. Harren, "Laser-based systems for trace gas detection in life sciences," *Appl. Phys. B*, vol. 92, no. 3, pp. 343–349, Sep. 2008.

[8] S.-Y. Lin, J. G. Fleming, E. Chow, J. Bur, K. K. Choi, and A. Goldberg, "Enhancement and suppression of thermal emission by a three-dimensional photonic crystal," *Phys. Rev. B*, vol. 62, no. 4, pp. R2243–R2246, Jul. 2000.

[9] A. Narayanaswamy and G. Chen, "Thermal emission control with one-dimensional metallodielectric photonic crystals," *Phys. Rev. B*, vol. 70, no. 12, p. 125101, Sep. 2004.

[10] I. Celanovic, D. Perreault, and J. Kassakian, “Resonant-cavity enhanced thermal emission,” *Phys. Rev. B*, vol. 72, no. 7, p. 075127, Aug. 2005.

[11] Z. Wang, J. K. Clark, Y.-L. Ho, B. Vilquin, H. Daiguji, and J.-J. Delaunay, “Narrowband Thermal Emission Realized through the Coupling of Cavity and Tamm Plasmon Resonances,” *ACS Photonics*, vol. 5, no. 6, pp. 2446–2452, Jun. 2018.

[12] M. De Zoysa, T. Asano, K. Mochizuki, A. Oskooi, T. Inoue, and S. Noda, “Conversion of broadband to narrowband thermal emission through energy recycling,” *Nat. Photonics*, vol. 6, no. 8, pp. 535–539, Jul. 2012.

[13] T. Inoue, M. De Zoysa, T. Asano, and S. Noda, “Single-peak narrow-bandwidth mid-infrared thermal emitters based on quantum wells and photonic crystals,” *Appl. Phys. Lett.*, vol. 102, no. 19, p. 191110, May 2013.

[14] T. Inoue, M. De Zoysa, T. Asano, and S. Noda, “Realization of dynamic thermal emission control,” *Nat. Mater.*, vol. 13, no. 10, pp. 928–931, Oct. 2014.

[15] V. Lehmann, “The Physics of Macropore Formation in Low Doped n-Type Silicon,” *J. Electrochem. Soc.*, vol. 140, no. 10, p. 2836, Oct. 1993.

[16] G. Mertens, R. B. Wehrspohn, H.-S. Kitzerow, S. Matthias, C. Jamois, and U. Gösele, “Tunable defect mode in a three-dimensional photonic crystal,” *Appl. Phys. Lett.*, vol. 87, no. 24, p. 241108, Dec. 2005.

[17] M. Garín, D. Hernández, T. Trifonov, and R. Alcubilla, “Three-dimensional metallo-dielectric selective thermal emitters with high-temperature stability for thermophotovoltaic applications,” *Sol. Energy Mater. Sol. Cells*, vol. 134, pp. 22–28, Mar. 2015.

[18] W. Konz *et al.*, “Micromachined IR-source with excellent blackbody like behaviour,” in *Smart Sensors, Actuators, and MEMS II. Vol. 5836. International Society for Optics and Photonics*, 2005, vol. 5836, pp. 540–548.

[19] D. Cardador, D. Segura, D. Vega, and A. Rodríguez, “Transmission and thermal emission in the NO2 and CO absorption lines using macroporous silicon photonic crystals with 700 nm Pitch,” in *PHOTOPTICS 2017 - Proceedings of the 5th International Conference on Photonics, Optics and Laser Technology*, 2017, pp. 191–194.

[20] D. Cardador, D. Vega, D. Segura, T. Trifonov, and A. Rodríguez, “Enhanced geometries of macroporous silicon photonic crystals for optical gas sensing applications,” *Photonics Nanostructures - Fundam. Appl.*, vol. 25, pp. 46–51, Jul. 2017.

[21] S. Matthias, R. Hillebrand, F. Müller, and U. Gösele, “Macroporous silicon: Homogeneity investigations and fabrication tolerances of a simple cubic three-dimensional photonic crystal,” *J. Appl. Phys.*, vol. 99, no. 11, p. 113102, Jun. 2006.

[22] D. Segura, D. Vega, D. Cardador, and A. Rodriguez, “Effect of fabrication tolerances in macroporous silicon photonic crystals,” *Sensors Actuators, A Phys.*, vol. 264, 2017.

[23] W. K. Widger, M. P. Woodall, J. W. K. Widger, and M. P. Woodall, “Integration

of the Planck Blackbody Radiation Function," *Bull. Am. Meteorol. Soc.*, vol. 57, no. 10, pp. 1217–1219, Oct. 1976.

[24] D. Cardador-Maza, D. Segura-Garcia, I. Deriziotis, A. Rodriguez, and J. Llorca, "Macroporous Silicon Filters, a Versatile Platform for NDIR Spectroscopic Gas Sensing in the MIR," *J. Electrochem. Soc.*, vol. 166, no. 12, pp. B1010–B1015, Jul. 2019.

[25] J. Hodgkinson, R. Smith, W. O. Ho, J. R. Saffell, and R. P. Tatam, "Non-dispersive infra-red (NDIR) measurement of carbon dioxide at 4.2μm in a compact and optically efficient sensor," *Sensors Actuators B Chem.*, vol. 186, pp. 580–588, Sep. 2013.

[26] R. Lee and W. Kester, "Complete Gas Sensor Circuit Using Nondispersive Infrared (NDIR)," 2016.

[27] H. S. Wang, Y. G. Zhang, S. H. Wu, X. T. Lou, Z. G. Zhang, and Y. K. Qin, "Using broadband absorption spectroscopy to measure concentration of sulfur dioxide," *Appl. Phys. B*, vol. 100, no. 3, pp. 637–641, Sep. 2010.

[28] S. A. Tashkun, V. I. Perevalov, R. R. Gamache, and J. Lamouroux, "CDSD-296, high resolution carbon dioxide spectroscopic databank: Version for atmospheric applications," *J. Quant. Spectrosc. Radiat. Transf.*, vol. 152, pp. 45–73, Feb. 2015.

Results and Discussion

This chapter describes the most important results reported in the previous publications, which are related to the specific and additional objectives introduced at the beginning of the report.

6.1 Fabrication and analysis of photonic crystals with 4 µm and 2 µm

During the first year of the Thesis the efforts were directed 1) to understand the underlying physics of photonic crystals, 2) to get familiarized with the simulation programs and the characterizing systems (FT-IR, basically), and 3) to reproduce experimentally structures previously obtained in the group through the photoelectrochemical etching. The aim was to establish both the theory and the existing know-how of the group in order to project this knowledge into further work, in essence to photonic crystals fabricated in a square lattice of 700 nm.

The results obtained over this period were reflected in ***Impact of the Absorption in Transmittance and Reflectance on Macroporous Silicon Photonic Crystals***, in which it was described the effect that losses in silicon have in the optical response of photonic crystals fabricated in 4 µm and 2 µm. A first attempt was also made in the fabrication of 700 nm pitch photonic crystals without defect. As expected, photonic crystals transmission and reflection experienced a decreasing for higher values of the extinction coefficient. However, results showed that absorption losses of silicon do not have a real impact in the optical response of the photonic crystals.

In this work the scalability property of photonic crystals, discussed in the third chapter *Photonic crystals*, was applied in order to extrapolate the design of the pores from 4 µm and 2 µm to 700 nm. As a consequence, the optical response moved towards lower wavelengths. Specifically, the working frequency of the peak moved from 20 µm to 5 µm. This was the first time that it was predicted that macroporous silicon PhCs could reach the mid-infrared region thanks to operate at lower pitch.

6.2 Consolidate photonic crystal technology with defects using a pitch of 700 nm

Once both the manufacturing process and the simulation tools were mastered, the design of the photonic crystals with 700 nm pitch was improved. Specifically, a defect

within the structure was introduced in order to obtain a transmission peak (or a dip in the reflection) within the bandgap. In ***Study of resonant modes in a 700 nm pitch macroporous silicon photonic crystal,*** the fabrication of such structures was reported for the first time. Results showed that the position of the resonant peak could be adjusted simply by linearly controlling the length of the defect. What is more, experimental results showed a good agreement with simulation, meaning that they could be theoretically predicted. It should be noticed that in this case, the profile used to simulate the photonic crystals was changed from previous publication (*Impact of the Absorption in Transmittance and Reflectance on Macroporous Silicon Photonic Crystals*). In this case, the pear-shape profile was adopted in order to enhance the optical response.

Despite the improvements, the optical response of the photonic crystals was still far from being suitable to be used for spectroscopic detection of gases. In essence, the quality factor of the peaks was too low and the bandgap too narrow. Therefore, efforts were focused on increasing both features of photonic crystals in two directions.

a) On one hand, new geometries were numerically studied in order to increase the quality factor of the transmission peaks in ***Enhanced geometries of macroporous silicon photonic crystals for optical gas sensing applications***. In concrete, more periods were added to the modulated areas of the pores as well as the resonances were enhanced using a *tail* after the pores. Results show an improvement of the quality factor of the peak from 50 for 4 periods to 800 for 11 periods. The counterpart of adding more periods in the structure is the decreasing of the peak transmission. Simulation results showed a variation from 90 % for 4 periods to 45 % for 11 periods. It was determined that a good compromise between the transmission factor and the quality factor was in 9 periods.

Experimental results showed the same tendency of increasing the quality factor when more periods were added. However, they were several times lower than the ones theoretically expected. In this case, the quality factor went from 12 (5 periods) to almost 120 (8 periods). At that time, pores with more periods in the modulation areas could not be achieved experimentally (later pores with more than 11 periods have been successfully fabricated with a quality factor above 150).

A quality factor of 120 is a remarkable achievement in mid-infrared filters (see Table 2.4). In the particular case of carbon dioxide, whose absorption spectrum is one of the narrowest in the MIR (see Figure 2.1), having a quality factor of 120 allows to point to the tightest branch of its spectrum, the R-branch. In consequence, simulations were performed in order to explore the optical response of these narrow transmission peaks (or narrowband filters) when exposed to gas. For this purpose, the carbon dioxide absorption spectrum was approximated by two Lorentzian curves that adjusted to the contour of the absorption lines of CO_2 (see Figure 3.16). Subsequent studies showed that it was not an accurate approximation because it did not correspond to the resolution used during the thesis.

Simulations with gas on the pores showed greater sensitivity as periods increased. This was due to the fact that the narrower the peaks, the smaller the area. Thus, for the same gas concentration, a greater percentage of area was reduced in the case of more periods, thereby increasing sensitivity.

b) On the other hand, in ***Photonic molecules for improving the optical response of macroporous silicon photonic crystals for gas sensing purposes***, a genuine approach was done in order to increase both quality factor and bandgap width. In this case, the use of photonic molecules in conjunction with a chirped modulation was reported to be an effective way to achieve better optical features. In concrete, the initial quality factor of 25 was increased to 175 using this strategy and the bandgap was enlarged almost twice (reaching more than 1.5 μm of width).

The concept is as follows: when an identical cavity is added to the structure, a new resonant peak rises within the bandgap (see section 3.1.2 *Multiple point defects or photonic molecules*). This causes the bandgap to widen by approximately the same value as the width of the base of the new peak. When this peak is eliminated by adequately tuning the cavity and the shape of the pores (by means of chirped modulation), the bandgap remains enlarged but now with a unique peak in the bandgap. Furthermore, adding a new cavity means to introduce a new modulation area as well. In consequence, resonant frequencies are more filtered which, in turn, increases the quality factor of the peak. Finally, a 30% of transmission was reported by performing a membrane in the back side of the sample. Optimized process gave transmissions above the 50% maintaining the same quality factor of the peak.

These experimental results fit the simulations very well. Therefore, a simulation of the optical response of these structures with CO_2 in the environment was carried out, showing their suitability for spectroscopic detection of gases.

Optical features of macroporous silicon technology are given in the following table (based on Table 2.4):

	Macroporous Technology	
	Min	**Max**
Center wavelength	3.5 µm	14 µm
FWHM	25 nm	65 nm
Q-factor	60	175
Min. Transmission	30 %	55 %
Block range	3.7-4.5 µm	4.7-6.5 µm
Size (outer diameter)	12.5 mm	12.5 mm

* The row comparing prices has been intentionally removed from the table because, at this point, it is not possible to determine the price in the market although macroporous silicon technology is expected to be a competitive platform.

Table 6.1. Optical characteristics of macroporous silicon filters.

It can be seen from the above table that the reported technology has a very wide range of working frequencies covering all MIR. In addition, it reports the highest values for the quality factor. Transmissions are slightly below the values offered by the technologies in Table 2.4. The main shortcoming is the blocking range, which is clearly below the market values. Future studies should focus on different strategies to block lateral transmission (see section 6.5.1).

6.3 Gas detection in relevant ambient

Next step focused in using the fabricated photonic crystals in the detection of carbon dioxide. Although several samples were available, the results were delayed due to modifications in the set-up in order to ensure a good calibration of the measuring system. ***Macroporous silicon filters, a versatile platform for NDIR spectroscopic gas sensing in the MIR*** provides an extensive description of CO_2 detection using macroporous silicon photonic crystals as narrow filters. It shows that these filters followed Beer-Lambert's reformulated law when exposed to the gas for three different path lengths. Experimental values gave a detecting range from 0% to 1% with a limit of detection of about ±100 ppm for a path length of 2.4 cm. It should be mentioned that both parameters were limited by the set-up configuration. Extrapolation of the results showed that concentration in the range of 0% to 2.5% could be measured for an optimal path length of 4.5 cm in the case of carbon dioxide. In addition, the technology exhibited a very robust behavior against temperature and pressure variations.

Results were extrapolated to other gases in the mid-infrared range. For this purpose, an in-house program was developed in order to apply the Beer-Lambert law for broadband sources with a filter (see equation 2.5 and Figure 2.7). In this software a more accurate approximation of the gases was used. In concrete, it was used the HITRAN parameters for the used resolution in the FT-IR (4 cm^{-1}) at normal conditions (see Figure 3.16). Results showed good sensitivity and selectivity for compact lengths of the final device in the case of (but not restricted to) four particular gases. It should be mentioned that these extrapolations could be applied to other gases in the infra-red region with similar absorption spectra with similar results. In addition, the comparison to other technologies showed a reduction in the cross detection due to higher quality factors.

Table 6.2, based on the same scheme as in Table 2.3 summarizes the characteristic of NDIR detection using macroporous silicon narrow filters. The election of the emitter and the detector is based on the first prototype of gas sensor using the reported technology (see Appendix III).

Emitter	**Detector**	**Central λ (μm)**	**Path Len. (cm)**	**Gas detected**	**Detect. Limit (ppm)**	**Topology cell**	**Power cons. (mW)**
LED	Photo-diode	4.22 4.45 4.85 6.20 7.35	4.5 7.5 3.0 8.0 12.5	CO_2 N_2O OCS NO_2 SO_2	<100 ppm	FF	~250

Table 6.2. Characteristics of NDIR detection using macroporous silicon photonic crystals technology.

This study reporting gas detection in the MIR with macroporous silicon photonic crystals completes the main objective of the thesis.

6.4 Exploring other options of gas sensing with macroporous silicon photonic crystals

During the Thesis, some studies have been carried out parallel to the main line of research, basically concerning to double thermal emission. As discussed in chapter *Spectroscopic detection*, there are two main emitter-receiver configurations: LED-photodiode and heater-thermopile. In the first gas sensor prototype the first configuration has been used because almost the entire emission window fitted inside the bandgap and therefore no extra filtering is required. However, this option is also the most expensive, so the other solution, using photonic crystals as selective emitters, was explored.

The first approach was done in ***Transmission and thermal emission in the NO_2 and CO absorption lines using macroporous silicon photonic crystals with 700 nm pitch***, where it was reported for the first time the use of a macroporous silicon photonic crystals with a defect as selective thermal emitters. Nevertheless, the reported emission spectra were too poor for spectroscopic gas sensing. In fact, an important difference between the emission spectrum and the transmission spectrum was observed. This suggested that the cause of this discrepancy was the lack of structural homogeneity of the pores. The latest publication of this thesis, up to the date, ***Empirical demonstration of CO_2 detection using macroporous silicon photonic crystals as selective thermal emitters***, confirms this assumption. Indeed, when photonic crystals act as emitters, the active area is much bigger than the one involved in the transmission filtering. Therefore, inhomogeneity plays a key role in the quality of emissions. In other words, the greater the structural dispersion in the pores, the higher the optical dispersion and, consequently, the emission peak widens. Efforts were therefore focused on reducing this dispersion. In particular, the set-up was modified for better light diffusion in the electrochemical process (see Figure 4.6) and more periods were added to the modulated areas in order to have a better filtration of the emission. These modifications led to an enhancement in the quality factor, reaching the value of 120. In addition, the emission baseline was substantially reduced and the total emissivity of the peak was around a 55%.

With these features spectroscopic detection was performed at the R-Branch of CO_2. Results showed that the evolution of the peak when exposed to gas followed the same trend as the one reported in *Macroporous silicon filters, a versatile platform for NDIR spectroscopic gas sensing in the MIR*. It was also calculated the expected radiated power in the peak region, which turned out to be 200 µW for 1 cm^2 of active area, a value comparable to those in literature. Moreover, due to the narrowband emission, detection could be done with high sensitivity and selectivity. However, this was a non-filterless configuration: an additional filter was needed to detect only the emissivity of the peaks. This filtering could be easily done with one of the cheapest mid-infrared filters in the market or with a combination with other macroporous silicon filters. Nevertheless, deposition of metal or dielectric layers in order to block extra signal apart from the one of the peak should be explored in future work.

Up to this point, all detection has been performed using a face-to-face topology with a single filter. Since NDIR detection requires a reference channel to validate measurements, the only option under these conditions is to add a beam splitter that divides the initial beam into two different signals, using one as a reference and the other as active filter (see image c) of Figure 2.8). This configuration has the disadvantage of higher complexity in sensor design, which also leads to less compact devices.

A widely option is to use a dual configuration as discussed in section 2.2.3 *Gas cells and path lengths*. This idea was firstly explored in ***Coupling Defects in Macroporous Silicon Photonic Crystals*** where a photonic molecule consisting on two coupled cavities was used to rise two peaks within the bandgap. In this publication it was proposed that one of this peaks acted as the reference peak and the other as the active filter. In this way, a real time reference with the same path length and exposed to exactly the same external conditions would be used to rectify the detected signal.

This preliminary study laid the basis of dual emission bands using macroporous silicon photonic crystals with coupled cavities. This study is currently being reported and, at the date of the submission of the present Thesis, it has not been approved for publication. Further details can be found in Appendix II. The basic idea is to use identical cavities for instantaneous correction of both transmission and emission measurements. In this particular case, carbon dioxide is detected again. It can be seen that the reference peak, placed in the 3.9 μm band, where there is no gas absorption, does not undergo any variation when the photonic crystal is exposed to gas, but the active peak does. Specifically, the active peak follows the same behavior as reported in *Macroporous silicon filters, a versatile platform for NDIR spectroscopic gas sensing in the MIR* and *Empirical demonstration of CO_2 detection using macroporous silicon photonic crystals as selective thermal emitters*. This is, it follows the reformulated Beer-Lambert law. It can also be observed that any optical variation due to a change in the external conditions affect both peaks very similarly. In such a way that a linear relationship can be stablished between the reference peak and the reference peak. Therefore, corrections can be applied instantaneously in order to correct uncertainty and enhance the detection precision.

This last study combines all developments achieved during the thesis. On one hand it uses enhanced geometries for increasing the optical features of the photonic crystal (quality factor, bandgap widening and the reduction of the base-line of the peak). On the other hand, photonic molecules are exploited in order to create two quasi-identical peaks within the bandgap. In addition, macroporous silicon structure is heated in order to have narrowband selective emission.

These new configurations have been done in order to reduce 1) the complexity of the system and 2) the costs of the final device. In addition, macroporous silicon photonic crystals with defects exhibit peaks with higher quality factors than most of the currently available mid-infrared filters or sources. The weakest point of this technology is the existence of lateral transmission/emission after the bandgap, which forces to work with an extra filtering. Further work should focus in solve this question for the new objective of creating a spin-off based on the technology being reported.

6.5 Future work

6.5.1 For the principal research line

There are two main suggestions for solving the problem of unwanted signal at both sides of the bandgap of macroporous silicon photonic crystals. The first one is, as just commented, a passband filter that blocks lateral transmission/emission at both sides of the bandgap. This could be done by adding a new (or news) photonic crystal(s) at the end of the reported photonic crystals. In this case two-filtering stages would be done in the same

piece of material. Special attention should be paid to the transmission loss due to the concatenation of different photonic crystals.

The second suggestion is to deposit layers of different materials at the end of the structure. Each material, or combination of materials, would be designed in such a way that they would absorb either the transmission/emission until the bandgap or just after it. Thus, those layers would act as stop-band filters and at least two different combinations would be required in order to block the signal on both sides. The main handicap of this strategy would be the loss of operability, as signal blockage would depend on the intrinsic properties of the material. Therefore, it could not be adjusted and consequently the design for certain gases might not be possible to do. Nevertheless, any progress in this direction would put this technology in the market of filtering and selective emission.

Finally, future work should focus on the development of a final device for the detection of several gases in the MIR, exploring all the different options of emitter-receiver combinations and cell's topology reported.

6.5.2 Other research lines

During the last months of the thesis, new applications of the technology were explored. In concrete, in the field of biosensing and terahertz. In this case, different photonic structures would be used. In fact, the idea would be to move from three-dimensional to one-dimensional photonic crystals. This would improve both the quality factor and the bandgap width. In addition, operating with such 1D photonic crystals would allow to work at different ranges of the electromagnetic spectrum.

These photonic crystals would be made through the *Millefeuille* process (see Appendix I). In essence, 3D pores similar to those studied (with slight variations in the aspect ratio) would be used and then thermal annealing would be performed to proceed with the reorganization of the silicon atoms. This reorganization will cause the initial pores to be restructured into alternate layers of silicon and air, allowing the thickness of the layers to be controlled thanks to the initial design of the pores. In this way, the frequency range of application can be chosen. In addition, a defect can easily be placed in the center of the structure using this method. The current development of these structures has yielded results in the long infrared region. It is expected to have high quality transmission peaks and large bandwidths in other frequency ranges, such as terahertz.

Furthermore, the *Millefeuille* process would allow to create in-depth or *buried* channels that can be used for drug delivery in biosensing applications. In fact, a project is currently being developed for lab-on-a-chip detection. The idea comes from the collaboration done at the CNRS/LAAS center in Toulouse.

The aim of all these future works is to demonstrate that macroporous silicon is not an old-fashioned technology but instead, it offers a variety of options and applications due to its versatility of design and the cheap of its fabrication.

Conclusions

The main objective when starting the thesis was to use photonic structure based on macroporous silicon for spectroscopic gas detection. The starting point was the 2 µm and 4 µm technology that had been developed in the previous years in the MNT group. The optical response of these photonic crystals was in the long-IR and the introduced defects were too wide. Therefore, the pitch was lowered to 700 nm to reduce the bandgap position in the same proportion as the pitch.

When this was achieved, the characteristics of the peak were improved. That is, increase the quality factor, widen the bandgap and reduce the transmission of the peak baseline. Several solutions were explored. The first was to increase the number of periodicities and add a *tail* to the pores. Photonic molecules were used in the second solution. In both cases, the achieved peaks were narrow enough and the bandgaps wide enough for spectroscopic gas detection. Moreover, thanks to high quality factors, it was possible to target not only at the entire gas absorption spectrum, but also at a specific area of it.

Specifically, carbon dioxide was detected in the R-branch with a wide detection range, between 0% and 1%, for path lengths of 2.4 cm. High selectivity and sensitivity were also demonstrated, as well as robustness to changes in temperature and humidity. Finally, the expected resolution is considerably lower than the 100 ppm obtained experimentally.

These results, given for CO_2, were extrapolated to other gases in the mid-infrared in order to study the applicability of the technology throughout the MIR, resulting in an ideal platform for gas detection.

As it has been said before, spectroscopic detection using macroporous silicon photonic crystals was, at the beginning, the main objective of the thesis. However, more work has been done to improve the characteristics of detection and its future application to an NDIR device. Specifically, the thermal emission of photonic crystals was explored, demonstrating its applicability as narrow-band selective thermal emitters. In addition, they would allow to improve certain characteristics such as sensitivity and selectivity with respect to other conventional and low-cost solutions.

Photonic molecules were also used for dual spectroscopic detection. That is to say, using one peak inside the bandgap as a referential measure and the other as an active gas filter.

These two contributions, which go beyond the initial objective, have allowed to advance in the development of a sensor prototype based on macroporous silicon technology.

Future work will focus on eliminating the signal on both sides of the bandgap to achieve filter-less transmission and emission. The goal is to create a spin-off based on the technology described in this document. Moreover, the idea is to go beyond gas detection and explore other fields such as biosensing and terahertz by incorporating new manufacturing techniques such as the Millefeuille process.

Appendix I: Optical response of 700 nm structures obtained through the Millefeuille process

In section 4.1.4.3 it has been explained the atomic reorganization used in the Millefeuille process. Initially this method was used to obtain thin silicon layers from a thick substrate. This was previously reported with straight pores and for a single layer [1], [2]. In this case, the thickness of the formed layer(s) could not be chosen. The improvement of silicon Millefeuille process was to use modulated pores to control both the thickness and the separation between layers, i.e. air layers, for the production of multiple thin silicon layers. As described in section 4.1.4.3 those layers follow a periodical arrangement that is determined by initial pore profile. Therefore, the refractive index in the z-direction, orthogonal to the surface, is also periodical. This conforms an all-silicon Bragg filter. The concept all-silicon is important because, as seen in chapter 3 and clearly represented in Figure 3.4, the bandgap is increased for higher refractive index contrast. In addition, silicon is one of the materials which has higher refractive index.

In this Thesis the Millefeuille process has been explored in order to obtain wider bandgaps and higher quality factors for the reported structures, since the refractive index contrast is higher than 3D macroporous silicon structures.

Figure A.1.1 shows one of the firsts profiles used for demonstrating the viability of doing the Millefeuille process in samples with 700 nm pitch. In the right image it can be observed that atomic restructuration has turned 3D structures into 1D photonic crystals.

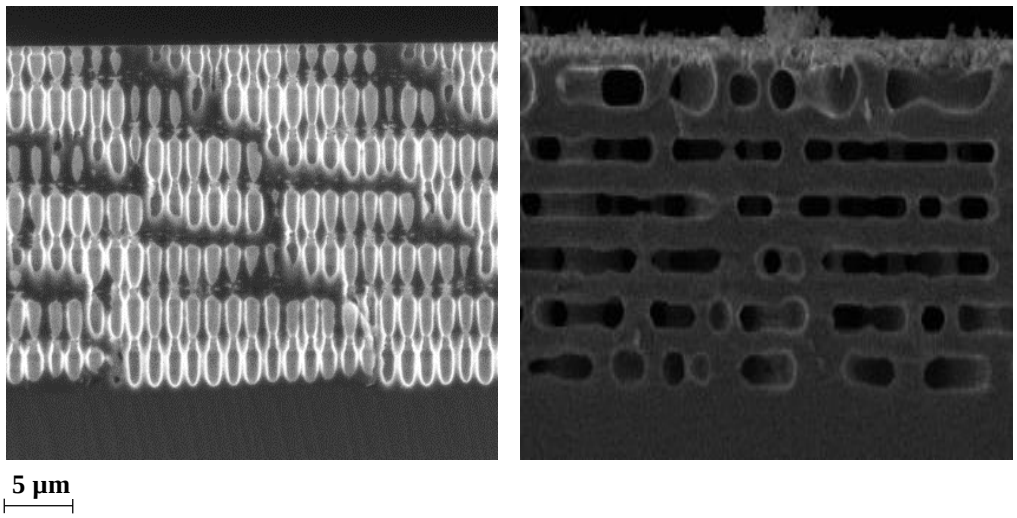

Figure A.1.1. SEM images for pores before (left) and after (right) the annealing. Although layers have not been completely formed, it can be seen that air layers correspond to the part of the period with more air, showing the controllability of the method.

The comparison between the optical response before and after the annealing shows an improvement in the reflectance of the structures (see Figure A.1.2). It should be noticed that despite the usual procedure for reporting the results during this document, mainly given in transmission, now the results are going to be given, mainly, using the reflection spectrum. This is due to the fact that the process is not totally controlled and transmission is much more sensitive to scattering and other phenomenon that disperse light than in reflection.

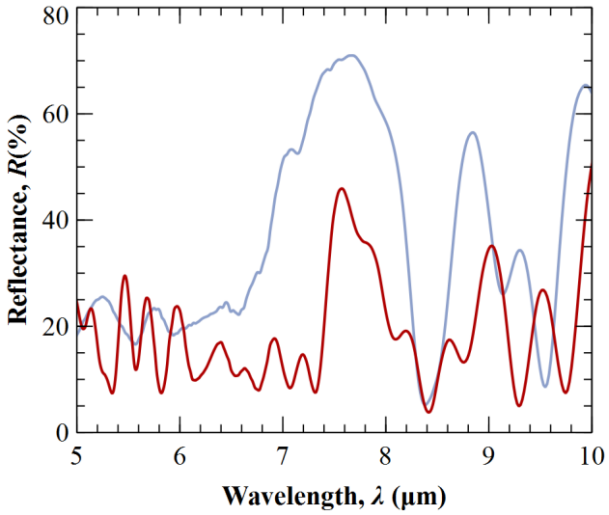

Figure A.1.2. Optical response of the structures of Figure A.1.1. Red line corresponds to before the annealing and blue line after the 1D structure formation. Bandgap widening can be clearly observed.

Figure A.1.3 shows an improved design for 3D photonic crystals and its atomic reorganization. In this case, a defect in the middle of the structure is inserted. As a consequence, resonant frequencies are introduced within the bandgap (see Figure A.1.4).

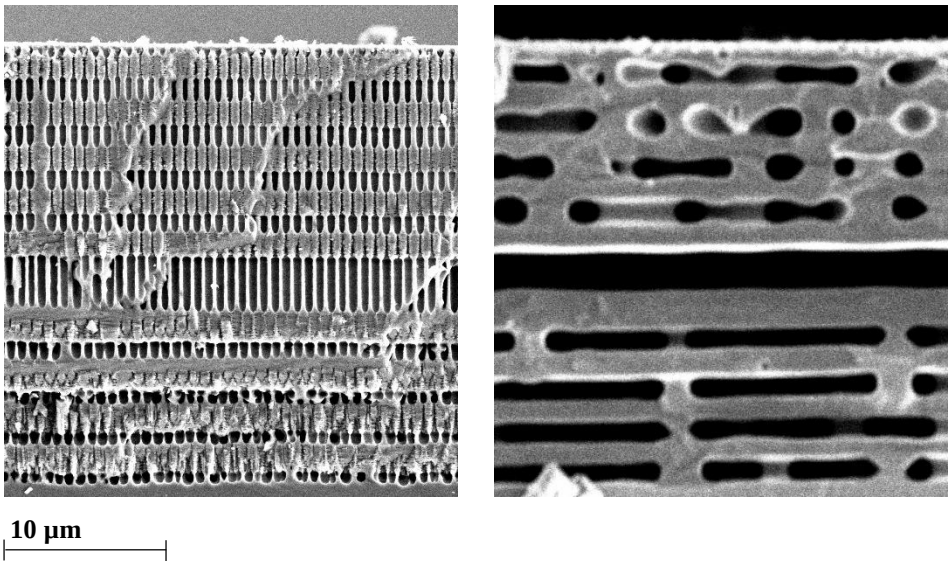

Figure A.1.3. A defect introduced in the photonic crystal (left) correspond to a deeper layer of air after the annealing (right).

The optical response is not as good as expected because layers are not completely formed. Only in very little regions of the samples it seems to be done. Generally talking, the optical response of the structure is the average of optical response of the different areas with their respective structures.

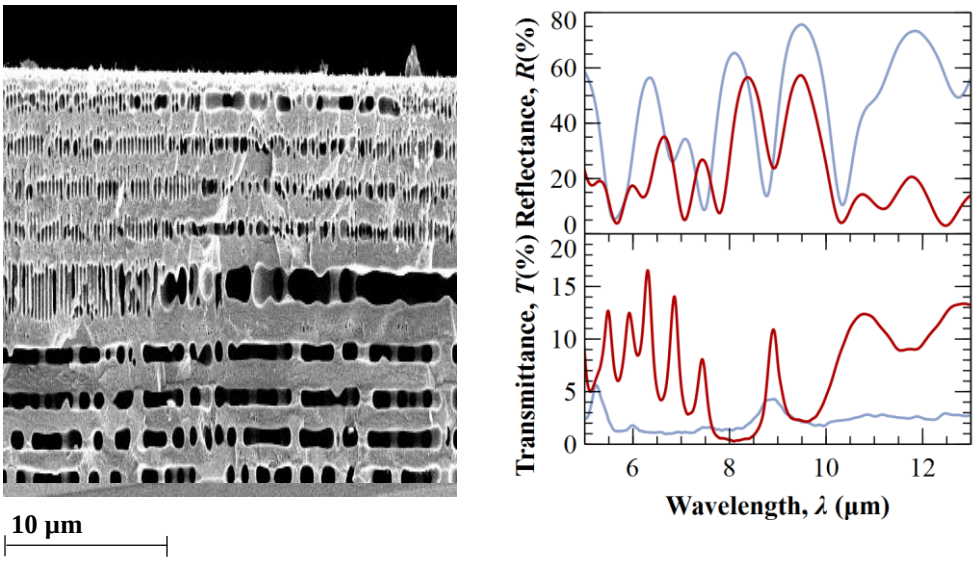

Figure A.1.4. (Left) The annealing dos not affect to every part of the photonic crystal in the same way. (Right) Although the features still have to be improved, it can be seen an enhancement of the optical response. Red line represents the response before the annealing and blue line after.

Others annealing have been performed with different initial profiles. Figure A.1.5 shows the first approach to achieve 1D photonic molecules through the Millefeuille process. Exposure time at furnace and Argon volume should be adjusted in order to obtain a homogeneous distribution of the silicon layers throughout the entire sample.

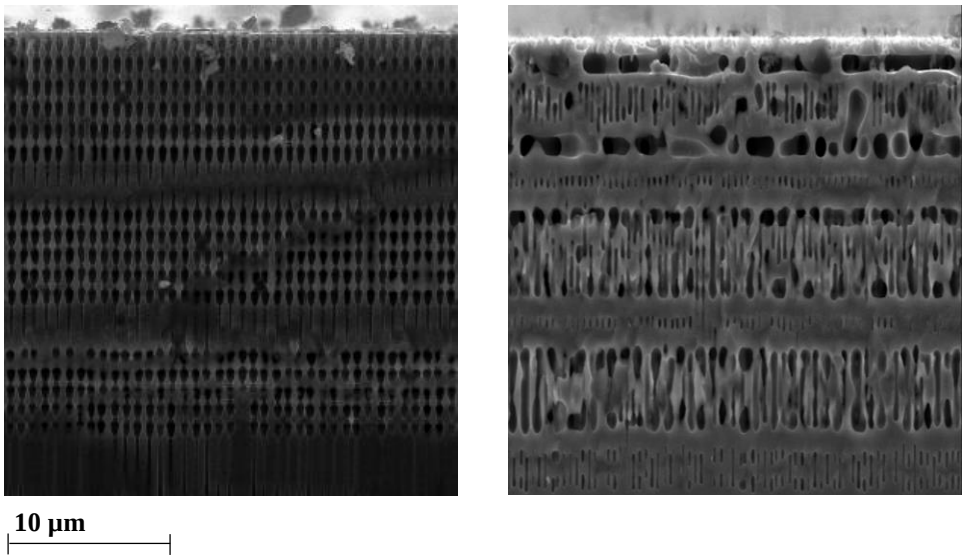

Figure A.1.5. SEM images for coupled cavities in 1D photonic crystals obtained through the Millefeuille process.

The optical response of this structure shows two clearly distinguishable resonances inside the bandgap (see Figure A.1.6). It can be also observed that there is a substantial enhancement of optical features after the annealing, in particular the reflectance.

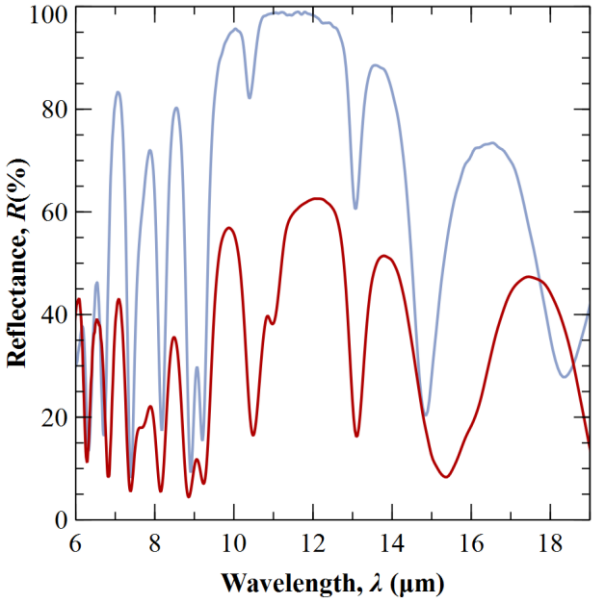

Figure A.1.6. Reflectance for the photonic crystal with photonic molecules of Figure A.1.5.

Although more improvements need to be made, these results are promising and seem to be in line with the initial assumption that 1D structures will substantially improve 3D results.

References

[1] V. Depauw, I. Gordon, G. Beaucarne, J. Poortmans, R. Mertens, and J.-P. Celis, "Proof of concept of an epitaxy-free layer-transfer process for silicon solar cells based on the reorganisation of macropores upon annealing," *Mater. Sci. Eng. B*, vol. 159–160, pp. 286–290, Mar. 2009.

[2] V. Depauw *et al.*, "Micrometer-Thin Crystalline-Silicon Solar Cells Integrating Numerically Optimized 2-D Photonic Crystals," *IEEE J. Photovoltaics*, vol. 4, no. 1, pp. 215–223, Jan. 2014.

Appendix II: macroporous silicon photonic molecules for dual detection of CO_2

This appendix describes the detection of carbon dioxide by means of photonic molecules, following the study initiated in section 5.5. In this case, the peaks have been optimized and exhibit nearly the same shape, which facilitates the correlation between peaks in order to determine the variation due to external influence. First attempts show two similar peaks placed at carbon dioxide and carbon monoxide. However, those peaks exhibit low quality factors and, as they are pointing to two different gases, cross-detection may be given. In some applications the simultaneous detection of these two gases (or other couple of gases) could be interesting. In the present case, the aim is to only sense carbon dioxide with high-quality and selectivity. For this purpose, the design of the photonic crystal was improved, finally obtaining the active peak at the carbon dioxide absorption spectrum and the reference peak centered at the 3.9 μm non-absorbent window. Results show satisfactory detection using the photonic crystals as narrow-band filters as well as dual selective emitters. In the latter case, the emission peaks become wider due to structural dispersion explained in section 5.8. Nevertheless, they are still narrow enough for high-quality spectroscopic detection.

* The purpose of this study is to be published in the short term. This is why it is structured as if it was an article of Chapter 5. However, please note that it has been written taking into account the discussions made along previous chapters.

Introduction

At the present there are multitude of spectroscopic gas sensors that use a reference to reduce the uncertainty of the measurement [1]. This reference can be done in different ways as explained in section 2.2.3. The beam splitter configuration allows to work with a single detector if the signal is conveniently chopped, alternating both reference and active signals. Otherwise, two identical detectors can be used to sense the two beams, as depicted in Figure 2.8. In both cases, this solution evaluates the same signal before and after the gas exposure using two optical paths, which adds complexity to the design [2]. An alternative is to use two different detectors, one for the reference and the other for the gas measurement, as explained in previous chapters. In this case, the optical path lengths can be designed in order to be exactly the same and, therefore, the signal arriving to both detectors will have experienced the same external conditions. This is a more compact option to detect gas but the counterpart is that different signals are compared. A third solution is to have a single detector and use a calibration curve that is stored in a device. By measuring the external parameters, such as temperature, pressure, humidity, etc., it can be inferred the state of the peak and, therefore, the variation of the measured peak can be compared with the reference in the known working conditions. This method would allow not to use a reference cell. In addition, comparing the fitting of the measured curve with an analytical model allows more accurate results than when compared to an instant reference curve, which also contains noise [3]. However, as in the first method, a certain complexity is required to store data, to evaluate external conditions, i.e. introducing sensors to the device, and to process them properly. In addition, this system does not contemplate the drifts in amplitude that emitters usually experience over time.

This study proposes dual detection by means of photonic molecules, as introduced in section 5.5. The aim is to perform instantaneous reference measurements by placing the active peak within the gas absorption spectrum and the reference in the 3.9 μm non-absorbent band. In this way both signals experience the same external conditions and suffer the same hypothetical amplitude drifts. In addition, as they exhibit almost the same shape, an easy correlation can be done in order to correct the detected signal. Moreover, by comparing the instantaneous reference with a previous calibration, the peak of measurement can be compared with its theoretical model in an instant, which would give high sensitivities to the final device with minimal data processing and storage.

Finally, to assess the abovementioned, carbon dioxide detection is successfully reported using the photonic crystals as narrow-band pass filters and selective emitters.

Experimental

The preparation of macroporous silicon photonic crystals with embedded photonic molecules has been done following the steps described in the section 4.1.3. This is, the sample is pre-processed, i.e. implantation and lithography, so that the electrochemical etching can be performed. The current profile used is similar to the one depicted in Figure 4.6. In this case, a second cavity and a third modulation area are introduced –see Figure A.2.1. The number of periods in each modulation area range between 5 and 8.

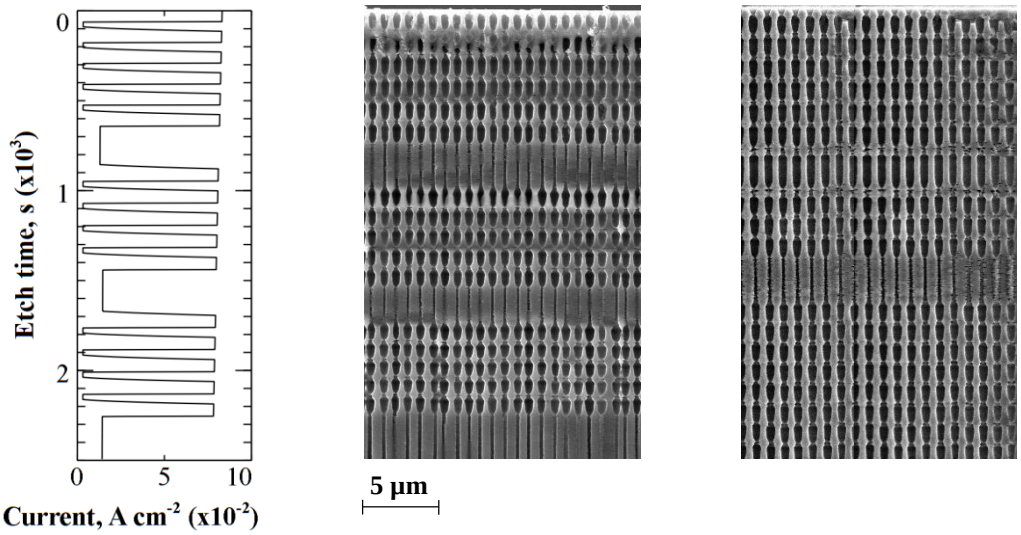

Figure A.2.1. (Left) Basic two-cavity profile. Number of periods between cavities and in modulation areas have been changed in order to place the position of the resonant peaks at the desired wavelength ranges. (Right) SEM images for the different profiles used in the study. From left to right: profile with 5 and 8 periods per modulation area and asymmetric configuration.

As usual, the optical response of the macroporous silicon PhC was obtained using the Bruker Optic's Vertex FT-IR spectrometer with an aperture of 1 mm and a resolution of 4 cm-1. The gas detection setup was the same as reported in sections 5.7 and 5.8.

Results and discussions

The study starts by shortening the vertical modulation of photonic crystals reported in section 5.5 in order to place one of the two resonant peaks inside the absorption spectrum of carbon dioxide. The first satisfactory sample, whose spectrum is depicted in the left image of Figure A.2.2 (grey dotted line), presented two main drawbacks; the low quality factor of the peaks and the position of the reference peak, located in the absorption spectrum of carbon monoxide (CO). To overcome these drawbacks, the number of periods was increased from 5 to 8. As explained in section 3.1.2, the distance of the peaks can be controlled by the coupling intensity, i.e. the number of periods between cavities. For higher number of periods, the cavities are less coupled and the peaks become more and more close one to each other –see Figure 3.8. In addition, the quality factor of both peaks are also increased as a consequence of more filtering. In the case of $N = 8$, an approximate value of $Q \sim 120$ was obtained, what enabled the spectroscopic detection at the R-branch of CO_2. However, the problem of the reference peak pointing to another gas was not solved. In effect, although it moved towards the active peak, thus remaining outside the CO range, it ended up pointing to another gas, nitrous oxide (N_2O). Therefore, there would still be the problem of cross-detection in an arbitrary mixture of different gases what, at the end, could lead to errors in the data treatment. To solve this issue, NDIR gas sensors usually work with the reference peak located within a window, centered at 3.9 µm, where there is no gas absorption. Hence, next step focused in tuning the whole spectrum to higher frequencies in order to have the active peak at the carbon dioxide range and the reference peak in the aforementioned window. To achieve this, the photonic crystal was redesigned in order to create a stronger coupling in the photonic molecule and, thus, increase the separation between the peaks by approximately 35%. The new structure, that can be seen in Figure

A.2.1, was composed of two asymmetric cavities with same length but different height – relation 4:1– and separated by only three periods.

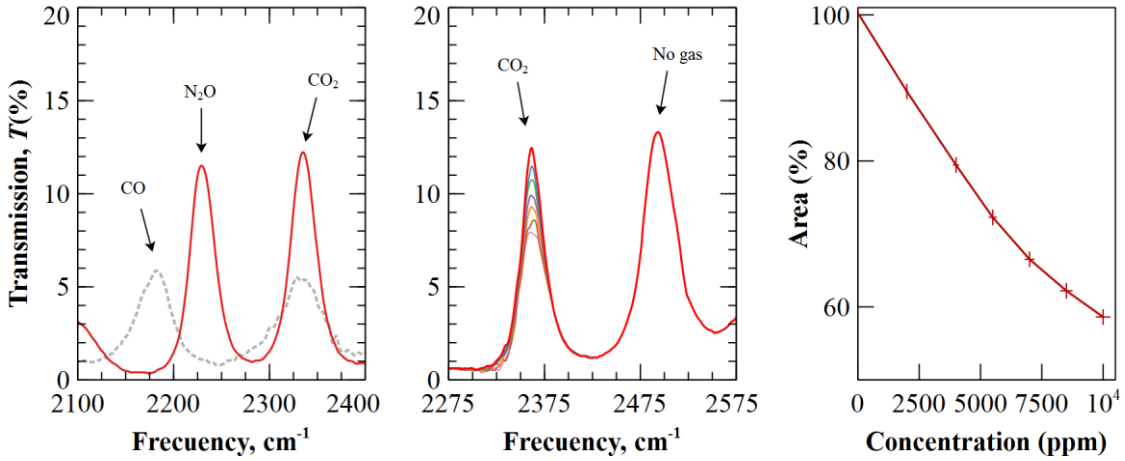

Figure A.2.2. (Left) Transmission spectra of the samples with two equal cavities with 5 (grey dotted line) or 8 (red line) periods in the modulation area; (Center) Optical response of the asymmetrical photonic crystal shown in right image of Figure A.2.1 when exposed to 0; 2,000; 4,000; 5,500; 7,000; 8,500 and 10,000 ppm. (Right) Area of the active peak vs the concentration.

The central image of Figure A.2.2 shows the response of the resulting photonic crystal when exposed to different concentrations of CO_2. As expected, the reference peak remains unaffected as the concentration increases, while the active peak decreases in amplitude following the reformulated Beer-Lambert law –see right image of Figure A.2.2, where the area-concentration curve follows the same tendency reported in sections 5.7 and 5.8.

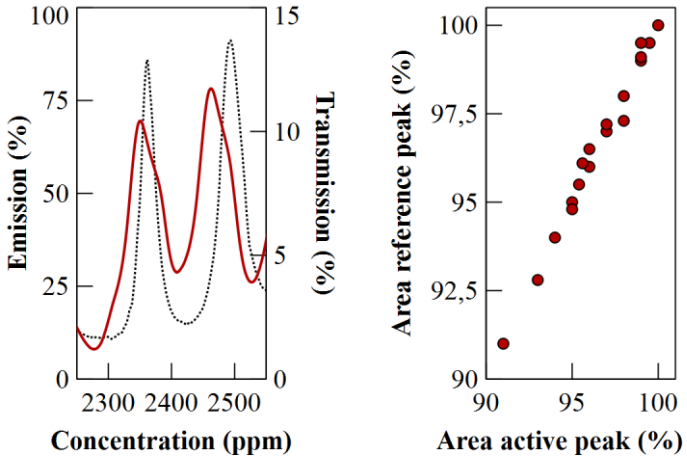

Figure A.2.3. (Left) Transmission and emission spectra for the asymmetric photonic crystal. (Right) Comparison between the variation in the area of reference and active peaks when the temperature ranges from 400 ºC (100 % of the area) and to 380 ºC (91% of the area).

Once verified the behavior of the photonic molecules working as transmission filters, efforts were directed to demonstrate that they could also be used as dual selective emitters. To do this, the photonic crystals were heated to 400 ° C in the Bruker annex of the FT-IR. As expected, the spectrum moved towards lower frequencies due to local refractive index modification of the medium. Therefore, the next step was to oxidize the samples so that when the oxide was removed, the whole spectrum shifted to higher frequencies –see the post-etching technique explained in section 4.1.4.1. Finally, the peaks pointed the CO_2 and the no-gas window as in transmission and new measurements with different concentrations were done. As it can be seen in Figure A.2.3, there is a significant difference between

curves in transmission and emission. This is because the active emitting area is wider than in transmission and cooperative resonators widen the emission band due to structural dispersion –see section 5.8.

Finally, it was stablished a linear correlation in the area of both peaks when thermic changes were performed in order to simulate temperature drifts over time. Results in right image of Figure A.2.3 show that the reference peak can be used to do linear corrections in the measurement and therefore reduce its uncertainty.

Conclusions

Dual detection of CO_2 using macroporous silicon photonic crystals has been demonstrated by means of photonic molecules. The coupling of the cavities has been used to rise two quasi-identical peaks within the bandgap in such a way that one of the peak acts as a reference the other as the active filter. The design of the profile has evolved in order to place high-quality peaks within the R-branch of CO_2 and the 3.9 non-absorbent band. Measurement show a good accordance to previous studies. Those structures demonstrated to be dual selective emitters when heated to 400 ºC. In addition, the correlation between peaks under temperature variation was studied, showing a linear dependency. Those results are a prove that macroporous silicon can be engineered in such a way that dual detection can be achieved either in transmission or emission. Both configurations would lead to advantages, such as lower complexity and more cost-effective solution, if introduced in NDIR devices.

References

[1] D. Popa, F. Udrea, D. Popa, and F. Udrea, “Towards Integrated Mid-Infrared Gas Sensors,” *Sensors*, vol. 19, no. 9, pp. 2076–2090, May 2019.

[2] J. Chen, “Compact laser-spectroscopic gas sensors using vertical-cavity surface-emitting lasers,” Technische Universität München, 2011.

[3] P. Kluczynski, J. Gustafsson, Å. M. Lindberg, and O. Axner, “Wavelength modulation absorption spectrometry — an extensive scrutiny of the generation of signals,” *Spectrochim. Acta Part B At. Spectrosc.*, vol. 56, no. 8, pp. 1277–1354, Aug. 2001.

[4] D. Cardador, D. Segura, and A. Rodríguez, “Photonic molecules for improving the optical response of macroporous silicon photonic crystals for gas sensing purposes,” *Opt. Express*, vol. 26, no. 4, pp. 4621–4630, Feb. 2018.

[5] T. Trifonov, A. Rodríguez, L. F. Marsal, J. Pallarès, and R. Alcubilla, “Macroporous silicon: A versatile material for 3D structure fabrication,” *Sensors Actuators A Phys.*, vol. 141, no. 2, pp. 662–669, 2008.

[6] D. Cardador, D. Segura, D. Vega, and A. Rodriguez, “Coupling defects in macroporous silicon photonic crystals,” in *2017 Spanish Conference on Electron Devices (CDE)*, 2017, pp. 1–3.

Appendix III: first prototype for NDIR detection using photonic macroporous silicon photonic crystals

This appendix describes the circuitry developed by Daniel Segura Garcia for the use of the macroporous silicon photonic crystals in NDIR gas detection. As explained in section 6.4, the LED-photodiode has been the chosen configuration for the prototype. Figure A.3.1 depicts the emission curve of the LED (red line) and the transmission of the filter (blue line). It can be observed that almost all the bandgap fits inside the emission window. There is only a few signal present at the edges of the bandgap. This unwanted signal will reach the detector and introduce some uncertainty in the measurement if there are gases whose absorption spectrum is in those frequencies. In addition, it will also increase the limit of detection. This is why an extra filtering is required. Nevertheless, the convolution of both figures, which is the signal that will reach to the gas and then the detector, shows that almost the 70% of the signal is that of the filter. Therefore, although the unwanted signal introduces some undesired effects in detection, the first prototype will work without an additional filter for the sake of simplicity and without substantial loss of detection capability.

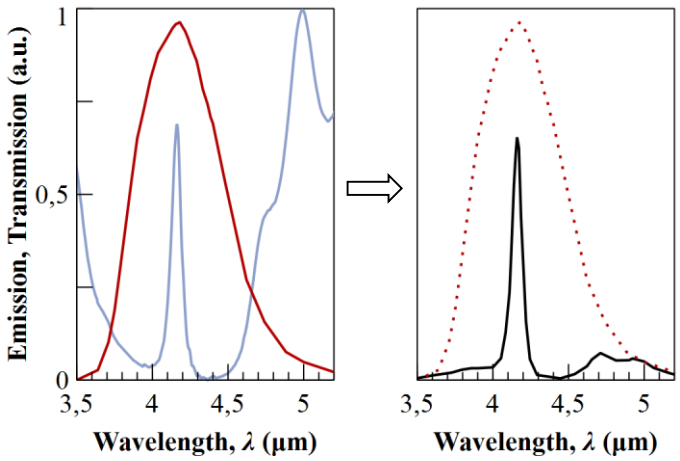

Figure A.3.1. (Left) Emission and transmission spectra for LED and filter (red and blue lines, respectively) and their convolution (black line in right image).

The circuit has two differentiated parts, the one corresponding to the emitter current driver (*LED43*, Frankfurt Laser Company) and the one corresponding to the receiver stabilization and amplification (*FDPSE2X2*, Thorlabs), as sketched in Figures A.3.2 and Figure A.3.3.

Due to thermal dissipation the LED must be operated with a pulsed signal. Thus, a square signal -1025 Hz and 50 % duty cycle – must provide approximately 150 mA to the LED. This, frequency is selected to reduce the interferences with the harmonics of most

common source of interference, i.e. incandescent tubes. To reduce the influence of the interferences, and taking advantage of the generated clock signal for the LED, a lock-in amplifier –synchronized with the LED- is designed after the photoconductive detector. A fixed voltage with low noise, directly dependent on the concentration, can be measured at the end of the amplifier.

Since the LED is switching and requires large currents, different voltage regulators together with decoupling capacitors are strategically placed in the board to reduce the effect of the electromagnetic noise, especially in the amplifier.

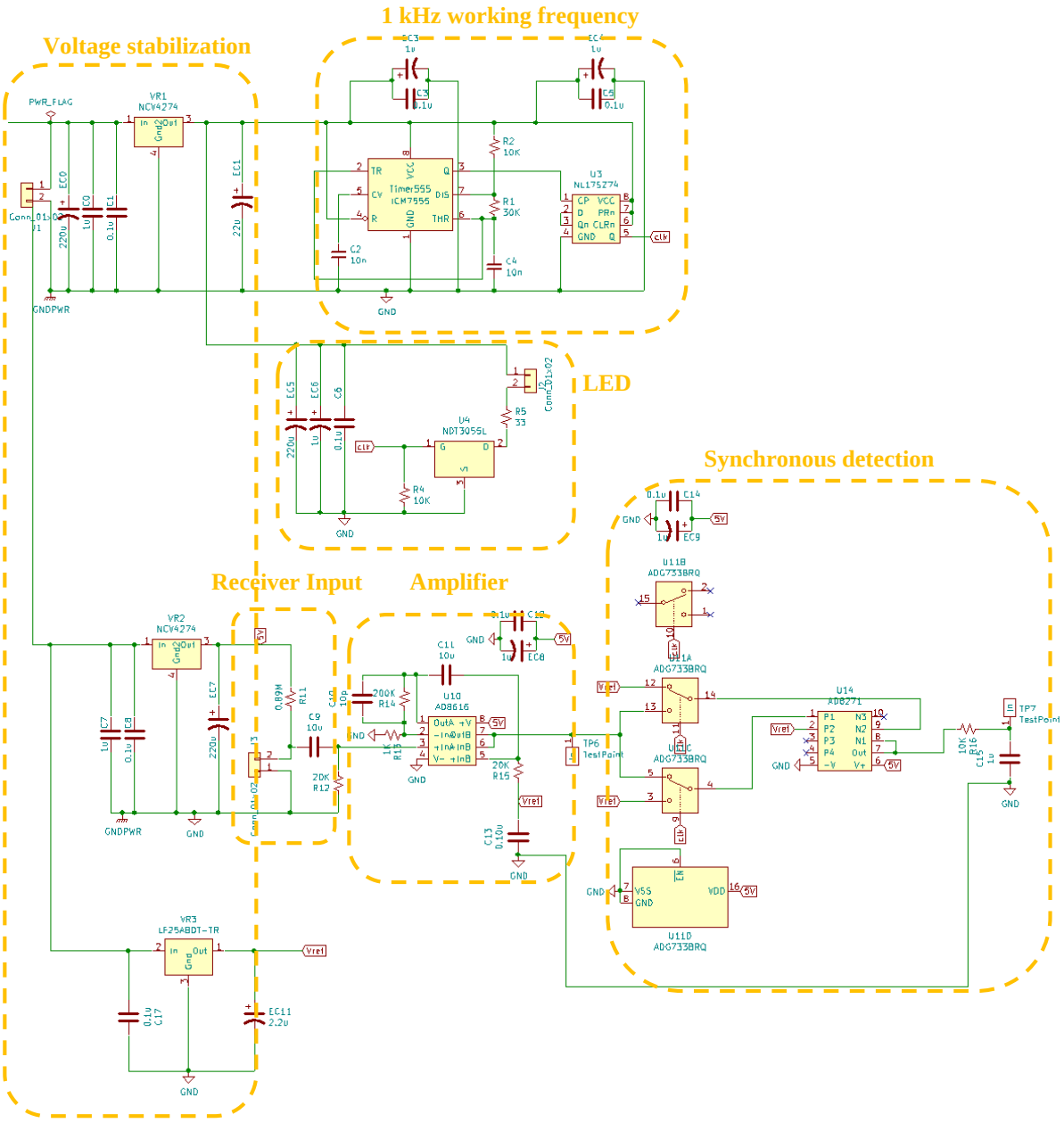

Figure A.3.2. Diagram of the circuitry that involves emitter and receiver and their respective stages.

The resulting board is shown in Figure A.3.3, where the detection and emission stages are separated to reduce the noise interference introduced by the LED driver. First measurements have been made to check the correct functioning of the design in the presence of gases. Once the adjustments to optimize the response have been made, the

photonic crystal will be placed in front of the receiver, thus avoiding the scattering of the rays.

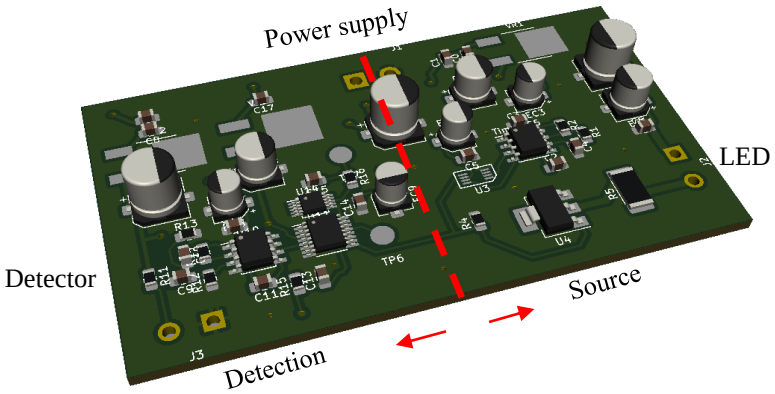

Figure A.3.3. Circuit board.

Finally, since the detector is sensitive to external radiation, it is necessary to design a coverture that prevents from it. In the case of the first prototype it has been fabricated a covering made of aluminum (see Figure A.3.4). This covering will act also as a gas cell and is 2 cm diameter x 4 cm wide. This is a first approach and can be miniaturized in a future, since, the synchronous detection should prevent the influence of non-synchronous interference signals.

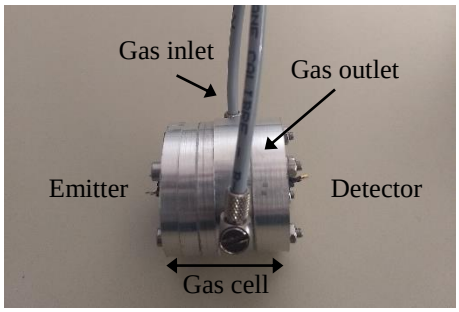

Figure A.3.4. First prototype for NDIR detection with macroporous silicon with an aluminum coverture.

Measurements with the photonic crystal as mid-infrared filter will give to the group a first experimental prove of high selectivity and sensitivity in NDIR devices thanks of using macroporous silicon photonic crystals. As explained in previous sections, more cost-effective devices will be achieved using those photonic crystals as (dual) thermal emitters. In this case, another circuitry would have to be developed because the mechanisms for detection and lightning vary from the ones exposed in this appendix.